

Search for Diboson Resonances with CMS and Pixel Barrel Detector Calibration and Upgrade

Dissertation

zur
Erlangung der naturwissenschaftlichen Doktorwürde
(Dr. sc. nat.)

vorgelegt der
Mathematisch-naturwissenschaftlichen Fakultät
der
Universität Zürich

von
Jennifer Ngadiuba
aus
Italien

Promotionskomitee

Prof. Dr. Benjamin Kilminster
Prof. Dr. Florencia Canelli
Dr. Andreas Hinzmann
Dr. Lea Caminada

Zürich 2017

Abstract

This doctoral thesis presents a search for new massive particles decaying to pairs of W, Z, and Higgs bosons performed with the CMS detector at the Large Hadron Collider (LHC). Such processes are the prominent feature of several extensions of the standard model that aim to clarify open questions in the SM, such as the apparently large difference between the electroweak and the gravitational scales. The lepton+jet final states are considered, in which one of the bosons decays leptonically and the other hadronically. The first study is focused on the search for a WH resonance decaying into the $\ell\nu b\bar{b}$ final state and based on data recorded in proton-proton (pp) collisions at a center-of-mass energy $\sqrt{s} = 8$ TeV during 2012 (LHC Run 1). The second study is focused on a WW or WZ resonance decaying into the $\ell\nu q\bar{q}$ final state and based on 2015 data corresponding to pp collisions at $\sqrt{s} = 13$ TeV (LHC Run 2). These final states are particularly challenging because for large resonance masses the bosons are highly energetic and the two quarks from the decay are separated by a small angle in space, resulting in the presence of one single merged jet after hadronization. This jet is identified as coming from a Higgs, W or Z boson by applying novel jet substructure techniques and dedicated algorithms for the identification of b jets. The results for these two studies are finally combined with limits derived in companion CMS searches for resonances decaying to a pair of bosons in several different final states, with data collected in both LHC Run 1 and Run 2. This is the first combined search for heavy resonances with both WW/WZ and WH/ZH signatures.

44

Excellent detector performance is of utmost importance to search for new and rare physical phenomena. The efficient reconstruction of secondary vertices and precise measurements of the track impact parameter rely on this detector. Hence, the inner tracking pixel detector is a key component to identify Higgs bosons in their dominant decay into b and \bar{b} quarks. Stable performance and future upgrades are thus necessary to maintain high identification efficiency of b jets for the entire lifespan of the LHC. Various aspects of my contributions to the CMS pixel barrel detector are detailed in the second part of the thesis. In particular, a major effort has been put forth LHC Run 1 to replace and test faulty channels, and to perform calibrations aimed at optimizing the detector after it has been heavily irradiated during Run 1. The detector has been re-installed into CMS in December 2014 and the large effort in commissioning and calibration resulted in the successful and stable operation of the CMS pixel detector during data-taking in 2015 and 2016. Despite the excellent performance up to now, the pixel detector has not been designed to cope with the upcoming high luminosities of the LHC in the next years. Hence, a stepwise upgrade is foreseen, which is referred to as the “Phase I Pixel Upgrade”, which has been recently installed in the spring of 2017. A test stand at the University of Zurich has been setup, which includes a slice of the CMS pixel data-acquisition system and all components of the upgraded read-out chain, together with a number of detector modules. The test system has been fundamental to develop new tests and procedures to be used during the upgraded detector assembly, commissioning and calibration.

Zusammenfassung

Die vorliegende Doktorarbeit stellt eine Suche nach neuartigen schweren Teilchen am CMS Detektor am Large Hadron Collider (LHC) vor. Die Suche befasst sich mit dem Zerfall dieser neuartigen Teilchen in Paare von W, Z oder Higgs Bosonen. Diese Zerfälle sind ein wichtiges Merkmal verschiedener Erweiterungen des Standard Modells, die beabsichtigen offene Fragen des SM, wie zum Beispiel die deutliche Differenz zwischen der elektroschwachen Skala und der Planck-Skala, zu beantworten. Die Suche basiert auf semileptonischen Zerfällen, in denen eines der Bosonen leptonisch und das andere hadronisch zerfällt. Die erste Analyse befasst sich mit WH Resonanzen im Endzustand $\ell\nu b\bar{b}$ und benutzt die Daten, die im Jahr 2012 bei Proton-Proton Kollisionen mit einer Schwerpunktsenergie von $\sqrt{s} = 8 \text{ TeV}$ (LHC Run 1) aufgezeichnet wurden. Die zweite Analyse befasst sich mit WW und WZ Resonanzen im Endzustand $\ell\nu q\bar{q}$ und benutzt die Daten, die im Jahr 2015 bei Proton-Proton Kollisionen mit einer Schwerpunktsenergie von $\sqrt{s} = 13 \text{ TeV}$ (LHC Run 2) aufgezeichnet wurden. Die Rekonstruktion dieser Zerfälle ist äussert anspruchsvoll. Aufgrund der grossen Masse der Resonanz haben die Bosonen eine sehr hohe Energie, wodurch die Quarks im hadronischen Zerfall in einen kleinen Raumwinkel emittiert werden und sich zu einem einzigen Teilchenjet im Detektor zusammenfügen. Um diesen Teilchenjet als das Zerfallsprodukt von Higgs, W oder Z Bosonen zu identifizieren, werden neuartige Methoden angewandt, um die Unterstruktur der Teilchenjets aufzulösen und spezielle Algorithmen benutzt, um b-Quarks zu identifizieren. Die Resultate der beiden Analysen werden mit den Resultaten weiterer CMS Analysen, die in anderen Zerfallskanälen nach massiven Resonanzen suchen, kombiniert. Die Kombination beinhaltet die Daten von LHC Run 1 und Run 2. Die hier vorgestellte Arbeit ist die erste Suche nach massiven Resonanzen, die sowohl WW/WZ als auch WH/ZH Signaturen behandelt.

Der einwandfreie Betrieb des CMS Detektors ist unerlässlich für die Suche nach neuen und seltenen physikalischen Phänomenen. Insbesondere beruht sie auf der effizienten Rekonstruktion von Sekundärvertices und der präzisen Messung des Stossparameters von rekonstruierten Spuren. Der Pixeldetektor im Innersten des CMS Detektors ist folglich eine Schlüsselkomponente, um Ereignisse mit Higgs Bosonen, die in Paare von b-Quarks zerfallen, zu identifizieren. Um die hohe Rekonstruktionseffizienz von b-Quarks am CMS Detektor während der gesamten Laufzeit des LHCs zu gewährleisten, sind eine zuverlässige Datennahme und später neue und verbesserte Detektoren erforderlich. Meine vielfältigen Beiträge zum CMS Barrel Pixeldetektor werden im zweiten Teil dieser Arbeit besprochen. Dabei ist insbesondere das Testen und die Reparatur des Detektors nach LHC Run 1 zu erwähnen, sowie die optimale neue Kalibration, die den Effekt allfälliger Strahlenschäden mildert. Der Pixeldetektor wurde im Dezember 2014 wieder in CMS installiert und die Anstrengungen, die unternommen wurden, um den Detektor in Betrieb zu nehmen und zu kalibrieren, bilden die Grundlage für die zuverlässige und äusserst erfolgreiche Datennahme während 2015 und 2016. Trotz des bis anhin einwandfreien Betriebs des Pixeldetektors, ist er nicht dafür geschaffen, die bevorstehenden hohen Luminositäten der nächsten Jahre am LHC zu bewältigen. Deshalb sind schrittweise Verbesserungen des Detektors vorgesehen. Der erste verbesserte Detektor, der sogenannte "Phase 1 Pixel Upgrade", wird im Frühling 2017 installiert. An der Universität Zürich wurde ein Testsystem für den Phase 1 Pixeldetektor aufgebaut, das einen Teil des CMS Datennahmesystems, sowie alle Komponenten der Ausleseelektronik des Pixeldetektors und einige Detektormodule umfasst. Die wichtigsten neuen Tests und Prozeduren, die für den Bau, die Inbetriebnahme und die Kalibration des Phase 1 Pixeldetektors benötigt werden, sind an diesem Testsystem entwickelt worden.

Contents

110

111	1 Introduction	1
112	2 The standard model and beyond	4
113	2.1 The standard model	4
114	2.1.1 Electroweak theory	6
115	2.1.2 Spontaneous symmetry breaking	9
116	2.1.3 The Higgs mechanism	10
117	2.1.4 The Higgs and Yukawa interactions	12
118	2.1.5 Observation of a particle compatible with the standard model Higgs boson	14
119	2.1.6 Quantum chromodynamics	17
120	2.2 Limitations of the standard model	18
121	2.3 Theories of new physics	21
122	2.3.1 Warped extra dimensions	21
123	2.3.2 Compositeness	25
124	2.3.3 Heavy vector triplet	26
125		
126	3 The CMS experiment at the LHC	30
127	3.1 The Large Hadron Collider	30
128	3.2 The CMS detector	33
129	3.2.1 Tracking detectors	35
130	3.2.2 Calorimetry	37
131	3.2.3 Muon detectors	40
132	3.2.4 The trigger system	42
133		
134	I Search for diboson resonances with CMS	45
135	5 Data sets and simulated samples	50
136	5.1 Simulation of proton-proton collisions	50
137	5.1.1 Monte Carlo event generators	50
138	5.1.2 CMS detector simulation	55
139	5.2 Simulated samples	55
140	5.2.1 Simulation of signal processes	55
141	5.2.2 Simulation of background processes	58
142	5.3 Data sets	59
143		
144	6 Object and event reconstruction	61
145	6.1 Tracks and primary vertices	61
146	6.1.1 Track reconstruction	61
147	6.1.2 Primary-vertex reconstruction	63
148	6.2 Electrons	64
149	6.2.1 Electron reconstruction	64
149	6.2.2 Electron trigger	67

150	6.2.3	Electron identification	69
151	6.3	Muons	74
152	6.3.1	Muon reconstruction	74
153	6.3.2	Muon trigger	76
154	6.3.3	Muon identification	77
155	6.4	Jets	79
156	6.4.1	Jet clustering algorithms	81
157	6.4.2	Jet reconstruction and calibration	82
158	6.4.3	Identification of b jets	88
159	6.5	Missing transverse energy	93
160	6.6	$W \rightarrow \ell\nu$ reconstruction	95
161	7	Identification of highly boosted $W/Z \rightarrow q\bar{q}^{(\prime)}$ and $H \rightarrow b\bar{b}$	97
162	7.1	Jet substructure observables	97
163	7.1.1	Pruned jet mass	97
164	7.1.2	N-subjettiness	98
165	7.2	The V tagging algorithm	100
166	7.3	The H tagging algorithm	102
167	8	Analysis strategy	106
168	8.1	Event selection and categorization	106
169	8.2	$W+jets$ background estimate with α ratio method	109
170	8.2.1	Background estimation procedure	110
171	8.2.2	Extraction of the $W+jets$ normalization	111
172	8.2.3	Extraction of the $W+jets$ shape	112
173	8.2.4	Validation of the α method	115
174	8.3	Modelling of top quark production	116
175	8.4	Signal modeling	118
176	8.5	Systematic uncertainties	122
177	8.5.1	Systematic uncertainties in the background estimation	122
178	8.5.2	Systematic uncertainties in the signal prediction	123
179	8.6	Testing for a new resonance hypothesis	125
180	8.6.1	Limit setting procedure	126
181	8.6.2	The asymptotic approximation	130
182	8.6.3	Quantifying an excess of events	131
183	9	Results of the search for $WH \rightarrow \ell\nu b\bar{b}$ resonance	132
184	9.1	Final m_{WH} distribution	132
185	9.2	Significance of the data	133
186	9.3	Cross section limits	134
187	10	Results of the search for WW and $WZ \rightarrow \ell\nu q\bar{q}$ resonances	136
188	10.1	Final m_{WV} distribution	136
189	10.2	Significance of the data and cross section limits	136
190	11	Combination of searches for diboson resonances at $\sqrt{s} = 8$ and 13 TeV	139
191	11.1	Inputs to the combination	140
192	11.1.1	Reinterpretations	140
193	11.2	Combination procedure	142
194	11.3	Results	143

195	11.3.1 Limits on W' and Z' singlets	143
196	11.3.2 Limits on heavy vector triplet V'	145
197	11.3.3 Limits on bulk graviton	146
198	11.3.4 Significance at 2 TeV	146
199	12 Conclusions	148
200	II Calibration and upgrade of the CMS pixel barrel detector	149
201	13 Introduction	150
202	14 The CMS pixel barrel detector	152
203	14.1 Design	152
204	14.2 Detector modules	153
205	14.2.1 Sensor	153
206	14.2.2 Readout chip	156
207	14.2.3 Token bit manager	158
208	14.3 Detector readout and control	158
209	14.3.1 Readout of the analog signal	159
210	14.3.2 Detector control and programming	160
211	14.3.3 Supply tubes	161
212	14.4 Pixel online software	162
213	15 Optimization and commissioning for LHC Run 2	164
214	15.1 Effects of radiation damage in LHC Run 1	164
215	15.2 Optimization for LHC Run 2	167
216	15.3 Overview of pixel calibrations	169
217	15.3.1 Adjustment of readout chain settings	169
218	15.3.2 Optimization of the pulse height information	177
219	15.4 Re-commissioning for LHC Run 2	181
220	15.4.1 Installation into CMS	181
221	15.4.2 Calibrations at -10 °C	182
222	15.5 Performance at the start of Run 2	183
223	16 Phase I upgrade of the CMS pixel barrel detector	187
224	16.1 Motivations	188
225	16.2 Detector layout	190
226	16.3 Pixel modules	191
227	16.3.1 The digital ROC	192
228	16.3.2 The TBM and readout	192
229	16.4 Supply tubes	195
230	16.5 The test stand	196
231	16.6 Testing and calibration	199
232	16.6.1 Delay adjustments	199
233	16.6.2 POH bias and gain	200
234	16.6.3 Read back test	201
235	16.6.4 ROC analog current and digital voltage	202
236	17 Conclusions	204

237	III Summary	205
238	A Studies on track reconstruction problems	208
239	Bibliography	212

Introduction

243 The current understanding of the fundamental constituents of matter and the interactions
 244 between them dates back to the middle of the 1970’s and is summarized in a theory called the
 245 *standard model* (SM) of particle physics [1]. Although the SM has demonstrated remarkable
 246 and continued successes in providing experimental predictions and describing the observations,
 247 it does leave some phenomena unexplained. Thus, it is believed to be only an approximation
 248 of a more complete theory. The SM does not incorporate a quantum description of gravitation
 249 as described by general relativity, or account for the accelerating expansion of the Universe
 250 (as possibly described by dark energy). The model does not contain any viable dark matter
 251 particle that possesses all of the required properties deduced from observational cosmology.
 252 Furthermore, it is not yet understood why gravitation is sixteen orders of magnitudes weaker
 253 than the electroweak interaction.

254 In order to obtain conditions in which production of elementary particles can be studied,
 255 particle accelerators are used. The start-up of the Large Hadron Collider (LHC) at CERN
 256 in 2009 marked the beginning of a new era in particle physics. Being the highest energy
 257 collider ever built, it allows one to probe particle physics in an energy domain previously
 258 out of reach so far. A first milestone was already recently reached, in 2012, when the last
 259 unproven prediction of the SM, namely the existence of the scalar Higgs boson, through
 260 the interaction of which the elementary particles can acquire mass, was finally confirmed by
 261 the LHC experiments, ATLAS [2] and CMS [3]. Despite this last remarkable confirmation
 262 of the SM, a major effort is ongoing to verify the existence of new physics exploiting the
 263 frontier energies achievable by the LHC. An important example of this quest is provided by
 264 the work described in this thesis. In fact, a search is presented for new massive particles
 265 decaying to pairs of W, Z, and Higgs bosons performed with the CMS detector. Several
 266 theories of new physics predict the existence of heavy particles that preferentially decay to
 267 such final states. These models usually aim to clarify open questions in the SM such as the
 268 apparently aforementioned large difference between the electroweak and the gravitational
 269 scales. Notable examples of such models include theories of extra dimensions [4, 5] and
 270 scenarios with composite Higgs bosons [6, 7].

271 First, a study has been conducted focused on the search for a WH resonance decaying
 272 to $\ell\nu b\bar{b}$ and based on data recorded in proton-proton (pp) collisions at a center-of-mass
 273 energy of $\sqrt{s} = 8$ TeV during 2012 (Run 1). This is one of the first searches for new physics
 274 with the Higgs boson in the final state, being made possible only after its discovery and
 275 the measurement of its mass. A second study has then been performed focusing on a WW
 276 or WZ resonance decaying to $\ell\nu q\bar{q}$ and based on 2015 data corresponding to pp collisions
 277 at $\sqrt{s} = 13$ TeV (Run 2). These final states are particularly challenging because for large
 278 resonance masses the bosons are highly energetic and the hadronization products from their
 279 decay overlap in the detector, preventing their identification as resolved jets. Thus, they
 280 are accessible only through novel jet reconstruction techniques, called “V tagging” (for a
 281 vector boson V = W or Z) and “H tagging”, which exploit the substructure of such objects
 282 and help to resolve the collimated decay products. Furthermore, additional sensitivity is
 283 achieved in the $\ell\nu b\bar{b}$ search channel by combining jet substructure algorithms with the specific
 284 characteristics of jets arising from the hadronization of bottom quarks (b jets).

The search in the $\ell\nu b\bar{b}$ final state performed with data collected during Run 1 reported a deviation of 2.2 standard deviations with respect to the SM expectations at a reconstructed WH invariant mass of 1.8 TeV, arousing large interest in the physics community. The excitement was further enhanced by the deviation reported in the same mass range by the ATLAS collaboration in a search for heavy diboson resonances in the all-hadronic final state. Therefore, when the LHC resumed physics collisions at higher energy in 2015, a major effort was put forth explore the mass region of the excess with the first new data. The results of the second search described in this thesis and based on 2015 data did not confirm the excess. However, in order to fully understand the compatibility of the excess, a statistical combination was performed of these results together with limits derived in similar CMS searches for resonances decaying to a pair of bosons in several different final states, with data collected in both LHC Run 1 and Run 2. This work presents for the first time the experimental status of the searches in CMS for heavy resonances decaying to boson pairs, including all three W, Z and H massive bosons. As all these searches have similar sensitivities, their combination significantly improves the results of the individual analysis.

The CMS pixel barrel detector constitutes the central part of the CMS detector with about 48 million readout channels. Thanks to its capability of measuring secondary vertices with high precision, it plays a key role in the identification of events with long-lived objects such as b quarks, which is fundamental for Higgs boson and top quark searches, and one of the analysis topics of this thesis. Its excellent performances are thus fundamental to access physical processes with a low cross section and b quarks in the final states, which is one of the main features of the analysis described in this thesis. The barrel part of the CMS pixel detector was developed, designed and built at PSI in cooperation with ETH Zurich and the University of Zurich. In the framework of this thesis important contributions were made. These include calibrations and testing of the detector after it has been heavily irradiated during the first LHC data-taking period. This work has been carried out during the two years (2013–2014) of shut down of the LHC after Run 1. Furthermore, after the re-installation of the pixel detector into CMS in December 2014, a large effort has been put in commissioning and calibration. The detector was then successfully operated during pp collision data-taking in 2015 and 2016.

My contributions have additionally been focused on the upgrade of the barrel pixel detector, required to cope with the LHC luminosity increases that lead to higher event rates. The project, referred to as “Phase 1 Pixel Upgrade”, was defined with a technical design report in 2012. The new system is currently under assembly and testing and has now been installed into CMS in the spring of 2017. During the design and prototyping phase of the upgrade barrel system, the University of Zurich has been responsible for the testing of the complete system. For this purpose, a test stand has been setup, which includes a slice of the full readout chain consisting of a group of pixel detector modules connected through optical links to the front-end boards for readout and control and powered using a set of DC-DC converters. The main goal of the system test was to test all components of the detector system prior to full production, as well as establish test and calibration procedures for the assembly and commissioning. I have contributed to the assembly of the test system and I implemented some of its functionalities. Furthermore, I employed the system to test new calibration procedures aimed at guaranteeing a quick verification of the detector functionality during assembly and commissioning, as well as stable operations at the beginning of the 2017 data-taking period.

This thesis is organized in two parts. The first part is dedicated to the search for diboson resonances introduced above. In particular, in Chapter 2 a review of the standard model of

334 particle physics is given, together with a discussion about its limitations and an introduction
335 on scenarios of new physics predicting the existence of massive resonances decaying to pairs
336 of W, Z, and Higgs bosons. Chapter 3 summarises the experimental setup, focusing on the
337 Large Hadron Collider and the CMS detector, that was used to collect the data analyzed
338 in this work. A brief overview of the signals under study and of the analysis strategy is
339 given in Chapter 4. The description of proton-proton collisions and their generation using
340 Monte Carlo simulations is the topic of Chapter 5, while Chapter 6 is devoted to a description
341 of the methods used in CMS to reconstruct the event and the physics objects relevant for
342 this analysis. The algorithms used to identify the substructure inside highly energetic jets
343 present in the decay of massive resonances represent a key aspect of this analysis and are
344 reviewed in Chapter 7. Chapter 8 contains the main steps of the analysis, including details
345 on the final event selection, the estimation of the SM background, the modelling of the signal,
346 systematic uncertainties and statistical methods. The final results for the two independent
347 searches are presented in Chapter 9 and Chapter 10 for the 8 TeV and 13 TeV data analyses,
348 respectively. In Chapter 11 the aforementioned statistical combination of all CMS searches
349 for diboson resonances is presented. Finally, Chapter 12 provides a brief summary of this work.
350

351 The second part of the thesis concentrates on hardware-related work including the various
352 aspects of my contributions to the CMS pixel barrel detector. An overview of the project
353 is first given in Chapter 13, followed by a description of the design and main features of
354 the present detector. Chapter 15 is dedicated to the efforts put during LS1 in optimizing
355 and maintaining the detector, as well as the steps of the re-installation into CMS and
356 commissioning for LHC Run 2. Since most of the work has been focused on calibrating the
357 detector, and overview of the calibration procedure is provided together with the results from
358 commissioning. Furthermore, the performance of the detector at the start up of Run 2 are
359 discussed. The design and main features of the upgraded system and of the test stand at
360 the University of Zurich are described in Chapter 16, where the new calibration procedure
361 developed for the commissioning of the new detector are also detailed. Finally, a summary of
362 this work is provided in Chapter 17.

The standard model and beyond

366 Elementary particles and their interactions are described by a fundamental theory called the
 367 standard model (SM) [1]. It describes three of the four fundamental forces of nature, namely
 368 the electromagnetic, weak and strong interactions, in the form of quantum field theories
 369 (QFT) with local gauge invariance. This theory has been confirmed by a large number of
 370 experimental results in the last forty years: from the precision electroweak measurements
 371 performed at the Large Electron-Positron (LEP) and Tevatron colliders [8], as well as the
 372 measurements of deep-inelastic scattering at the HERA electron-proton collider [9], to the
 373 recent LHC era (Chapter 3). The SM constitutes one of the most successful achievements in
 374 modern physics. It provides a very elegant theoretical framework, which is able to describe
 375 most of the known experimental phenomena in particle physics with high precision.

376 The basic ingredients of the SM are reviewed in Section 2.1. This is followed by a
 377 discussion in Section 2.2 about a few of the main open issues of the SM, which motivate
 378 theories of new physics. Finally, three of the most popular theories beyond the standard
 379 model are introduced in Section 2.3. These models provide the theoretical framework in
 380 which the search for new particles described in this thesis is conducted.

381 2.1 The standard model

382 The standard model attempts to explain all the phenomena in nature in terms of the proper-
 383 ties and interactions of a small number of fundamental particles of three distinct categories
 384 (Table 2.1): two spin-1/2 families of fermions called *leptons* and *quarks*, and one family of
 385 spin-1 bosons called *gauge bosons*, which act as ‘force carriers’ in the theory. All particles
 386 of the SM are assumed to be *elementary*, i.e. they are treated as point particles, without
 387 internal structure or excited states.

389 The class of fermions include six quarks (up, down, charm, strange, top, bottom) and six
 390 leptons (electron, electron neutrino, muon, muon neutrino, tau, tau neutrino), and to each of
 391 them is associated an anti-particle with the same mass and opposite quantum numbers. The
 392 fermions are organized in three groups (generations) of pairs from each category:

$$\begin{pmatrix} \nu_e & u \\ e & d \end{pmatrix}, \quad \begin{pmatrix} \nu_\mu & c \\ \mu & s \end{pmatrix}, \quad \begin{pmatrix} \nu_\tau & t \\ \tau & b \end{pmatrix}.$$

393 The defining property of the quarks is that they carry color charge, and hence, interact
 394 via the *strong* interaction. A phenomenon called color confinement results in quarks being
 395 very strongly bound to one another, forming color-neutral composite particles (*hadrons*)
 396 containing either a quark and an antiquark (*mesons*) or three quarks (*baryons*). Familiar
 397 examples of baryons are the proton and neutron, which also have the smallest mass among
 398 this family of particles. As quarks also carry electric charge and weak isospin, they interact
 399 with other fermions both via the *electromagnetic* and *weak* interactions. The three neutrinos
 400 do not carry electric charge, so their interaction is only driven by the weak force, which
 401 makes them difficult to detect. However, since the electron, muon, and tau all carry an

Table 2.1: Particles of the standard model [10].

	Symbol	Name	Mass (MeV)	Charge (e)	Spin
Up-type quarks	u	up	2.2	+2/3	1/2
	c	charm	1.27	+2/3	1/2
	t	top	173.21	+2/3	1/2
Down-type quarks	d	down	4.7	-1/3	1/2
	s	strange	96	-1/3	1/2
	b	bottom	4.18	-1/3	1/2
Up-type leptons	ν_e	electron neutrino	< 2 eV	0	1/2
	ν_μ	muon neutrino	< 0.19	0	1/2
	ν_τ	tau neutrino	< 18.2	0	1/2
Down-type leptons	e	electron	0.51	-1	1/2
	μ	muon	105.7	-1	1/2
	τ	tau	1776.9	-1	1/2
Gauge bosons	γ	photon	0	0	1
	W^\pm	W	80.4 GeV	± 1	1
	Z	Z	91.2 GeV	0	1
	g	gluon	0	0	1
Higgs boson	H	Higgs	125.1 GeV	0	0

402 electric charge, they interact electromagnetically. Each member of a generation is heavier
 403 than the corresponding particle of lower generations. As the first generation charged particles
 404 do not decay, all ordinary matter is composed of such particles. In particular, all atoms
 405 consist of electrons orbiting around atomic nuclei, ultimately constituted by up and down
 406 quarks. Second and third generation charged particles, on the other hand, decay with very
 407 short half-lives, and are observed only in very high-energy environments. Neutrinos of all
 408 generations also do not decay, and pervade the universe, but rarely interact with ordinary
 409 matter. Although neutrinos were originally assumed to be massless in the standard model, it
 410 is now known from experimental results that they have very small but finite masses.

411 In the SM, gauge bosons are defined as force carriers that mediate the strong, weak, and
 412 electromagnetic fundamental interactions. The use of the word ‘gauge’ refers to the fact that
 413 all three fundamental interactions arise as the consequence of requiring invariance under local
 414 gauge symmetries. Specifically, the gauge symmetry group of the SM is $SU(3)_C \times SU(2)_L \times$
 415 $U(1)_Y$. Among the gauge bosons, the *photons* mediate the electromagnetic force between
 416 electrically charged particles. The photon is massless and is described by the theory of
 417 *quantum electrodynamics* (QED). The W^\pm and Z gauge bosons mediate the weak interactions
 418 between particles of different flavors (all quarks and leptons). They are massive, with the
 419 Z being slightly heavier than the W. The weak interactions involving the W exclusively
 420 act on left-handed particles and right-handed antiparticles. Furthermore, the W carries an
 421 electric charge and therefore couples via the electromagnetic interaction. The electrically
 422 neutral Z boson interacts with both left-handed particles and antiparticles. These three gauge
 423 bosons along with the photons are grouped together, as collectively mediating the *electroweak*
 424 *interaction*, which is described in Section 2.1.1.

425 Eight massless *gluons* carrying color charge, mediate the strong interactions between
 426 quarks and also interact among themselves. The gluons and their interactions are described
 427 by the theory of *quantum chromodynamics* (QCD), which is described in Section 2.1.6.

As discussed in more in detail in Section 2.1.2, one additional spin-0 particle, called the *Higgs boson*, is postulated to explain the origin of mass within the theory, since without it all the particles in the model are predicted to have zero mass.

In addition to the strong, weak and electromagnetic interactions between quarks and leptons, there is a fourth force of nature, the gravitational force, which is not accounted for in the standard model. In fact, the gravitational interaction between elementary particles is so small that it can be neglected at the presently accessible energies.

2.1.1 Electroweak theory

The theory of electroweak interactions is based on the $SU(2)_L \times U(1)_Y$ gauge group with the quantum numbers of weak isospin I and hypercharge Y . Quarks and leptons are represented by spinor fields ψ , which are functions of continuous space-time coordinates x^μ . From experimental evidences it is known that the weak interaction is of the form of vector minus axial current ($V - A$), or in other words, it couples only to left-handed chirality states. It is therefore convenient to write the field ψ as the sum of the two chirality components:

$$\psi_L(x) = \frac{1 - \gamma^5}{2} \psi(x) \quad \text{and} \quad \psi_R(x) = \frac{1 + \gamma^5}{2} \psi(x). \quad (2.1)$$

The left-handed fields are grouped into $SU(2)_L$ doublets consisting of one charged and one neutral lepton, or one up and one down quark, with a weak isospin $I = 1/2$:

$$\begin{pmatrix} \nu_\ell \\ \ell \end{pmatrix}_L \quad \text{and} \quad \begin{pmatrix} q_u \\ q_d \end{pmatrix}_L.$$

For up-type quarks and neutrinos the third component of the weak isospin is assigned as $I_3 = +1/2$; for down-type quarks and charged leptons the component is $I_3 = -1/2$. The right-handed partners (ℓ_R , q_{uR} , q_{dR}) transform as $SU(2)_L$ singlet with weak isospin $I_3 = 0$. The weak hypercharge Y aforementioned is then defined via electric charge Q and weak isospin to be $Y = 2Q - 2I_3$. Thus, members within a doublet carry the same hypercharge: $Y = -1$ for leptons and $Y = 1/3$ for quarks.

In quantum field theories, the equations of motion for the different fields considered are derived from the Lagrangian that contains all the information on the fields and on their interaction. In the SM, the fermionic fields are added by hand to the Lagrangian to account for experimental observations. The situation is however different for the bosonic fields, as their existence is a direct consequence of invariance properties of the Lagrangian. This mechanism can be understood by starting from the Lagrangian for a free spin-1/2 particle with mass m :

$$\mathcal{L}_0 = i\bar{\psi}\gamma^\mu\partial_\mu\psi - m\bar{\psi}\psi, \quad (2.2)$$

where γ^μ are the Dirac matrices. It is straightforward to verify that the \mathcal{L}_0 is invariant under global $U(1)$ transformations

$$\psi(x) \xrightarrow{U(1)} \psi'(x) \equiv e^{iQ\theta}\psi(x), \quad (2.3)$$

where Q is the electric charge carried by the particle involved and θ an arbitrary constant. However, the free Lagrangian is no longer invariant if one allows the phase transformation to depend on the space-time coordinate, i.e. under local phase redefinitions $\theta = \theta(x)$, because

$$\partial_\mu\psi(x) \xrightarrow{U(1)} e^{iQ\theta}(\partial_\mu + iQ\partial_\mu\theta)\psi(x), \quad (2.4)$$

and \mathcal{L}_0 picks up an extra term. The *gauge invariance* is the requirement that the $U(1)$ phase invariance should hold locally. This is only possible if some additional terms are added to the Lagrangian, so to cancel the $\partial_\mu \theta$ term in Eq. 2.4. This is achieved by introducing a new spin-1 field $A_\mu(x)$, called a “gauge” field, that transforms as

$$A_\mu(x) \xrightarrow{U(1)} A'_\mu(x) \equiv A_\mu(x) + \frac{1}{e} \partial_\mu \theta, \quad (2.5)$$

and by defining a covariant derivative

$$\mathcal{D}_\mu \equiv \partial_\mu - ieQ A_\mu, \quad (2.6)$$

which has the required property of transforming like the field itself:

$$\mathcal{D}_\mu \psi(x) \xrightarrow{U(1)} (\mathcal{D}_\mu \psi)'(x) \equiv e^{iQ\theta} \mathcal{D}_\mu \psi(x). \quad (2.7)$$

The resulting Lagrangian

$$\mathcal{L} = i\bar{\psi} \gamma^\mu \mathcal{D}_\mu \psi - m\bar{\psi} \psi = \mathcal{L}_0 + eQ A_\mu \bar{\psi} \gamma^\mu \psi \quad (2.8)$$

is then invariant under local $U(1)$ transformations. For the new gauge field to be a true propagating field, a gauge-invariant kinetic term has to be added to the Lagrangian

$$\mathcal{L}_A = -\frac{1}{4} F_{\mu\nu} F^{\mu\nu}, \quad (2.9)$$

where $F_{\mu\nu} \equiv \partial_\mu A_\nu - \partial_\nu A_\mu$. A possible mass term for the gauge field, $m^2 A^\mu A_\mu$, is forbidden because it would violate gauge invariance, so that it is predicted to be massless. The new gauge field can be easily identified with the electromagnetic potential, and the total Lagrangian

$$\mathcal{L} = [i\bar{\psi} \gamma^\mu \partial_\mu \psi - m\bar{\psi} \psi] + \left[-\frac{1}{4} F_{\mu\nu} F^{\mu\nu} \right] + [eQ A_\mu \bar{\psi} \gamma^\mu \psi] \quad (2.10)$$

gives rise to the well-known Maxwell equations of the electrodynamics

$$\partial_\mu F^{\mu\nu} = J^\nu, \quad J^\nu = -eQ \bar{\psi} \gamma^\nu \psi, \quad (2.11)$$

where J^ν is the fermion electromagnetic current. Thus, the final Lagrangian in Eq. 2.10 represents the final expression for the Lagrangian of quantum electrodynamics, describing Dirac fields (fermions) interacting with Maxwell fields (photons).

To describe weak interactions, a more elaborated structure is needed, with several fermionic flavors and different properties for left- and right-handed fields. Moreover, the left-handed fermions must appear in doublets, and massive gauge bosons W^\pm and Z must be present in addition to the photon. The simplest group with doublet representations is $SU(2)$, and since the theory must include QED as well, the additional $U(1)$ group is needed. Hence, the obvious symmetry group to consider is $SU(2)_L \times U(1)_Y$, where L refers to left-handed fields and Y to the hypercharge.

The free Lagrangian for a generation of quarks (or leptons) is given by

$$\mathcal{L}_0 = \sum_{j=1}^3 i\bar{\psi}_j \gamma^\mu \partial_\mu \psi_j, \quad (2.12)$$

where the following notation has been introduced:

$$\psi_1(x) = \begin{pmatrix} u \\ d \end{pmatrix}_L, \quad \psi_2(x) = u_R, \quad \psi_3(x) = d_R. \quad (2.13)$$

488 The free Lagrangian \mathcal{L}_0 is invariant under global G transformations in flavor space:

$$\begin{aligned} \psi_1(x) &\xrightarrow{G} \psi'_1(x) \equiv e^{iY_1\beta} U_L \psi_1(x) \\ \psi_2(x) &\xrightarrow{G} \psi'_2(x) \equiv e^{ig'Y_2\beta} \psi_2(x) \\ \psi_3(x) &\xrightarrow{G} \psi'_3(x) \equiv e^{ig'Y_3\beta} \psi_3(x) \end{aligned} \quad (2.14)$$

489 where the $SU(2)_L$ transformation

$$U_L \equiv e^{ig\frac{\tau^i}{2}\alpha^i} \quad (i = 1, 2, 3) \quad (2.15)$$

490 only acts on the doublet field ψ_1 . The parameters Y_i are three different values (one per
491 each field) of the hypercharge, which represents the generator of the symmetry group $U(1)_Y$.
492 The β parameter is the phase of the $U(1)_Y$ transformation and is one-dimensional. The
493 matrices τ_i are the Pauli matrices and represent the three $SU(2)_L$ transformation generators
494 which are combined in the weak isospin operator $\mathbf{T} = (\tau_1, \tau_2, \tau_3)$. These matrices form a
495 Lie group, which is defined by the commutator relation $[\tau_i, \tau_j] = i\epsilon_{ijk}\tau_k$. As the τ_i do not
496 commute, the $SU(2)_L$ group is called non-Abelian. Due to the generator structure, the phase
497 $\alpha = (\alpha_1, \alpha_2, \alpha_3)$ of the $SU(2)_L$ transformation has to be extended to a three-component
498 vector with the same dependencies as above. The couplings g and g' have been introduced
499 for the $SU(2)_L$ and $U(1)_Y$, respectively, quantifying the strength of the interactions.

500 The free Lagrangian in Eq. 2.12 is then required to be invariant under local $SU(2)_L \times U(1)_Y$
501 gauge transformations, i.e. with $\alpha_i = \alpha_i(x)$ and $\beta = \beta(x)$. In order to satisfy this symmetry
502 requirement, the fermion derivatives are exchanged with covariant objects. Since there are
503 now four gauge parameters, $\alpha_i(x)$ and $\beta(x)$, four different gauge fields are needed:

$$\mathcal{D}_\mu \equiv \partial_\mu + ig\mathbf{W}_\mu \cdot \mathbf{T} + ig'\frac{Y}{2}B_\mu. \quad (2.16)$$

504 Thus, four additional vector fields of spin 1 have been added: the isotriplet $\mathbf{W}_\mu =$
505 $(W_{1\mu}, W_{2\mu}, W_{3\mu})$ for the $SU(2)_L$ and the singlet B_μ for the $U(1)_Y$. The quanta of these fields
506 are called gauge bosons. In order to build the gauge-invariant kinetic term for the gauge
507 bosons, the corresponding field strengths are introduced:

$$\begin{aligned} B_{\mu\nu} &\equiv \partial_\mu B_\nu - \partial_\nu B_\mu \\ W_{\mu\nu}^i &\equiv \partial_\mu W_\nu^i - \partial_\nu W_\mu^i - g\epsilon_{ijk}W_\mu^jW_\nu^k. \end{aligned} \quad (2.17)$$

508 The final $SU(2)_L \times U(1)_Y$ Lagrangian is then given by

$$\mathcal{L}_{SU(2)_L \times U(1)_Y} = \mathcal{L}_f + \mathcal{L}_g, \quad (2.18)$$

509 where \mathcal{L}_f is the Lagrangian for the free fermion fields

$$\mathcal{L}_f = i \sum_j \bar{\psi}_L^j \gamma^\mu [\partial_\mu + ig\mathbf{W}_\mu \cdot \mathbf{T} + ig'\frac{Y_L}{2}B_\mu] \psi_L^j + i \sum_j \bar{\psi}_R^j [\partial_\mu - g'Y_R B_\mu] \psi_R^j \quad (2.19)$$

510 and \mathcal{L}_g is the Lagrangian for the gauge bosons

$$\mathcal{L}_g = -\frac{1}{4} \mathbf{W}_{\mu\nu} \cdot \mathbf{W}^{\mu\nu} - \frac{1}{4} B_{\mu\nu} \cdot B^{\mu\nu}. \quad (2.20)$$

511 Since the field strengths $W_{\mu\nu}^i$ contain a quadratic term, the Lagrangian \mathcal{L}_g gives rise to
 512 cubic and quartic self-interactions among the gauge fields. The strength of these interactions
 513 is given by the same $SU(2)_L$ coupling g which appears in the fermionic piece of the Lagrangian.
 514 The final Lagrangian represents the unified electroweak theory, developed by Glashow [11],
 515 Weinberg [12] and Salam [13]. However, this is not the entire theory since the gauge
 516 symmetry forbids writing a mass term for the gauge bosons. Fermionic masses are also not
 517 possible, because they would connect the left- and right-handed fields, which have different
 518 transformation properties, and therefore would produce an explicit breaking of the gauge
 519 symmetry. Thus, the $SU(2)_L \times U(1)_Y$ Lagrangian in Eq. 2.17 only contains massless fields.
 520 The mass terms are introduced through a procedure that exploits spontaneous symmetry
 521 breaking as described in the following.

522 2.1.2 Spontaneous symmetry breaking

523 In order to generate masses, the gauge symmetry needs to be broken in such way to maintain
 524 the full symmetry of the Lagrangian. The main idea is based on the possibility of obtaining
 525 non-symmetric results from a Lagrangian that possesses the following properties: it is invariant
 526 under a group G of transformations and has a degenerate set of states with minimal energy,
 527 which transform under G as the members of a given multiplet. As it will be demonstrated in
 528 the following, by arbitrarily selecting one of those states as the ground state of the system,
 529 one says that the symmetry becomes spontaneously broken.

530 In order to explain this mechanism the Lagrangian for a complex scalar field $\phi(x) =$
 531 $\phi_1(x) + i\phi_2(x)$ is considered

$$\mathcal{L} = \partial_\mu \phi^\dagger \partial^\mu \phi - V(\phi), \quad V(\phi) = \mu^2 \phi^\dagger \phi + h(\phi^\dagger \phi)^2 \quad (2.21)$$

532 where $V(\phi)$ is a potential. The Lagrangian \mathcal{L} is invariant under global phase transformations
 533 of the scalar field

$$\phi(x) \xrightarrow{U(1)} \phi'(x) \equiv e^{i\theta} \phi(x). \quad (2.22)$$

534 In order to allow for a minimum or “ground state” of the potential, the parameter h has
 535 to be ≥ 0 . For the quadratic term there are the two following possibilities. If $\mu^2 \geq 0$, the
 536 potential acquires only the trivial minimum $\phi_m = 0$. If $\mu^2 \leq 0$ the minimum is obtained for
 537 all those field configurations satisfying

$$|\phi_m| = \sqrt{\frac{-\mu^2}{2h}} \equiv \frac{v}{\sqrt{2}} \geq 0 \quad \Rightarrow \quad V(\phi_m) = -\frac{h}{4} v^4 \quad (2.23)$$

538 As the Lagrangian is invariant under $U(1)$ phase transformations, there is an infinite
 539 number of degenerate states of minimum energy given by $\phi_m(x) = \frac{v}{\sqrt{2}} e^{i\theta}$. A particular
 540 solution can be chosen, e.g. $\theta = 0$, corresponding to the minimum of the field given by
 541 $\phi_{1m} = v/\sqrt{2}$ and $\phi_{2m} = 0$. Since the Feynman calculus is a perturbation procedure, in which,
 542 starting from a ground state, the fields are treated as fluctuations about that state, two new
 543 real fields $\eta(x)$ and $\xi(x)$ are introduced representing these fluctuations

$$\eta(x) = \phi_1(x) - \frac{v}{\sqrt{2}} \quad \text{and} \quad \xi(x) = \phi_2(x). \quad (2.24)$$

544 In terms of these new fields, the potential $V(\phi)$ takes the form

$$V(\phi) = V(\phi_m) - \mu^2 \eta^2 + h v \eta (\eta^2 + \xi^2) + \frac{h}{4} (\eta^2 + \xi^2)^2 \quad (2.25)$$

545 and the resulting Lagrangian does not share the same symmetry as the original one. Thus, by
546 choosing a particular solution as the ground state, the symmetry gets spontaneously broken.
547 At the same time, the second term of the potential in Eq. 2.25 is a mass term, so the real
548 field η describes a massive state of mass $m_\eta = -2\mu^2$. The second real field ξ is massless, and
549 its appearance can be understood as follows. The field ξ describes excitations around a flat
550 direction in the potential, i.e. into states with the same energy as the chosen ground state.
551 Since those excitations do not cost any energy, they correspond to a massless state. The
552 fact that there are massless excitations associated with the spontaneous symmetry breaking
553 mechanism is a general result, known as the *Goldstone theorem*: if a Lagrangian is invariant
554 under a continuous symmetry group G , but the vacuum is only invariant under a subgroup
555 $H \subset G$, then there must exist as many massless spin-0 particles (*Goldstone bosons*) as broken
556 generators (i.e. generators of G which do not belong to H).
557

558 2.1.3 The Higgs mechanism

559 The mechanism of spontaneous symmetry breaking described in the previous section does
560 not account for the mass of the gauge fields of the weak interaction, since it introduces an
561 additional massless scalar boson that is not included in the set of the known elementary
562 particles. However, further elements are added to the theory when applying the idea of
563 spontaneous symmetry breaking to the case of local gauge invariance. In order to achieve this,
564 the complex scalar field $\phi(x)$ introduced in the previous section is replaced with a $SU(2)_L$
565 doublet of complex scalar fields with $U(1)$ hypercharge $Y = +1/2$:

$$\phi(x) \equiv \begin{pmatrix} \phi^+(x) \\ \phi^0(x) \end{pmatrix} = \frac{1}{\sqrt{2}} \begin{pmatrix} \phi_1(x) - i\phi_2(x) \\ \phi_3(x) - i\phi_4(x) \end{pmatrix}. \quad (2.26)$$

566 The gauged scalar Lagrangian of the Goldstone model (Eq. 2.21) is now given by

$$\begin{aligned} \mathcal{L}_\phi &= \mathcal{D}_\mu \phi^\dagger \mathcal{D}^\mu \phi - \mu^2 \phi^\dagger \phi + h (\phi^\dagger \phi)^2, & (h \geq 0, \mu^2 \leq 0), \\ \mathcal{D}^\mu \phi &= [\partial^\mu + ig \mathbf{W}_\mu \cdot \mathbf{T} + ig' \frac{Y}{2} B_\mu], & (Y = Q - \tau_3 = \frac{1}{2}), \end{aligned} \quad (2.27)$$

567 and it is invariant under local $SU(2)_L \times U(1)_Y$ transformations. The value of the scalar
568 hypercharge is fixed by the requirement of having the correct couplings between $\phi(x)$ and
569 $B_\mu(x)$, i.e. that the photon does not couple to ϕ^0 , and one has the right electric charge for
570 ϕ^+ . As observed in the previous section, there is an infinite set of degenerate states with
571 minimum energy satisfying

$$\begin{aligned} \langle 0 | \phi_i | 0 \rangle &= 0 \quad \text{for } i = 1, 2, 4 \\ \langle 0 | \phi_3 | 0 \rangle &= \sqrt{\frac{-\mu^2}{2h}} \equiv \frac{v}{\sqrt{2}}. \end{aligned} \quad (2.28)$$

572 Since the electric charge is a conserved quantity, only the neutral scalar field can acquire
573 a vacuum expectation value. Once a particular ground state is chosen, the $SU(2)_L \times U(1)_Y$
574 symmetry gets spontaneously broken. On the other hand, the vacuum carries no electric
575 charge, so the $U(1)_Q$ of QED is not broken. Thus, the $SU(2)_L \times U(1)_Y$ group of the electroweak
576 theory is spontaneously broken to the $U(1)_Q$ subgroup, i.e. $SU(2)_L \times U(1)_Y \rightarrow U(1)_Q$.

577 The scalar doublet can now be written in its general, gauge-invariant form as a fluctuation
 578 over the ground state

$$\phi(x) = e^{i\frac{\tau^i}{2}\theta^i(x)} \frac{1}{\sqrt{2}} \begin{pmatrix} 0 \\ v + H(x) \end{pmatrix} \quad (2.29)$$

579 with 4 real fields $\theta^i(x)$ and $H(x)$. The crucial point is that the local $SU(2)_L$ invariance of the
 580 Lagrangian allows one to rotate away any dependence on $\theta^i(x)$. These three fields would be
 581 precisely the massless Goldstone bosons associated with the spontaneous symmetry breaking
 582 mechanism. The additional ingredient of gauge symmetry makes these massless excitations
 583 unphysical. In fact, it can be demonstrated that by choosing the physical (unitary) gauge
 584 $\theta^i(x) = 0$, the 3 massless Goldstone bosons arising from the three broken generators can be
 585 eliminated from the Lagrangian. At the same time, the kinetic piece of the scalar Lagrangian
 586 in Eq. 2.27 takes the form

$$(\mathcal{D}_\mu \phi)^\dagger \mathcal{D}^\mu \phi \xrightarrow{\theta^i=0} \frac{1}{2} \partial_\mu H \partial^\mu H + (v + H)^2 \left\{ \frac{g^2}{4} W_\mu^\dagger W^\mu + \frac{g^2}{8 \cos^2 \theta_W} Z_\mu Z^\mu \right\}. \quad (2.30)$$

587 The vacuum expectation value of the neutral scalar has generated a quadratic term, i.e.
 588 mass terms, for the gauge bosons. Usually, one rewrites the fields in terms of the three
 589 massive vector bosons W^\pm and Z , and a massless vector boson, the photon A . One finds that
 590 they are mixtures of the original gauge fields \mathbf{W}_μ and B_μ :

$$W_\mu^\pm = \frac{(W_\mu^1 \mp iW_\mu^2)}{\sqrt{2}}, \quad (2.31)$$

$$\begin{pmatrix} A_\mu \\ Z_\mu \end{pmatrix} = \begin{pmatrix} \cos \theta_W & \sin \theta_W \\ -\sin \theta_W & \cos \theta_W \end{pmatrix} \begin{pmatrix} B_\mu \\ W_\mu^3 \end{pmatrix} \quad (2.32)$$

591 where the Weinberg angle θ_W is defined as the ratio of coupling constants: $\tan \theta_W \equiv g'/g$.
 592 The masses of the gauge bosons W^\pm and the Z are then given by:

$$M_W = \frac{1}{2} v g \quad \text{and} \quad M_Z = \frac{v \sqrt{g^2 + g'^2}}{2} = \frac{M_W}{\cos \theta_W}. \quad (2.33)$$

593 The Lagrangian \mathcal{L}_ϕ has to be added to the electroweak theory given by the Lagrangian of
 594 Eqs. 2.18–2.20, such that

$$\mathcal{L}_{SU(2)_L \times U(1)_Y} = \mathcal{L}_f + \mathcal{L}_g + \mathcal{L}_\phi. \quad (2.34)$$

595 The total Lagrangian is invariant under gauge transformations, which guarantee the
 596 renormalizability of the associated quantum field theory. After spontaneous symmetry
 597 breaking, three massless Goldstone bosons are generated. However, they are then eliminated
 598 from the Lagrangian by exploiting local gauge symmetry. Going to the unitary gauge, the
 599 W^\pm and the Z (but not the photon, because $U(1)_Q$ is an unbroken symmetry) have acquired
 600 masses given by Eq. 2.33. In fact, before the spontaneous symmetry breaking mechanism,
 601 the massless W^\pm and Z bosons lead to $3 \times 2 = 6$ degrees of freedom (d.o.f.), due to the two
 602 possible polarizations of a massless spin-1 field. The four real scalar fields are also present at
 603 this stage, corresponding to an additional four d.o.f.. After spontaneous symmetry breaking,
 604 the three Goldstone modes are “eaten” by the weak gauge bosons, which become massive, and
 605 therefore acquire one additional longitudinal polarization. This leads to a total of $3 \times 3 = 9$
 606 d.o.f. in the gauge sector, plus the remaining scalar particle H , which is called the *Higgs*

607 *boson*. The total number of d.o.f. is obviously conserved. This theory is generally called the
 608 *Higgs mechanism* and it was proposed by three independent groups in 1964: by Brout and
 609 Englert [14], by Higgs [15–17], and by Guralnik, Hagen, and Kibble [18].

610 The W and Z were discovered at CERN by the UA1 [19] and UA2 [20] groups in 1983.
 611 Subsequent measurements of their masses and other properties at Tevatron and LEP have
 612 been in excellent agreement with the standard model expectations [21, 22]. The current values
 613 are $M_W = 80.385 \pm 0.015$ GeV and $M_Z = 91.1876 \pm 0.0021$ GeV [10].

614 2.1.4 The Higgs and Yukawa interactions

615 The scalar Lagrangian in Eq. 2.27 has introduced a new scalar particle into the model: the
 616 Higgs boson H. In terms of the physical fields (unitary gauge), \mathcal{L}_ϕ takes the form

$$\mathcal{L}_\phi = \frac{1}{4}hv^4 + \mathcal{L}_H + \mathcal{L}_{HG^2}, \quad (2.35)$$

617 where

$$\begin{aligned} \mathcal{L}_H &= \frac{1}{2}\partial_\mu H\partial^\mu H - \frac{1}{2}M_H^2 H^2 - \frac{M_H^2}{2v}H^3 - \frac{M_H^2}{8v^2}H^4, \\ \mathcal{L}_{HG^2} &= M_W^2 W_\mu^\dagger W^\mu \left\{ 1 + \frac{2}{v}H + \frac{H^2}{v^2} \right\} + \frac{1}{2}M_Z^2 Z_\mu Z^\mu \left\{ 1 + \frac{2}{v}H + \frac{H^2}{v^2} \right\}, \end{aligned} \quad (2.36)$$

618 and the Higgs boson mass is given by

$$M_H = \sqrt{-2\mu^2} = \sqrt{2}hv. \quad (2.37)$$

619 A fermionic mass term $-m\bar{\psi}\psi$ is not allowed, because it breaks the gauge symmetry.
 620 However, by adding Yukawa interaction terms of the fermion and Higgs field to the Lagrangian,
 621 the fermion masses can also be generated by spontaneous symmetry breaking. This procedure
 622 is briefly described in the following.

623 The most general Yukawa Lagrangian can be written in the form

$$\sum_{jk} \left\{ (\bar{u}'_j, \bar{d}'_j)_L \left[c_{jk}^{(d)} \begin{pmatrix} \phi^+ \\ \phi^0 \end{pmatrix} d'_{kR} + c_{jk}^{(u)} \begin{pmatrix} \phi^{0*} \\ -\phi^- \end{pmatrix} u'_{kR} \right] + (\bar{\nu}'_j, \bar{\ell}'_j)_L c_{jk}^{(\ell)} \begin{pmatrix} \phi^+ \\ \phi^0 \end{pmatrix} \ell'_{kR} \right\} + h.c. \quad (2.38)$$

624 where the indexes run over the three generations of fermions; u'_j , d'_j , ℓ'_j and ν'_j denote the
 625 weak eigenstates for the members of each generation j , and $c_{jk}^{(d)}$, $c_{jk}^{(u)}$, and $c_{jk}^{(\ell)}$ are the so-called
 626 Yukawa couplings. After spontaneous symmetry breaking, the Yukawa Lagrangian in the
 627 unitary gauge takes the simpler form

$$\mathcal{L}_Y = -(1 + \frac{H}{v}) \{ \bar{\mathbf{d}}'_L \mathbf{M}'_d \mathbf{d}'_R + \bar{\mathbf{u}}'_L \mathbf{M}'_u \mathbf{u}'_R \} + \bar{\mathbf{l}}'_L \mathbf{M}'_\ell \mathbf{l}'_R + h.c., \quad (2.39)$$

628 where $\bar{\mathbf{d}}'$, $\bar{\mathbf{u}}'$ and $\bar{\mathbf{l}}'$ denote vectors in the 3-dimensional generation space, and the corresponding
 629 mass matrices are given by

$$(\mathbf{M}'_d)_{ij} \equiv -c_{ij}^{(d)} \frac{v}{\sqrt{2}}, \quad (\mathbf{M}'_u)_{ij} \equiv -c_{ij}^{(u)} \frac{v}{\sqrt{2}}, \quad (\mathbf{M}'_\ell)_{ij} \equiv -c_{ij}^{(\ell)} \frac{v}{\sqrt{2}}. \quad (2.40)$$

630 Therefore, the spontaneous symmetry breaking mechanism generates fermion masses,
 631 which in turn fix all Yukawa couplings. In general the mass matrices in Eq. 2.40 are not

diagonal, Hermitian, or symmetric. Thus, to identify the physical mass eigenstates d_j , u_j , and ℓ_j , which are linear combinations of the corresponding weak eigenstates d'_j , u'_j , and ℓ'_j , it is necessary to diagonalize the matrices by separate unitary transformations on the left- and right-handed fermion fields. This is achieved as follows. The matrix \mathbf{M}'_d can be decomposed as $\mathbf{M}'_d = \mathbf{H}_d \mathbf{U}_d = \mathbf{S}_d^\dagger \mathcal{M}_d \mathbf{S}_d \mathbf{U}_d$, where $\mathbf{H}_d \equiv \sqrt{\mathbf{M}'_d \mathbf{M}'_d^\dagger}$ is an hermitian positive-definite matrix, while \mathbf{U}_d is unitary. The \mathbf{H}_d matrix can be diagonalized by a unitary matrix \mathbf{S}_d ; the resulting matrix \mathcal{M}_d is diagonal, hermitian and positive definite. Similarly, one has $\mathbf{M}'_u = \mathbf{H}_u \mathbf{U}_u = \mathbf{S}_u^\dagger \mathcal{M}_u \mathbf{S}_u \mathbf{U}_u$. In terms of the diagonal mass matrices

$$\mathcal{M}_d = \text{diag}(m_d, m_s, m_b), \quad \mathcal{M}_u = \text{diag}(m_u, m_c, m_t), \quad \mathcal{M}_\ell = \text{diag}(m_e, m_\mu, m_\tau) \quad (2.41)$$

the Yukawa Lagrangian takes the simpler form

$$\mathcal{L}_Y = -(1 + \frac{H}{v}) \{ \bar{\mathbf{d}} \mathcal{M}_d \mathbf{d} + \bar{\mathbf{u}} \mathcal{M}_u \mathbf{u} + \bar{\mathbf{l}} \mathcal{M}_\ell \mathbf{l} \} \quad (2.42)$$

where the mass eigenstates are defined by

$$\begin{aligned} \mathbf{d}_L &\equiv \mathbf{S}_d \mathbf{d}'_L, & \mathbf{u}_L &\equiv \mathbf{S}_u \mathbf{u}'_L, & \mathbf{l}_L &\equiv \mathbf{S}_\ell \mathbf{l}'_L, \\ \mathbf{d}_R &\equiv \mathbf{S}_d \mathbf{U}_d \mathbf{d}'_R, & \mathbf{u}_R &\equiv \mathbf{S}_u \mathbf{U}_u \mathbf{u}'_R, & \mathbf{l}_R &\equiv \mathbf{S}_\ell \mathbf{U}_\ell \mathbf{l}'_R, \end{aligned} \quad (2.43)$$

One observes that the Higgs interactions (Fig. 2.1) have a very characteristic form: they are always proportional to the squared mass of the coupled boson or fermion. All Higgs couplings are therefore determined by M_H , M_W , M_Z , the mass m_f of fermions, and the vacuum expectation value v .

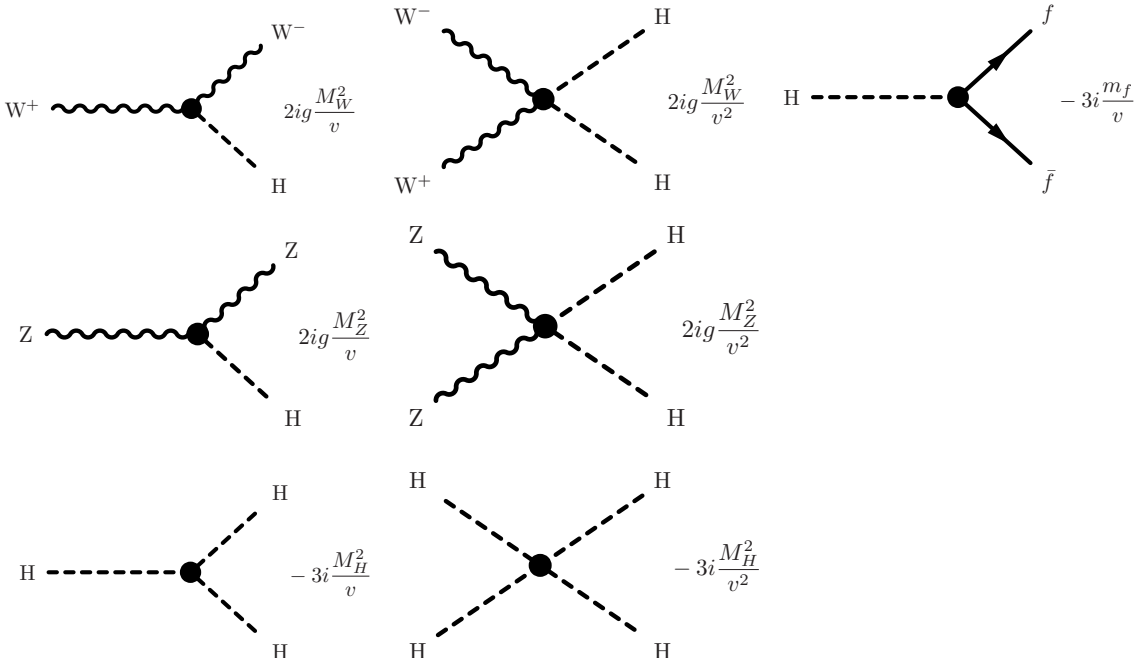


Figure 2.1: Higgs interaction vertices in the standard model.

2.1.5 Observation of a particle compatible with the standard model Higgs boson

Before the Higgs boson was discovered, its production cross sections at a proton-proton collider and its branching fractions as a function of the mass hypothesis were predicted to be as shown in Fig. 2.2. The Feynman diagrams for the different leading production mechanisms are shown in Fig. 2.3. The gluon fusion process ($gg \rightarrow H$) is the dominating Higgs production mechanism over the entire mass range accessible at the LHC. In the vector boson fusion process ($qq' \rightarrow qq'H$), which is about one order of magnitude weaker than gluon fusion, the Higgs boson is produced through a direct coupling with vector bosons (W or Z), which are radiated by a pair of incoming quarks from the proton beams. The associated production with a W or Z boson ($q\bar{q} \rightarrow WH$, $q\bar{q} \rightarrow ZH$) have a smaller cross section than the previous mechanisms but the presence of the vector boson helps in reconstructing the events by reducing the contamination from other SM processes. The associated production with $t\bar{t}$ pairs ($q\bar{q}, gg \rightarrow t\bar{t}H$) has the smallest cross section, however, it allows for a direct access to the Higgs coupling to top quarks, which is important since the Higgs coupling to the top quark is the strongest, of order 1. The Higgs boson does not couple to photons and gluons at LO, but such processes can arise via fermion or vector boson loops, giving a sizable contribution below the mass at which the Higgs boson would decay to on-shell vector bosons.

664

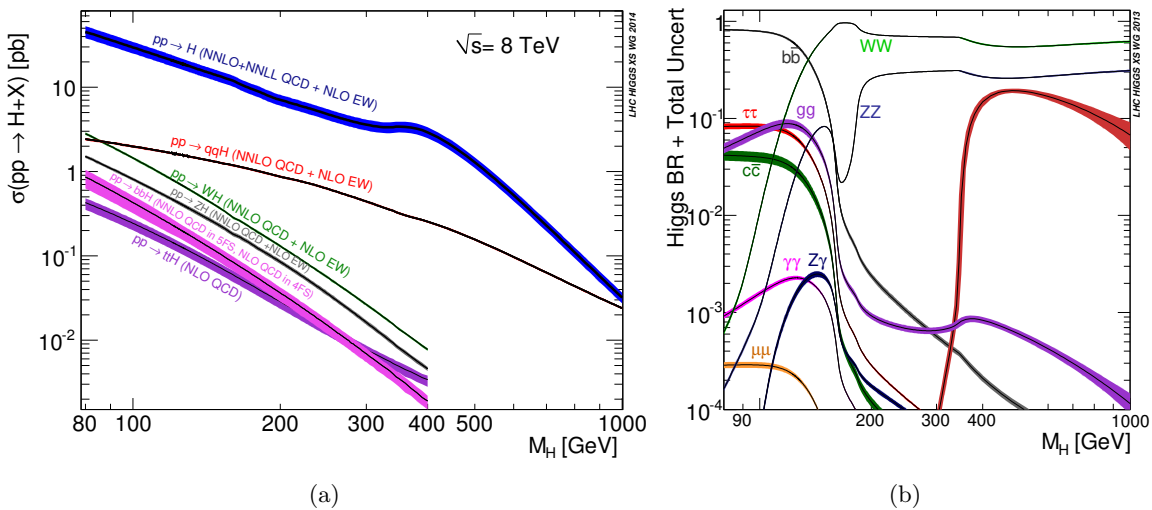


Figure 2.2: Predictions for (a) the SM Higgs production cross-sections at $\sqrt{s} = 8$ TeV for the different production mechanisms and (b) branching fractions for its decays in the different channels as a function of the Higgs boson mass hypothesis [23]. After the Higgs boson discovery these properties are well predicted for the measured mass.

The search for the massive Higgs boson has been long and tedious. However, in summer 2012, the ATLAS and the CMS collaborations announced the observation of a new particle in data taken in 2011 and 2012 [2,3]. A combination of the measurements targeting its decay into fermions ($b\bar{b}$, $\tau\tau$) or vector bosons (ZZ^* , WW^* , $\gamma\gamma$) and all the different production modes, led to an excess of events above the expected background around a mass of 125 GeV. The CMS result yielded a local significance of 5.0σ with a global significance of 4.6σ in the Higgs mass search range of $115 < m_H < 130$ GeV (Fig. 2.4(b)). For ATLAS, the local significance was found to be 5.9σ with a global significance of 5.1σ in the range $100 < m_H < 600$ GeV (Fig. 2.4(a)). A simultaneous fit to the reconstructed invariant mass peaks in the two

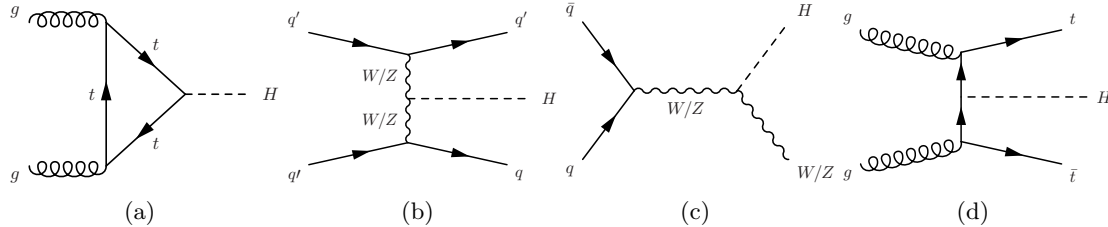


Figure 2.3: Feynman diagrams for the most important production processes of the SM Higgs boson: (a) gluon fusion, (b) vector boson fusion, (c) Higgs-strahlung and (d) $t\bar{t}$ associated production.

674 channels with the highest mass resolution, $H \rightarrow ZZ^* \rightarrow 4\ell$ and $H \rightarrow \gamma\gamma$, and for the
675 two experiments has been performed. The resulting combined measured mass of the Higgs
676 boson was $m_H = 125.09 \pm 0.21(\text{stat.}) \pm 0.11(\text{syst.}) \text{ GeV}$ (Fig. 2.5) [24]. Subsequent studies on
677 production and decay rates [25] and spin-parity [26–28] of the new boson showed that its
678 properties are compatible with those expected for the SM Higgs boson.

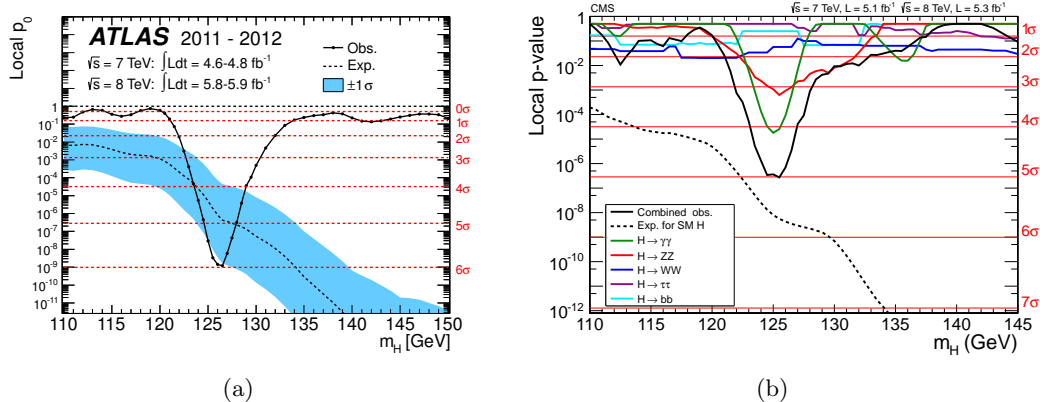


Figure 2.4: The observed (solid) local p-value as a function of the Higgs boson mass m_H for the (a) ATLAS and (b) CMS experiments obtained with data collected in pp collisions at $\sqrt{s} = 7$ and 8 TeV. In (a) the results for each individual channel are also shown. The dashed curve shows the expected local p-value under the hypothesis of a SM Higgs boson signal at that mass. The horizontal red lines indicate the p-values corresponding to significances of 1 to 7σ [2,3].

679 Finally, the Higgs boson couplings to SM particles are investigated simultaneously in
680 different production and decay processes, including the possibility that the Higgs boson
681 couples to BSM particles [25]. To test possible deviations from the SM predictions, the
682 coupling modifiers, $k_j^2 = \sigma_j/\sigma_j^{\text{SM}}$ and $k_j^2 = \Gamma_j/\Gamma_j^{\text{SM}}$, for production and decay rates, are
683 introduced. However, to directly measure the individual coupling modifiers, an assumption
684 about the Higgs boson width Γ_H is necessary. Thus, another modifier is introduced and
685 defined as $k_H = \sum_j \mathcal{B}_j^{\text{SM}} k_j^2$, where $\mathcal{B}_j^{\text{SM}}$ are the branching fractions for the Higgs boson decay
686 to the final state f as predicted by the SM. In the case where the SM decays of the Higgs
687 boson are the only ones allowed, the relation $k_H^2 = \Gamma_H/\Gamma_H^{\text{SM}}$ holds. If instead deviations from
688 the SM are introduced in the decays, the width can be expressed as:

$$\Gamma_H = \frac{k_H^2 \Gamma_H^{\text{SM}}}{1 - B_{\text{BSM}}}, \quad (2.44)$$

689 where B_{BSM} indicates the total branching fraction into BSM decays. The two possible
690 scenarios are considered: the first leaves B_{BSM} free, provided that $B_{\text{BSM}} \geq 0$, whereas the

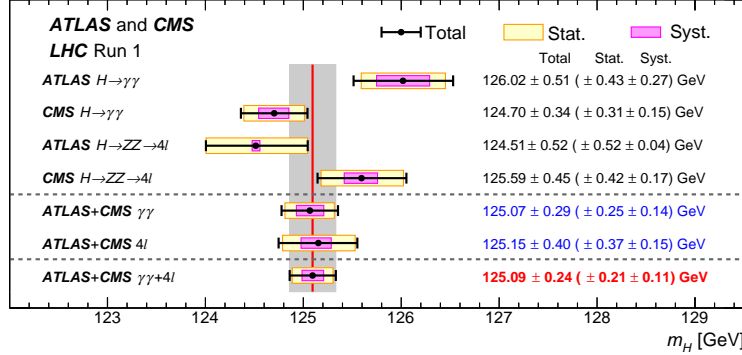


Figure 2.5: Summary of Higgs boson mass measurements from the individual analyses of ATLAS and CMS and from their combination. The magenta and yellow bands correspond to the systematic and statistical uncertainties, respectively. The total uncertainties are also indicated as black error bars. The red vertical line and corresponding gray shaded column indicate the central value and the total uncertainty of the combined measurement, respectively [24].

second assumes $B_{\text{BSM}} = 0$. The parameters of interest in the fits to data are thus the seven independent coupling modifiers, k_Z , k_W , k_t , k_τ , k_b , k_g , and k_γ , one for each SM particle involved in the production processes and decay modes studied, plus B_{BSM} in the case of the first scenario. The results of the two fits are shown in Fig. 2.6. The overall branching fraction of the Higgs boson into BSM decays is determined to be less than 34% at 95% CL. This constraint applies to invisible decays into BSM particles, decays into BSM particles that are not detected as such, and modifications of the decays into SM particles that are not directly measured by the experiments.

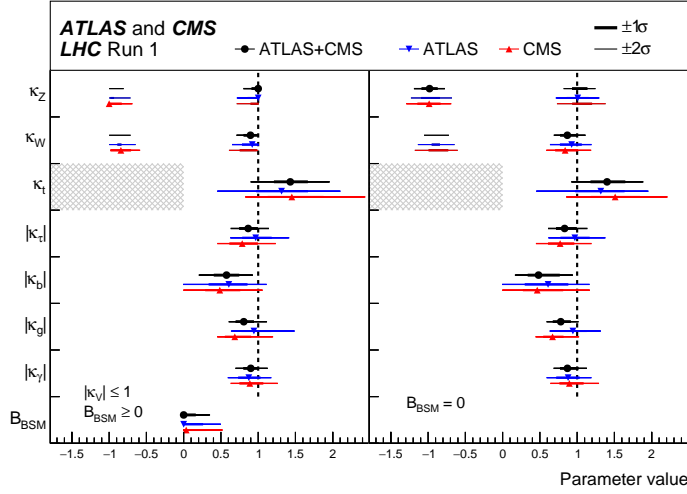


Figure 2.6: Fit results for two parameterizations: the first one assumes that $B_{\text{BSM}} \geq 0$, and the second one assumes that there are no additional BSM contributions to the Higgs boson width ($B_{\text{BSM}} = 0$). The measured results for the combination of ATLAS and CMS are reported together with their uncertainties, as well as the individual results from each experiment [24].

2.1.6 Quantum chromodynamics

Quantum Chromodynamics (QCD) is the gauge theory of strong interactions, describing the dynamics of colored quarks and gluons. The QCD represents the $SU(3)_C$ component of the standard model, where C denotes the color. After applying the principle of gauge invariance to the free Lagrangian for the quark fields holding color α that runs from 1 to 3 (usually identified with red, green, blue), and flavor q , one obtains the following expression for the final gauge invariant QCD Lagrangian

$$\mathcal{L}_{\text{QCD}} = \sum_q \bar{\psi}_{q,\alpha} (i\gamma^\mu \partial_\mu \delta_{\alpha\beta} - g_s \gamma^\mu t_{\alpha\beta}^a \mathcal{A}_\mu^a - m_q \delta_{\alpha\beta}) \psi_{q,b} - \frac{1}{4} G_{\mu\nu}^a G_a^{\mu\nu}. \quad (2.45)$$

In the equation above, the quark fields are represented by the spinors ψ . The fields \mathcal{A}_μ^a corresponds to the eight gluon fields, since C runs from 1 to $N_C^2 - 1 = 8$. Each gluon carries one unit of color and one unit of anticolor. The eight 3×3 matrices $t_{\alpha\beta}^a$ are the $SU(3)_C$ generators and rotate the quark color in the $SU(3)_C$ space in a quark-gluon interaction. The field tensor is

$$G_{\mu\nu}^a = \partial_\mu \mathcal{A}_\nu^a - \partial_\nu \mathcal{A}_\mu^a - g_s f_{abc} \mathcal{A}_\mu^b \mathcal{A}_\nu^c, \quad (2.46)$$

where f_{abc} are the structure constants of the $SU(3)$ group. As $[t^a, t^b] = i f_{abc} t^c$ the group is non-Abelian. Owing to this property, $G_{\mu\nu}^a G_a^{\mu\nu}$ term generates the cubic and quartic gluon self-interactions. The fundamental parameters of QCD are the *strong coupling constant* g_s , often written in terms of $\alpha_s = g_s^2/4\pi$, and the quark masses m_q . All interactions appearing in Eq. 2.44 have strength given by g_s (Fig. 2.7).

716

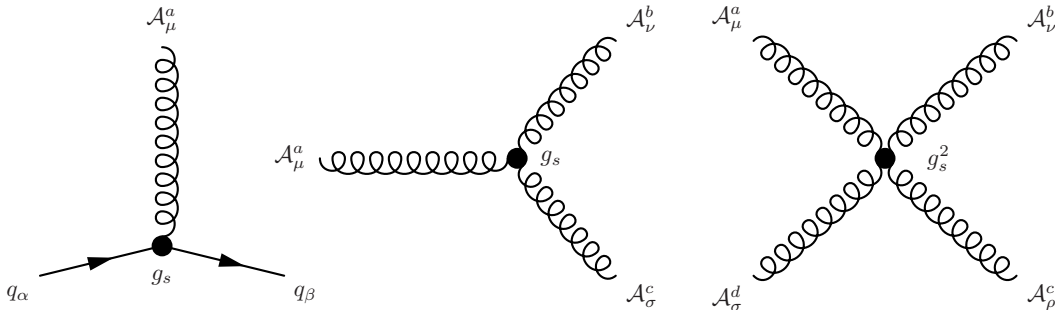


Figure 2.7: Interaction vertices of the QCD Lagrangian.

QCD has the property of *asymptotic freedom*, i.e. the coupling becomes weak at high energies or short distances, and for energies approaching zero or for very large distances, it tends toward infinity. As a consequence, the further away a quark is pulled from another one, the stronger the force gets, such that it is more energetically favorable for a new quark-antiquark pair to be spontaneously produced from the vacuum. This process continues until the formation of a stable colourless hadron consisting of either a quark and an antiquark (mesons) or three quarks or antiquarks (baryons), such that quarks cannot exist as free particles.

In the regime of very high momentum transfer interactions, perturbation theory is a very satisfactory description of QCD physics observables, giving precise predictions about what can be tested in collider experiments. This approach is called perturbative-QCD, or pQCD. In this framework, QCD predictions are calculated using the formalism of the Feynman rules which are derived from the \mathcal{L}_{QCD} . The transition amplitudes for a given process from a set of initial state particles to a set of final state particles are computed by sorting the diagrams by the

factors of the coupling constants and calculating them up to a certain order. However, higher order diagrams generally contain loops which contribute and lead to divergences. In order to obtain finite predictions for the cross sections, a renormalization of the theory is performed, resulting in a cancellation of the divergent terms. The predictions for observables are then expressed in terms of the renormalized coupling $\alpha_s(\mu_R^2)$, a function of the renormalisation scale μ_R . The coupling satisfies the renormalisation group equation:

$$\mu_R^2 \frac{d\alpha_s}{d\mu_R^2} = \beta(\alpha_s) = -(b_0\alpha_s^2 + b_1\alpha_s^3 + b_2\alpha_s^4 + \dots) \quad (2.47)$$

where the b_i are the i -loop coefficients of the β function. They depend on the number of quark flavors n_f , and for sixteen or less flavors the strong coupling gets smaller for processes that involve large momentum transfer, leading to the asymptotic freedom. Choosing μ_R close to the typical scale of the process of interest Q^2 , the $\alpha_s(\mu_R)$ represents the effective strength of the strong interaction between particles under study. Neglecting all the b_i coefficients but b_0 , an exact leading order expression for the running coupling α_s can be obtained

$$\alpha_s(\mu_R^2) = \frac{1}{b_0 \log \left(\frac{\mu_R^2}{\Lambda_{\text{QCD}}^2} \right)} = \frac{12\pi}{(33 - 2n_f) \log \left(\frac{\mu_R^2}{\Lambda_{\text{QCD}}^2} \right)} \quad (2.48)$$

where Λ_{QCD} is the perturbative cut-off over the renormalization's integrals, and is not predicted by the theory. The meaning of this cut-off is the validity of the perturbative regime approximation, beyond which the integrals would diverge. For many experimental studies, the strong coupling is evaluated at a fixed energy scale, typically of the order of the electroweak scale, $\mu_R \simeq M_Z$ (Fig. 2.8).

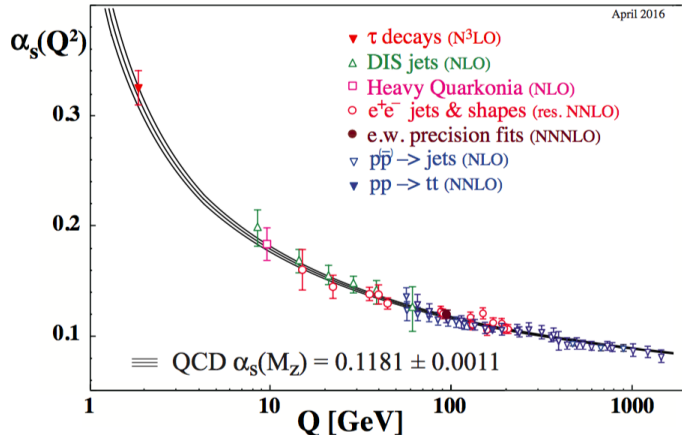


Figure 2.8: Summary of measurements of the running coupling α_s as a function of the energy scale Q of the process [10].

2.2 Limitations of the standard model

The standard model has been remarkably confirmed by experimental data collected over the last few decades, validating most of its predictions. The ultimate verification of the model has been provided by the latest discovery of a scalar particle at the LHC (Section 2.1.5), whose properties are statistically compatible with the SM predictions for the Higgs boson. Nevertheless, there are fundamental physical phenomena in nature that cannot be adequately

explained by the SM. Furthermore, some features of the model represent *ad hoc* additions to the theory and, although providing predictions that have been confirmed, imply a lack of understanding, making the framework theoretically unsatisfactory. Some of the main unresolved issues of the SM are briefly described in the following.

757 The hierarchy problem

This issue arises from the observation of a large discrepancy between the electroweak and gravitational scales. This is reflected in the mass difference between the masses of the W and Z bosons that define the scale of electroweak interactions ($\mathcal{O}(10^2 \text{ GeV})$), and the Planck mass ($M_{\text{Pl}} = \sqrt{\hbar c/G_{\text{Newton}}} = \mathcal{O}(10^{19})$), that defines the scale beyond which the gravitational force must be described by quantum mechanics. This feature is commonly known as *hierarchy problem* or as well “problem of *naturalness*”, meaning an “unnatural” or equivalently “unexpected” behaviour. More technically, the question is why the Higgs boson of mass m_H (Eq. 2.37) is so much lighter than the Planck mass. The problem is that m_H^2 receives enormous quantum corrections from the virtual effects of every particle that couples, directly or indirectly, to the Higgs field. There are three types of radiative corrections to the Higgs mass that arise from the diagrams in Fig. 2.9. Each of them gives a correction to the Higgs mass:

$$\begin{aligned} \text{top loop} & - \frac{3}{8\pi^2} \lambda_t \Lambda^2 \\ \text{gauge loop} & + \frac{1}{16\pi^2} g^2 \Lambda^2 \\ \text{Higgs loop} & + \frac{1}{16\pi^2} \lambda^2 \Lambda^2 \end{aligned} \quad (2.49)$$

where λ_t is the Yukawa coupling with the top quark, g is the gauge coupling, λ is the Higgs self coupling, and Λ represents the energy scale up to which the SM remains valid, and beyond which an unknown new physics theory enters to alter the high-energy behavior of the theory. Each of the leptons and quarks of the SM also contribute, however the largest correction arises from the top quark. If Λ is of the order of M_{Pl} , then this quantum correction to m_H^2 is about 30 orders of magnitude larger than the measured value of m_H of 125 GeV. Thus, in order to obtain such a small value for the Higgs boson mass an incredible fine-tuning cancellation must occur between the quadratic radiative corrections and the physical mass. Avoiding such a miraculous cancellation can only happen if the cut-off scale is $\Lambda \simeq \mathcal{O}(1 - 10 \text{ TeV})$ rather than the Planck scale, which implies that new physical processes show up at that energy. This is only directly a problem for corrections to the Higgs scalar boson squared mass, because quantum corrections to fermion and gauge boson masses do not have the direct quadratic sensitivity to Λ found in Eq. 2.49. However, the quarks and leptons and the electroweak gauge bosons of the SM all obtain masses from the Higgs boson, so that the entire mass spectrum of the theory is directly or indirectly sensitive to the cut-off Λ .

Many extensions of the SM suggest new physics at the TeV scale to address the hierarchy problem, providing more “natural” options. Models of *supersymmetry* [29, 30] introduce a new heavy scalar called *stop* as a *superpartner* of the SM top quark, which produces loop corrections to the Higgs mass that cancel out those of the top quark. Non-supersymmetric models have also been proposed, which predict heavier partners to the top quark. Another possibility to address the hierarchy problem is to assume the Higgs boson to be a composite particle as in the *composite Higgs* models (Section 2.3.2), rather than an elementary particle as predicted in the SM.

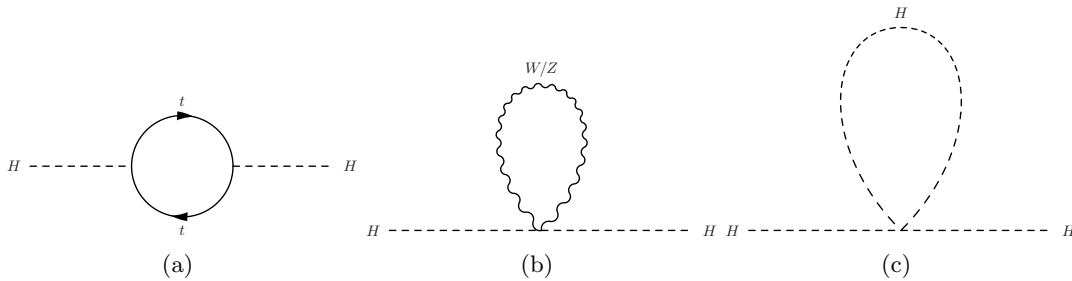


Figure 2.9: Radiative corrections to the Higgs squared mass parameter m_H^2 due to: (a) Yukawa coupling with the top quark; (b) gauge boson loop; (c) Higgs quartic self-interaction.

793 Dark matter and dark energy

794 Several cosmological observations have demonstrated that the standard model only describes
 795 5% of the total energy content of the Universe. First, the measured orbital velocities of
 796 stars around their galaxy center is incompatible with the observed matter density of the
 797 galaxy [31, 32]. In particular, assuming the gravitational mass is due to only visible matter,
 798 stars far from the center of galaxies have much higher velocities than expected. The easiest
 799 way to account for this discrepancy is to postulate the existence of another kind of matter,
 800 called *dark matter*, that does not interact through electromagnetic or strong interactions.
 801 A second major result in cosmology is the discovery that the Universe is in accelerated
 802 expansion: it was measured that on average galaxies recede from each other and that this
 803 expansion rate increases with the distance. Such a feature cannot be achieved with usual
 804 particles or with dark matter, but rather a new type of energy with a negative pressure,
 805 called *dark energy*, has to be added to the Universe content. To account for the experimental
 806 observations, dark matter and dark energy have been estimated to compose respectively 26%
 807 and 69% of the total Universe content [33], but their fundamental nature remains nowadays
 808 a mystery. The most widely accepted hypothesis on the form for dark matter is that it is
 809 composed of weakly interacting massive particles (WIMPs) that interact only through the
 810 gravitational force and an unknown force which is as weak as or weaker than the SM weak
 811 force. The search from the point of view of experimental and theoretical dark matter hunting
 812 is one of the major efforts in particle physics. There are two fronts: direct searches in cosmic
 813 rays by underground experiments, and searches at hadron colliders, where dark matter would
 814 be produced as a pair of neutral particles that may be predicted by different models. No dark
 815 matter particle has been conclusively identified by any of these experiments.

816 Gravitational force

817 The standard model does not include the fourth fundamental interaction, the gravitational
 818 force. In fact, the gravitational force is by many aspects very different from the three other
 819 forces, and establishing a common framework to describe both raises several challenges. In
 820 the decades after the discovery of general relativity, it was realized that general relativity is
 821 incompatible with quantum mechanics. It is possible to describe the gravitational force in the
 822 framework of quantum field theory like the other fundamental forces, such that the attractive
 823 gravitational force arises due to exchange of virtual spin-2 *gravitons*, in the same way as the
 824 electromagnetic force arises from exchange of virtual photons. The theory arising from this
 825 approach is known as *quantum gravity*. This theory is known not to be renormalizable, as the
 826 loop corrections including a graviton induce divergencies that cannot be reabsorbed through
 827 the renormalisation procedure, as opposed to the electroweak and chromodynamics quantum

theories. Thus, quantum gravity cannot be used to make meaningful physical predictions. Moreover, quantum gravitational effects are only expected to become apparent near the Planck scale, a scale far smaller in distance (equivalently, far larger in energy) than what is currently accessible at high energy particle accelerators. Several theoretical approaches to the problem of quantum gravity have been proposed, the most popular one being *string theory* [34].

It has to be noted that most of these approaches only attempt to describe the quantum behavior of the gravitational field and should not be confused with the objective of unifying all fundamental interactions into a single mathematical framework. However, the present understanding of the gravitational force would aid further work towards unification.

2.3 Theories of new physics

The standard model of particle physics has been very successful in describing observations. However, as explained in the previous section, this framework leaves several unanswered fundamental questions. Many extensions to the standard model have been proposed that attempt to address the open issues and to achieve a more fundamental theory that could explain the entirety of current phenomena. These new theoretical developments are referred to as theories *beyond standard model* (BSM). In this section, three specific BSM scenarios are reviewed, which are of particular interest because of their highly predictive features. Specifically, with the aim of addressing the hierarchy problem of the SM, they predict the existence of new resonances with masses in the TeV range, which can be produced at hadron colliders. Furthermore, since the new resonances can decay into pairs of well-known standard model particles, their existence and properties can be directly probed by collider experiments. In particular, the decay modes into a pair of electroweak bosons W, Z or H, can provide striking signatures, as new techniques have been developed by the experiments to efficiently reconstruct the decay and mass of the bosons in the final state.

2.3.1 Warped extra dimensions

A class of theories beyond the standard model postulates the existence of new compactified spatial dimensions. They attempt to explain the apparent weakness of the gravitational force by assuming that SM particles are confined in a (3+1)-dimensional hypersurface called a *3-brane*, as opposed to the gravitational force which is allowed to propagate in a (4+n)-dimensional *bulk*. In this scenario, the strength of the gravitational force is diluted in the extra dimensions (thereby weakening our perception of the gravitational force), while the other fundamental forces would not.

The basic idea comes from the so-called *large extra dimensions* scenario proposed by Arkani-Hamed, Dimopoulos and Dvali (ADD model) [35]. If spacetime has 4+n dimensions, then the effective 4-dimensional (reduced) Planck scale, $\overline{M}_{\text{Pl}} = M_{\text{Pl}}/\sqrt{8\pi}$, is determined by the fundamental (4+n)-dimensional Planck scale, M_* , and the geometry of the extra dimensions:

$$\overline{M}_{\text{Pl}}^2 = V_n M_*^{n+2} \simeq R^n M_*^{n+2}, \quad (2.50)$$

where V_n is the volume of the n-dimensional compactified space and R its radius. The hierarchy problem is thus eluded if $M_* \sim 1 \text{ TeV}$, which turns into a condition on the size R of the extra dimensions. Assuming $n = 1$, one can solve Eq. 2.50 and obtain $R \sim 10^8 \text{ m}$. This is a scale of the order of the Earth-Sun distance, over which we know that the $1/r^2$ Newton's law of gravitational attraction works very well. Thus, $n = 1$ is excluded. For $n = 2$,

one obtains $R \sim 100 \mu\text{m}$ or $R^{-1} \sim 10^{-4} \text{ eV}$, which is close to the limit of current table top experimental searches for deviations from the Newton's law [36].

The purpose of this model was to eliminate the hierarchy problem, i.e. to remove the large ratio between the weak scale v and the true fundamental scale \overline{M}_{Pl} , hence the requirement $M_* \sim 1 \text{ TeV}$. However, it introduces a new hierarchy, namely that between the compactification scale $\mu_c = 1/R$ and v . Thus, the ADD really only trades one large ratio for another and does not really eliminate the hierarchy problem. An alternative solution, represented by the so-called *warped extra dimensions* (WED) scenario, has been proposed by Randall and Sundrum (RS) [4].

The basic RS model, referred to as RS1, assumes the existence of only one extra dimension with size r_c . This fifth, extra dimension is labelled by the coordinate $\phi \in [-\pi, \pi]$, such that it can be described by a line segment between two 4-dimensional branes (or 3-branes), known as the *Planck* and *TeV* brane, located, respectively, at the $\phi = 0$ and $\phi = \pi$ boundary of the fifth dimension (Fig. 2.10). In the simplest version of the RS model, it is assumed, as in the ADD case, that the SM fields exist on the *TeV* brane, while the gravitational force lives everywhere. The *Planck* brane is where the gravitational force is relatively strong. The classical action describing the above set-up is given by the sum of the gravitational action in the bulk, $\mathcal{S}_{\text{gravity}}$, and on the two branes, \mathcal{S}_{TeV} and $\mathcal{S}_{\text{Planck}}$,

$$\begin{aligned} \mathcal{S} &= \mathcal{S}_{\text{gravity}} + \mathcal{S}_{\text{TeV}} + \mathcal{S}_{\text{Planck}}, \\ \mathcal{S}_{\text{gravity}} &= \int d^4x \int_{-\pi}^{+\pi} d\phi \sqrt{-G} - \Lambda + 2M_*^3 R, \\ \mathcal{S}_{\text{TeV}} &= \int d^4x \sqrt{-G(x^\mu, \phi = \pi)} \Lambda, \\ \mathcal{S}_{\text{Planck}} &= \int d^4x \sqrt{-G(x^\mu, \phi = 0)} \Lambda. \end{aligned} \quad (2.51)$$

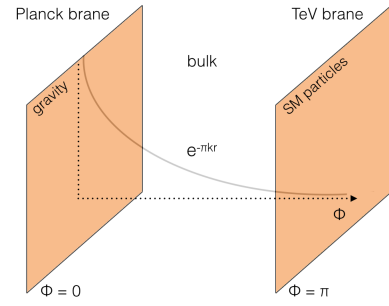


Figure 2.10: Set-up of the five dimensions in the RS model. The *Planck* and *TeV* branes are the 4-dimensional boundaries of the extra dimension ϕ compactified in an interval $[0, \pi]$.

In the above equation, G is the 5-dimensional metric $G_{\mu\nu}$, Λ a cosmological constant, and R the 5-dimensional Ricci tensor. By requiring a solution of the 5-dimensional Einstein's equation for the above action that respects the 4-dimensional Poincaré invariance in the x^μ coordinates, one finds that the 5-dimensional metric must take the form

$$ds^2 = e^{-2\sigma(\phi)} \eta_{\mu\nu} dx^\mu dx^\nu + r_c^2 d\phi, \quad (2.52)$$

where $\eta_{\mu\nu} = \text{diag}(1, -1, -1, -1)$ is the usual Minkowski metric and $\sigma(\phi)$ is some a-priori unknown function. This type of geometry is called “non-factorizable”, because the metric of the 4-dimensional subspace is ϕ -dependent. Solving the 5-dimensional Einstein's equations provides a unique solution for $\sigma(\phi)$:

$$\sigma(\phi) = \sqrt{\frac{-\Lambda}{24M_*^3}} \equiv r_c |\phi| k, \quad (2.53)$$

where k is referred to as the *curvature factor*. By plugging the solution back into the original action and integrating over the extra dimension ϕ , one finds that the 4-dimensional Planck mass is given by

$$\overline{M}_{\text{Pl}} = \frac{M_*^3}{k} (1 - e^{-2\pi kr_c}). \quad (2.54)$$

It is assumed that $k \sim M_* \sim \overline{M}_{\text{Pl}}$ in order to avoid producing a strong hierarchical difference between the mass scales of the theory. However, the electroweak energy scale v or any physical mass m in the TeV brane is exponentially suppressed compared to the 5-dimensional energy v_0 or mass m_0 :

$$m = e^{-\pi kr_c} m_0, \quad v = e^{-\pi kr_c} v_0. \quad (2.55)$$

This means that by taking v_0 of the order of the 5-dimensional fundamental mass scale M_* , the separation between the Planck and electroweak scales is produced by the metric when $kr_c \sim 11$ (small hierarchy). Such a factor indeed would already suppress a parameter with value of order 10^{18} GeV to only 1 TeV. The hierarchy is thus naturally established by the warp factor $e^{-\pi kr_c}$. This Planck-electroweak hierarchy explanation is the most celebrated achievement of WED scenarios.

A distinctive novel feature of the RS scenario is the existence of a so-called tower of Kaluza-Klein (KK) excitations of a spin-2 field, the KK graviton, arising from tensor fluctuations around the 4-dimensional part of the metric. Scalar fluctuations around the fifth extra dimension give rise to a spin-0 field called the *radion*. Massive graviton excitations appear, with 4-dimensional effective masses given by

$$m_G^{(n)} = kx_n e^{-\pi kr_c}, \quad (2.56)$$

where x_n is the n -th root of the Bessel function J_1 . These masses are of order of a TeV, so that Kaluza-Klein gravitons can be detected as massive resonances in collider experiments. The zero-mode of the graviton field corresponds to the mediator of the gravitational interaction, and its wave function is highly peaked at $\phi = 0$. The gravitational force is thus localized on the *Planck* brane, while on the TeV brane we feel only the tail of the graviton wave-function.

The coupling of an excited graviton to matter is described by the Lagrangian

$$\mathcal{L} = -\frac{1}{\Lambda_\pi} T^{\mu\nu} \sum_{n>0} h_{\mu\nu}^{(n)}, \quad (2.57)$$

where $T^{\mu\nu}$ is the energy-momentum tensor of the matter field, $h_{\mu\nu}^{(n)}$ is the n -th excitation of the graviton, and $\Lambda_\pi = \overline{M}_{\text{Pl}} e^{-\pi kr_c}$ is of order of a TeV. It is interesting to note that this model has only two free parameters: the mass of the first (lightest) KK-graviton excitation, m_1 , and the ratio $\tilde{k} \equiv k/\overline{M}_{\text{Pl}}$, which controls the widths of the new resonances:

$$\Gamma_n = \rho m_n x_n^2 \tilde{k}^2, \quad (2.58)$$

where ρ is a constant depending on the number of open decay channels. The RS model in its simplest form is thus highly predictive.

In the original RS1 model the SM matter is localized on the TeV brane, as the Higgs field. A well-motivated extension of the original RS1 model explores an alternative scenario, in which SM fields propagate in the warped bulk, except for the Higgs field which is required on the TeV brane to avoid a large hierarchy. This extension is referred thereafter as the *bulk scenario* [5, 37]. Similarly to the KK-graviton excitations, in the bulk scenario a KK expansion is applied to each SM field. The zero-mode of each KK tower represents the correspondent SM particle. The first and second generation fermions are localized near the

941 *Planck* brane, leading to the small Yukawa couplings to the Higgs field which is localized
 942 on the *TeV* brane. Similarly, the top quark can be localized near the *TeV* brane to account
 943 for its large Yukawa coupling. In the original RS1 scenario all the particles are localized
 944 on the *TeV* brane, therefore the strength of the couplings between KK-graviton and SM
 945 particles are democratic. As a consequence, the RS gravitons are produced via both $q\bar{q}$
 946 annihilation and gluon fusion processes. In the bulk scenario, couplings of KK gravitons to
 947 light fermions are highly suppressed since, as mentioned above, KK gravitons are localized
 948 near the *TeV* brane, whereas light fermions are localized near the *Planck* brane. As a result,
 949 $q\bar{q}$ annihilation at hadron collider for KK graviton production is negligible in this case. In
 950 contrast, SM gluons have a flat localization in the bulk, so that the coupling of gluons to
 951 KK gravitons and hence KK graviton production via gluon fusion is dominant. Furthermore,
 952 decays of KK graviton into top quarks and Higgs bosons are enhanced due to being localized
 953 near the *TeV* brane, resulting in couplings to KK gravitons (which are also localized there)
 954 being only \sim TeV-suppressed just like in the original RS1 model (Eq. 2.57). Another crucial
 955 point of the bulk scenario is that before symmetry-breaking, the W and Z gauge bosons start
 956 out with flat localization in the bulk. However, after symmetry-breaking, the gauge bosons
 957 absorb the Higgs degrees of freedom, and their wave functions are still mostly flat in the bulk
 958 but fall sharply near the brane. Thus, in the bulk scenario, branching fractions for decays
 959 into a pair of vector bosons are the same level as those for decays into Higgs bosons or top
 960 quarks. The branching fractions for the different decay modes of the graviton in both the
 961 bulk and RS1 scenarios are shown in Fig. 2.11 as a function of the graviton mass. It can also
 962 be shown that in RS1 scenario the graviton decays preferentially to transversely polarized
 963 vector bosons, whereas in the bulk scenario it decays preferentially to longitudinally polarized
 964 modes, making those two benchmarks an excellent framework for studying the sensitivity of
 965 the vector boson identification techniques used at the collider experiments to the polarization
 966 (Chapter 7).

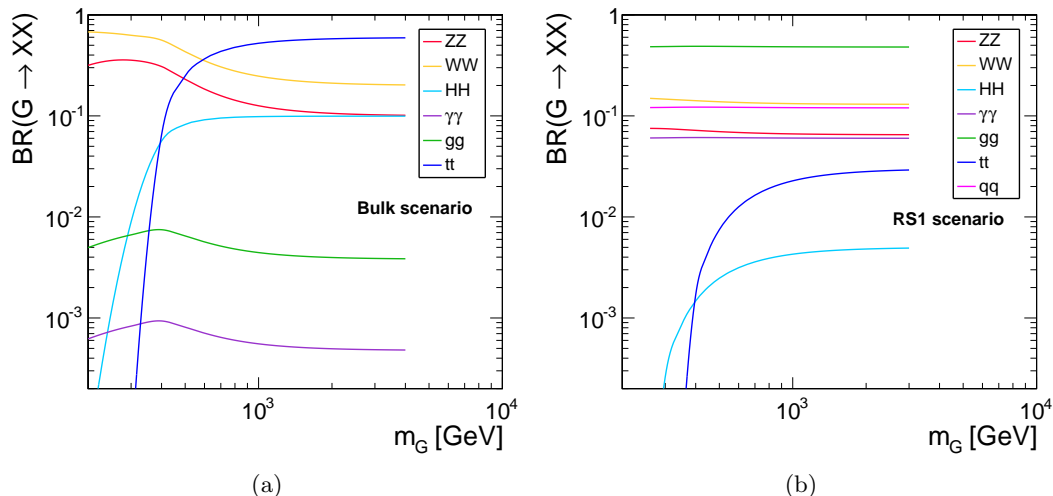


Figure 2.11: Branching fractions for the different decay modes of the graviton in the (a) bulk and (b) RS1 scenarios, as a function of the graviton mass.

967 2.3.2 Compositeness

968 One of the approaches to the hierarchy problem compatible with observations is based on the
 969 assumption that the Higgs boson is a composite particle, a bound state of more fundamental
 970 constituents held together by a new strong force. In composite Higgs models [6, 7, 38], Λ is
 971 the energy scale where the composite nature of the Higgs boson becomes important, which
 972 roughly coincides with the confinement scale of the new strong interaction. Thus, the solution
 973 to the hierarchy problem is that there is no elementary scalar, and beyond Λ an experiment
 974 becomes sensitive to the underlying “partons” that compose the Higgs boson. However,
 975 precision electroweak data rule out new strong interactions at scales below about 10 TeV.
 976 One key question is therefore the lightness of the Higgs boson with respect to such a scale.

977 By comparing with the QCD sector, one observes that the strong coupling scale is
 $\Lambda_{\text{QCD}} \sim \mathcal{O}(300 \text{ MeV})$, whereas most bound states, such as the ρ meson and proton, are at
 979 least as heavy as this. However, a counter-example in QCD is given by the existence of
 980 the pions, which are all lighter than Λ_{QCD} , although only by a $\mathcal{O}(1)$ factor. The reason for
 981 the pions to be appreciably lighter than the other QCD bound states is found in the chiral
 982 perturbation theory. In fact, the pions represent the Goldstone bosons of the spontaneously
 983 broken $SU(2)_L \times SU(2)_R$ flavor symmetry coming from chiral rotations of the up and down
 984 quarks. The spontaneous symmetry breaking of the flavor symmetry into the vectorial
 985 isospin subgroup $SU(2)_V$, is induced by a non-perturbative QCD vacuum state, characterized
 986 by a non-vanishing quark condensate $\langle \bar{q}_L^a q_R^b \rangle \sim \delta^{ab} \Lambda_{\text{QCD}}^3$. However, because of the non-
 987 vanishing and differing masses of the quarks, the $SU(2)_L \times SU(2)_R$ is only an approximate
 988 symmetry, and therefore the pions are not massless, but have small masses, so that they are
 989 *pseudo-Goldstone bosons*.

990 In composite Higgs models, a similar structure is assumed, where the Higgs is a pseudo-
 991 Goldstone boson of some symmetry with strong coupling scale $\Lambda \approx 4\pi f$, where f is the
 992 scale at which the symmetry is spontaneously broken. The main idea is that the Higgs mass
 993 parameter is protected against quadratic quantum corrections up to the compositeness scale
 994 because it is a pseudo-Goldstone boson. Above the scale of compositeness, it is simply not an
 995 elementary scalar. Furthermore, the pseudo-Goldstone nature of the Higgs is an explanation
 996 for why the Higgs mass is so much lighter than the other bound states in the strongly coupled
 997 sector.

998 Such models start with a large global symmetry group G , analogous to the “large”
 999 $SU(2)_L \times SU(2)_R$ global symmetry of low energy QCD. The strong dynamics spontaneously
 1000 breaks G to a subgroup H , similarly to the QCD chiral symmetry breaking $SU(2)_L \times$
 $SU(2)_R \rightarrow SU(2)_V$. In particular, for a minimal composite Higgs model $G = SO(5) \rightarrow H =$
 $SO(4)$. The SM electroweak group $SU(2)_L \times U(1)_Y$ is a subgroup of H , thus introducing
 1003 a preferred orientation in the coset space $SO(5)/SO(4)$ with respect to the global $SO(4)$.
 1004 In this way, the electroweak scale v is distinct from the $G \rightarrow H$ symmetry breaking scale
 1005 f . The parameter $\xi = (v/f)^2$ is introduced to characterize this separation of scales and
 1006 to quantify the degree of vacuum misalignment. In a theory with little hierarchy $\xi \sim 1$,
 1007 while a small amount of fine-tuning can give rise to $\xi \ll 1$. In particular, compatibility with
 1008 the constraints coming from electroweak precision tests and Higgs coupling measurements
 1009 generically implies $\xi \lesssim 0.2$. This bound places the scale f at about 1 TeV, resulting in a strong
 1010 coupling scale $\Lambda \approx 4\pi f \sim 10 \text{ TeV}$. Such large value results in a large one-loop contribution to
 1011 the Higgs mass parameter (Eq. 2.49), so that a generic composite Higgs setup still requires
 1012 some tuning between the v and f scales. One way to generate a “little hierarchy” is through
 1013 the mechanism of *collective symmetry breaking* as in *little Higgs* (LH) scenarios [39–43],
 1014 which is now a key ingredient in composite Higgs models. The main idea of this approach
 1015 is that one can separate the scales v and f by introducing new particles, which cancel the

quadratic divergences at one-loop order. In particular, the quadratic divergence induced by the SM gauge boson loops are canceled by the quadratic divergence induced by heavy gauge bosons at one loop level. Heavy fermionic states are also introduced, which couple to the Higgs field such that the one-loop quadratic divergence induced by the top-quark Yukawa coupling to the Higgs boson is canceled. Furthermore, extra Higgs fields exist as the Goldstone boson multiplets from the global symmetry breaking. This is achieved by enlarging the simple global group G and embedding two parallel global symmetries $G_1 \times G_2$, such that $G \supset G_1 \times G_2 = [SU(2)_1 \times U(1)_1] \times [SU(2)_2 \times U(1)_2]$. A specific implementation, called the *littlest Higgs* [42, 43], starts with the global symmetry $G = SU(5)$, which is spontaneously broken down at the scale Λ to its subgroup $SO(5)$ via a vacuum expectation value of order f . At the same time, the gauge symmetry $[SU(2) \times U(1)]^2$ is also broken into $[SU(2)_L \times U(1)_Y]$, identified as the SM gauge group. The global symmetry breaking leaves 14 massless Goldstone bosons, which become the longitudinal components of the W'^{\pm} and Z' gauge bosons associated with the broken gauge groups, giving them masses of the order f :

$$M(W'^{\pm}) \simeq M(Z') = \frac{g}{\sin 2\theta} f, \quad (2.59)$$

where θ is given by the gauge couplings of the two broken $SU(2)$ groups: $\tan \theta = g_1/g_2$. The partial decay widths are computed using the formalism of Feynman rules:

$$\begin{aligned} \Gamma(W'^{\pm} \rightarrow \ell\nu) &\simeq \Gamma(Z' \rightarrow \ell\ell) &= \frac{g^2 \cot^2 \theta}{96\pi} M \\ \Gamma(W'^{\pm} \rightarrow q\bar{q}') &\simeq \Gamma(Z' \rightarrow q\bar{q}) &= \frac{g^2 \cot^2 \theta}{32\pi} M \\ \Gamma(W'^{\pm} \rightarrow WH) &\simeq \Gamma(Z' \rightarrow ZH) &= \frac{g^2 \cot^2 2\theta}{192\pi} M \\ \Gamma(W'^{\pm} \rightarrow WZ) &\simeq \Gamma(Z' \rightarrow WW) &= \frac{g^2 \cot^2 2\theta}{192\pi} M \end{aligned} \quad (2.60)$$

where M is the mass of the V' triplet given by Eq. 2.59. Summing over all the quark and lepton channels results in a total width

$$\Gamma_{\text{tot}} = \frac{g^2}{96\pi} (\cot^2 2\theta + 24 \cot^2 \theta) M. \quad (2.61)$$

One can immediately observe that the fermionic decay modes dominate for $\cot \theta \geq 1/2$, while bosonic decay modes become significant only below this value. However, since the V' resonances are produced mainly via the Drell-Yan process $q\bar{q}^{(\prime)} \rightarrow V'$, one should notice that the production cross section would be at the same time suppressed for the enhanced bosonic channels. Thus, the interactions of the new predicted particles are described within these theories, and detailed predictions of their properties are made. Furthermore, they provide distinct signatures that can be searched for at a hadron collider of sufficient energy.

2.3.3 Heavy vector triplet

New heavy spin-1 resonances are predicted by several extensions of the standard model, such as the composite Higgs and little Higgs models described in the previous section. A model-independent strategy has been proposed in Ref. [44] to study these resonances, based on a simplified phenomenological Lagrangian, which reproduces a large class of explicit models. The main reason for introducing a simplified model is that the experimental searches for new resonances are typically not sensitive to all the details and the free parameters of the chosen benchmark model, but only to those parameters or combinations of parameters

that control the mass of the resonance and the interactions involved in its production and decay. Therefore one can employ a simplified description of the new phenomena, where only the relevant couplings and mass parameters are retained. In turn, the experimental results expressed in terms of the phenomenological parameters can be easily translated into the free parameters of any explicit model by computing the phenomenological/explicit parameter relations.

In this approach, a new real vector in the $SU(2)_L$ representation is introduced in addition to the SM fields, describing one charged and one neutral heavy spin-1 particle (heavy vector triplet or HVT) with the charge eigenstate fields given by

$$V_\mu^\pm = \frac{V_\mu^1 \mp i V_\mu^2}{\sqrt{2}} \quad V_\mu^0 = V_\mu^3. \quad (2.62)$$

The dynamics of the new vector is described by a simple phenomenological Lagrangian

$$\begin{aligned} \mathcal{L}_V = & -\frac{1}{4} \mathcal{D}_{[\mu} V_{\nu]}^a \mathcal{D}^{[\mu} V^{\nu]a} + \frac{m_V^2}{2} V_\mu^a V^{\mu a} \\ & + ig_V c_H V_\mu^a H^\dagger \tau^a \overleftrightarrow{D}^\mu H + \frac{g^2}{g_V} c_F V_\mu^a J_F^{\mu a} \\ & + \text{extra terms} \end{aligned} \quad (2.63)$$

where g denotes the gauge coupling. The first line of the above equation contains the kinetic and mass terms for the field V , plus trilinear and quadrilinear interactions with the vector bosons from the covariant derivatives. The second line contains direct interactions of V with the Higgs current in the first term, and with the SM left-handed fermionic currents $J_F^{\mu a}$ in the second term. The Higgs current term with coefficient c_H leads to vertices involving the physical Higgs field and the three unphysical goldstone bosons. Since the goldstone bosons represent the longitudinally polarized SM vector bosons W and Z, the parameter c_H controls the interactions of V with the SM vector bosons and with the Higgs boson, and in particular its decay modes into these electroweak particles. Similarly, the parameter c_F describes the direct interaction with fermions, which is responsible for both the resonance production via $q\bar{q}$ annihilation and for its fermionic decays. One observes that a universal coupling of the new field V to fermions is assumed in Eq. 2.63 for simplicity, such that c_F represents the couplings to leptons (c_ℓ), light quarks (c_q) and the third quark family (c_3). The third line of the equation contains new operators and free parameters, which however have a sub-leading effect on the phenomenology of interest for resonant searches, and therefore to a first approximation they can be neglected.

In the adopted simplified description, the free parameter g_V represents the typical strength of V interactions, while the dimensionless coefficient c_H parametrizes the departure from the typical strength. Such a parametrization is convenient because, although the coefficient c_F is of order one in most of the explicit models, the parameter c_H is of order one in the strongly-coupled scenario (e.g., composite Higgs models) but can be reduced in a weakly coupled case (e.g., extensions of the SM gauge group [45, 46]). The coefficients are never larger than one in all cases, whereas the coupling g_V can vary over a large range in different scenarios, from $g_V \sim g \sim 1$ in the typical weakly-coupled case up to $g_V \sim 4$ in the strong limit. Therefore, it is more convenient to factor it out of the parametrization, although it is not a fundamental parameter of the model. For the purpose of presenting experimental results, the combinations $g_V c_H$ and $g^2 c_F / g_V$ that enter in the vertices are instead treated as fundamental parameters, as they control production and decay rates.

After electroweak symmetry breaking the heavy vector acquires mass and one finds that the charged and neutral V 's are practically degenerate ($M_{\pm} \simeq M_0 \simeq M_V$), and therefore they are expected to have comparable production and decay rates at the hadron collider. The partial widths are as well immediately computed in this framework:

$$\begin{aligned}\Gamma_{V^{\pm} \rightarrow f\bar{f}} &\simeq 2\Gamma_{V^0 \rightarrow f\bar{f}} \simeq N_c[f] \left(\frac{g^2 c_F}{g_V}\right)^2 \frac{M_V}{48\pi} \\ \Gamma_{V^{\pm} \rightarrow WZ} &\simeq \Gamma_{V^0 \rightarrow WW} \simeq \frac{g_V^2 c_H^2 M_V}{192\pi} \\ \Gamma_{V^{\pm} \rightarrow WH} &\simeq \Gamma_{V^0 \rightarrow ZH} \simeq \frac{g_V^2 c_H^2 M_V}{192\pi},\end{aligned}\quad (2.64)$$

where $N_c[f]$ is the number of colors and is equal to three for the diquark and to 1 for the dilepton decays. It can be observed that, through the partial width to qq , the parameter $c_F = c_q$ controls the Drell-Yan production rate. The channels which are not reported in Eq. 2.64 are either forbidden, like HH and $\gamma\gamma$ decays, or suppressed like the decays to transverse polarizations or to $W\gamma$.

Two exemplary benchmark models, called A and B, are studied in Ref. [44], which correspond to two explicit models describing heavy vectors, namely those in Refs. [45] and [7], respectively. The c_F and c_H coefficients are fixed to specific values in these models, and the only free parameters are the resonance coupling g_V and its mass M_V . Moreover, since models A and B are inspired, respectively, by weakly-coupled extensions of the SM gauge group and strongly-coupled scenarios, i.e. composite Higgs models, the two benchmark models are considered in different regions of g_V , relatively small, $g_V \lesssim 3$, and relatively large, $g_V \gtrsim 3$, respectively. In particular, the branching fractions for the different decay modes of the neutral spin-1 resonance in models A $_{g_V=1}$ and B $_{g_V=3}$ are shown in Fig. 2.12 as a function of the resonance mass. For these values of g_V , model A predicts comparable branching fractions for decay modes into fermions and bosons, as expected from Eq. 2.64. In model B, on the contrary, c_H is unsuppressed, and therefore the dominant branching fractions are into dibosons, whereas the fermionic decays are extremely suppressed.

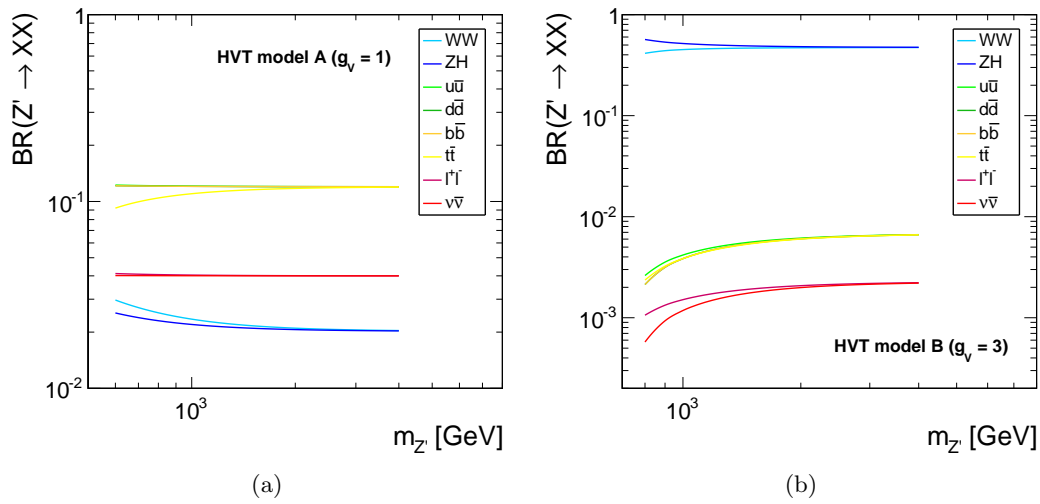


Figure 2.12: Branching fractions for the different decay modes of the neutral spin-1 resonance Z' (V^0) for the benchmarks (a) $A_{g_V=1}$ (a) and (b) $B_{g_V=3}$, as a function of the resonance mass.

It has to be noted that the predictions of this simplified model are only valid for sufficiently narrow resonances. In fact, several effects due to new physics, not included in this simplified

1112 framework, might contribute to the tail and radically change its prediction. As a consequence,
1113 the results of an experimental search which is sensitive to the tail cannot be easily translated
1114 into bounds on the phenomenological parameter space.

1115

1116

The CMS experiment at the LHC

1117

3.1 The Large Hadron Collider

1118 The Large Hadron Collider (LHC) [47] is a proton-proton (pp) collider located at the European
 1119 Particle Physics Laboratory (CERN) near Geneva, Switzerland. It is situated in the former
 1120 CERN LEP tunnel with a circumference of 27 km about 100 m underground crossing the
 1121 border between France and Switzerland. A circular hadron collider has been chosen to allow
 1122 higher center-of-mass energies (\sqrt{s}) compared to circular electron-positron colliders, the
 1123 latter limited by synchrotron radiation due to the low mass of the particles to be accelerated.
 1124 High center-of-mass energies are required for the production of heavy SM particles such as
 1125 the top quark and the Higgs boson, and to search for new BSM interactions at the TeV
 1126 scale. For this purpose, the LHC is designed to produce pp collisions up to a \sqrt{s} of 14 TeV,
 1127 superseding previous high energy hadron colliders, such as the Tevatron, by a factor of 7.
 1128 Higher center-of-mass energies lead to larger cross sections for the production of the physics
 1129 processes of interest in parton-parton interactions. This allows to accumulate higher numbers
 1130 of signal events and it has been essential for the discovery of the Higgs boson and to improve
 1131 the sensitivity of the searches for new BSM processes. The dependence of the discovery
 1132 potential on the energy of the proton beams is usually estimated through the so-called parton
 1133 luminosities, which represent the cross sections of the parton-parton interactions. Figure 3.1
 1134 illustrates this dependence as a function of the mass of a potential resonance produced in
 1135 such interactions. In addition to colliding protons, the LHC is also capable of accelerating
 1136 and colliding heavy nuclei, which is, however, not considered in this work.

1137 The LHC is the final element in a succession of machines that accelerate protons to
 1138 increasingly higher energies. Protons, obtained from a hydrogen source, are first accelerated
 1139 by a linear accelerator (LINAC 2) to energies of 50 MeV. The beam is then injected into the
 1140 Proton Synchrotron Booster (PSB), which accelerates the protons to 1.4 GeV, followed by
 1141 the Proton Synchrotron (PS), which accelerates the beam to 25 GeV. Protons are then sent
 1142 to the Super Proton Synchrotron (SPS) where they are accelerated to 450 GeV. Finally, the
 1143 beam is injected in the LHC ring, where it is accelerated through several revolutions to reach
 1144 the targeted energy. The LHC ring and the acceleration chain are sketched in Fig. 3.2.

1145 Inside the ring, the two proton beams circulate in opposite directions in two tubes kept
 1146 at ultrahigh vacuum, referred to as beam pipes. The acceleration of protons inside the LHC
 1147 is made by radio-frequency cavities (400 MHz), giving a 492 keV energy gain per revolution,
 1148 with a 7 keV loss per turn due to synchrotron radiation. It takes 4 minutes and 20 seconds to
 1149 fill each LHC ring, and 20 minutes for the protons to reach their maximum energy of 7 TeV.
 1150 The maximum energy of the protons is limited by the strength of the magnetic field that can
 1151 be obtained for bending the protons according to the Lorentz force with the radius of the ring.
 1152 For 7 TeV-protons a magnetic field of 8.3 T has to be produced, which can only be reasonably
 1153 obtained by using superconducting magnets. The ring is equipped with 1232 dipole magnets
 1154 for bending and 392 quadrupole magnets for focusing made of niobium-titanium (NbTi),
 1155 which are cooled down to a temperature of 1.9 K using circulating superfluid-helium. After
 1156 acceleration, the protons move through the ring in separate bunches of protons with fixed
 1157 spatial separation.

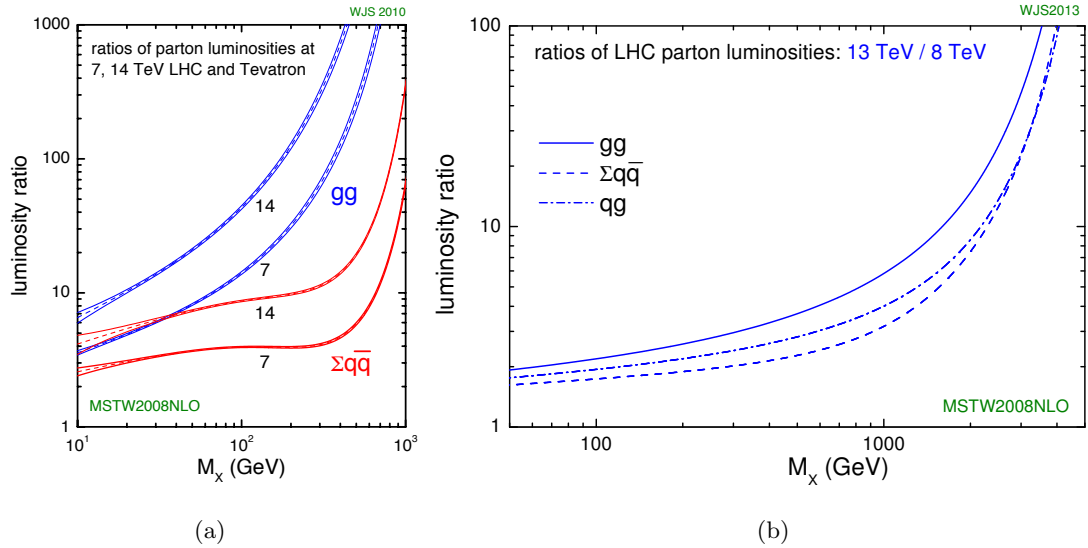


Figure 3.1: (a) Parton luminosity ratios of pp collisions at LHC at $\sqrt{s} = 7, 14$ TeV and p \bar{p} collisions at Tevatron at $\sqrt{s} = 1.96$ TeV as a function of the mass M_x of a potential resonance produced in parton-parton (gg and $q\bar{q}$) interactions. (b) Parton luminosity ratios of pp collisions at LHC at $\sqrt{s} = 13$ TeV and at $\sqrt{s} = 8$ TeV as a function of M_x [48].

The LHC ring has four interaction points at which the two counter rotating beams are made to cross in the center of the four LHC experiments. Before collision, particles in the incoming beams must be squeezed closer to maximize the chances of interaction. For this purpose, a system of three quadrupole magnets, a so-called inner triplet, is located at both sides of each interaction point, that squeezes the beams and leads them to collide in the center of the detector. Inner triplets tighten the beam, making it 12.5 times narrower from 0.2 mm down to 16 μ m across.

Besides the high center-of-mass energy required for the production of heavy particles, a high event rate has to be obtained to allow the discovery of processes with low production cross sections. The instantaneous luminosity \mathcal{L} characterizes the interaction rate. For a process with a cross section σ , the interaction rate is given by

$$\frac{dN_{ev}}{dt} = \sigma \mathcal{L}. \quad (3.1)$$

The instantaneous luminosity depends only on the beam parameters and can be written for a Gaussian beam distribution as:

$$\mathcal{L} = \frac{N_b^2 n_b f_{rev} \gamma_r}{4\pi \sigma_x \sigma_y}, \quad (3.2)$$

where N_b is the number of particles per bunch, n_b the number of bunches per beam, f_{rev} the revolution frequency, γ_r the relativistic gamma factor, while σ_x and σ_y characterize the widths of the transverse beam profiles in the horizontal and vertical direction, respectively. The number of interaction events in a period of running time of the collider can be derived as

$$N_{ev} = \sigma \int \mathcal{L} dt = \sigma L, \quad (3.3)$$

where L is called the integrated luminosity. It is a measurement of the collected data size and it is usually expressed in units inverse to the cross section.

The LHC beams can reach very high luminosity with a high frequency bunch crossing and a high density of protons per bunch. In the ring, 2808 bunches of 1.15×10^{11} protons are circulated, with an average length of 7.5 cm, a width of about $16 \mu\text{m}$ and a bunch spacing of 25 ns (collision frequency of 40 MHz). This corresponds to the design instantaneous luminosity of $10^{34} \text{ cm}^{-2} \text{ s}^{-1}$ for pp collisions, which supersedes by a factor of 100 the luminosity reached by previous hadron colliders.

Proton collisions take place in four points of the LHC tunnel where the four main experiments are located: ATLAS (*A Toroidal LHC ApparatuS*) [49], CMS (*Compact Muon Solenoid*) [50], LHCb (*LHC beauty experiment*) [51] and ALICE (*A Lead Ion Collider Experiment*) [52]. ATLAS and CMS are general-purpose experiments, designed to extensively study SM and BSM physics and to operate at the design luminosity. The LHCb experiment is instead optimized for bottom quark physics studies while the ALICE experiment is dedicated to the study of lead-lead collisions at the design luminosity of $10^{27} \text{ cm}^{-2} \text{ s}^{-1}$.

1191

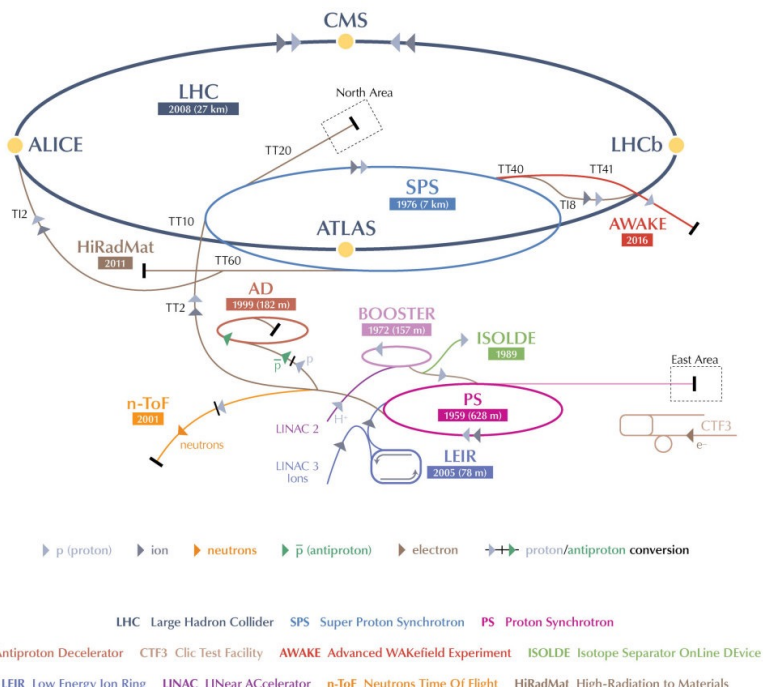


Figure 3.2: The CERN accelerator complex, showing the chain of injection of protons into the LHC ring and the locations of the four main experiments ATLAS, CMS, LHCb and ALICE [53].

LHC operation officially started at the beginning of September 2008 but it was interrupted after a short period, due to an incident with the superconducting magnets. The collider was reactivated in November 2009 with first pp collisions at $\sqrt{s} = 900 \text{ GeV}$, officially starting a new era in particle physics experiments. The operating center-of-mass energies in pp collisions have so far been 7 TeV in 2010-2011, 8 TeV in 2012 and 13 TeV in 2015-2016. The 7 and 8 TeV periods together comprise the *LHC Run 1*, while the 13 TeV period is called the *LHC Run 2*. The work presented in this document is based on data sets collected with pp collisions in both Run 1 and Run 2.

During the whole Run 1, the LHC operated with a 50 ns bunch spacing. The peak of

1190

instantaneous luminosity in 2011 was $\approx 0.4 \times 10^{34} \text{ cm}^{-2} \text{ s}^{-1}$, with a total delivered integrated luminosity of 6.1 fb^{-1} [54]. In 2012 the beam energy increased to 4 TeV per beam with a peak luminosity of $\approx 0.8 \times 10^{34} \text{ cm}^{-2} \text{ s}^{-1}$ and 23.3 fb^{-1} delivered integrated luminosity by the end of that year [54]. The incrementally increasing instantaneous luminosity leads to a non-negligible number of simultaneous pp interactions per bunch crossing, so-called *pileup* (PU) events, which depends on the cross section of inelastic collisions (75 mb at $\sqrt{s} = 8 \text{ TeV}$ [55]) and is proportional to the instantaneous luminosity. The average number of PU interactions for the data collected in 2012 is equal to 21 (Fig. 3.3) while it was approximately 15 in 2011 [54].

A long shut-down period for the LHC (LS1) occurred during the whole 2013 and 2014, where upgrades and technical improvements were performed in order to reach the design instantaneous luminosity and center-of-mass energy. On March, 21st 2015 the first pp collisions at $\sqrt{s} = 13 \text{ TeV}$ were obtained, at a new record-breaking energy. For the first three months the machine operated with 50 ns bunch spacing while, from August 2015, it was reduced to 25 ns and the number of bunches per beam was increased. The first year of this Run 2 phase ended on November 2015 with a total delivered integrated luminosity of 4.2 fb^{-1} and a peak luminosity of $\approx 0.5 \times 10^{34} \text{ cm}^{-2} \text{ s}^{-1}$ with an average pileup of 12 [54].

The LHC Run 2 was restarted in April 2016, after an end-of-the-year technical stop, reaching a peak luminosity of $\approx 1.5 \times 10^{34} \text{ cm}^{-2} \text{ s}^{-1}$. The machine remained in operation at $\sqrt{s} = 13 \text{ TeV}$ for the whole year with a total delivered integrated luminosity of 40 fb^{-1} . Accordingly to the current LHC schedule, the Run 2 will proceed up to the end of 2018 with a total expected integrated luminosity of $\approx 150 \text{ fb}^{-1}$. The data collected in 2016 are not considered in this work.

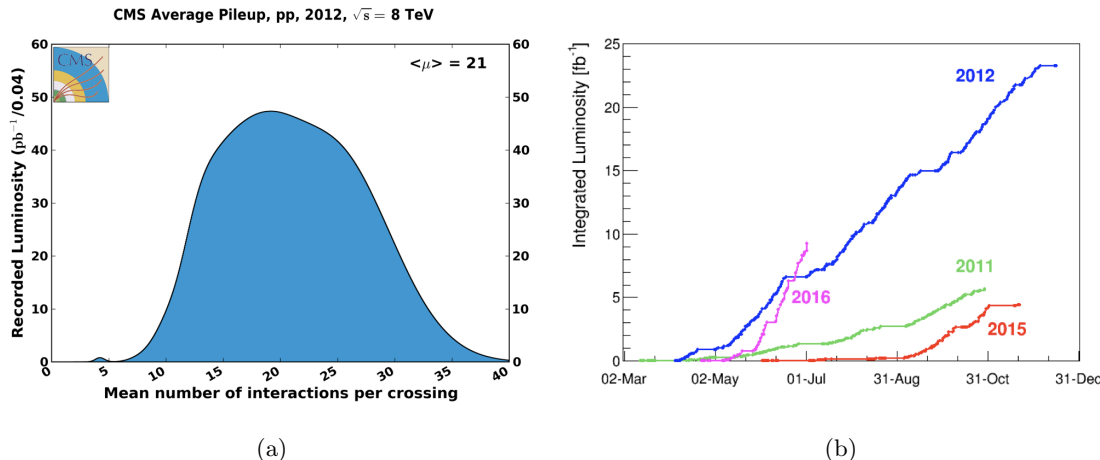


Figure 3.3: (a) Number of simultaneous interactions per bunch crossing in data collected in 2012 by the CMS experiment at LHC. (b) Cumulative luminosity versus day delivered by LHC in 2011, 2012, 2015 and first part of 2016 [54].

3.2 The CMS detector

The CMS detector is a general purpose detector installed 100 m underground at the LHC interaction point 5 (P5) near the village of Cessy in France. It has been designed to exploit the different properties of the wide range of particles and physics processes produced in high-energy collisions at the LHC.

The design of this detector is driven by the challenges of a physics experiment in the LHC environment. Many of the physics processes of interest have a small cross section and the background from QCD jet production is overwhelmingly dominant. In order to achieve an optimal efficiency for rare channels and high rejection power for QCD background, the detector has to be able to reconstruct the primary interaction entirely and to reduce the influence of overlapping interactions on its reconstruction. Therefore, one needs to collect all the relevant information on the particles passing through the detector. Since these have different properties, a mixture of subdetectors is required for a complete event reconstruction. The reconstruction of lepton signatures is essential for the extraction of rare processes. An excellent muon and electron identification and momentum resolution is therefore desired. A precise measurement of secondary vertices and track impact parameters is fundamental for an efficient identification of heavy flavor quarks and τ leptons. Moreover, a large hermetic geometric coverage is preferred, which allows for a precise estimate of the transverse momentum carried away by invisible particles by reconstructing the missing momentum of all of the visible particles.

The high peak luminosities of the LHC lead to a large number of PU interactions, imposing further challenges to the design. As a consequence of pileup, the products of an interaction under study may be confused with those from other interactions in the same bunch crossing. This effect can be reduced by using high-granularity detectors resulting in low occupancy per recorded event. In addition, the short bunch crossing period requires fast response time and good time resolution of each detector element. Hence, a large number of detector channels and an excellent synchronization among them are necessary. Another challenge arises from the large flux of particles near the interaction point which leads to high radiation levels and the need of radiation-hard detectors and front-end electronics.

Figure 3.4 shows the layout of the CMS detector. The detector is built in a cylindrical structure composed of a barrel in the center and endcaps at both sides. This structure is 21.6-m-long, 14.6 m in circumference and has a mass of 12500 tons. The detector design and layout was driven by the choice of the magnetic field configuration. Large bending power is needed for a precise measurement of the momentum of high-energy charged particles. Within the CMS detector this is achieved by a superconducting solenoid with a length of 12.9 m and an inner diameter of 5.9 m generating a magnetic field of 3.8 T. The bore of the magnet coil is large enough to accommodate the inner tracker and the calorimetry inside. The inner tracker consists of silicon pixel and strip detectors, representing the key component of CMS to measure the momenta of charged particles and identify primary and secondary vertices. The calorimetry system is comprised of a crystal electromagnetic calorimeter (ECAL) and a brass and scintillator hadronic calorimeter (HCAL), which provide information on the energies and directions of all charged and neutral particles. Outside the magnet are the large muon detectors, which, integrated inside the return yokes of the magnet, provide identification of muons and measurement of their momenta.

For the description of the CMS detector the following coordinate system is used. The origin is centered at the nominal collision point inside the experiment with the y -axis pointing vertically upward, the x -axis pointing radially inward toward the center of the LHC, and the z -axis pointing along the beam direction. The azimuthal angle ϕ is measured from the x -axis in the x - y plane. The polar angle θ is measured from the z -axis. Pseudorapidity is defined as $\eta = -\ln \tan(\theta/2)$. Thus, the momentum and energy measured transverse to the beam direction, denoted by p_T and E_T , respectively, are computed from the x and y components.

1278 In the following sections the three main components of the CMS detector will be described
 1279 together with a section on the triggering system.

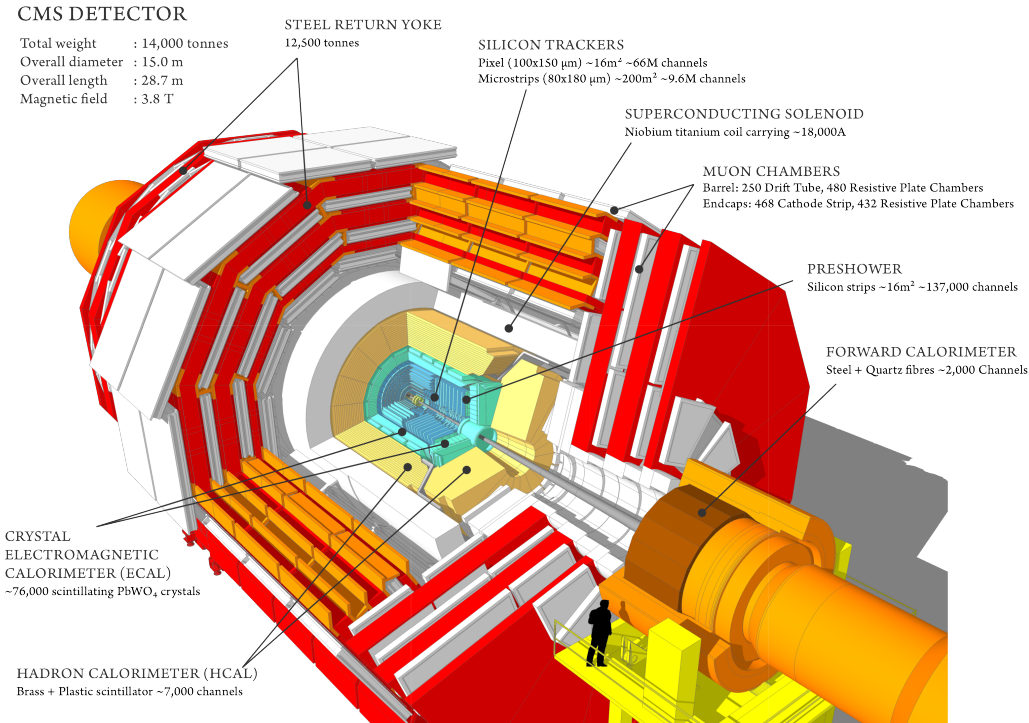


Figure 3.4: Layout of the CMS experiment and its subdetectors.

3.2.1 Tracking detectors

1280 The tracking system of CMS (Fig. 3.5) is designed to provide a precise and efficient mea-
 1281 surement of the trajectories of charged particles emerging from the LHC collisions, as well as
 1282 a precise reconstruction of secondary vertices [56]. It surrounds the interaction point and
 1283 has a length of 5.8 m and a diameter of 2.5 m providing coverage up to $|\eta| < 2.5$. In order
 1284 to achieve high tracking efficiency at the high luminosities of LHC, a detector technology
 1285 featuring granularity, speed and radiation hardness is required. Furthermore, the material
 1286 budget of the tracking system has to be as low as possible in order to avoid a worsening of the
 1287 tracking efficiency and resolution due to material interaction effects of the charged particle,
 1288 such as multiple scattering, bremsstrahlung, photon conversion and nuclear interactions.
 1289 These requirements lead to a tracker design entirely based on silicon detector technology.
 1290 With about 200 m^2 of active silicon area the CMS tracker is the largest silicon tracker ever
 1291 built. It is divided into a pixel detector close to the interaction region and a strip detector in
 1292 the outer region. The motivations for this layout are explained in what follows.

1293 At LHC design luminosity more than 1000 particles are hitting the tracking volume in
 1294 each bunch crossing. This leads to a hit rate density of 1 MHz/mm^2 at a radius of 4 cm
 1295 which imposes severe challenges to the design of the tracking detectors. With a pixel size
 1296 of $100 \times 150 \mu\text{m}^2$ in $r-\phi$ and z , respectively, an occupancy of the order of 10^{-4} per pixel
 1297 per LHC bunch crossing can be achieved. The hit rate density falls with the distance from
 1298 the interaction point to 60 kHz/mm^2 at a radius of 22 cm and to 3 kHz/mm^2 at a radius of
 1299 115 cm. Therefore, at intermediate radii (20–55 cm), silicon micro-strip detectors are used,

1301 with a typical cell length of 10 cm and a pitch of 80 μm . At the outermost radii (55-110 cm)
 1302 the strip size can be further increased to 25 cm \times 180 μm . With this choice an occupancy of
 1303 less than 3% is maintained in the strip detector. However, the strip capacitance scales with
 1304 its length and therefore the electronics noise is a linear function of the strip length as well,
 1305 becoming not negligible in the outermost region where the strip size is the largest. In order
 1306 to maintain a good signal to noise ratio well above 10, CMS uses thicker silicon sensors for
 1307 the outer tracker region (500 μm thickness as opposed to the 320 μm in the inner tracker)
 1308 with correspondingly higher signal. To mitigate the radiation damage effects and prolong
 1309 the lifetime of the detector modules, the tracking detectors are designed to run at subzero
 1310 temperatures. The cooling is established using a mono-phase liquid cooling system with
 1311 C₆F₁₄ as cooling fluid. The whole tracker system operated at +4° C during Run 1. After
 1312 this phase, several improvements were implemented and an operative temperature of -15° C
 1313 is currently maintained for Run 2.

1314

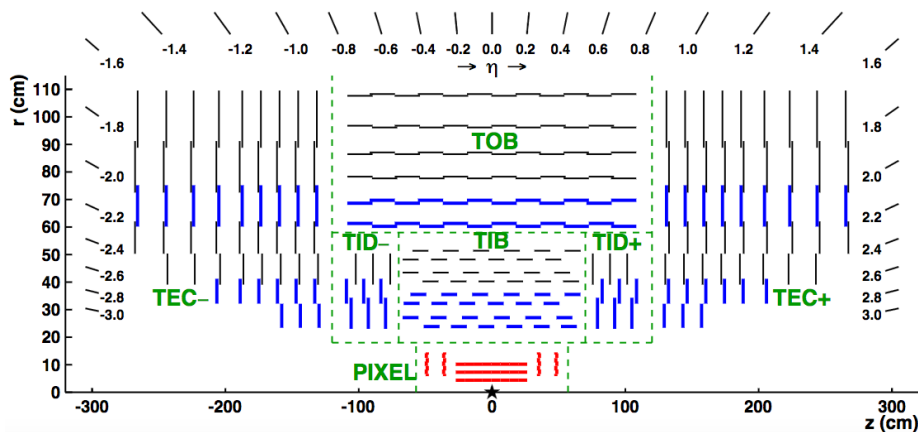


Figure 3.5: Longitudinal section of half of the original CMS silicon tracker system; the different detector types are indicated.

1315 The original pixel detector is built from 3 barrel layers at radii of 4.4, 7.3 and 10.2 cm
 1316 (BPix) and two end disks (FPix) on each side at a distance of $z = \pm 34.5, \pm 46.5$ cm from the
 1317 interaction point. It consists of 1440 segmented silicon sensor modules with a total of 66
 1318 million readout channels covering an area of about 1 m². The pixel detector is essential for
 1319 the reconstruction of the primary and pileup vertices, as well as of the secondary vertices
 1320 from the decay of bottom quarks and τ leptons. It provides precise track point measurements
 1321 in r - ϕ and z and therefore guarantees a small impact parameter resolution important for
 1322 good secondary vertex reconstruction. This is achieved thanks to the readout of the analog
 1323 pulse height information. The sensor surface in the barrel layers is parallel to the magnetic
 1324 field, hence the charge carriers produced by a particle traversing experience a Lorentz drift,
 1325 which leads to charge spreading over more than one pixel (“charge-sharing”). The analog
 1326 pulse height information can be used to calculate a center of gravity of the charge distribution
 1327 improving the hit information. The forward FPix disks are tilted at 20° in a turbine-like
 1328 geometry to induce charge-sharing. As shown in Fig. 3.6, a spatial resolution of 10 μm in
 1329 the transverse plane and 30 μm in the longitudinal direction can be achieved for BPix. For
 1330 FPix a spatial resolution of 20 μm is obtained in both directions. A detailed description of
 1331 the design and the functioning of the CMS pixel barrel detector is given in Chapter 14.

1332

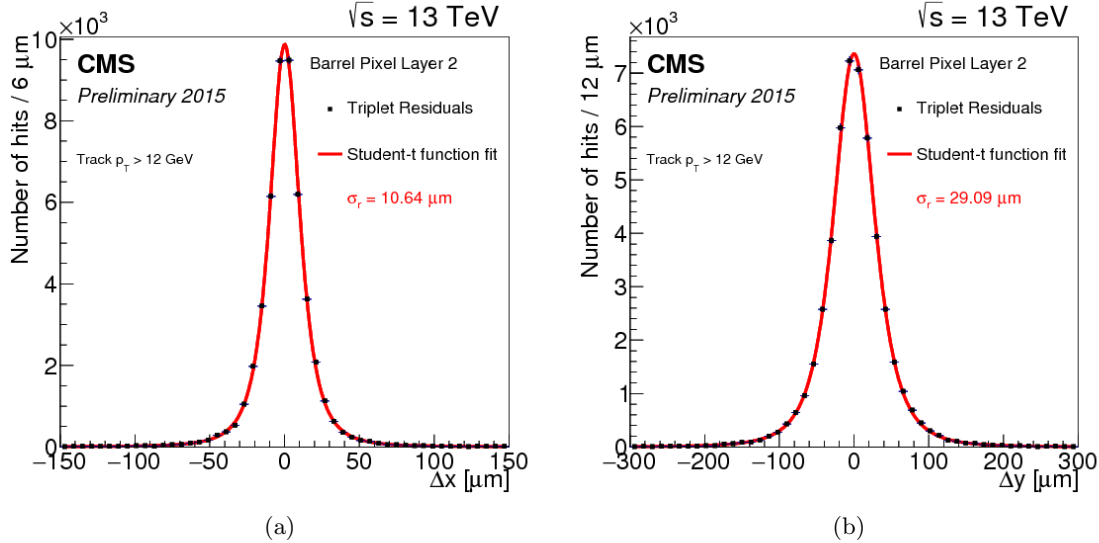


Figure 3.6: Distributions of the hit residuals on the pixel barrel layer 2 in the transverse (a) and longitudinal (b) direction with respect to the beam. The distributions are fitted with a Student's t-function. The fitted width parameter σ_r is reported on the plot [57].

The strip detector occupies the radial region between 20 cm and 1.16 m. As illustrated in Fig. 3.5, it is composed of four subsystems: the four-layer Tracker Inner Barrel (TIB), the six-layer tracker outer barrel (TOB) and on each side three-disk Tracker Inner Disks (TID) and nine-disk Tracker Endcaps (TEC). The silicon micro-strip sensors have strips parallel to the beam axis in the barrel and radially on the disks. The modules in the first two layers and rings, respectively, of TIB, TID, and TOB as well as rings 1, 2, and 5 of the TECs carry a second micro-strip detector module which is mounted back-to-back with an angle of 100 mrad in order to provide a measurement of the second coordinate (z in the barrel and r on the disks). This tracker layout ensures at least 9 hits in the silicon strip tracker in the full range $|\eta| < 2.4$ with at least 4 of them being two-dimensional measurements. The total number of silicon sensors in the strip tracker is 24244, making up a total active area of 198 m^2 , with about 9.3 million of strips.

3.2.2 Calorimetry

The calorimeter measures the energies and directions of all neutral and charged particles traversing the detector, with the exception of muons and neutrinos. It consists of two parts, the electromagnetic calorimeter (ECAL) [58] and the hadronic calorimeter (HCAL) [59].

The goal of the ECAL is to measure precisely the energy of electrons and photons which generate electromagnetic showers inside it. It is a hermetic and homogeneous calorimeter with a large pseudorapidity coverage up to $|\eta| < 3$. As illustrated in Fig. 3.7, the ECAL is divided into barrel and endcap detectors consisting of scintillation crystals made from lead tungstate (PbWO_4). The choice of this material is motivated by its high density (8.28 g/cm^3), short radiation length ($X_0 = 0.89 \text{ cm}$) and small Molière radius (2.2 cm), resulting in high stopping power, fine granularity and a compact size that fits inside the solenoid. The ECAL comprises 61200 crystals in the barrel and 7324 crystals in each of the 2 endcaps, for a total volume of 8.14 m^3 and 2.9 m^3 , respectively. The crystals have a tapered shape

and are mounted in a quasi-projective geometry. The barrel extends radially between 1.29 and 1.75 cm covering the region $|z| < 3.05$ m and $|\eta| < 1.479$. The crystals have a front face cross-section of 22×22 mm 2 and a length of 2.3 cm ($25.8 X_0$). They are organized in 36 identical supermodules each covering 20° in ϕ . The crystals are contained in thin-walled glass-fibre alveola structures (“submodules”) with $2(\phi) \times 5(\eta)$ crystals each resulting in a granularity 360-fold in ϕ and 2 \times 85-fold in η . The endcaps are placed at a distance of 3.14 m from the interaction point and they extend radially between 3.16 and 17.11 cm, covering the region $1.479 < |\eta| < 3.0$. The crystals have a front face cross section of 28.6×28.6 mm 2 and a length of 2.2 cm ($24.7 X_0$). A preshower detector with a thickness of $3 X_0$ is placed in front of the endcaps ($1.653 < |\eta| < 2.6$) to guarantee a reliable discrimination of single photons and photons produced in pairs from neutral pion decays. The relatively low light yield of the crystals ($30 \gamma/\text{MeV}$) requires use of photodetectors with intrinsic gain that can operate in a magnetic field. Silicon avalanche photodiodes (APDs) are used as photodetectors in the barrel and vacuum phototriodes (VPTs) in the endcaps. The light output and the amplification have a strong temperature dependence. The response to an incident electron changes by $(3.8 \pm 0.4)\%/\text{C}$ which in turn means that the temperature has to be closely monitored and kept stable to a precision of $\pm 0.05^\circ\text{C}$. The nominal operating temperature of the ECAL is 18°C and is provided by a water cooling system.

The energy resolution of the electromagnetic calorimeter can be parametrized by the following expression:

$$\frac{\sigma_E}{E} = \frac{S}{\sqrt{E(\text{GeV})}} \oplus \frac{N}{E(\text{GeV})} \oplus C. \quad (3.4)$$

The first term is stochastic, including contributions from the shower containment, the number of photoelectrons and the fluctuations in the gain process. The second contribution corresponds to the noise term, which includes noise in the readout electronics and fluctuations in pileup. The third term is a constant dominating the energy resolution for high-energy electron and photon showers. It depends on non-uniformity of the longitudinal light collection, energy leakage from the back of the calorimeter, single-channel response uniformity and stability. The values of the three coefficients were determined by measurements with an electron beam in a matrix of 3×3 crystals to be $S = 2.8\%$, $N = 12\%$ and $C = 0.3\%$ [60].

The energy measurement of the ECAL is complemented by the measurement of the hadronic calorimeter. The HCAL is designed to be as near to hermetic around the interaction region as possible to allow events with missing energy to be identified. It is a sampling calorimeter composed of layers of brass absorber interlaced with tiles of plastic scintillators as active material to detect the showers generated by the hadrons in the brass. The energy released in the scintillator tiles causes them to emit blue-violet light, a fraction of which is absorbed and re-emitted by embedded wavelength-shifting fibres in the green region of the spectrum. The green light is then carried by special fibre-optic waveguides to the readout system. The photodetection readout is based on multi-channel hybrid photodiodes (HPDs), which are photodetectors configured especially for CMS that can provide gain and operate in a high magnetic field.

Figure 3.8 shows a schematic cross section of the HCAL detectors. The hadron barrel (HB) and endcap (HE) calorimeters sit behind the tracker and the electromagnetic calorimeter as seen from the interaction point. The HB is radially restricted between the outer extent of the electromagnetic calorimeter ($r = 1.77$ m) and the inner extent of the magnet coil ($r = 2.95$ m). This constrains the total amount of material that can be put in to absorb the energy of the hadronic shower. Therefore, an Outer Hadron (HO) calorimeter is placed

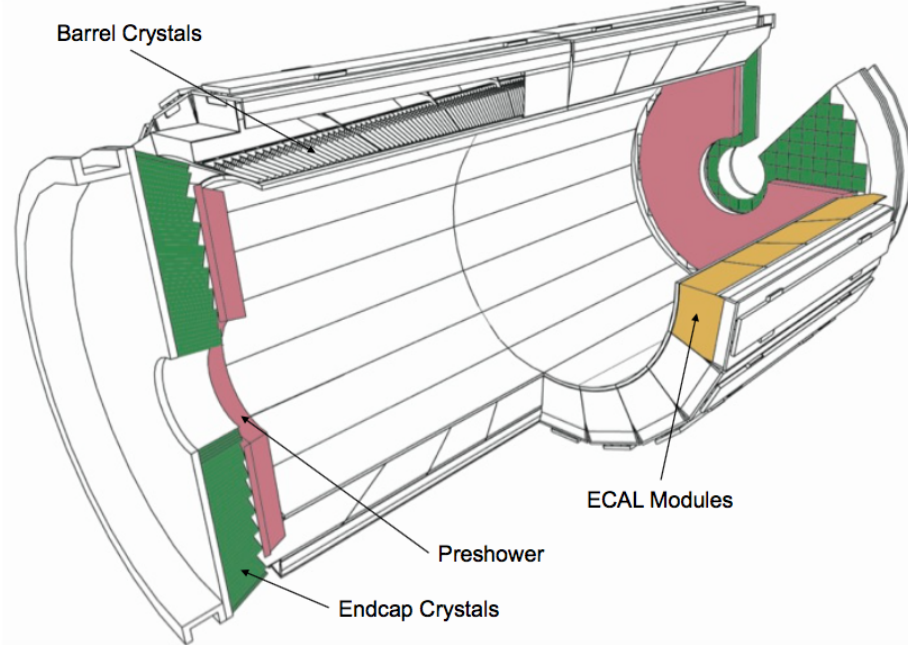


Figure 3.7: Schematic view of the CMS electromagnetic calorimeter [50].

1405 outside the solenoid complementing the barrel calorimeter. The HO uses the solenoid as
 1406 additional absorbing material and provides sufficient containment for hadronic showers with a
 1407 thickness of 11.8 interaction lengths (λ_l). The first scintillators are placed in front of the first
 1408 absorber plate in order to sample showers developing in the material between the ECAL and
 1409 the HCAL, while the last scintillators are installed after the last absorber plate to correct for
 1410 late developing showers leaking out. A total amount of 70000 and 20916 scintillator tiles are
 1411 installed in the HB and the HE, respectively. The HB and HE cover the region $|\eta| < 1.3$ and
 1412 $1.3 < |\eta| < 3.0$, respectively. Beyond $|\eta| = 3$, the Hadron Forward (HF) calorimeter placed at
 1413 11.2 m from the interaction point extends the pseudorapidity coverage up to $|\eta| = 5.2$. The HF
 1414 is a sampling calorimeter made from steel absorber plates composed of 5 mm-thick, grooved
 1415 plates with quartz fibers inserted as active medium. The signal is generated when charged
 1416 shower particles above the threshold generate Cherenkov light in the quartz fibres, thereby
 1417 rendering the calorimeter mostly sensitive to the electromagnetic component of showers. The
 1418 calorimeter is segmented and arranged in towers as summarized in Table 3.1.

1419 The HCAL energy resolution is

$$\frac{\sigma_E}{E} = \frac{a}{\sqrt{E(\text{GeV})}} \oplus 5\% \quad (3.5)$$

1420 where a is 65% in the barrel, 85% in the endcaps and 100% in the forward calorimeter.

Table 3.1: Tower segmentation in azimuthal and polar angle for the hadronic barrel, endcap and forward calorimeters.

	HB/HO	HE ($ \eta \leq 2.5$)	HE ($ \eta > 2.5$)	HF ($ \eta \leq 4.7$)	HF ($ \eta > 4.7$)
$\Delta\phi \times \Delta\eta$	0.087×0.087	0.087×0.087	0.175×0.175	0.175×0.175	0.175×0.35

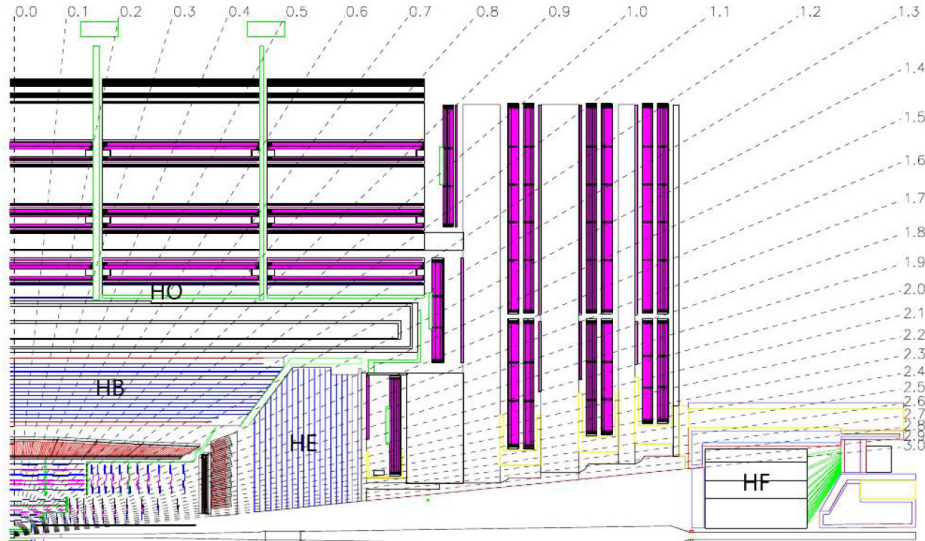


Figure 3.8: Longitudinal view of the CMS detector showing the locations of the hadron barrel (HB), endcap (HE), outer (HO) and forward (HF) calorimeters [50].

3.2.3 Muon detectors

The muon system is the outermost part of the CMS detector. It is located in the steel return yoke of the solenoid, covering the pseudorapidity region $|\eta| < 2.4$. This is possible because muons are hardly affected by the large amount of material placed between the interaction point and the muon system. The coil acts as a shield from electromagnetic and hadronic particles escaping the calorimeters, and the yoke provides a magnetic field between consecutive muon stations, allowing a momentum measurement independent from the inner tracker. The muon system is designed for three major functions: robust and fast identification of muons, good resolution of momentum measurement, and integration to a fast and reliable trigger system. The gaseous detectors have been chosen since they are robust and with a relative fast response. Furthermore, the area to be covered is extremely wide and a gaseous detector system allows the reduction of cost and amount of readout channels. The muon system is thus composed of three types of gaseous detectors arranged in barrel and endcap sections, as shown in Fig. 3.9: Drift Tubes (DTs), Resistive Plate Chambers (RPCs) and Cathode Strip Chambers (CSCs). The choice of different detector topologies lies essentially in the different expected particle rates.

In the barrel region, where the neutron-induced background is small, the muon rate is low, and the 3.8-T magnetic field is uniform, DTs with standard rectangular drift cells are used covering the pseudorapidity region $|\eta| < 1.2$. A DT cell is a 4 cm wide gas tube with a positively charged, stretched wire inside. The barrel DT chambers are organized in five separate wheels. Each wheel is divided into 12 sectors, each covering a 30° azimuthal angle. In each of the 12 sectors there are 4 chambers per wheel which are concentric around the beam line and separated by the iron return yoke. Each DT chamber, on average $2\text{ m} \times 2.5\text{ m}$ in size, consists of 12 layers of DT cells, arranged in three groups of four. For the first 3 stations in each wheel, the middle group measures the z coordinate while the two outside groups measure the $r\phi$ coordinate. The fourth and outermost station does not contain the z -measuring planes. Each one of the 250 DT chambers has a resolution of $\approx 100\text{ }\mu\text{m}$ in $r\phi$ and up to $150\text{ }\mu\text{m}$ in z , and can measure the particle direction with 1 mrad accuracy.

In the two endcap regions of CMS, where the muon rates and background levels are high

and the magnetic field is large and non-uniform, CSCs are used with their fast response time, fine segmentation, and radiation resistance, covering the pseudorapidity region between 0.9 and 2.4. Each CSC is trapezoidal shaped multiwire proportional chambers which consists of 6 gas gaps, each gap having a plane of radial cathode strips and a plane of anode wires running almost perpendicularly to the strips. The gas ionization and subsequent electron avalanche caused by a charged particle traversing each plane of a chamber produces a charge on the anode wire and an image charge on a group of cathode strips. Thus, each CSC provides a two-dimensional position measurement, where the r and ϕ coordinates are determined by the cathode strips and the anode wires, respectively. A total amount of 540 CSCs are arranged in 4 disks per endcaps, divided in concentric rings (3 rings in the innermost station, 2 in the others). Each chamber has a spatial resolution of about 200 mm in r , and $75 \times 150 \mu\text{m}$ in the $r\text{-}\phi$ coordinate.

In addition, there is a total of 610 RPCs added in both the barrel and endcap regions to provide a fast, independent, and highly-segmented trigger over a large portion of the rapidity range ($|\eta| < 1.6$) of the muon system. They produce a fast response, with good time resolution ($\approx 2 \text{ ns}$) but coarser position resolution than the DTs or CSCs. RPCs are made from two high resistive plastic plates with a voltage applied and separated by a gas volume. The signal generated by the muon when passing through the gas volume is detected by readout strips mounted on top of one of the plastic plates. Six layers of RPCs are installed in the barrel muon system, two layers in each of the first two stations and one layer in each of the last two stations. One layer of RPCs is built into each of the first three stations of the endcap.

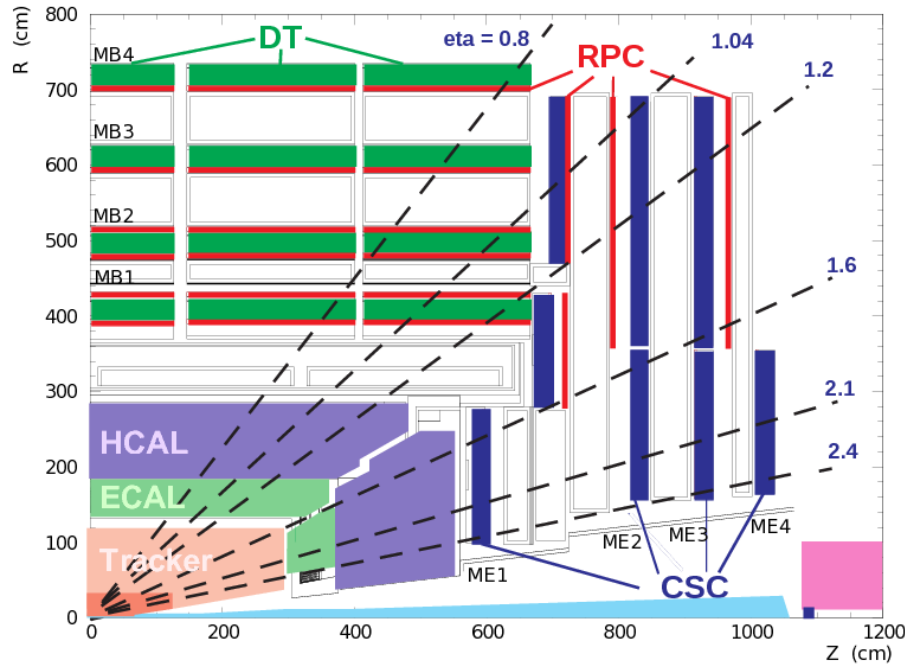


Figure 3.9: A longitudinal view of one quarter of the CMS experiment; the three muon detectors detector types are highlighted.

1472 3.2.4 The trigger system

1473 The LHC provides proton-proton and heavy-ion collisions at unprecedented high luminosity
 1474 and interaction rates. Given the high segmentation of the CMS detector, about 100 million
 1475 readout channels are present and this corresponds to an enormous volume of data at the
 1476 detector front-ends. At the design luminosity and collision frequency, each crossing produces
 1477 approximately 1 MB of zero-suppressed data resulting in a raw data rate of about 40 TB
 1478 per second. These figures are many orders of magnitude larger than the archival storage
 1479 capability of ≈ 1 kHz at data rates of $\mathcal{O}(10^2)$ MB/s. Technical difficulties in handling, storing
 1480 and processing such extremely large amounts of data impose a reduction factor on the rate
 1481 of events that can be written to permanent storage. This task is performed by the trigger
 1482 system, which is the baseline of the physics event selection process. The key point of the
 1483 trigger system is a fast time rejection of all the “non-interesting” events. This can be done by
 1484 exploiting event topologies common to a group of physics processes, such as the presence of
 1485 one or more leptons in the event. The trigger system needs to be as inclusive as possible, in
 1486 order to collect data for all the physics searches that can be performed with pp collisions, but
 1487 it has also to operate within the CMS time restriction and avoid the saturation of the storage
 1488 capability. The required rejection power of $\mathcal{O}(10^5)$ is too large to be achieved in a single
 1489 processing step, since a high efficiency has to be maintained for the physics phenomena that
 1490 CMS plans to study. For this reason, the full selection task is split into two steps. The first
 1491 step (Level-1 Trigger) is designed to reduce the rate of events accepted for further processing
 1492 to less than 100 kHz. The second step (High-Level Trigger or “HLT”) is designed to reduce
 1493 this maximum L1 accept rate of 100 kHz to a final output rate of 1 kHz.

1494

1495 The L1 Trigger is built from custom-designed, programmable electronics and is housed
 1496 partly on the detectors, partly in the underground control room located at a distance of
 1497 approximately 90 m from the experimental cavern. It is designed to take a fast accept/reject
 1498 decision every bunch crossing, on the basis of a rough reconstruction of the event. The
 1499 detector information used at L1 are coarsely segmented data from the calorimeters and
 1500 the muon system only. Within a time budget of $3.2 \mu\text{s}$, the system must decide if an event
 1501 should be discarded or kept, and transfer this decision back to the subdetectors, which in the
 1502 meantime store the high resolution data in the front-end electronics. Figure 3.10 shows the
 1503 L1 Trigger architecture: it has local, regional and global trigger components.

1504

Trigger primitives are generated by calculating the transverse energy of a trigger tower
 and assigning it to the correct bunch crossing. A regional calorimeter trigger then determines
 regional electron, photon and jet candidates and information relevant for muon and τ lepton
 identification. The global calorimeter trigger provides information about the jets, the total
 transverse energy and the missing energy in the event and identifies the highest-energy trigger
 candidates.

1510

In the muon system all three types of detectors take part in the trigger decision. The
 DT chambers provide track segments in the projection and hit pattern in η , while the CSCs
 provide three-dimensional track segments. The track finders in the DT chambers and the
 CSCs calculate the transverse momentum of a track segment and its location and quality.
 The RPCs deliver an independent measurement derived from regional hit patterns. The
 global muon trigger receives up to four candidates from each subsystem (DT, barrel RPC,
 CSC and endcap RPC) together with the isolation information from the global calorimeter
 trigger. The aim is to improve the efficiency and to reduce the rate by making use of the
 complementarity and the redundancy of the subsystems. In the end, the global muon trigger
 selects a maximum of four muon trigger candidates and determines their momentum, charge,
 position and quality.

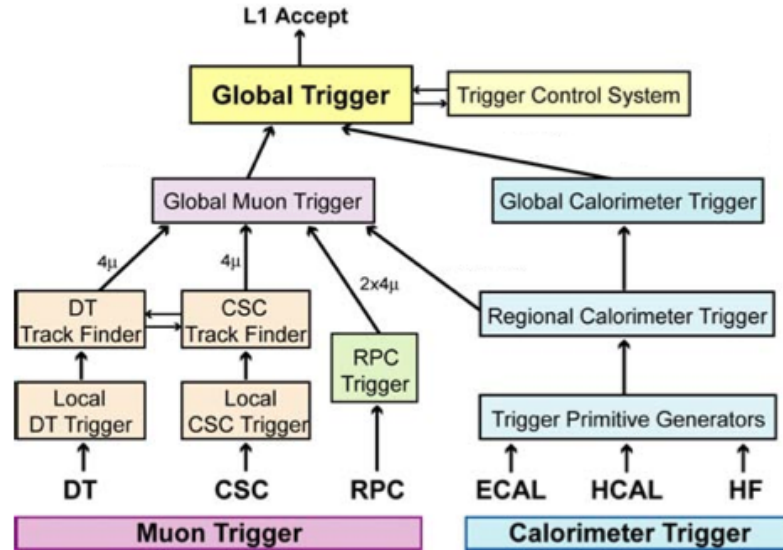


Figure 3.10: Architecture of the Level-1 Trigger [50].

1521 The trigger objects extracted by the global calorimeter trigger and the global muon trigger
 1522 are sent to the global trigger where the decision to accept or reject an event is taken and
 1523 distributed to the subdetectors. The simplest triggers are in general those based on the
 1524 presence of one object with an E_T or p_T above a predefined threshold (single-object triggers)
 1525 and those based on the presence of two objects of the same type (di-object triggers) with
 1526 either symmetric or asymmetric thresholds. Other requirements are those for multiple objects
 1527 of the same or different types (“mixed” and multiple-object triggers). The decision is also
 1528 based on the readiness of the subdetectors and the data acquisition system (DAQ), which
 1529 is supervised by the Trigger Control System (TCS). The Level-1 Accept (L1A) decision is
 1530 communicated to the subdetectors through the Timing, Trigger and Control (TTC) system.
 1531

1532 If an event is accepted by the L1 trigger, the full detector information (≈ 1 MB) is read out
 1533 by the DAQ system and passed to the HLT system for further analysis. The HLT is a special
 1534 part of the CMS software which runs on a farm of several thousand processors performing
 1535 high-level object reconstruction and analysis. Each processor works on the reconstruction of
 1536 one event at a time, to get to a trigger decision within on average 100 ms. Since the time
 1537 budget for one event is much larger than at the L1 trigger, more complicated algorithms,
 1538 including tracking, can be executed at the HLT. Once an event is accepted, it is stored on
 1539 disk and fully reconstructed offline at a later time.

1540 The full detector readout is available at HLT, but in order to meet the timing requirements
 1541 given by the input rate from L1, events are discarded before being fully reconstructed, as
 1542 soon there is enough reconstructed information to take the decision. Therefore the selection is
 1543 organized in a sequence of logical steps. The Level-2 uses the full information from calorimeters
 1544 and muon detectors to reconstruct the physical objects and to reduce the event rate by roughly
 1545 one order of magnitude. The data from the silicon tracker represent almost 80% of the event
 1546 size and require complex and time consuming algorithms for the reconstruction. For this
 1547 reason this information is used only during the Level-3 selection.

1548 The HLT consists of approximately 400 trigger paths. Each trigger path starts from the
 1549 seed provided by the L1 trigger and it is built from reconstruction modules and filter modules.

1550 After some parts of the data are reconstructed, a filter module decides if the reconstructed
1551 objects pass the thresholds and the next step in reconstruction is started, or if the event is
1552 not accepted by the path. In the later case, the execution of the path is stopped and the
1553 following reconstruction steps and filter steps are not performed to save computation time. If
1554 an event is not accepted by a path, it can still be accepted by a different path.

1555 If, for some paths with low thresholds, the acceptance rate is too high, they can be
1556 prescaled to lower the rate. A prescale value of ten means, for example, that the path is
1557 executed only for every tenth event that was accepted by the L1 trigger, and, consequently,
1558 the trigger rate for that path is ten times smaller. The prescale value for one trigger path
1559 has several predefined levels, depending on the instantaneous luminosity of the LHC machine.
1560 During an LHC fill, the instantaneous luminosity decreases, and the prescale values can be
1561 changed during a CMS run to keep the global trigger rate at an optimal level.

1562

Part I

1563

Search for diboson resonances with CMS

1564

1565

1566 Diboson resonances as signature for 1567 new physics

1568

1569 This part of the thesis is dedicated to the description and discussion of searches for new physics
 1570 in proton-proton collision data collected with the CMS experiment at LHC. As pointed out
 1571 in Chapter 2, the remarkable compatibility of the discovered scalar resonance by the ATLAS
 1572 and CMS collaborations with the SM predictions for the Higgs boson, forces physicists to
 1573 deeply understand the role of naturalness in the dynamics of this particle. Several theoretical
 1574 extensions to the SM have been proposed offering a concrete realization of naturalness, where
 1575 new particles with masses in the TeV range generate loop corrections with the necessary
 1576 cancellations to stabilize the Higgs boson mass. More natural solutions can therefore be
 1577 probed at the LHC through the direct discovery of these new, heavy particles in final states
 1578 with SM objects with known properties. The research described in this work follows exactly
 1579 this approach and it is focused on the direct search for new massive resonances decaying to
 1580 pairs of vector bosons (WW, WZ, or ZZ) or to a vector boson and a Higgs boson (WH or
 1581 ZH). These decay modes can have large branching fractions in several BSM models. Popular
 1582 examples include the bulk scenario of the Randall–Sundrum warped extra-dimensions model
 1583 described in Section 2.3.1, as well as the composite Higgs and littlest Higgs models discussed
 1584 in Section 2.3.2. Furthermore, the heavy vector triplet model (Section 2.3.3) generalizes
 1585 a large class of explicit theories that predict new heavy spin-1 vector bosons, adopting a
 1586 simplified model strategy. The two HVT models A and B are considered, which correspond,
 1587 respectively, to a weakly- and a strongly-coupled theoretical option. In this context, spin-1
 1588 resonances are studied that couple both as a vector triplet ($V' = W'$ and Z') and as singlets
 1589 (W' or Z'), i.e. only a charged or a neutral resonance is expected at a given mass. The
 1590 properties of the above benchmark models studied in this thesis are summarized in Table 4.1.

1591

Table 4.1: Summary of the properties of the heavy-resonance models considered in the combination. The polarization of the produced W and Z bosons in these models is mostly longitudinal, as decays to transverse polarizations are suppressed.

Model	Particles	Spin	Charge	Main production	Main decay
HVT model A, $g_V = 1$	W' singlet	1	± 1	$q\bar{q}'$	$q\bar{q}'$
	Z' singlet	1	0	$q\bar{q}$	$q\bar{q}$
	W' and Z' triplet	1	$\pm 1, 0$	$q\bar{q}', q\bar{q}$	$q\bar{q}', q\bar{q}$
HVT model B, $g_V = 3$	W' singlet	1	± 1	$q\bar{q}'$	WZ, WH
	Z' singlet	1	0	$q\bar{q}$	WW, ZH
	W' and Z' triplet	1	$\pm 1, 0$	$q\bar{q}', q\bar{q}$	WZ, WH, WW, ZH
RS bulk, $\tilde{k} = 0.5$	G_{bulk}	2	0	gg	WW, ZZ

1592 The signal under investigation is a narrow resonance, referring to the assumption that
 1593 the resonance's natural width is smaller than the experimental resolution, covering a large
 1594 fraction of the parameter space of the reference models considered. This assumption allows a
 1595 “model-independent” type of search, where the description of the resonance mass distribution

1596 can be restricted to the detector effects only and hence, independent of the chosen benchmark
 1597 model.

1598 The semi-leptonic final states are considered, where one of the two bosons is a W decaying
 1599 into a charged lepton (ℓ) and a neutrino (ν). The lepton can be either a muon (μ) or an
 1600 electron (e), however, the results include the $W \rightarrow \tau\nu$ contribution from the decay $\tau \rightarrow \ell\nu\bar{\nu}$.
 1601 Moreover, the gain in sensitivity from τ leptons is limited by the small branching fractions
 1602 involved. The second boson in the final state decays into quarks, and can be either a vector
 1603 boson $V = W$ or Z , or a Higgs boson. In the first case, the final state is labelled as $\ell\nu q\bar{q}$
 1604 including $W \rightarrow q\bar{q}'$ and $Z \rightarrow q\bar{q}$ decays (Figures 4.1(a), 4.1(b) and 4.1(d)). For the Higgs
 1605 boson, the final state is labeled as $\ell\nu b\bar{b}$ referring to the Higgs boson decay into a bottom
 1606 quark and anti-quark (Fig. 4.1(c)). Each quark from the V or H boson decays results in
 1607 a shower of hadrons in the final state called a *jet*. These particles are collected through a
 1608 jet algorithm which allows to reconstruct the kinematics of the original quark. These final
 1609 states provide high sensitivity to this search as the presence of the lepton in the final state
 1610 highly suppresses the QCD background, while the large branching fractions of the dominant
 1611 $V \rightarrow q\bar{q}^{(\prime)}$ and $H \rightarrow b\bar{b}$ decay modes allow to maintain high signal cross sections.

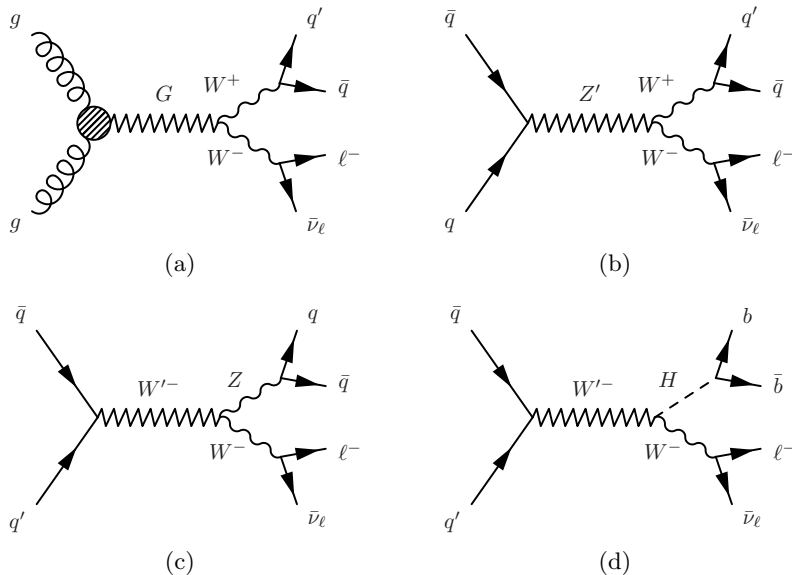


Figure 4.1: Feynman diagrams for the production of a neutral spin-2 G (a), and a neutral Z' (b) and charged W' (c and d) spin-1 resonances. All resonances decay to a pair of bosons (WW , WZ , or WH) with their subsequent semi-leptonic decay. Charge conjugate modes for W' production and decay are implied.

1612 The search in the $\ell\nu b\bar{b}$ final state is based pp collision data at $\sqrt{s} = 8$ TeV collected
 1613 in 2012 and corresponding to an integrated luminosity of 19.7 fb^{-1} . The second analysis
 1614 described in this thesis and focused on the $\ell\nu q\bar{q}$ final state is instead based on the pp collision
 1615 data at $\sqrt{s} = 13$ TeV collected in 2015 and corresponding to an integrated luminosity of
 1616 2.3 fb^{-1} . Although different algorithms are used for the reconstruction and identification of
 1617 the hadronically decaying boson, the analysis strategy is similar in the two searches.

1618
 1619 The key challenge of these analyses is the reconstruction of the highly energetic decay
 1620 products. Since the resonances under study have masses of \approx TeV, their decay products,
 1621 i.e. the bosons, have on average transverse momenta of several hundred GeV or more. As a
 1622 consequence, the particles emerging from the boson decays are very collimated. In particular,

the decay products of the bosons cannot be resolved using the standard algorithms, but are instead reconstructed as a single jet object. Dedicated techniques, so-called jet “V tagging” and “H tagging” techniques, are applied to exploit the substructure of such jet objects, and can help resolve jet signatures of massive bosons. In particular, the jet is tagged as coming from a V or H boson through the estimation of its invariant mass. These techniques also help to suppress SM background, which mainly originates from the production of W bosons in association with jets (W+jets). Further discrimination is achieved in the $\ell\nu b\bar{b}$ analysis channel exploiting the specific characteristics of jets arising from the hadronization of bottom quarks. As these algorithms aim at tagging V and H bosons of large Lorentz-boost in the final state, a lower limit is placed on the resonance mass hypothesis. In fact, for values of the resonance mass below 0.6 TeV, the jets arising from the hadronization of the two quarks are not collimated enough to be reconstructed as a single jet, such that the gain in sensitivity becomes significantly lower. In such cases, analysis techniques exploiting the kinematics of the two resolved jets provide higher sensitivity. Specifically, the searches in the $\ell\nu q\bar{q}$ and $\ell\nu b\bar{b}$ final states are restricted to masses of the mother particle with values above 0.6 and 0.8 TeV, respectively. A higher value is chosen for the $\ell\nu b\bar{b}$ search because, being the H boson slightly heavier than the W and Z bosons, it acquires a smaller boost for a given resonance mass.

1640

The aim is to reconstruct the full event to be able to search for a localized enhancement in the invariant mass of the WV or WH system on the top of a smoothly falling SM background distribution. The invariant mass of the WV and WH system is determined by estimating the neutrino transverse momentum as the measured missing transverse energy in the event, while an estimate of the neutrino longitudinal momentum is derived by imposing the constraint of the W mass on the invariant mass of the $\ell\nu$ system. In the following, the diboson invariant mass will be labelled either $m_{\ell\nu+\text{jet}}$, or m_{WV} and m_{WH} for the $\ell\nu q\bar{q}$ and $\ell\nu b\bar{b}$ final states, respectively. The SM background is mainly comprised of W+jets production, although another significant contribution is represented by the production of top quark-antiquark pairs ($t\bar{t}$). Other minor backgrounds are represented by single top quark and SM diboson (WW, WZ or ZZ) production processes. The Feynman diagrams for W+jets, $t\bar{t}$, single top-quark and SM diboson production processes are shown, respectively, in Figures 4.2, 4.3, 4.5, and 4.4. The mass spectrum for the dominant W+jets background is estimated from observed events with a reconstructed jet mass not compatible with the V or H hypothesis.

1655

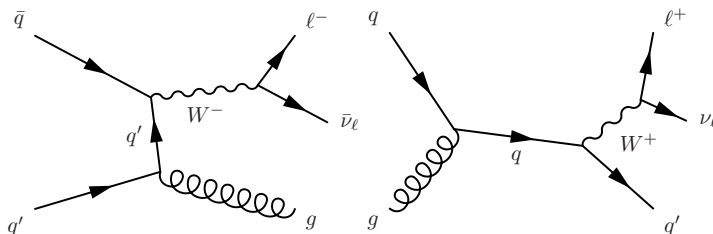


Figure 4.2: Feynman diagrams for the production of W bosons in association with jets and subsequent semi-leptonic decay. Charge conjugate production and decay modes are implied.

This part of the thesis is organized as follows. Chapter 5 gives an overview of the methods used to simulate the physics processes happening in pp collisions at the LHC together with a description of the specific simulated background and signal events used in this analysis, as well as a discussion about the data sets analyzed. Chapter 6 provides a detailed description of the algorithms used in CMS for the reconstruction of the event and of the physics objects expected in the lepton+jet final states under investigation. Particular attention is given to the

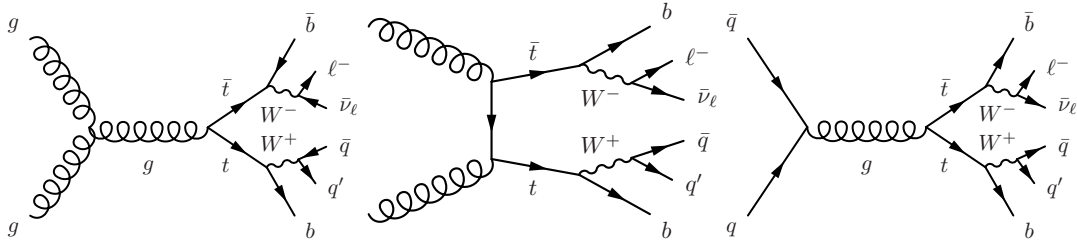


Figure 4.3: Feynman diagrams for the production of top quark-antiquark pairs and subsequent semi-leptonic decay. Charge conjugate modes for the decays of W bosons are implied.

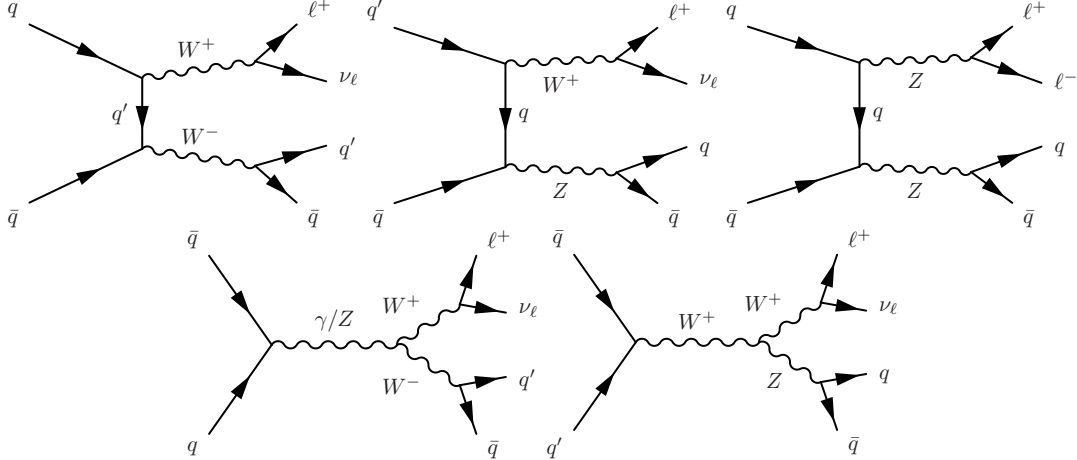


Figure 4.4: Feynman diagrams for the production of SM vector boson pairs and subsequent semi-leptonic decay. Charge conjugate production and decay modes are implied.

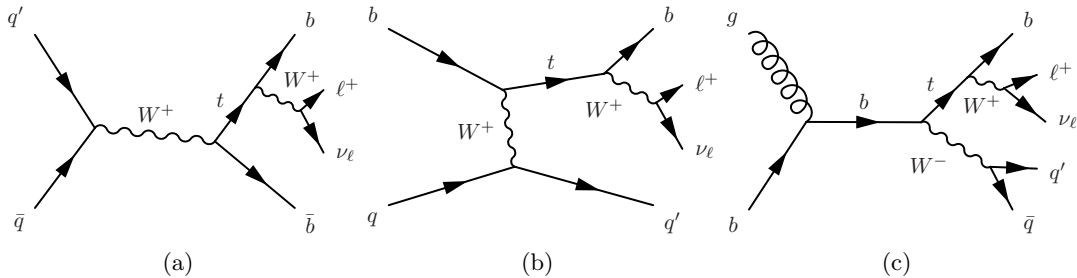


Figure 4.5: Feynman diagrams for the production of single top quarks and subsequent semi-leptonic decay: (a) s-channel, (b) t-channel, (c) tW-channel.

1662 V- and H-tagging algorithms which represent the key feature of this analysis and therefore are
 1663 separately discussed in Chapter 7. The analysis strategy, already outlined here, is explained
 1664 in detail in Chapter 8. This includes the final event selection and categorization optimized to
 1665 enhance the analysis sensitivity, as well as the strategy for the estimation of the expected
 1666 background, the modelling of the signal and the related systematic uncertainties which will be
 1667 used as input to the statistical analysis of the diboson invariant mass distribution observed in
 1668 data. The final results are discussed in Chapters 9 and 10 for the 8 and 13 TeV data analysis,
 1669 respectively. Eventually, these results are combined with limits derived in companion CMS
 1670 searches for resonances decaying to a pair of bosons in several different final states, with data
 1671 collected in both LHC Run 1 and Run 2. The statistical combination represents the last
 1672 piece of this work and it is presented in Chapter 11.

Data sets and simulated samples

1675

1676 The simulation of pp collisions is usually performed by means of Monte Carlo (MC) event
 1677 generators, providing an accurate modelling of the event kinematics and topology. The hard
 1678 inelastic scattering has to be fully calculated: from the hard interaction between the partons
 1679 inside the protons, where perturbative QCD calculations (Section 2.1.6) can be used, to
 1680 the formation of particle jets from the outgoing partons. Furthermore, it is fundamental
 1681 to understand the exact response of the detector to the outgoing particles produced in pp
 1682 collisions. Consequently, the stable outgoing particles are input into a full detector simulation
 1683 that models the interaction of these particles with the detector material and the corresponding
 1684 detector response. The simulated detector data are then subject to the same reconstruction
 1685 algorithms that are also used for real data. In this chapter, MC event generators are described
 1686 in detail, followed by a brief description of the CMS detector simulation. Finally, details are
 1687 given in the last section on the pp collision data sets used to perform the searches described
 1688 in this thesis.

1689 5.1 Simulation of proton-proton collisions

1690 5.1.1 Monte Carlo event generators

1691 The generation of hard inelastic pp collisions is factorized into different steps ordered by the
 1692 timescale on which they happen, as illustrated in Fig. 5.1, and described in the following.
 1693

1694 The basis of theoretical event generation at the LHC is a parametrisation of the incoming
 1695 partons (quarks, anti-quarks and gluons) stemming from the proton, which is given by the
 1696 parton density functions (PDF). They describe the probability to find a quark or gluon with
 1697 a given proton momentum fraction x in a proton of a pp collision taking place at the LHC.
 1698 In pQCD the PDFs depend on a factorization scale μ_F^2 at which the proton is probed. All
 1699 interactions between quarks and gluons happening at scales below the scale μ_F^2 are absorbed
 1700 into the PDFs. Therefore at small μ_F^2 the proton is observed basically as a combination of
 1701 its three valence quarks uud . At higher scales, however, it is dominated by sea quarks and
 1702 gluons.

1703 A collision between two partons, one from each side, gives the hard process of interest,
 1704 which can be due to an interaction described within or beyond the standard model. Using
 1705 the incoming partons as input, the simulation of the hard process is performed by the event
 1706 generator. It produces hypothetical events with the distributions and rates predicted by
 1707 theory based on the cross section formulae of the physics process of interest.

1708 The cross section can be calculated by means of the so-called *factorization theorem* [62].
 1709 According to the theorem, the hadron itself is described by the whole particle composition
 1710 interacting on a soft binding energy scale, whereas the collisions occur between the partons
 1711 on a hard energy scale with large transverse momenta. The cross section for the process is
 1712 then given by the convolution of the PDF $f_i(x, Q^2)$, integrated over the proton momentum
 1713 fraction x , for the colliding protons (A, B) at an energy scale Q^2 , and the hard parton-parton
 1714 cross sections $\hat{\sigma}_{ij} \rightarrow X$ for all combinations of two partons i and j:

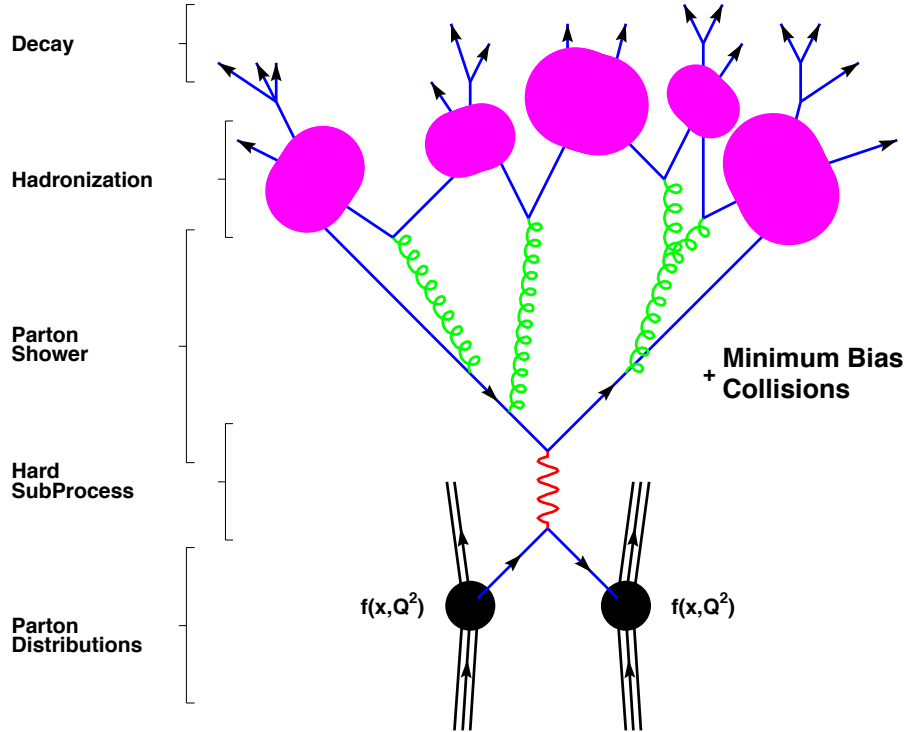


Figure 5.1: Steps of Monte Carlo event generation as described in the text evolving in time from bottom to top [61].

$$\sigma(AB \rightarrow X) = \sum_{q,g=0}^n \alpha_S^n(\mu_R^2) \sum_{ij} \int dx_i dx_j f_{i,A}(x_i, \mu_F^2) f_{j,B}(x_j, \mu_F^2) \cdot \hat{\sigma}_{ij \rightarrow X}^{(n)}(s; x_i, x_j, \mu_R^2, \mu_F^2). \quad (5.1)$$

In the above equation α_S is the strong coupling constant (Section 2.1.6), the index n runs over the perturbative order and s is the squared center-of-mass energy of the collision. The tree-level process, where no emission of gluons or quarks happens, is called ‘‘Leading Order’’ (LO) and takes place when $n = 0$. Further orders are called ‘‘Next-to-Leading Order’’ (NLO, $n = 1$), ‘‘Next-to-Next-to-Leading Order’’ (NNLO, $n = 2$) and so on.

As it can be seen from the formula, the PDFs play a fundamental role in the description of the hard process, and it is very important to have several experimental tests to access their values. In fact, perturbative QCD cannot predict the PDFs, since they contain also the low energy (non-perturbative) information about the scattering. As a consequence, PDF distributions are extracted from the data of deep-inelastic scattering experiments. Most of the parametrizations of proton PDFs now used for the LHC have been extracted from the ZEUS [63] and H1 [64] experiments in electron-proton collisions at the HERA collider and fixed target experiments. The more recent parametrizations also take into account vector boson production and single-inclusive jet production from the Tevatron experiments, as well as LHC data. Once measured for a certain momentum fraction x_i at an energy scale Q^2 , they can be extrapolated to another scale using the DGLAP (Dokshitzer-Gribov-Lipatov-Altarelli-Parisi) evolution equation [65]. The PDF sets used for the simulation of signal and background samples with $\sqrt{s} = 8$ TeV are provided by the CTEQ/CT group [66, 67]. This set especially incorporates the effects of Tevatron Run I jet production data on the gluon

1734 distribution and is therefore expected to describe the mainly gluon-based LHC processes
 1735 realistically. The CT sets additionally include measurements from HERA-1 data, new data
 1736 on the asymmetry in the rapidity distribution of the charged lepton from W boson decay
 1737 from CDF, and rapidity distributions of Z bosons from both CDF and DØ. The NNPDF
 1738 sets [68], calculated with an approach based on artificial neural networks, are used for the
 1739 13 TeV simulations and the newest versions include LHC data as well. An example of the
 1740 most important parton distributions inside the proton is shown in Fig. 5.2.

1741

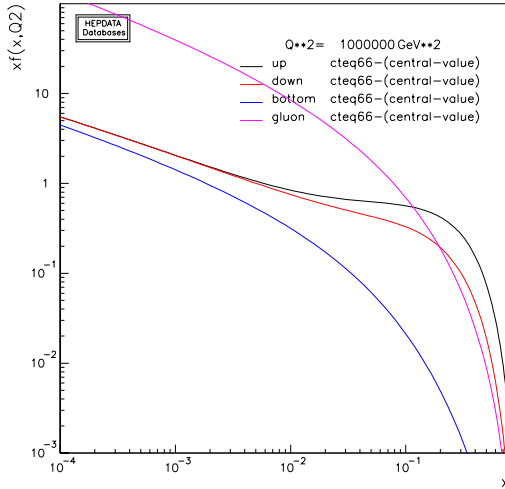


Figure 5.2: CTEQ6.6 central value parton distribution functions at the typical mass scale of a new diboson resonance ($Q^2 = (1000 \text{ GeV})^2$) for up, down and bottom quarks, and gluons in the proton in double-logarithmic scale.

1742 An accurate description of the process must take into account radiative corrections to the
 1743 tree-level or LO description of the process of interest. In particular, one has to include the
 1744 effects of real and virtual higher-order corrections in perturbation theory. This is achieved by
 1745 computing the matrix element between the initial and final states as the sum of contributions
 1746 with increasing powers of α_S . For instance, the LO contribution to the W boson production
 1747 process can be calculated from the diagram in Fig. 5.3. The diagrams contributing at NLO
 1748 to this process and corresponding to the real and virtual radiative corrections at the first
 1749 order are shown in Fig. 5.4.

1750

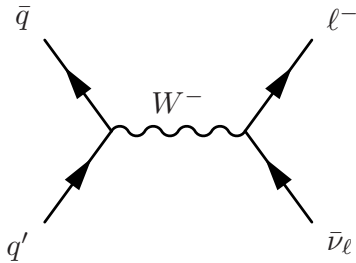


Figure 5.3: (top) Feynman diagram contributing to the W boson production at leading order. The charge conjugate production mode is implied. Only the leptonic decay of the W boson is considered.

1751 Perturbative calculations in QCD are limited to processes in which the coupling constant
 1752 α_S is small, and by the complexity of higher order calculations preventing their evaluation.

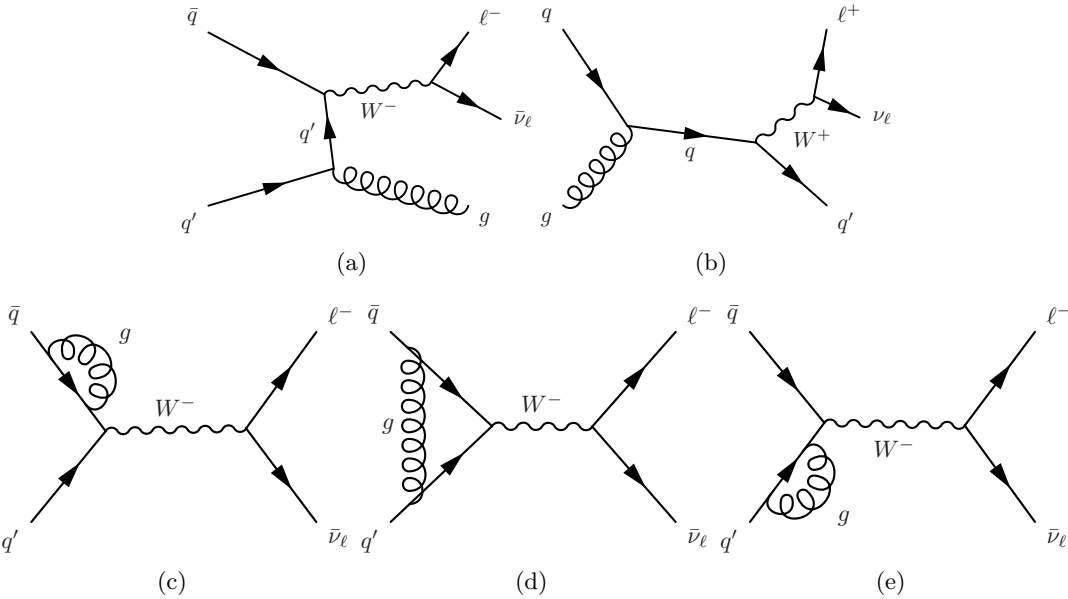


Figure 5.4: Feynman diagrams contributing at next-to-leading order to the W boson production and corresponding to the first order real (top) and virtual (bottom) radiative corrections. The charge conjugate production modes are implied. Only the leptonic decay of the W boson is considered.

Consequently, the current generators are only able to treat a limited number of partons in the final state. Parton showering algorithms extend the fixed-order calculations beyond these limiting factors by calculating emissions of additional partons from the incoming and outgoing partons of the main interaction. This approach in principle takes into account emissions of an unlimited number of partons, but, as opposed to full higher order calculations, does not take into account loop diagrams. Parton showering algorithms start from the hard process allowing the partons to split (or branch) into pairs of other partons. These again may also branch and so on, so that an event then consists of a large number of elementary particles, including quarks and gluons. The cascade of splittings is stopped once the energy scale reaches values where the coupling constant α_S becomes large.

At this stage, quarks and gluons, which carry colour, cannot be considered as free anymore and recombine to form neutral hadrons, through the so-called *hadronization* process. The formation of color-neutral hadrons from the colored partons is treated in phenomenological non-perturbative models. Eventually, many short-lived resonances will be present after hadronization which are then decayed.

The showering and hadronization programs often bring along the possibility to add underlying events. The underlying event arises from the colored remains of the protons that did not take part in the hard collisions, the so-called beam remnants. They are usually included in the hadronization process, because they might be colour-connected to the hard subprocess. The produced hadrons will however carry a very small transverse momentum and will be very forward. The probability for colour reconnection to take place between two partons can also be adjusted based on experimental data. It is also possible that more than one parton interacts with the other proton. This phenomenon, called multiple parton interaction, and it is usually added to the description of the process.

As a last step the pileup is also accounted for. Additional simulated inelastic pp interactions are added to the generated events to match the additional particle production due to

pileup. The exact number of average collisions per bunch crossing in the data is estimated by multiplying the instantaneous luminosity, a value which is continuously monitored, by the total inelastic cross section. One can then reconstruct the distribution of the number of pileup interactions in the data for the complete data taking. The corresponding distributions for the 2012 and 2015 data are shown in Figs. 5.5(a) and 5.5(c), respectively, together with the corresponding simulated pileup scenarios. Simulated events are then reweighted such that they match the data distribution. The description of the pileup by the simulation can be verified by counting the number of reconstructed vertices in the event as illustrated in Figs. 5.5(b) and 5.5(d).

1789

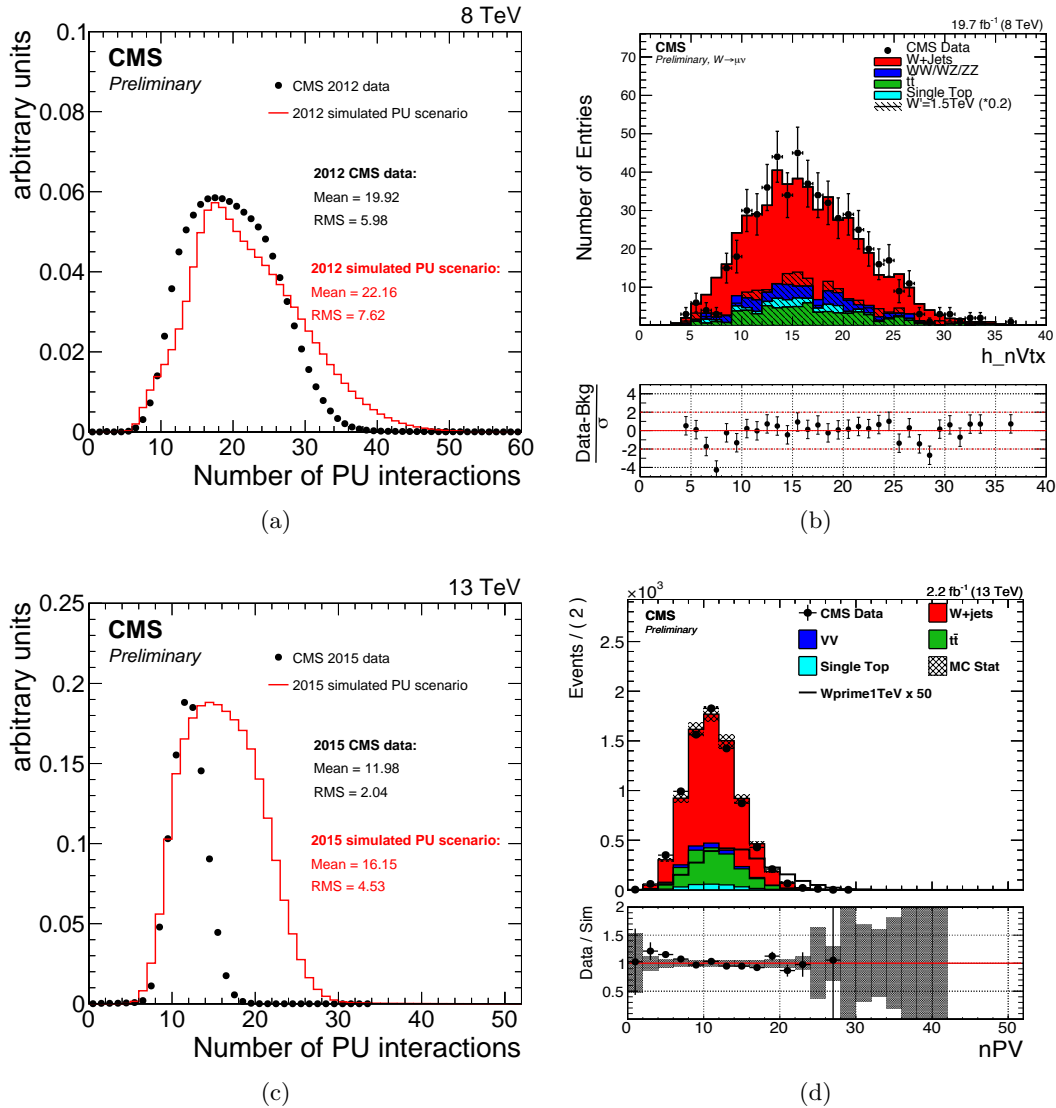


Figure 5.5: Distributions of the estimated average number of pileup collisions in the full data set of pp collisions recorded at $\sqrt{s} = 8$ TeV in 2012 (a) and at $\sqrt{s} = 13$ TeV (c), together with the corresponding simulated pileup scenarios. Also shown are the distributions of the number of reconstructed primary vertices in 8 TeV (b) and 13 TeV (d) data (black dots) and in various simulated samples after pileup reweighting, for lepton+jet events.

1790

Currently, available NLO calculations included in MC event generators cover a wide range

of physics processes, starting with two-particles annihilation to a maximum of five final state objects. A widely-used generator is PYTHIA [69, 70], a general purpose program which, in addition to the hard process, also takes care of the parton showering, the hadronization, and the description of the underlying event. For the matrix element calculation, PYTHIA only considers the leading order hard subprocess (diagram in Fig. 5.3 for the W production case), and higher order effects are added by “evolving” the event using the parton shower. A more accurate approach is followed by MADGRAPH [71] where the hard (higher momentum), real radiative corrections are included in the matrix element (Fig. 5.4). This generator is well suited to study processes such as those with a W or Z produced in association with hard jets. Since it does not completely simulate the events, it needs an additional program, typically PYTHIA, to perform the parton shower after the calculation of the matrix element. It has to be noted that matrix element generators as well as shower and hadronization generators are usually treated independently: the matrix element generators compute the hard process at fixed-order and the parton shower processes the soft and collinear emissions. However, this fails to correctly represent higher order processes in which an additional parton is emitted at the hard scale because parts of this process overlap with the soft one. Combining an NLO matrix element program with a parton shower program therefore leads to double-counting of events. However, a dedicated interface between the matrix element calculation and the parton shower has been developed to correct for this effect [72]. The NLO matrix element generators, such as POWHEG [73] and MC@NLO [74], take special care of the matching to the parton shower by merging soft and collinear emissions with the hard ones.

5.1.2 CMS detector simulation

For a detailed understanding on how interactions in pp collisions at the LHC are observed by the CMS detector, a dedicated simulation of the whole detector is needed. The CMS simulation is based on the GEANT4 [75] toolkit, which takes as input the collections of particles produced by MC event generators. The program calculates the trajectory of the various particles generated during the collision, simulates their electromagnetic and hadronic interaction with the crossed material and the signal they will produce in the various subdetectors. The detector geometry is given as an input to the program, and to obtain a description as close as possible to the reality, any available information such as the existence of insensitive materials or dead channels and their position, is included. The electronic readout of the hits produced by particles is simulated, taking into account resolution and detector response effects. The same algorithms as for real data are then used to reconstruct the various physical objects (Chapter 6).

5.2 Simulated samples

5.2.1 Simulation of signal processes

For the 8 TeV data analysis, the signal hypothesis has been simulated at LO accuracy with a W' boson produced via quark-antiquark annihilation and decaying into W and Higgs bosons in the $\ell\nu q\bar{q}$ final state with $q = b, c$ or g and $\ell = e, \mu$ or τ . Resonance masses in the range 0.8–2.5 TeV are considered in this analysis. The events are generated at parton level using a model of a generic narrow spin-1 W' resonance implemented with MADGRAPH. Showering and hadronization are performed using PYTHIA6 using the Z2* tune to describe the underlying event [76, 77]. It has been verified that the kinematic distributions obtained with the implementation of the generic model agree with those predicted by implementations of the LH, composite Higgs and HVT models in MADGRAPH. The resonance width differs in

1836 the three models, but in each case it is found to be negligible with respect to the experimental
 1837 resolution.

1838 The following parameters are used to compute the cross sections: $g_V = 3$, $c_H \simeq -1$, and
 1839 $c_F \simeq 1$ in the HVT model B (Section 2.3.3) and $\cot 2\theta = 2.3$, $\cot \theta = -0.20799$ in the LH
 1840 model, where θ is a mixing angle parameter that determines W' couplings (Section 2.3.2)
 1841 such that $\cot 2\theta$ and $\cot \theta$ can be directly related to c_H and c_F .

1842 The intrinsic width and cross section for both models are listed in Table 5.1 for the
 1843 resonance masses considered. The widths for the HVT model B are computed by means
 1844 of Eq. 2.64, while the cross sections were obtained using the online tools provided by the
 1845 authors of the simplified model described in Section 2.3.3.

Table 5.1: Intrinsic total widths (Γ) and cross sections for $\sqrt{s} = 8$ TeV (σ) for the LH model and HVT model B for different masses of a resonance W' decaying to WH. The $WH \rightarrow \ell\nu b\bar{b}$ branching fraction is not included in the calculation.

Resonance mass [TeV]	LH model		HVT model B	
	Γ [GeV]	σ [pb]	Γ [GeV]	σ [pb]
0.8	7.22	5.09×10^{-1}	24.1	3.37×10^{-1}
0.9	8.12	3.03×10^{-1}	27.1	2.48×10^{-1}
1.0	9.02	1.87×10^{-1}	30.1	1.71×10^{-1}
1.1	9.92	1.18×10^{-1}	33.1	1.16×10^{-1}
1.2	10.8	7.65×10^{-2}	36.1	8.05×10^{-2}
1.3	11.7	5.06×10^{-2}	39.1	5.59×10^{-2}
1.4	12.6	3.39×10^{-2}	42.2	3.88×10^{-2}
1.5	13.5	2.29×10^{-2}	45.2	2.51×10^{-2}
1.6	14.4	1.56×10^{-2}	48.2	1.87×10^{-2}
1.7	15.3	1.08×10^{-2}	51.2	1.30×10^{-2}
1.8	16.2	7.43×10^{-3}	54.2	9.03×10^{-3}
1.9	17.1	5.17×10^{-3}	57.2	6.27×10^{-3}
2.0	18.0	3.61×10^{-3}	60.2	4.25×10^{-3}
2.1	19.0	2.53×10^{-3}	63.2	3.02×10^{-3}
2.2	19.8	1.76×10^{-3}	66.2	2.10×10^{-3}
2.3	20.8	1.24×10^{-3}	69.2	1.46×10^{-3}
2.4	21.6	8.67×10^{-4}	72.2	1.01×10^{-3}
2.5	22.6	6.07×10^{-4}	75.3	7.31×10^{-4}

1846 Figure 5.6 shows the ratio of the natural width to the mass of a W' resonance in the LH
 1847 and the HVT model B. The relative width is less than 5% for the following parameter values:
 1848 $0.95 < g_V < 3.76$, $c_H = -1$, and $c_F = 1$; $g_V < 3.9$, $c_H = -1$, and $c_F = 0$; or $g_V < 7.8$, $c_H = 0.5$,
 1849 and $c_F = 0$. The relative widths for the LH model have been computed by means of Eq. 2.61,
 1850 and they are less than 5% for values of $0.084 < |\cot \theta| < 1.21$. Hence, in both models the
 1851 resonance's natural width can be considered to be negligible compared to the experimental
 1852 resolution.

1853
 1854 For the 13 TeV data analysis, the bulk graviton model and HVT models are used as
 1855 benchmark signal processes. In these models, a resonance is simulated which decays only to
 1856 pairs of vector gauge bosons in the $\ell\nu q\bar{q}$ final state, with $\ell = e, \mu$, and τ . The vector gauge
 1857 bosons are produced with a longitudinal polarization in more than 99% of the cases. For each
 1858 resonance hypothesis, masses are considered in the range 0.6 to 4.0 TeV. Simulated signal
 1859 events are generated at LO accuracy with MADGRAPH5_AMC@NLO with a relative resonance
 1860 width of 0.1%.

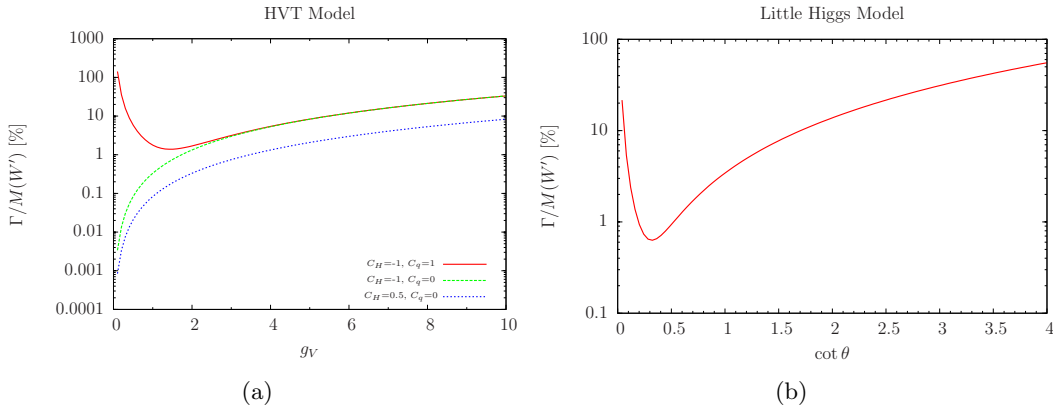


Figure 5.6: Ratio of the natural width to the mass of a W' resonance in the LH and the HVT model B.

1861 The natural width of a bulk graviton as a function of the curvature parameter \tilde{k} and for
 1862 different mass hypotheses is shown in Fig. 5.7. For cases in which $\tilde{k} \leq 0.5$ the relative width
 1863 of the graviton resonance (Γ_G/M_G) is predicted to be below 1%. Hence, it can be neglected
 1864 when compared to the detector resolution over the whole explored mass range.

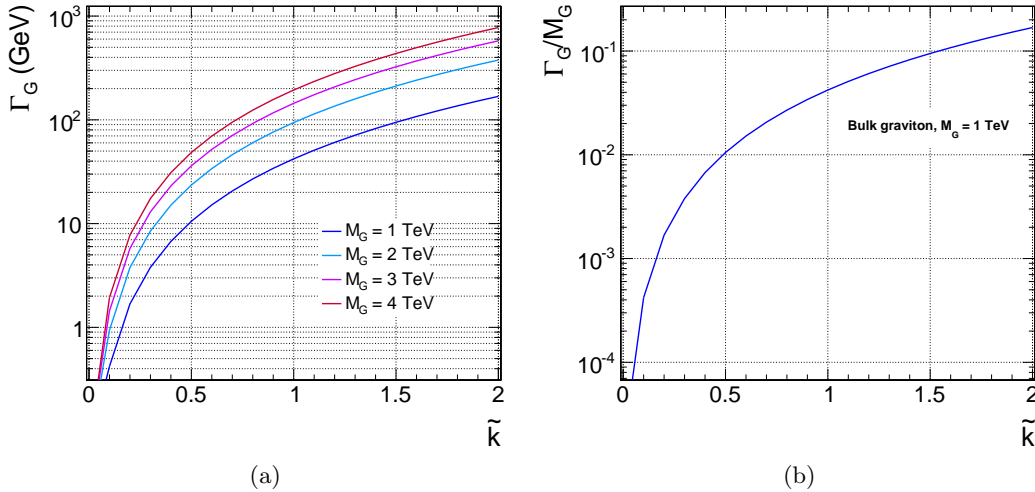


Figure 5.7: (a) Natural width of a bulk graviton as a function of the coupling constant \tilde{k} and for various mass hypotheses. (b) The same dependence is expressed as relative fraction of the signal width with respect to a reference graviton mass of 1 TeV.

1865 Figure 5.8 compares the production cross sections $\sigma(pp \rightarrow X)$ of the resonance for $\sqrt{s} = 8$
 1866 and 13 TeV, for a bulk graviton with $\tilde{k} = 0.5$, and W' and Z' in the HVT model B, as a
 1867 function of the resonance mass. Cross sections for the bulk graviton model are computed
 1868 with MADGRAPH with the model used for the event generation, while values for the HVT
 1869 model B are obtained using the online tools provided by the authors of Ref. [44] using the
 1870 same parameters as for the 8 TeV data analysis.

1871 For a resonance mass of 2 TeV, the production rates at $\sqrt{s} = 13$ TeV are expected to
 1872 increase by a factor of ≈ 17 for a resonance produced via gluon-gluon fusion such as the
 1873 graviton; a smaller factor of ≈ 7 is expected instead for resonances produced via quark-

1874 antiquark annihilation such as W' and Z' .

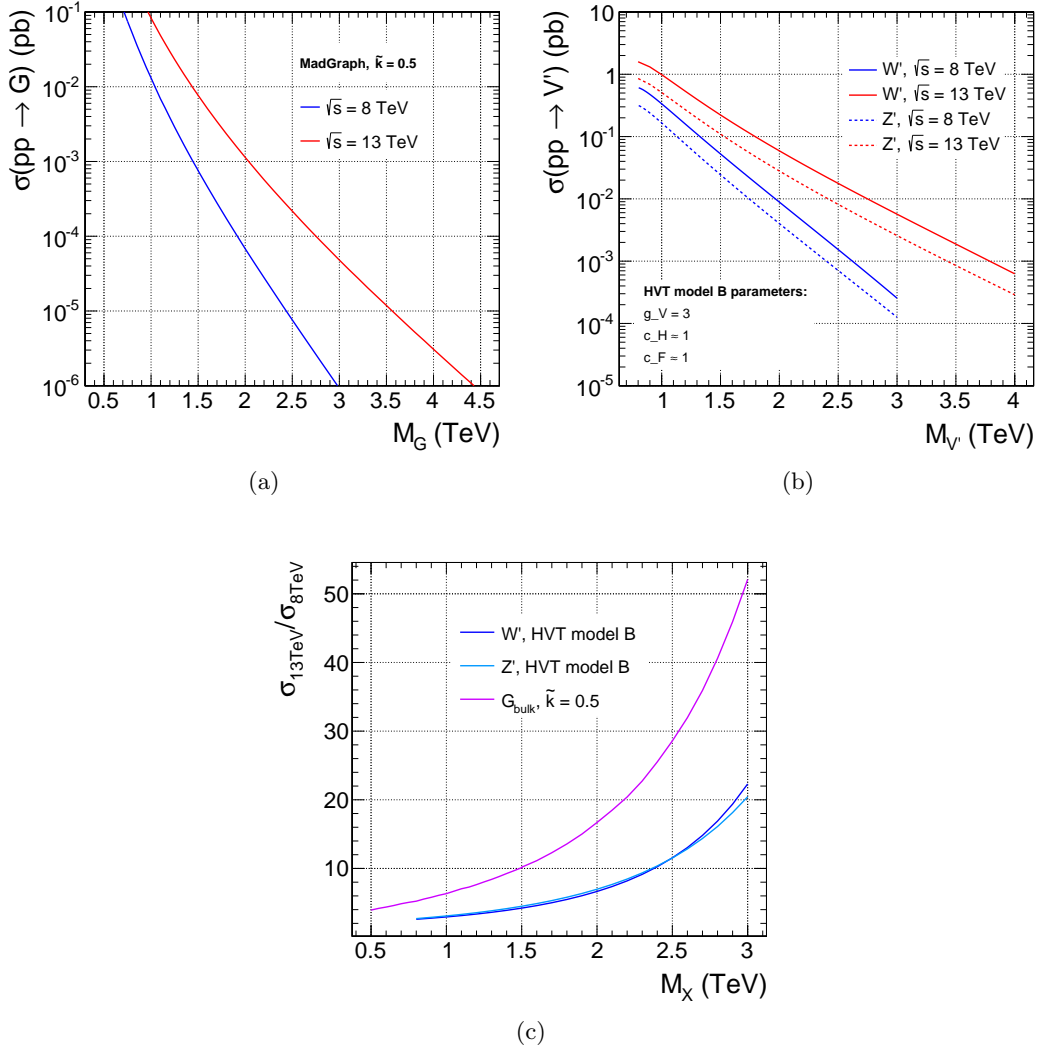


Figure 5.8: Comparison of the production cross sections of the resonance for $\sqrt{s} = 8$ and 13 TeV for the bulk graviton (a), and W' and Z' in the HVT model B (b), as a function of the resonance mass. (c) Ratio of the production cross sections for $\sqrt{s} = 8$ and 13 TeV for all models.

1875 5.2.2 Simulation of background processes

1876 For the 8 TeV data analysis, the background is modelled using the MADGRAPH5 v1.3.30
1877 event generator to simulate the production of a W boson in association with jets at LO, the
1878 POWHEG 1.0 r1380 package to generate $t\bar{t}$ and single top quark events at NLO accuracy,
1879 and PYTHIA6.424 for SM diboson (WW , WZ , and ZZ) production at LO. All simulated
1880 event samples are generated using the CTEQ6L1 PDF set with α_S also at LO, except for
1881 the POWHEG $t\bar{t}$ sample, for which the CT10 NNLO PDF set is used. All the samples are
1882 then processed further by PYTHIA6, using the Z2* tune for simulation of parton showering
1883 and subsequent hadronization, and for simulation of the underlying event. All simulated
1884 background samples are normalized to the integrated luminosity of the recorded data, using
1885 inclusive cross sections determined at NLO, or NNLO when available, calculated with the

cross section integrators MCFM [78–81] and FEWZ [82], except for the $t\bar{t}$ sample, for which TOP++ [83] is used. The NNLO cross section for the W+jets process is obtained by rescaling the LO value given by the generator to the NNLO cross section derived from the inclusive production by means of a flat factor equal to 1.3. The simulated samples used in the 8 TeV data analysis described in this work are listed in Table 5.2 together with the corresponding cross sections.

1892

Table 5.2: Summary of the MC generated samples for background processes used for the 8 TeV data analysis. The cross sections used to normalize the samples are also indicated.

Process	Cross section (pb)	Generator	PDF set
W+jets, $W \rightarrow \ell\nu$, $p_T^W > 180$ GeV	29.0 (NNLO)	MADGRAPH	CTEQ6L1
$t\bar{t}$ (inclusive)	252.9 (NNLO+NNLL)	POWHEG	CT10
single t quark (t-channel, inclusive)	54.9 (NNLO)	POWHEG	CTEQ6L1
single \bar{t} quark (t-channel, inclusive)	29.7 (NNLO)	POWHEG	CTEQ6L1
single t quark (tW-channel, inclusive)	11.2 (NNLO)	POWHEG	CTEQ6L1
single \bar{t} quark (tW-channel, inclusive)	11.2 (NNLO)	POWHEG	CTEQ6L1
single t quark (s-channel, inclusive)	3.8 (NNLO)	POWHEG	CTEQ6L1
single \bar{t} quark (s-channel, inclusive)	1.8 (NNLO)	POWHEG	CTEQ6L1
WW (inclusive)	54.8 (NLO)	PYTHIA6	CTEQ6L1
WZ (inclusive)	33.2 (NLO)	PYTHIA6	CTEQ6L1
ZZ (inclusive)	8.1 (NLO)	PYTHIA6	CTEQ6L1

For the 13 TeV analysis, the W+jets SM process is simulated with MADGRAPH5_AMC@NLO at LO accuracy. A set of W+jets samples are used, each containing generated events where the scalar p_T sum of all jets (H_T) is in a given range. This splitting provides the analyses with large MC statistics for a wide range of jet transverse momenta. The $t\bar{t}$, single top quark and diboson events are generated with both POWHEG and MADGRAPH5_AMC@NLO at NLO accuracy. Parton showering and hadronization are implemented through PYTHIA8 using the CUETP8M1 tune [84, 85]. The NNPDF 3.0 PDFs with α_S at NLO, are used for all simulated samples. The simulated background is normalized using inclusive cross sections calculated at NLO, or NNLO order in QCD where available, using MCFM and FEWZ, except for the $t\bar{t}$ sample, for which TOP++ [83] is used. A flat factor equal to 1.21 is used to rescale the W+jets simulation to the NNLO cross section.

The simulated samples used in the 13 TeV data analysis described in this work are listed in Table 5.3 together with the corresponding cross sections.

5.3 Data sets

Two independent data sets are analyzed in this work to search for diboson resonances decaying to two different final states.

The analysis focused on the $\ell\nu b\bar{b}$ decay channel is performed with the complete set of data recorded in 2012 by the CMS detector and corresponding to an integrated luminosity of 19.7 fb^{-1} of pp collisions at $\sqrt{s} = 8 \text{ TeV}$.

The second analysis described in this work is focused on the $\ell\nu q\bar{q}^{(\prime)}$ decay channel and it is performed with only the largest part of the full set of data recorded in 2015 by the CMS detector, corresponding to an integrated luminosity of 2.3 fb^{-1} of pp collisions at $\sqrt{s} = 13 \text{ TeV}$. During 2015, there have been three running periods labeled from B to D. In fact, after a

Table 5.3: Summary of the MC generated samples for background processes used for the 13 TeV data analysis. The cross sections used to normalize the simulated events are also indicated. The NNPDF 3.0 PDFs are used for all simulated samples

Process	Cross section (pb)	Generator
W+jets, $W \rightarrow \ell\nu$, $100 < H_T < 200$ GeV	1627.5 (NNLO)	MADGRAPH5_AMC@NLO
W+jets, $W \rightarrow \ell\nu$, $200 < H_T < 400$ GeV	435.2 (NNLO)	MADGRAPH5_AMC@NLO
W+jets, $W \rightarrow \ell\nu$, $400 < H_T < 600$ GeV	59.2 (NNLO)	MADGRAPH5_AMC@NLO
W+jets, $W \rightarrow \ell\nu$, $600 < H_T < 800$ GeV	14.6 (NNLO)	MADGRAPH5_AMC@NLO
W+jets, $W \rightarrow \ell\nu$, $800 < H_T < 1200$ GeV	6.7 (NNLO)	MADGRAPH5_AMC@NLO
W+jets, $W \rightarrow \ell\nu$, $1200 < H_T < 2500$ GeV	1.6 (NNLO)	MADGRAPH5_AMC@NLO
W+jets, $W \rightarrow \ell\nu$, $H_T > 2500$ GeV	0.04 (NNLO)	MADGRAPH5_AMC@NLO
$t\bar{t}$ (inclusive)	831.8 (NNLO+NNLL)	POWHEG
single t quark (t-channel), $W \rightarrow \ell\nu$	44.5 (NNLO)	POWHEG
single \bar{t} quark (t-channel), $W \rightarrow \ell\nu$	26.5 (NNLO)	POWHEG
single t quark (tW-channel, inclusive)	35.9 (NNLO)	POWHEG
single \bar{t} quark (tW-channel, inclusive)	35.9 (NNLO)	POWHEG
single $t+\bar{t}$ quark (s-channel), $W \rightarrow \ell\nu$	3.7 (NNLO)	MADGRAPH5_AMC@NLO
$WW \rightarrow \ell\nu q\bar{q}'$	50.0 (NNLO)	POWHEG
$WZ \rightarrow \ell\nu q\bar{q}$	10.7 (NLO)	MADGRAPH5_AMC@NLO
$ZZ \rightarrow \ell\ell q\bar{q}$	3.22 (NLO)	MADGRAPH5_AMC@NLO

1916 short period of 50 ns operation (period B), the machine collected data with a bunch spacing
1917 of 25 ns (period C and D). However, since the first two periods include data taken under
1918 different detector and LHC conditions and only add a tiny contribution to the total integrated
1919 luminosity of 2015 collisions, the analysis is based on period D only, corresponding to the
1920 largest data set.

1921 Even though run periods of stable LHC collisions are chosen for the analyses, not all runs
1922 can be used. This analysis requires the whole detector to be functional since the objects
1923 employed are reconstructed from all parts of the detector as described in the next chapter.
1924 Therefore, only data-taking runs and luminosity blocks during which the detector was in a
1925 state sufficiently good for further analysis are used. In 2015, additional data equivalent of
1926 0.37 fb^{-1} of integrated luminosity were collected with the HF running in suboptimal conditions.
1927 The analysis relies on the measurement of the missing transverse energy as an estimate of
1928 the kinematics of the original neutrino, requiring the detector to provide complete geometric
1929 coverage. Events without fully operational HF calorimeter are therefore not considered for
1930 this analysis. However, these additional data are included in the search for diboson resonances
1931 in the all-jet final state detailed in Ref. [86] and included in the combination described in
1932 Chapter 11. In this case, the jets reconstructed online and used for the trigger decision are in
1933 the range $|\eta| < 3$, and hence not falling in the acceptance of the HF.

Object and event reconstruction

1937 In the pp collisions at the LHC a large number of particles are produced which must be
 1938 efficiently reconstructed and identified. These particles travel through the CMS detector and
 1939 they are classified as objects depending on their specific signature in each subdetector. This
 1940 chapter covers the reconstruction of physics objects that are needed for the identification of
 1941 signal events in the lepton plus jet event topology described in Chapter 4.

1942 The measurement of tracks in the tracker detector for charged particles and the reconstruc-
 1943 tion of the primary vertices represent key aspects of the reconstruction of the various objects
 1944 and are detailed in Section 6.1. Details on the methods for reconstructing electrons, muons
 1945 and jets present in the final states of these analyses are given, respectively, in Sections 6.2,
 1946 6.3, and 6.4. In addition to leptons and jets, the last type of particle present in the final
 1947 state is the neutrino, whose presence can be inferred from an imbalance of the transverse
 1948 momentum (Section 6.5). The identified lepton and the missing transverse energy in the event
 1949 are associated with the $W \rightarrow \ell\nu$ candidate which is reconstructed through the algorithms
 1950 described in Section 6.6.

1951 **6.1 Tracks and primary vertices**

1952 The reconstruction of tracks of charged particles in a magnetic field allows for their momentum
 1953 measurement and aids in particle identification as described in subsequent sections. The
 1954 reconstruction of the tracks' vertices is important to distinguish the primary interaction,
 1955 i.e. the hard interaction, from additional interactions that might take place in the event
 1956 and also for the identification of secondary vertices in jets that contain c or b quarks called
 1957 c-/b-tagging (see Sec. 6.4.3).

1958 **6.1.1 Track reconstruction**

1959 The track reconstruction at CMS [87] is based on information coming from the silicon tracker
 1960 system. A charged particle passing through a tracker layer can in general induce a signal
 1961 in more than one pixel or more than one strip. The first step of the tracking procedure is
 1962 the assembly of nearby tracker channels into one hit cluster. The particle position and its
 1963 uncertainty is then inferred from the relative signal amplitudes in each channel.

1964 Because of the magnetic field, charged particles travel through the tracking detectors on
 1965 a helical trajectory which is described by 5 parameters: the curvature k , the track azimuthal
 1966 angle ϕ and polar angle θ , the signed transverse impact parameter d_0 and the longitudinal
 1967 impact parameter z_0 . The transverse (longitudinal) impact parameter of a track is defined as
 1968 the transverse (longitudinal) distance of closest approach of the track to the primary vertex.

1969 The trajectories of charged particles are reconstructed through an iterative procedure
 1970 consisting of multiple iterations of the *Combinatorial Track Finder algorithm* (CTF) [88],
 1971 which uses the reconstructed hits in the silicon detectors to determine the track parameters.
 1972 In the first iterations the algorithm searches for tracks of relative large p_T and produced near
 1973 the interaction region. Then, hits associated to high quality tracks are iteratively removed
 1974 from the input list to reduce the combinatorial complexity of the next iterations, and to allow

1975 the more difficult reconstruction of low p_T or displaced tracks. Each iteration of the CTF
 1976 algorithm is made of three steps: track seeding, track finding and track fitting.

1977 In the first step, a first estimate of the helix parameters and of its covariance matrix
 1978 is provided using only pairs or triplets of hits compatible with the hypothesis of a track
 1979 coming from the pp interaction region. Track candidates are best seeded from hits in the
 1980 pixel detector because of the low occupancy, high efficiency and unambiguous 3-dimensional
 1981 position information.

1982 The track finding stage associates new hits in the next tracker layers to the trajectory
 1983 obtained from seeds using a standard Kalman Filter (KF) pattern recognition approach [89,90],
 1984 which takes into account the effect of multiple scattering in the tracker layers. The current
 1985 trajectory is extrapolated to the next tracker layer and compatible hits are assigned to the
 1986 track on the basis of the χ^2 between the predicted and measured positions. In case multiple
 1987 compatible hits are found when extrapolating the helix to a single layer, the algorithm creates
 1988 one trajectory candidate for each hit and they are propagated independently. Furthermore,
 1989 in order to take into account possible inefficiencies, one additional candidate is created
 1990 without including any hit information. A quality index is assigned to the tracks, based on
 1991 the χ^2 , the number of missing hits, and how compatible they are with originating from a
 1992 primary interaction vertex. Only the best quality tracks are kept for further propagation and
 1993 ambiguities are resolved between tracks during and after track finding. In case two tracks
 1994 share more than 50% of their hits, the lower quality track is discarded. The fake rate, defined
 1995 as the fraction of reconstructed tracks not associated with a charged particle, is substantially
 1996 reduced by these quality requirements.

1997 For each trajectory the finding stage results in an estimate of the track parameters.
 1998 However, since the full information is only available at the last hit and constraints applied
 1999 during trajectory building can bias the estimate of the track parameters, all valid tracks are
 2000 refitted using the KF to determine the most accurate estimate of the helix parameters. The
 2001 usual fit starting from the interaction point to the end of the tracker is complemented with a
 2002 second fit running backward from the outermost tracker layer to the interaction point. The
 2003 second fit is found to improve the accuracy of the p_T and impact parameter measurement by
 2004 0.5% and 1%, respectively.

2005
 2006 The performance of the track reconstruction is shown in Fig. 6.1 for simulated muons,
 2007 electrons and pions. For isolated muons with $1 < p_T < 100$ GeV, the track reconstruction
 2008 efficiency is $> 99\%$ over the full η -range of tracker acceptance, and does not depend on p_T
 2009 (Fig. 6.1(a)). The fake rate is completely negligible. For pions and electrons the efficiency is
 2010 in general lower along with a higher fake rate because of interactions with the material in the
 2011 tracker. The material budget of the CMS tracker in units of radiation length is presented in
 2012 Fig. 6.2. By comparing this distribution with the tracking efficiencies presented in Fig. 6.1,
 2013 it can be noticed that the efficiency for electrons and pions are significantly reduced in
 2014 correspondence of the regions of the detector with the highest material budget.

2015 In Fig. 6.3(a) the transverse momentum resolution for muon tracks with $p_T = 1, 10$, and
 2016 100 GeV is shown. At high transverse momentum (100 GeV), the resolution is 2–3% up to
 2017 $|\eta| = 1.6$. The material of the tracker accounts for 20–30% of the transverse momentum
 2018 resolution. At lower momenta, the resolution is dominated by multiple scattering and its
 2019 distribution reflects the amount of material traversed by the track. The resolutions of the
 2020 track impact parameter in the transverse and longitudinal plane are also shown in Fig. 6.3.
 2021 At high momentum the transverse impact parameter resolution is fairly constant and is
 2022 dominated by the hit resolution in the first pixel layer. It is progressively degraded by
 2023 multiple scattering at lower momenta. The same applies to the longitudinal impact parameter

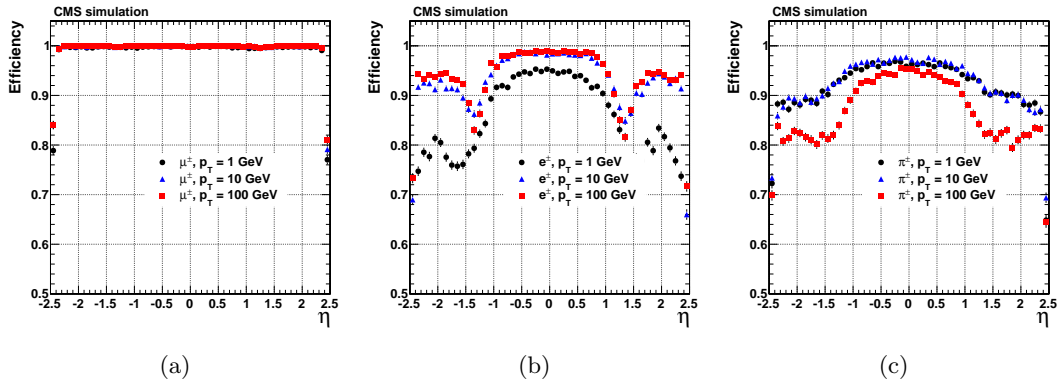


Figure 6.1: Track reconstruction efficiency for simulated muons (a), electrons (b), and pions (c) passing the high-purity quality requirements as a function of η and for $p_T = 1, 10, \text{ and } 100 \text{ GeV}$ [87].

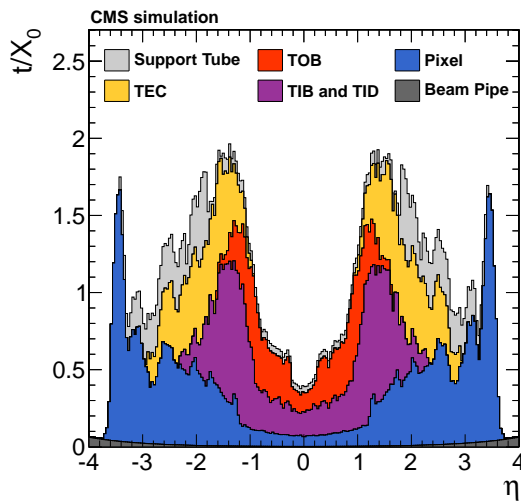


Figure 6.2: Material budget of the CMS tracker in units of radiation length X_0 as a function of pseudorapidity divided into the contributions of the different subdetectors [87].

2024 resolution. The improvement of the z_0 resolution up to $|\eta| = 0.5$ is due to the charge sharing
2025 effects among neighboring pixels.

6.1.2 Primary-vertex reconstruction

2027 The identification of primary vertices is essential to distinguish the primary vertex associated
2028 with the hard interaction from additional pileup vertices that might be present in the event.
2029 This became even more important at the highest LHC luminosity reached at the end of 2016
2030 where an average of 25 pp interactions took place simultaneously.

In the primary-vertex reconstruction [91], the measurements of the location and uncertainty of an interaction vertex are computed from a given set of reconstructed tracks. The prompt tracks originating from the primary interaction region are selected based on the transverse impact parameter significance with respect to the beam line, the number of strip and pixel hits, and the normalized track χ^2 from a fit to the trajectory. The selected tracks are then clustered on the basis of their z -coordinates at their point of closest approach to the center of

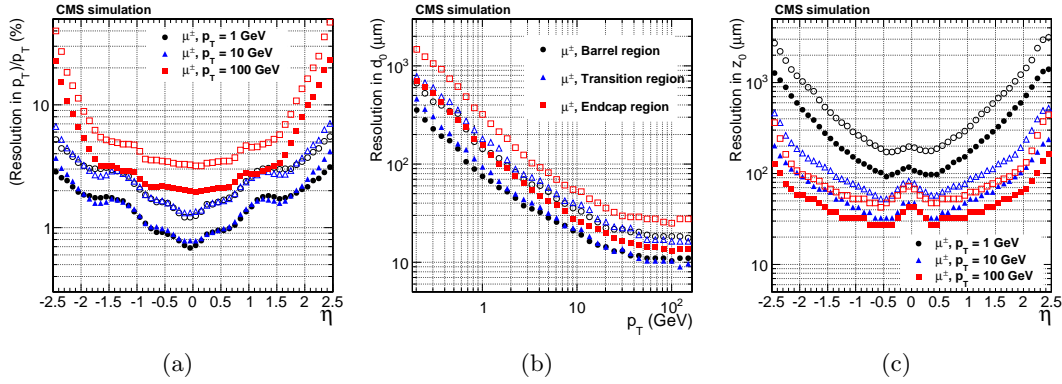


Figure 6.3: Resolution of track transverse momentum (a), transverse (b) and longitudinal (c) impact parameter for simulated muons passing the high-purity quality requirements as a function of η and for $p_T = 1, 10$, and 100 GeV [87].

2038 the beam spot using a *deterministic annealing* (DA) algorithm [92]. This clustering allows for
 2039 the reconstruction of any number of pp interactions in the same LHC bunch crossing. Vertices
 2040 are resolved with separations of about 1 mm, appropriate for a multiplicity of interactions
 2041 per bunch crossing up to 20, as the longitudinal RMS spread of the luminous region is about
 2042 6 cm.

2043 After identifying candidate vertices based on the DA clustering in z , those candidates
 2044 containing at least two tracks are then fitted using an *adaptive vertex fitter* [93], to compute
 2045 the best estimate of vertex parameters, including its x , y , and z position, and covariance
 2046 matrix. This algorithm addresses the issue of secondaries and fake tracks in the cluster by
 2047 iteratively down-weighting the tracks which are not compatible with the fitted common vertex.
 2048 The primary vertex, where the hard process of interest takes place, is chosen as the vertex
 2049 with the highest sum of p_T^2 of the clustered tracks.

2050
 2051 The primary vertex spatial resolution depends on the event topology and on the number
 2052 of tracks related to the vertex, as shown in Fig. 6.4. For minimum-bias events, the resolutions
 2053 in x and z are, respectively, less than $20 \mu\text{m}$ and $25 \mu\text{m}$, for primary vertices reconstructed
 2054 using at least 50 tracks. The resolution is better for the jet-enriched sample where tracks
 2055 have significantly higher mean p_T resulting in better resolution in the track impact parameter,
 2056 and consequently better vertex resolution. For these events, the resolutions approach $10 \mu\text{m}$
 2057 in x and $12 \mu\text{m}$ in z for primary vertices using at least 50 tracks.

2058
 2059 In the analysis described in this work, all events are required to have at least one primary
 2060 vertex reconstructed within a 24 cm window along the beam axis, with a transverse distance
 2061 from the nominal pp interaction region of less than 2 cm.

2062 6.2 Electrons

2063 6.2.1 Electron reconstruction

2064 The electron reconstruction in CMS [95] is based on the association of an energy deposit in
 2065 the ECAL with a track reconstructed in the silicon tracker system. Electrons lose energy
 2066 primarily through bremsstrahlung when interacting with the tracker layers, and consequently
 2067 they suffer from large energy losses. Given the non-Gaussian properties of the energy loss

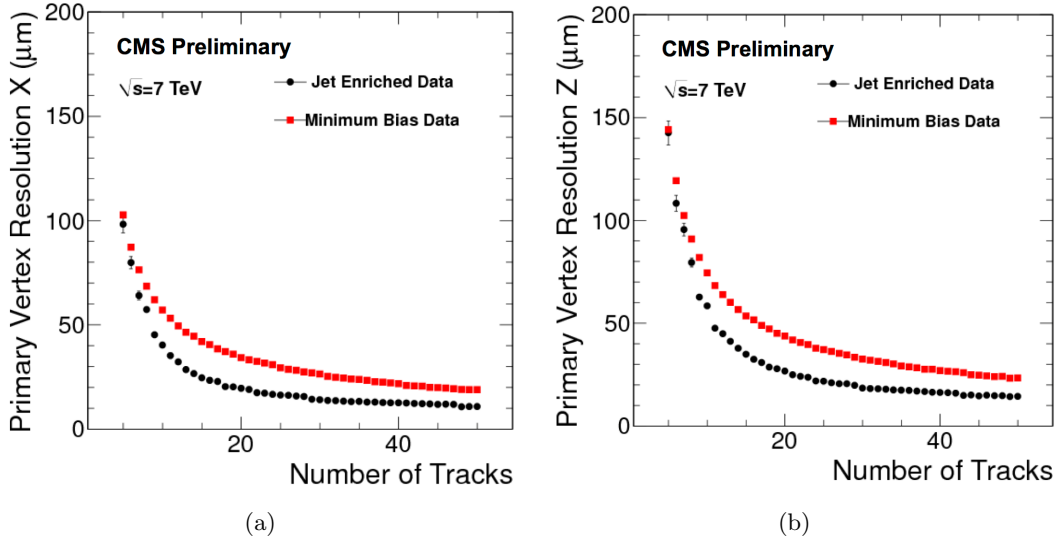


Figure 6.4: Primary-vertex resolution in x (a) and z (b) as a function of the number of tracks at the fitted vertex, for two kinds of events with different average track p_T values. The results in y are almost identical to the one in x [94].

distributions, the standard track reconstruction algorithm based on the KF is not appropriate and leads in general to a reduced hit-collection efficiency, as well as to a poor estimation of track parameters. A better performance for electron reconstruction is achieved by using dedicated techniques that make use of information, not only from the tracker, but also from the ECAL, as described in the following.

The electron reconstruction starts by searching for clusters of energy in the ECAL. As the electrons are degraded in energy, the effect of the magnetic field is to enhance the bending of their trajectories, resulting in a spread of irradiated photons along the ϕ coordinate. To recover this radiated energy, ECAL superclusters are formed, by merging clusters of similar η over some range of ϕ . Because of the different geometry of the detector in barrel and endcap, different clustering algorithms are used in different regions.

For the electron track reconstruction two approaches are used. In the first one, referred to as “ECAL-driven”, the supercluster energy and position, and the assumption that the electron originated near the center of the beam spot, are used to extrapolate the electron trajectory in the tracker. Tracker seeds compatible with the predicted trajectory are sought in the first or second layer of the pixel detector (and also in the TEC to improve efficiency in the forward region). This method is designed for isolated electrons with $p_T > 5 \text{ GeV}$.

A second approach, referred to as “tracker-driven”, complements the electron track reconstruction, especially for low- p_T or non-isolated electrons, as well as for electrons in the barrel-endcap transition region. This method is developed as part of the particle-flow (PF) reconstruction algorithm [96, 97] described in Section 6.4.2. It takes the standard track collection reconstructed with the KF algorithm and attempts to identify a subset of these tracks that are compatible with being electrons. Electrons that suffer only little bremsstrahlung loss can be identified by searching for tracks extrapolated to the ECAL that pass close to an ECAL PF cluster. Electrons that suffer large bremsstrahlung loss can be identified by the fact that the fitted track will often have poor χ^2 or few associated hits. The track seeds originally used to generate these electron-like tracks are retained.

The seed collections obtained by using these two methods are merged, and used to initiate

2097 electron track finding. This procedure is similar to that used in standard tracking, except
 2098 that the χ^2 threshold, used by the KF to decide whether a hit is compatible with a trajectory,
 2099 is weakened. This is to accommodate tracks that deviate from their expected trajectory
 2100 because of bremsstrahlung.

2101 To obtain the best estimate of the track parameters, the final track fit is performed
 2102 using a modified version of the KF method, called the Gaussian Sum Filter (GSF) [98]. The
 2103 fractional energy loss of an electron, as it traverses a layer of material, follows a Bethe–Heitler
 2104 distribution. This distribution is non-Gaussian, making it unsuitable for use in a conventional
 2105 KF algorithm. The GSF technique solves this by approximating the Bethe–Heitler energy-loss
 2106 distribution as the sum of several Gaussian functions. This method is then a generalization
 2107 of the KF where the trajectory in each tracker layer is described by a weighted sum of
 2108 KF components for which the energy loss follows a Gaussian law with a given width. The
 2109 propagation of each component is done separately from one layer to another and the weights
 2110 are then updated given the measurement in the new site. The allowed window to search for a
 2111 hit in the next tracker layer is larger than for the usual KF track. This procedure is iterated
 2112 until the last tracker layer, unless no hit is found in two subsequent layers. A minimum of
 2113 five hits is finally required to create a track. A GSF electron candidate is finally built by
 2114 associating an ECAL supercluster with a GSF track with compatible η and ϕ positions.

2115 The electron transverse energy E_T is equal to the transverse energy of the correspondent
 2116 ECAL energy deposit (or supercluster) E_T^{SC} , and defined as $E_T = E \sin \theta$, where θ is the
 2117 polar angle of the supercluster (ST) relative to the beam axis, and E the energy measured in
 2118 the supercluster.

2119 The performance of the GSF electron reconstruction are studied using a “tag-and-probe”
 2120 (T&P) method [99]. The method uses a known SM resonance mass and decay (e.g. $Z \rightarrow e^+e^-$)
 2121 to select particles of the desired type and probe the efficiency of a particular selection criterion
 2122 on those particles. In general the “tag” is an object that passes a set of very tight selection
 2123 criteria designed to isolate the required particle type (in this case an electron, though the
 2124 method is not strictly limited to this case). A generic set of the desired particle type (i.e.
 2125 with potentially very loose selection criteria) known as “probes”, is selected by pairing these
 2126 objects with tags such that the invariant mass of the combination is consistent with the mass
 2127 of the resonance. Combinatorial backgrounds are usually eliminated through a variety of
 2128 background subtraction methods. The definition of the probe object depends on the specifics
 2129 of the selection criterion being examined. The efficiency itself is measured by counting the
 2130 number of “probe” particles that pass the desired selection criteria. It is found that the
 2131 estimated efficiencies are almost insensitive to any specific definition of the tag. The GSF
 2132 electron reconstruction efficiency measured with this method is above 95% for electrons in
 2133 the ECAL barrel with $E_T > 35$ GeV, as shown in Fig. 6.5(a). Slightly lower efficiencies are
 2134 obtained for electrons reconstructed in the ECAL endcaps (Fig. 6.5(b)). A good agreement is
 2135 found between data and simulation, resulting in scale factors consistent with unity almost
 2136 in the entire range. The performance are presented here for the electron reconstruction in
 2137 Run 1 but similar results are obtained in CMS for Run 2.

2138

2139 Once a GSF electron candidate is reconstructed, the energy measurement provided by
 2140 the electromagnetic calorimeter can be combined with the tracker momentum measurement
 2141 to improve the estimate of electrons with energies below 35 GeV as shown in Fig. 6.6. At
 2142 energies above 35 GeV however, the momentum measurement is completely driven by the
 2143 supercluster.

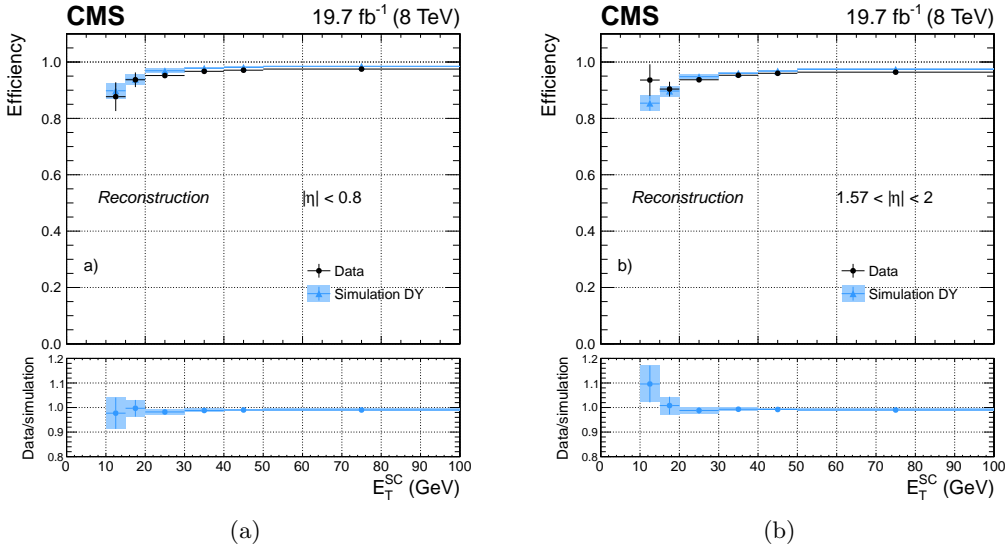


Figure 6.5: Electron reconstruction efficiency measured in dielectron events in data (dots) and Drell-Yan simulation (triangles), as a function of the E_T for electrons reconstructed in the ECAL barrel (a) and endcaps (b). The bottom panels show the corresponding data-to-simulation scale factors [100].

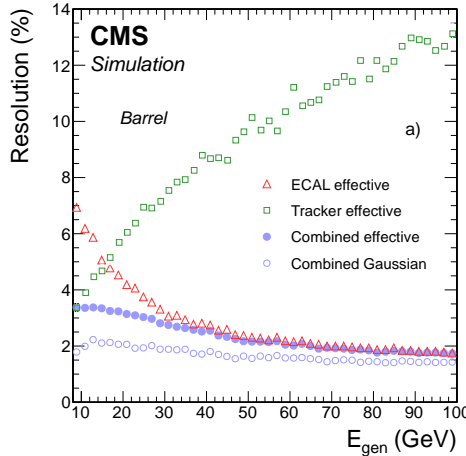


Figure 6.6: Expected resolution in E_T for isolated electrons in the ECAL barrel as a function of the electron generated energy, obtained from the ECAL, the tracker and the combined estimates [100].

6.2.2 Electron trigger

As explained in Section 3.2.4, the events of interest for physics analyses are selected by the trigger system in two steps, namely, the L1 and HLT. At the L1, where the tracker information is not available, electrons and photons are indistinguishable and based on calorimeter trigger towers, consisting, in the barrel, of a 5×5 matrix of ECAL crystals and the corresponding HCAL tower, while a more complex definition of the tower is used in the endcaps. An L1 candidate is formed combining the highest-energy central trigger tower together with its next-highest adjacent tower. At this stage, the trigger choice is based on the energy distribution among the central and neighbouring towers, on the amount of energy in the

2153 HCAL downstream the central tower, and on the E_T of the e/γ candidate. Events passing
 2154 L1 are then filtered by the HLT. Here, the pixel tracker information is used to separate
 2155 electrons from photons. The starting point of any electron HLT selection consists of building
 2156 a supercluster and a trajectory as described in Section 6.2.1. Many different triggers involving
 2157 electrons are designed at the HLT level and various additional identification and isolation
 2158 requirements on the electrons are made for each of them. They consist of conditions on:

- 2159 • transverse profile of the cluster of energy in the ECAL;
- 2160 • the amount of energy in the HCAL downstream the ECAL cluster;
- 2161 • the existence of a KF or GSF track matching the supercluster position;
- 2162 • quality of association between the track and the ECAL cluster;
- 2163 • activity in the ECAL, HCAL, or tracker around the candidate.

2164 The conditions used and their severity depend on the number of electrons requested by
 2165 the trigger and their transverse energy threshold, each trigger being designed to have a rate
 2166 of accepting events of 50 Hz or less. Practically, all the HLT steps and criteria involving
 2167 only calorimeters information are done first, while the time consuming steps involving track
 2168 reconstruction are only performed at the end for events passing the previous criteria. The
 2169 L1 and HLT triggers used to collect the data analyzed in this thesis are listed in Tables 6.1
 2170 and 6.2 for the 8 and 13 TeV data sets, respectively. The tables also detail the conditions
 2171 imposed on several variables described in Section 6.2.3. Figure 6.7 shows the L1 trigger
 2172 efficiencies for different E_T thresholds as a function of the electron E_T . The curves exhibit
 2173 the typical turn on behaviour in correspondence of the imposed E_T threshold.

Table 6.1: The L1 and HLT single-electron triggers used to collect the 8 TeV data analyzed in this thesis together with the imposed requirements on the electron candidate.

Trigger	Name	Selections
Level 1	L1_SingleEG20	1 e/γ candidate $E_T > 20$ GeV
HLT	HLT_Ele80_CaloIdVT_GsfTrkIdT	1 GSF electron: $E_T > 80$ GeV $ \Delta\eta_{in} < 0.008$ $ \Delta\phi_{in} < 0.07$ (barrel) or 0.05 (endcaps) $H/E < 0.05$ $\sigma_{i\eta i\eta} < 0.011$ (barrel) or 0.031 (endcaps)

2174 Both the L1 and HLT triggers require one electron (or γ) candidate. The E_T thresholds
 2175 imposed for the data collected in pp collisions at 13 TeV are higher compared to the one used
 2176 in Run 1, in order to keep low trigger rates given the higher production rates of low-energy
 2177 multijet background expected in Run 2. The chosen HLT triggers require a reconstructed
 2178 GSF track whose association to the ECAL cluster has to pass tight quality criteria ($|\Delta\eta_{in}|$ and
 2179 $|\Delta\phi_{in}|$). Requirements are also applied at this level on the transverse profile of the cluster of
 2180 energy in the ECAL ($\sigma_{i\eta i\eta}$) and on the amount of energy in the HCAL downstream the ECAL
 2181 (H/E). There are no requirements imposed on the electron candidate isolation. In general,
 2182 this results in high fake rates of jets misreconstructed as electrons from multijet background,
 2183 and, as a consequence, in high trigger rates which would require a prescale. However, the
 2184 high E_T threshold allows for an unprescaled trigger, as jets from multijet background are

Table 6.2: The L1 and HLT single-electron triggers used to collect the 13 TeV data analyzed in this thesis together with the imposed requirements on the electron candidate.

Trigger	Name	Selections
Level 1	L1_SingleEG35 OR L1_SingleEG40	1 e/ γ candidate $E_T > 35$ GeV OR $E_T > 40$ GeV
HLT	HLT_Ele105_CaloIdVT_GsfTrkIdT OR HLT_Ele115_CaloIdVT_GsfTrkIdT	1 GSF electron: $E_T > 105$ GeV OR > 115 GeV $ \Delta\eta_{in} < 0.008$ $ \Delta\phi_{in} < 0.07$ (barrel) or 0.05 (endcaps) $H/E < 0.05$ $\sigma_{i\eta i\eta} < 0.011$ (barrel) or 0.031 (endcaps)

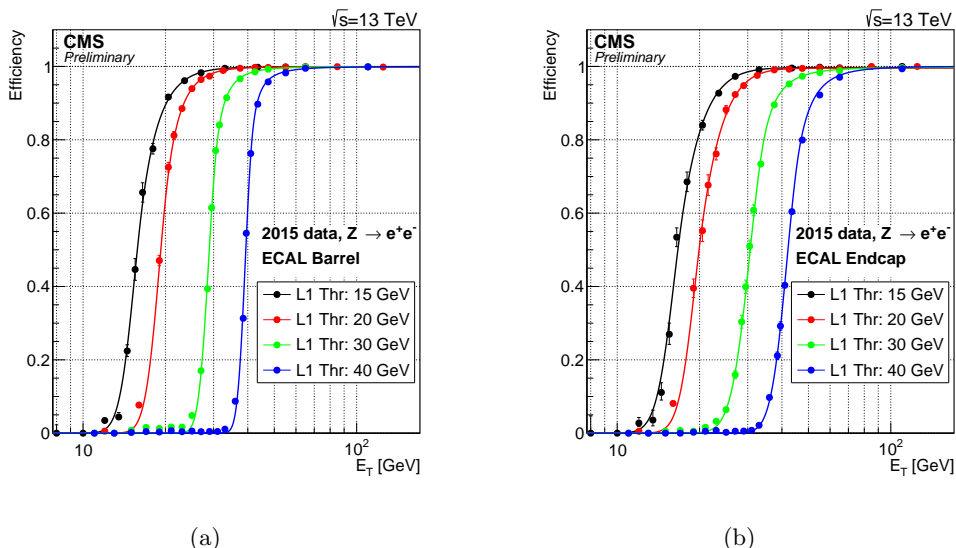


Figure 6.7: L1 electron triggering efficiency in ECAL barrel (a) and endcaps (b) as a function of the offline reconstructed electron E_T . The efficiency is shown for the 15, 20, 30, 40 GeV EG trigger thresholds [101].

characterized by low momentum. In addition, the kinematic region of the analyses presented in this thesis is located at very high lepton p_T and the signal efficiency is mainly affected at very low resonance masses (< 1 TeV) with a loss in efficiency of 20–25%.

The efficiency for an electron passing the high- E_T selections described in Sec. 6.2.3 to fire the HLT triggers of Tables 6.1 and 6.2 have been measured in data with T&P method and are found to be 98–99% for electrons with E_T in the trigger plateau, with data-to-simulation scale factors close to unity.

6.2.3 Electron identification

All the physics analyses in CMS involving one or two electrons in the final state start with the general electron reconstruction algorithm presented in Section 6.2.1. A high efficiency in any kinematical conditions is therefore needed to maximize each analysis sensitivity and, as a consequence, the probability for other particles to be reconstructed as electrons is sizeable. For instance, a charged pion can mimic the signature of an electron if it interacts early and

leaves most of its energy in the ECAL. Moreover electrons can emerge in a jet through the weak decay of a hadron containing a c or b quark. Finally, in addition to jets, photons can also lead to GSF electron candidates. This happens if the photon converts into a dielectron pair in one of the first layers of the tracker detector. If one of the electron takes most of the photon momentum, a GSF electron candidate is likely to be reconstructed. An analysis-dependent selection, which takes into account the specific kinematics and background level, has therefore to be applied on top of the electron reconstruction. This thesis focuses on the search for massive resonances decaying to pairs of SM bosons where one of the bosons is a W decaying leptonically, with a highly energetic electron or muon in the final state. A high and stable selection efficiency for E_T above 100 GeV is therefore an important requirement. Since this is a common feature of many searches for new physics, a specific cut-based selection has been developed in CMS [102], consisting of requirements on several variables that exploit the characteristics of high- E_T electrons. Only GSF electron candidates with $E_T > 35$ GeV and well reconstructed in the tracker and ECAL sensitive regions are selected. Candidates in the ECAL transition region ($1.442 < |\eta_{SC}| < 1.56$) and beyond the η coverage ($|\eta_{SC}| > 2.5$) of the tracker are therefore discarded. A different selection is applied for candidates reconstructed in the ECAL barrel ($|\eta_{SC}| < 1.442$) and endcaps ($1.56 < |\eta_{SC}| < 2.5$). For Run 2 the values of η_{SC} have been slightly adjusted to match the acceptance of the detector more accurately. The selections are summarized in Tables 6.3 and 6.4, for the 8 and 13 TeV data analysis, respectively, and discussed in the following.

Table 6.3: List of the variables used in the high- E_T electron selections for the 8 TeV data analysis, together with the corresponding requirements for electrons reconstructed in the ECAL barrel and endcaps.

Variable	ECAL barrel	ECAL endcaps
ECAL-driven	yes	yes
E_T	> 35 GeV	> 35 GeV
$ \eta_{SC} $	< 1.442	$1.56\text{--}2.5$
$ \Delta\eta_{in} $	< 0.005	< 0.007
$ \Delta\phi_{in} $	< 0.06	< 0.06
Relative track isolation	5%	5%
Calorimeter isolation	$< 2 + 0.03E_T + 0.28\rho$	$< 2.5 + 0.28\rho$ if $E_T < 50$ $< 2.5 + 0.03(E_T - 50) + 0.28\rho$ if $E_T \geq 50$
Transverse shower shape	$E_{2\times 5}/E_{5\times 5} > 0.94$ OR $E_{1\times 5}/E_{5\times 5} > 0.83$	$\sigma_{i\eta i\eta} < 0.03$
H/E	< 0.05	< 0.05
$ d_{xy} $	< 0.02	< 0.05
Lost hits in innermost tracking layers	≤ 1	≤ 1

As a starting point, electrons are selected if the reconstruction was seeded in the ECAL (Section 6.2.1). In fact, while useful for low-energy and non-isolated electrons, the PF algorithm is less suitable for high-energy electrons.

The difference in η , $\Delta\eta_{in}$, and in ϕ , $\Delta\phi_{in}$, between the track position as measured in the inner layers, extrapolated to the interaction vertex and to the calorimeter, and the position of the supercluster, are required to be < 0.005 and < 0.06 , respectively. In fact, for jets, the position of the center of the ECAL deposit can be far from the track position, as all of the constituents can leave an energy deposit in the ECAL. The $\Delta\phi_{in}$ distribution is however much broader than $\Delta\eta_{in}$, because of the wider spread of the energy in ϕ due to photons from bremsstrahlung, resulting in a looser requirement. The distributions of $\Delta\phi_{in}$ and $\Delta\eta_{in}$

Table 6.4: List of the variables used in the high- E_T selections for the 13 TeV data analysis, together with the corresponding requirements for electrons reconstructed in the ECAL barrel and endcaps.

Variable	ECAL barrel	ECAL endcaps
ECAL-driven	yes	yes
E_T	$> 35 \text{ GeV}$	$> 35 \text{ GeV}$
$ \eta_{SC} $	< 1.4442	$1.566\text{--}2.5$
$ \Delta\eta_{in} $	< 0.004	< 0.006
$ \Delta\phi_{in} $	< 0.06	< 0.06
Relative track isolation	5%	5%
Calorimeter isolation	$< 2 + 0.03E_T + 0.28\rho$	$< 2.5 + 0.28\rho \text{ if } E_T < 50$ $< 2.5 + 0.03(E_T - 50) + 0.28\rho \text{ if } E_T \geq 50$
Transverse shower shape	$E_{2\times 5}/E_{5\times 5} > 0.94$ OR $E_{1\times 5}/E_{5\times 5} > 0.83$	$\sigma_{in in} < 0.03$
H/E	$< 1/E + 0.05$	$< 5/E + 0.05$
$ d_{xy} $	< 0.02	< 0.05
Lost hits in innermost tracking layers	≤ 1	≤ 1

2229 become narrower with increasing E_T , and therefore a higher discrimination power can be
 2230 achieved with a tighter requirement at high E_T compared to the usual selections for low
 2231 or intermediate energetic electrons. The reason of this behaviour comes from the fact that
 2232 bremsstrahlung photons are more collinear to the electron at higher E_T . The definition of
 2233 $\Delta\eta_{in}$ has been changed for Run 2 to use instead the η of the seed cluster of the supercluster
 2234 which is found to provide a more accurate indication of the η of the original electron before
 2235 bremsstrahlung.

2236 To suppress the misidentification of jets as electrons, the sum of the p_T of all other tracks
 2237 in a cone of $\Delta R < 0.3$ around the track of the electron candidate is required to be less
 2238 than 5 GeV, imposing an isolation condition on the electron candidate track. To be used in
 2239 the calculation of the isolation of the candidate track, the tracks have to be within 0.2 cm,
 2240 in the z direction, of the primary vertex with which the electron candidate is associated.
 2241 This requirement reduces the impact of pileup and it does not show a dependency with the
 2242 electron E_T for values above 100 GeV. For electrons with E_T much lower than 100 GeV, the
 2243 efficiency decreases up to 10% depending on the region of the detector in which the electrons
 2244 are detected.

2245 A calorimeter-based isolation is applied and defined as the sum of:

- 2246 • ECAL isolation: sum of the E_T of the energy deposits in the ECAL calorimeter in a
 2247 cone of $\Delta R < 0.3$ around the track of the electron candidate excluding those associated
 2248 with the candidate;
- 2249 • HCAL1 isolation: sum of the E_T of the energy deposits in the first layer of the HCAL
 2250 calorimeter in a cone of $\Delta R < 0.3$ around the track of the electron candidate excluding
 2251 those associated with the candidate.

2252 The isolation variable so defined, is required to be less than 3% (plus a small η -dependent
 2253 offset) of the candidate E_T . This sum, which allows a selection on the isolation of the
 2254 electron candidate, is corrected for the average energy density in the event, ρ , to minimize
 2255 the dependence of the efficiency of this selection criterion on pileup. This requirement differs
 2256 from the selection usually applied for electrons of low or intermediate E_T . For these cases, a
 2257 PF-based isolation is generally used, which merges the information of the tracker, the ECAL

and the HCAL allowing to measure the contribution to the isolation from charged hadrons, neutral hadrons and photons separately. One of the main advantage of the PF-based isolation is that the energy deposit in the calorimeters associated to a charged hadron produced in another interaction, characterized by a different primary vertex, can be removed from the isolation sum. For very high energy (> 1 TeV) electrons, however, the PF algorithm might fail to recognize an electron from a GSF electron candidate and assigns all its energy deposit to the photon isolation. Furthermore, the PF isolation is generally required to be below a fixed fraction of the electron E_T independently on its value. However, for high E_T values the background rejection can be improved while keeping an acceptable efficiency by following the E_T dependence of the ECAL+HCAL1 isolation variable. In fact, this isolation tends to increase for high- E_T electrons due to the extension of the shower.

Further suppression of the misidentification of jets as electrons is achieved by requiring that the ratio H/E of the energy in the HCAL towers in a cone of $\Delta R < 0.15$ centered on the electron candidate position, to the electromagnetic energy of the electron candidate supercluster is required to be less than 5%. This requirement is tighter compared with the threshold applied for low- or medium-energy electrons, where it becomes quite inefficient for a high number of pileup interactions. For Run 2, the selection on this variable has been increased. Additionally, the transverse profile of the energy deposition in the ECAL is required to be consistent with that expected for an electron, being defined by the following variables:

- $E_{1\times 5}/E_{5\times 5}$: ratio of the energy contained in the 1×5 matrix in $\eta \times \phi$ in the barrel ($x \times y$ in the endcaps) centered on the seed crystal of the supercluster over the energy of the 5×5 matrix centered on the seed crystal;
- $E_{2\times 5}/E_{5\times 5}$: ratio of the energy contained in the most energetic 2×5 matrix in $\eta \times \phi$ in the barrel ($x \times y$ in the endcaps) centered on the seed crystal of the supercluster over the energy of the 5×5 matrix centered on the seed crystal;
- $\sigma_{in\eta}$: measure of the spread in η in units of crystals of the electrons energy in the 5×5 block centered on the seed crystal.

In the barrel, the best performance is obtained applying a selection on both $E_{1\times 5}/E_{5\times 5}$ and $E_{2\times 5}/E_{5\times 5}$. The two variables are indeed complementary: while $E_{1\times 5}/E_{5\times 5}$ is well designed for electrons hitting the center of a crystal, $E_{2\times 5}/E_{5\times 5}$ allows the recovery of electrons that hit the crystal close to its edge. Combining the two variables with a logic OR instead of using just one of them allows a tight requirement to be set on both and thus reasonably reject background while keeping a high efficiency on simulated electrons. The distributions of these variables are much broader for electrons in the endcaps and a higher discrimination power is obtained applying a selection on the variable $\sigma_{in\eta}$.

Two additional requirements are applied to reject photons that convert into an electron and positron in the tracker. First, the track associated with the cluster is required to have no more than one hit missing in the pixel layers. In fact, the signature arising from the photon conversion process is very similar to the one from real electrons, and the gain in discrimination using shower shape variables is limited. However, one of the main differences is the absence of hits in the first layers of the tracker, before the conversion happens. Furthermore, the transverse impact parameter d_{xy} , defined as the closest distance in the transverse plane between the primary vertex and the track of the electron candidate, is required to be < 0.02 cm (barrel) or 0.05 cm (endcaps). The distribution of the transverse impact parameter is usually wider in the endcaps due to the poorer resolution of the track position in that region.

The efficiency of the high- E_T electron selection measured with the T&P method in pp collisions at $\sqrt{s} = 8$ TeV and in simulation as a function of the electron p_T is shown in Fig. 6.8, for electrons reconstructed in the ECAL barrel and endcaps. Similar results are obtained using 13 TeV data. The efficiencies and data-to-simulation scale factors are summarized in Tables 6.5 and 6.6, as measured in 8 and 13 TeV data and simulation, respectively. The scale factors are close to unity, indicating a good agreement between data and simulation. They are used in the analysis presented in this thesis to correct the normalization of simulations.

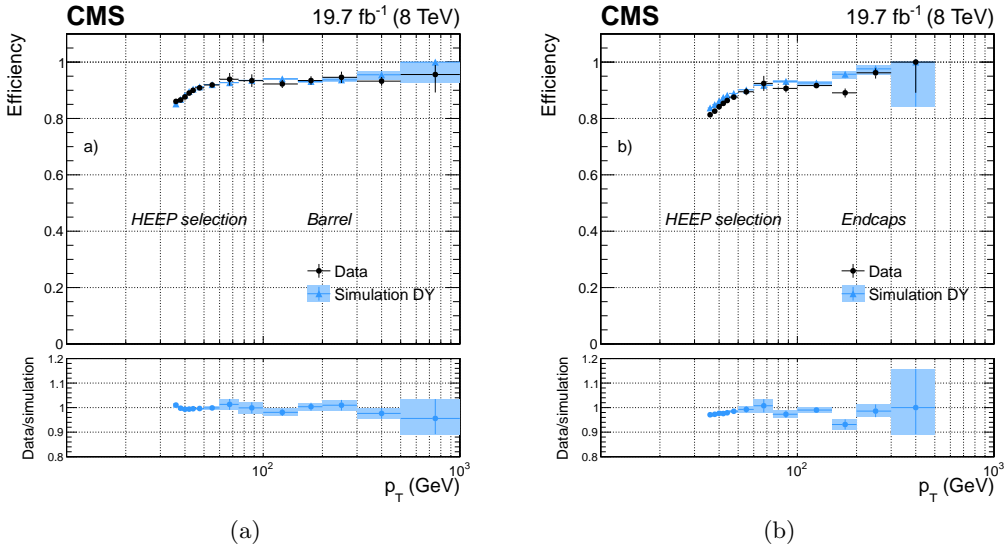


Figure 6.8: Efficiency of the high- E_T electron selection as a function of electron p_T for dielectron events in pp collisions at $\sqrt{s} = 8$ TeV (dots) and in DY simulation (triangles) for electrons reconstructed in the ECAL barrel (a), and endcaps (b) [100].

Table 6.5: Efficiencies and data-to-simulation scale factors for the high- E_T electron selection, as measured in pp collisions at $\sqrt{s} = 8$ TeV for electrons with $E_T > 90$ GeV. The quoted uncertainties are statistical.

	ECAL barrel	ECAL endcaps
Efficiency simulation	$90.2\% \pm 0.2\%$	$92.2\% \pm 0.5\%$
Efficiency data	$88.7\% \pm 0.2\%$	$90.7\% \pm 0.6\%$
Data/simulation scale factor	0.983 ± 0.004	0.984 ± 0.010

Table 6.6: Efficiencies and data-to-simulation scale factors for the high- E_T electron selection as measured in pp collisions at $\sqrt{s} = 13$ TeV for electrons with $E_T > 120$ GeV. The quoted uncertainties are statistical.

	ECAL barrel	ECAL endcaps
Efficiency simulation	$91.4\% \pm 0.10\%$	$84.4\% \pm 0.3\%$
Efficiency data	$91.6\% \pm 0.04\%$	$82.3\% \pm 0.1\%$
Data/simulation scale factor	1.002 ± 0.001	0.975 ± 0.004

2312 6.3 Muons

2313 6.3.1 Muon reconstruction

2314 The CMS detector is specifically designed for the optimization of muon detection, as its
 2315 name clearly states. In general, muons will not be absorbed by the calorimeters, as is what
 2316 happens with electrons, so a specific muon detection system (Section 3.2.3) is needed in order
 2317 to identify them.

2318

2319 In the standard CMS reconstruction [103], tracks are first reconstructed independently
 2320 in the inner tracker (tracker track) and in the muon system (standalone-muon track). A
 2321 standalone-muon track is reconstructed from pre-built track segments (i.e. a set of aligned
 2322 DT or CSC hits) in the muon chambers. The state vector associated to the segments found
 2323 in the innermost chambers is used to seed the muon trajectory, from inside out, using the
 2324 KF technique: the predicted state vector at the next measurement surface is compared with
 2325 existing hits and updated accordingly. A suitable χ^2 cut is applied to reject bad hits and
 2326 the procedure is iterated until the outermost surface of the muon system is reached. Finally,
 2327 the track is extrapolated to the nominal interaction point and a vertex-constrained fit is
 2328 performed. The magnetic field, the multiple scattering inside the steel yoke, and the energy
 2329 loses are taken into account.

2330 Based on reconstructed standalone-muon and tracker tracks, two reconstruction approaches
 2331 are then used:

- 2332 • **global-muon reconstruction (outside-in)**: each standalone-muon track is extrapolated
 2333 to the tracker and a search is performed in a cone around it to match a tracker track;
 2334 a global-muon track is fitted combining hits from the tracker track and standalone-muon
 2335 track, using the KF technique;
- 2336 • **tracker-muon reconstruction (inside-out)**: all tracker tracks with $p_T > 0.5 \text{ GeV}$
 2337 are considered as possible muon candidates and are extrapolated to the muon system
 2338 while searching for a match with at least one muon segment.

2339 Tracker-muon reconstruction is more efficient than the global-muon reconstruction at low
 2340 momenta, $p_T \leq 5 \text{ GeV}$, because it requires only a single muon segment in the muon system,
 2341 whereas global-muon reconstruction is designed to have high efficiency for muons penetrating
 2342 through more than one muon station, and typically requires segments in at least two muon
 2343 stations. However, given the high efficiency of both the tracker track and muon segments
 2344 reconstruction, about 99% of muons produced within the geometrical acceptance of the muon
 2345 system and having sufficiently high momentum ($p_T \geq 5 \text{ GeV}$) are reconstructed by both
 2346 methods. As shown in Fig. 6.9 the additional information provided by the muon system is
 2347 precious for the momentum reconstruction of high-energy muons ($p_T \geq 200 \text{ GeV}$), for which
 2348 the tracker-only momentum measurement is degraded. In fact, as a particle's momentum
 2349 increases and the curvature of its corresponding track decreases, the momentum resolution in
 2350 the tracker becomes limited by position measurement resolution. One can then benefit from
 2351 the large lever arm and 3.8 T magnetic field in the region between the tracker and the muon
 2352 system by including hits in the muon chambers. For lower momenta, instead, the resolution
 2353 of the tracking system is dominating.

2354 Figure 6.10 shows the muon tracking efficiency as a function of the η of the probe muon
 2355 and the number of primary vertices for 13 TeV data and simulation, evaluated using the T&P
 2356 method described in Section 6.2.1. In the region $|\eta| < 2.2$ and for events with number of
 2357 reconstructed primary vertices lower than 25, the measured tracking efficiency for isolated

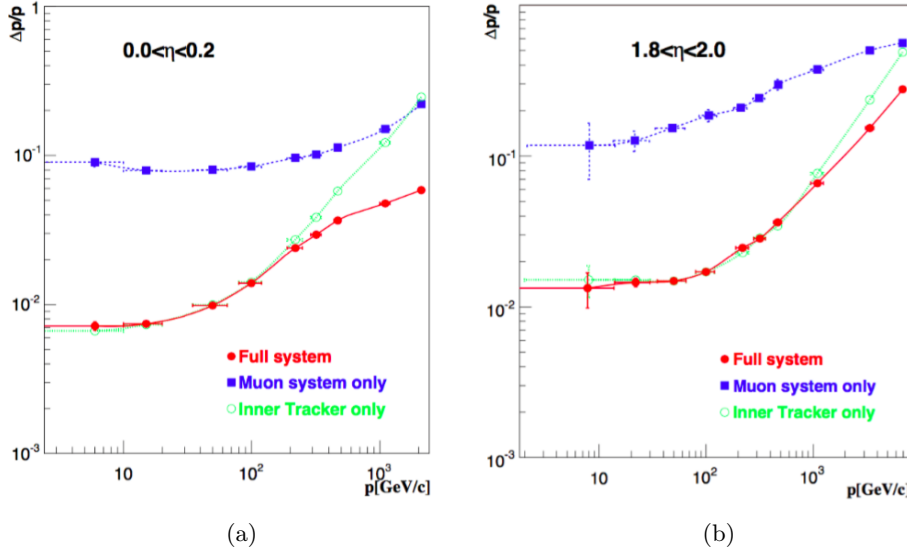


Figure 6.9: Relative resolution of the muon momentum measurement for the reconstruction with the inner tracker only, the muon system only and for the combination of the inner tracker and the muon system, for simulated muons emitted in the central (a) and forward (b) regions [104].

muons is $> 99\%$ in both data and simulation. The efficiency is constant as a function of the number of vertices in the event, hence it does not depend on the pileup.

2358
2359
2360

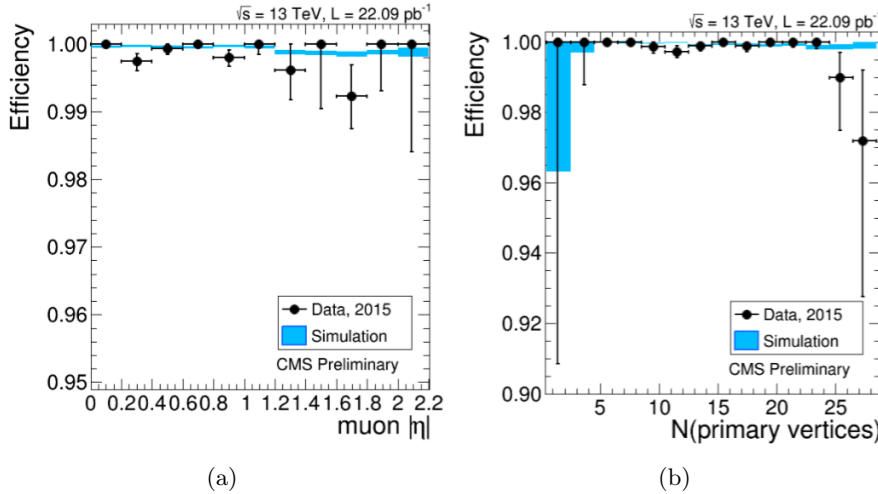


Figure 6.10: Tracking efficiency measured with a T&P technique, for muons from Z decays, as a function of the muon η (a) and the number of primary vertices (b), for 2015 data (black dots) and simulation (blue bands) [105].

The combination of different algorithms provides robust and efficient muon reconstruction. After the completion of both algorithms, the reconstructed stand-alone, global, and tracker muons are merged into a single software object, with the addition of further information, like isolation and energy collected in matching calorimeter towers. This information can be used for further identification, in order to achieve a balance between efficiency and purity of the muon sample as described in Section 6.3.3.

2361
2362
2363
2364
2365
2366

2367

2368 The performance of the reconstruction for high- p_T muons is strongly affected by radiative
 2369 processes and by the muon detector alignment. Electromagnetic showers and large energy
 2370 losses can arise as the muon traverses the steel layers of the magnet return yoke, producing
 2371 additional segments in the muon chambers. These events can affect the measurement done
 2372 in the muon detectors. Therefore, specialized reconstruction algorithms for high- p_T muons,
 2373 known as “TeV-muon” refits, have been developed in CMS as described in the following.

2374 The *tracker-plus-first-muon-station* fit (TPFMS) only uses hits from the tracker and the
 2375 innermost muon station with hits, to reduce the sensitivity to possible showering starting
 2376 deeper in the muon system. The *Picky* fit uses all tracker hits, while a selection is applied to
 2377 muon hits. Hits from chambers with a high probability of shower contamination (determined
 2378 from the hit occupancy) are required to be compatible with the extrapolated trajectory by
 2379 applying a χ^2 cut. The *dynamic truncation* algorithm (DYT) starts from the idea that the
 2380 muon track reconstruction should be stopped after a large energy loss, as hits produced
 2381 after that can only bias the momentum measurement. For every global muon trajectory
 2382 the algorithm starts from the corresponding tracker track and propagates it out to the
 2383 muon stations. Compatible segments (or hits) in the muon chambers are found by using an
 2384 estimator which takes into account the propagation of the tracker covariance matrix through
 2385 the material and the magnetic field, and the covariance matrices of the candidate muon
 2386 segments (or hits).

2387 Momentum assignment is then performed by the *Cocktail* algorithm which combines
 2388 the above methods to further improve the resolution at high p_T reducing the tails of the
 2389 momentum resolution distribution. In particular, the algorithm chooses, on a track-by-track
 2390 basis, the best muon reconstruction. For Run 1, the Cocktail-algorithm decision is taken
 2391 between the tracker-only, TPFMS, and Picky fits. This version of the algorithm is also known
 2392 as the *Tune P* algorithm. It starts with the Picky fit, then switches to the tracker-only fit
 2393 if the goodness of fit ($\chi^2/\text{n.d.f.}$) of the latter is significantly better. Then it compares the
 2394 $\chi^2/\text{n.d.f.}$ of the chosen track with that of TPFMS; TPFMS is chosen if it is found to be
 2395 better. For high- p_T muons, TPFMS and Picky algorithms are selected by Tune P in most of
 2396 the cases, in approximately equal amounts, while the tracker-only fit is selected only in a few
 2397 percent of events.

2398 For Run 2, the Tune P algorithm was extended to include also the DYT fit. The selection
 2399 is still made on a track-by-track basis, but using both the $\chi^2/\text{n.d.f.}$ of the track and the
 2400 relative error of the p_T measurement. The algorithm starts with the Picky fit, then switches
 2401 to DYT if the DYT track has a lower relative p_T error. It then compares the $\chi^2/\text{n.d.f.}$ of
 2402 the chosen track with that of the tracker-only fit and picks tracker-only if its $\chi^2/\text{n.d.f.}$ is
 2403 significantly better. Then the $\chi^2/\text{n.d.f.}$ of the chosen track and TPFMS are compared and
 2404 the one giving the best result is kept. At the end, if the final candidate track has p_T lower
 2405 than 200 GeV or the tracker-only p_T is lower than 200 GeV, the tracker-only track is selected.

2406 The momentum resolution obtained with the Tune P algorithm for muons with p_T in
 2407 the range $350 < p_T < 2000$ GeV is found to be $\approx 6\%$, as measured with cosmic-ray muon
 2408 data [103, 106].

2409 6.3.2 Muon trigger

2410 The Level-1 muon trigger uses signals from all three CMS muon detector systems: DT, CSC,
 2411 and RPC. It has a latency of $3.2 \mu\text{s}$ and reduces the rate of the readout of events with muon
 2412 candidates at the detector front-end electronics to a few kHz by applying selections on the
 2413 estimated muon p_T and quality. In the muon HLT, first a Level-1 trigger object is used as a
 2414 seed to reconstruct a standalone-muon track in the muon system, leading to an improved

2415 2416 2417 2418 2419 2420 2421 p_T estimate. At this point, p_T threshold filters are applied to the standalone-muon (also called Level-2 muon). Then seeds in the inner tracker are generated in the region around the extrapolated Level-2 muon, and tracker tracks are reconstructed. If a successful match is made between a tracker track and the Level-2 muon, a global fit combining tracker and muon hits is performed, yielding a Level-3 muon track on which the final p_T requirements are applied. In this way, the rate of recorded inclusive muon events is reduced to a few tens of Hz. The average processing time of the HLT reconstruction is about 50 ms.

2422 2423 2424 2425 2426 2427 2428 2429 2430 2431 The L1 and HLT trigger used to collect the data analyzed in this thesis are listed in Tables 6.7 and 6.8 for the 8 and 13 TeV data analysis, respectively. For both analyses the HLT used to select the events is the unprescaled single-muon trigger with the lowest p_T threshold that does not include muon isolation requirements. In fact, although muons produced by the leptonic decay of a high- p_T W boson tend to be isolated, their high momentum enhances the production of electromagnetic showers, that can mimic a non-isolated muon candidate. Therefore, only requirements on the muon p_T and η are applied at this stage. The efficiency of the L1 single-muon trigger with the 16 GeV threshold is shown in Fig. 6.11 as a function of the offline reconstructed muon p_T and η . In 2012 the efficiency for this trigger was greater than 90%. A similar result is obtained in 2015.

Table 6.7: The L1 and HLT single-muon triggers used to collect the 8 TeV data analyzed in this thesis together with the imposed requirements on the muon candidate.

Trigger	Name	Selections
Level 1	L1_SingleMu16_eta2p1	1 global muon with: $p_T > 16 \text{ GeV}$ $ \eta < 2.1$
HLT	HLT_Mu40_eta2p1	1 global muon with: $p_T > 40 \text{ GeV}$ $ \eta < 2.1$

Table 6.8: The L1 and HLT single-muon triggers used to collect the 13 TeV data analyzed in this thesis together with the imposed requirements on the muon candidate.

Trigger	Name	Selections
Level 1	L1_SingleMu25	1 global muon with: $p_T > 25 \text{ GeV}$
HLT	HLT_Mu45_eta2p1	1 global muon with: $p_T > 45 \text{ GeV}$ $ \eta < 2.1$

2432 2433 2434 The efficiency for a muon passing the high- p_T selections described in Section 6.3.3 to fire the HLT single-muon triggers have been measured in data with T&P method and are summarized in Tables 6.9 and 6.10.

2435 6.3.3 Muon identification

2436 2437 2438 2439 2440 The standard CMS muon reconstruction provides additional information for each muon, useful for muon quality selection and identification in physics analyses [103]. In general, particles detected as muons are produced in pp collision from different sources which lead to different experimental signatures. The so-called *prompt muons* arise either from decays of W, Z, or promptly produced quarkonia states. Real muons are also produced in the decay of

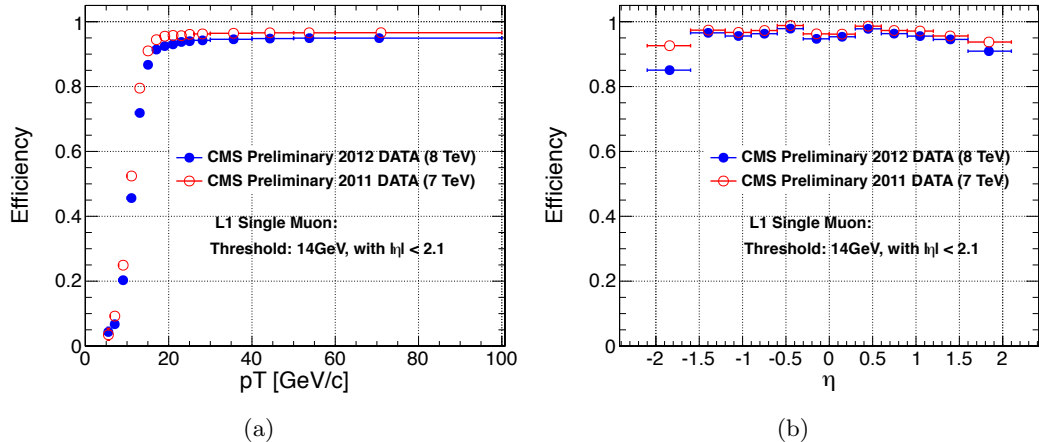


Figure 6.11: Efficiency of the L1 single-muon trigger with a threshold of 14 GeV on the muon p_T as a function of the muon p_T (a) and η (b) [107].

Table 6.9: Efficiencies and scale factors for the single-muon HLT trigger used in the 8 TeV analysis for muons with $p_T > 50$ GeV, $|\eta| < 2.1$, and satisfying the high- p_T and isolation selections described in Section 6.3.3. The quoted uncertainties are statistical.

	$0 < \eta < 0.9$	$0.9 < \eta < 1.2$	$1.2 < \eta < 2.1$
Efficiency simulation	$95.10\% \pm 0.03\%$	$87.01\% \pm 0.03\%$	$81.56\% \pm 0.03\%$
Efficiency data	$92.90\% \pm 0.02\%$	$83.14\% \pm 0.06\%$	$80.27\% \pm 0.05\%$
Data/simulation scale factor	0.9768 ± 0.0004	0.956 ± 0.001	0.984 ± 0.001

Table 6.10: Efficiencies and scale factors for the single-muon HLT trigger used in the 13 TeV analysis for muons with $p_T > 53$ GeV, $|\eta| < 2.1$, and satisfying the high- p_T and isolation selections described in Section 6.3.3. The quoted uncertainties are statistical.

	$0 < \eta < 0.9$	$0.9 < \eta < 1.2$	$1.2 < \eta < 2.1$
Efficiency simulation	$97.6\% \pm 0.1\%$	$93.4\% \pm 0.4\%$	$94.8\% \pm 0.2\%$
Efficiency data	$94.6\% \pm 0.2\%$	$89.7\% \pm 0.4\%$	$91.8\% \pm 0.2\%$
Data/simulation scale factor	0.969 ± 0.002	0.961 ± 0.006	0.968 ± 0.003

heavy flavour particles, such as beauty or charmed mesons, as well as in light hadron (pions or kaons) decays. Less frequently, muons might originate from a calorimeter shower or from a nuclear interaction in the detector. Furthermore, the so called “punch-through” effect, i.e. hadron shower remnants penetrating through the calorimeters and reaching the muon system, can lead to the reconstruction of a muon candidate. Most of the physics analyses in CMS studying SM processes or searching for BSM signals use prompt muons, while all the other categories of muons constitute the background. These analyses exploit the same set of information, although the applied selections might be different depending on the signature of interest and the expected background. In this section only the specific selection developed for high- p_T muons is described. One of the main difference with respect to the low- and medium- p_T muon selection is that this particular identification procedure does not use the PF algorithm. It is aimed at the best reconstruction of the muon track parameters without relying on external information on the event. Moreover, the goodness of the global-muon track fit selection, based on the χ^2 of the track, is not requested, but an additional selection based on the relative p_T resolution for the track used for momentum determination is applied.

The high- p_T muon selection criteria are described in the following and they have not been changed since Run 1:

- The muon must be reconstructed both as a tracker- and a global-muon. This is effective against decays-in-flight, punch-through and accidental matching (with noisy or background tracks or segments).
- Number of pixel hits in the tracker track ≥ 1 . To further suppress muons from decays in flight.
- Number of tracker layers involved in the track measurement ≥ 6 . This guarantees a good p_T measurement, for which some minimal number of measurement points in the tracker is needed. It also suppresses muons from decays in flight.
- Number of muon-chamber hits included in the global-muon track fit ≥ 1 . This requirement assures that the global muon is not an accidental match between the information from the muon system and the tracker. This could happen in particular for non-prompt muons or fake muons from punch-through.
- The muon track is required to have muon segments in at least 2 muon stations to further suppress punch-through and accidental track-to-segment matches. This selection is furthermore consistent with the logic of the single-muon trigger, which requires segments in at least two muon stations to obtain a meaningful estimate of the muon p_T .
- Transverse impact parameter of the muon track $< 2 \text{ mm}$. This assures the compatibility of the muon track with the interaction point hypothesis and it is effective against cosmic background and further suppress muons from decays in flight.
- Longitudinal impact parameter of the muon track $< 5 \text{ mm}$. To further suppress cosmic muons, muons from decays in flight and tracks from pileup.
- Relative p_T error $< 30\%$. To further suppress mis-reconstructed muons.

In addition to these identification criteria, an isolation requirement is applied to the well-identified muons. In particular, the muon must pass a relative tracker-only isolation selection: the scalar sum of the p_T of all other tracks in a cone of $\Delta R < 0.3$ around but not including the muon tracker track must be less than 10% of the muon p_T , also as measured by the tracker. To be used in the calculation of the tracker-based isolation, tracks have to be within 2 mm, in the z direction, of the primary vertex with which the muon candidate is associated. These additional criteria help suppress the effect of tracks originating from pileup on the reconstructed quantities.

The efficiency and data-to-simulation scale factors for the high- p_T muon identification and isolation criteria measured with the T&P method in 8 and 13 TeV data are summarized, respectively, in Tables 6.11 and 6.12. The scale factors are close to unity, indicating a good agreement between data and simulation. They are used in the analyses presented in this thesis to correct the normalization of simulations.

6.4 Jets

Quarks and gluons produced in the high-energy processes such as hard scattering of partons in proton-proton collisions carry a color charge and cannot exist in free form because of QCD confinement which only allows for colorless states (Section 2.1.6). At detector level,

Table 6.11: Efficiencies and scale factors for the high- p_T muon identification and isolation criteria used in the 8 TeV data analysis for muons with $p_T > 50$ GeV and $|\eta| < 2.1$.

Muon $ \eta $	$0 < \eta < 0.9$	$0.9 < \eta < 1.2$	$1.2 < \eta < 2.1$
High- p_T muon identification			
Efficiency simulation	$96.51\% \pm 0.02\%$	$96.61\% \pm 0.04\%$	$95.54\% \pm 0.03\%$
Efficiency data	$95.54\% \pm 0.02\%$	$95.87\% \pm 0.04\%$	$95.06\% \pm 0.03\%$
Data/simulation scale factor	0.9900 ± 0.0003	0.992 ± 0.001	0.9949 ± 0.0004
Tracker-based muon isolation			
Efficiency simulation	$99.49\% \pm 0.01\%$	$99.58\% \pm 0.01\%$	$99.59\% \pm 0.01\%$
Efficiency data	$99.46\% \pm 0.01\%$	$99.51\% \pm 0.01\%$	$99.56\% \pm 0.01\%$
Data/simulation scale factor	0.9996 ± 0.0001	0.9994 ± 0.0001	0.9997 ± 0.0001

Table 6.12: Efficiencies and scale factors for high- p_T muon identification and isolation criteria used in the 13 TeV data analysis for muons with $p_T > 53$ GeV and $|\eta| < 2.1$.

Muon $ \eta $	$0 < \eta < 1.2$	$1.2 < \eta < 2.1$
High- p_T muon identification		
Efficiency simulation	$97.6\% \pm 0.2\%$	$99.81\% \pm 0.2\%$
Efficiency data	$96.7\% \pm 0.4\%$	$1.0\% \pm 0.7\%$
Data/simulation scale factor	0.991 ± 0.005	1.002 ± 0.007
Tracker-based muon isolation		
Efficiency simulation	$99.8\% \pm 0.1\%$	$99.6\% \pm 0.1\%$
Efficiency data	$99.7\% \pm 0.1\%$	$99.7\% \pm 0.1\%$
Data/simulation scale factor	0.999 ± 0.001	1.001 ± 0.001

only the ensemble of the final colourless stable hadrons, simulated by the parton shower algorithms, can be observed. This exhibits as a jet of collimated particles which reflects the energy and the flight direction of the initial parton. Therefore, a jet is a cluster of charged particle tracks and calorimetric energy deposits, whose properties depend on the algorithm used for its definition. The jet clustering algorithms cluster particles (at parton, particle or detector level) into jets and reconstruct the energy and direction of the original parton. The task of a jet clustering algorithm is to allow comparisons between theoretical predictions, which are usually described by perturbative calculations, and experimental data. This is achieved reducing the complex structure of particle jets from a scattered parton to a simple four-momentum, which represents the main property of particle jets. In order to guarantee a meaningful calculation of theory predictions, jet clustering algorithms are characterized by two important properties. Clustering algorithms need to be infrared-safe, which means that the emission of infinitesimally-low-energy partons from partons inside a jet does not affect the jet properties. Furthermore, they need to be collinear-safe, which means that jet properties are not affected by the splitting of a parton inside a jet into two collinear partons. Jet algorithms for hadron colliders can be divided into two classes: cone [108] and sequential clustering [109–113] algorithms. The main algorithms used by LHC experiments belong to the second class and are the anti- k_t [113] (AK) and the Cambridge–Aachen (CA) [109, 111] algorithms. In fact, they are found to fulfil theory requirements and to exhibit good properties for experimental measurements. For this work both algorithms are used and described in the following.

2518 6.4.1 Jet clustering algorithms

2519 In sequential jet clustering algorithms, jets are defined through sequential, iterative procedures
 2520 that combine four-vectors of input pairs of particles until certain criteria are satisfied and jets
 2521 are formed. In particular, for each pair of particles i and j , a distance variable between the
 2522 two particles (d_{ij}), and the so-called “beam distance” for each particle (d_{iB}), are computed:

$$d_{ij} = \min(p_{Ti}^{2n}, p_{Tj}^{2n}) \frac{\Delta R^2 ij}{R^2} , \quad d_{iB} = p_{Ti}^{2n} , \quad (6.1)$$

2523 where p_{Ti} and p_{Tj} are the transverse momenta of particles i and j , respectively, “min”
 2524 refers to the smaller of the two p_T values, the integer n depends on the specific jet algorithm,
 2525 $\Delta R^2 ij$ is the distance between i and j in the $\eta\phi$ plane, and R is a free distance parameter,
 2526 with all angles expressed in radians. The particle pair (i, j) with smallest d_{ij} is combined
 2527 into a single object. All distances are recalculated using the new object, and the procedure is
 2528 repeated until, for a given object i , all the d_{ij} are greater than d_{iB} . Object i is then classified
 2529 as a jet and not considered further in the algorithm. The process is repeated until all input
 2530 particles are clustered into jets.

2531 The distance parameter R is responsible for defining the angular size of the jet. The
 2532 parameter n governs the topological properties of the jets and depending on its value three
 2533 different classes of clustering algorithms are distinguished. For $n = 1$ the procedure is referred
 2534 to as the k_t algorithm (KT) [113], which clusters soft objects before harder ones are added to
 2535 the final jet, figuratively reproducing in reverse the parton fragmentation and gluon emission
 2536 processes. For this reason, the algorithm tends to construct jets of irregular shapes which
 2537 depend on the detailed distribution of soft particles in an event. In addition, they are sensitive
 2538 to the presence of low- p_T pileup contributions. For $n = 0$, the procedure corresponds to the
 2539 CA algorithm. This relies only on angular information, and, like the KT algorithm, provides
 2540 irregularly-shaped jets. The CA algorithm is useful in identifying jet substructure as described
 2541 in Chapter 7. For $n = -1$, the procedure corresponds to the AK algorithm, which compares
 2542 the inverse square of the transverse momenta. The AK algorithm is used extensively in LHC
 2543 experiments and by the theoretical community for finding well-separated jets. The use of
 2544 inverse square of the p_T as a weight in the d_{ij} distances has the advantage that hard objects
 2545 collect adjacent soft ones before these are clustered among themselves into harder object.
 2546 This property makes the algorithm independent on soft radiation preserving infrared-safety.
 2547 Low energy gluons emitted at large angles are picked up by the algorithm rather late in the
 2548 clustering process and therefore do not affect the jet properties. They are picked up after all
 2549 hard emissions at small angles and before two soft particles can cluster with each other. Soft
 2550 emissions will therefore not cluster into separate jets, preserving infrared-safety. The AK
 2551 algorithm is also collinear-safe as the clustering is driven by the angular distance between
 2552 two particles. Furthermore, as soft particles clustered later have a minimal impact on the
 2553 larger four-momentum of the jet core, the AK algorithm tends to cluster particles out to
 2554 distances R from the core of a jet, yielding very regular jets. This allows for straight-forward
 2555 calibration and understanding of the detector acceptance. The behaviours of the CA and AK
 2556 jet algorithms are illustrated in Fig. 6.12.

2557 The choice of the distance parameters R , generally depends on the analysis. While
 2558 large cone size jets collect all energy from the scattered parton, they also pick up a large
 2559 contribution of background energy from the underlying event or pileup interactions. Small
 2560 cone size jets pick up little contamination, but may not collect all energy from the scattered
 2561 parton. The default choice in CMS for physics analyses in Run 1 and Run 2 uses the AK
 2562 algorithm with $R = 0.5$ (AK5) and $R = 0.4$ (AK4), respectively, since more collimated jets
 2563 are expected at higher \sqrt{s} . The AK5 or AK4 algorithms are used in this analysis to put

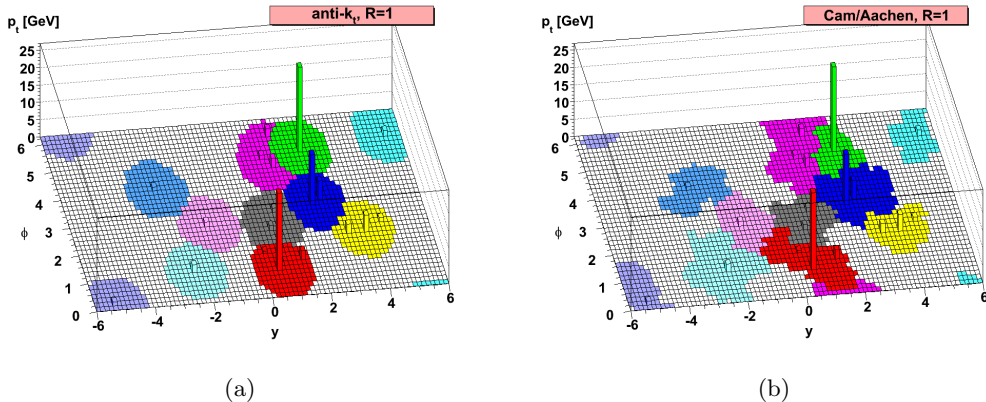


Figure 6.12: An example of jet clustering with the AK (a) and CA (b) algorithms. The reconstructed jets are shown as colored regions [113].

requirements on additional b jets in the event selection (Section 8.1), along with the b tagging algorithm described in Section 6.4.3.

A larger value of R increases the efficiency to entirely reconstruct the highly energetic products in the decays into hadrons of boosted V and Higgs bosons. In fact, the average angular distance between the decay products is inversely proportional to the p_T of the mother particle. The default choice in CMS for physics analyses involving boosted V or Higgs bosons decaying hadronically is $R = 0.8$. In particular, CA8 and AK8 jets are used for Run 1 and Run 2 analyses, respectively. The chosen value of R provides a high efficiency for V or Higgs bosons with small boost and ensures that no efficiency is lost in the transition from the classical reconstruction in two small jets at low boson p_T to the reconstruction as a single large-cone jet at higher values. Another point to consider when choosing the value of R , is the $t\bar{t}$ data sample available for validating highly boosted W jets (Section 7.2). If R is chosen too large, the b quark from the $t \rightarrow Wb$ decay tends to merge into the W jet. The chosen value of R is the result of a compromise between high efficiency for V or Higgs bosons with small boost and a sufficiently large sample of W jets in $t\bar{t}$ data for validating the boosted boson jet identification procedure. Figure 6.13 shows the p_T range of W bosons for which the CA8 algorithm is efficient and compares this to the efficiency for reconstructing W bosons from two AK5 jets. Above a p_T of 200 GeV, the CA8 jet algorithm, used to identify W jets, becomes more efficient than the reconstruction of a W boson from two AK5 jets.

6.4.2 Jet reconstruction and calibration

In CMS, the jet reconstruction is performed using the PF algorithm, which gives different reconstructed objects as input to the above explained jet clustering algorithms to build the so-called “PF jets”. As sketched in Fig. 6.14, the PF algorithm aims at reconstructing all the stable particles produced in an event, combining the information coming from all CMS sub-detectors to optimize particle identification, direction and energy determination. These particles are classified in several types: charged hadrons, photons, neutral hadrons, electrons and muons. Jets are typically composed by 65% charged hadrons, 25% photons, 10% neutral hadrons (Fig. 6.15). The PF algorithm is optimized to identify all these different components inside the jet, contrary to a calorimetric-only reconstruction. Typically, photons correspond to ECAL deposits not compatible with a tracker track. Charged hadrons correspond to HCAL and/or ECAL deposits matched to a inner track and not compatible with an electron, whereas

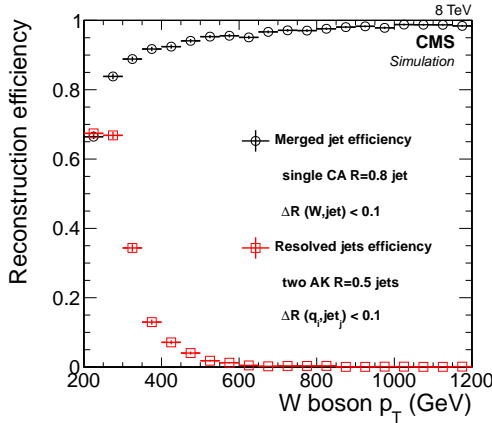


Figure 6.13: Efficiency to reconstruct a CA8 jet within $\Delta R < 0.1$ of a generated W boson, and the efficiency to reconstruct two AK5 jets within $\Delta R < 0.1$ of the generated quarks in the W boson decay, as a function of the p_T of the W boson [114].

neutral hadrons are identified as HCAL deposits not matched to any track. The momentum of neutral particles is obtained from the corresponding calorimeter energy deposits, calibrated for the non-linear response of the calorimeters. For charged particles, the momentum is determined combining the track momentum measured by the tracker with high resolution and the corresponding calibrated calorimeter energy deposits. Hence, both the position and energy measurements are greatly improved with respect to calorimeter jets as this algorithm makes use of the tracking detectors and high granularity of the ECAL which is much higher than that of the HCAL. Once all the PF candidates in the event are reconstructed, they are used as input to the jet clustering algorithms described in the previous section and a PF jet is formed. The jet momentum is determined as the vectorial sum of all PF candidates in the formed jet providing its “raw” estimate.

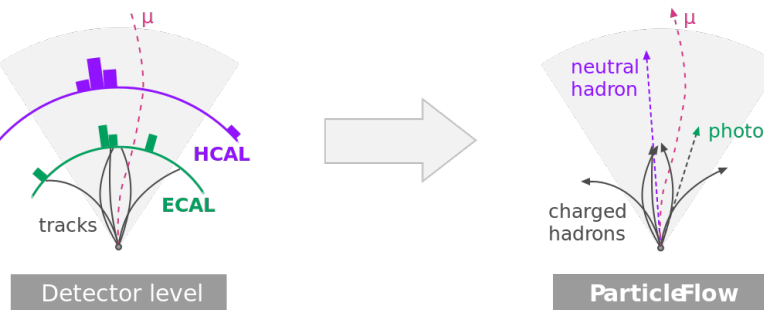


Figure 6.14: Sketch of the CMS particle-flow algorithm.

The additional pp collisions occurring within the same bunch-crossing as the primary hard interaction produce additional tracks in the tracker and deposit energy in the calorimeters. This contribution is usually referred to as in-time pileup. Due to the finite signal decay time in the calorimeters, the pp collisions occurring in the previous and subsequent beam crossings also contribute to calorimetric energy in the same time window as the primary hard interaction. This contribution is called out-of-time pileup. The out-of-time contribution is mitigated at the level of signal processing, while the in-time one is partially removed using tracking

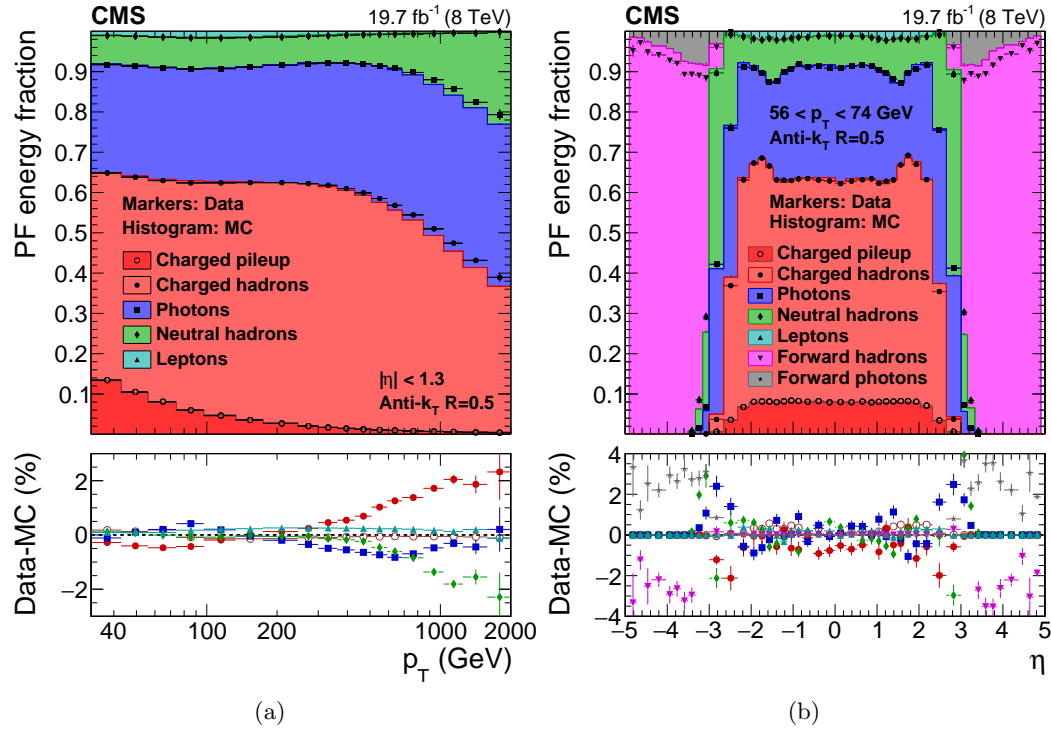


Figure 6.15: PF jet composition in data and simulation as a function of jet p_T for jets with $|\eta| < 1.3$ (a), and as a function of η for jets with p_T in the range $56 < p_T < 74 \text{ GeV}$ (b) [115].

information. This is achieved identifying which vertex the charged PF candidates originate from, and removing those unambiguously associated with pileup vertices before clustering jets. This method is referred to as *charged-hadron subtraction* (CHS), and represents the reference standard method for jet reconstruction in CMS for Run 1 and beginning of Run 2.

There are many possible sources of residual biases in the jet energy reconstruction, mainly due to the several intrinsic limitations of the system, such as the non-linear response of the calorimeters, the detector segmentation, the presence of material in front of calorimeters, electronic noise and pileup. The raw jet energy and resolution are thus corrected for several factors in order to obtain the energy value as close as possible to the true energy of the initial parton. CMS has adopted a factorized approach [116] to the problem of jet energy corrections, where each level of correction takes care of a different effect as described in the following.

The first step in this approach is a correction to the jet energies to mitigate additional pileup effects. In particular, the CHS jets are corrected to subtract residual contributions from neutral pileup particles, overlapping inside the jet cone. These corrections are determined from the simulation of a sample of QCD dijet events processed with and without pileup contaminations. This correction is usually parametrized as a function of the pileup energy density (ρ) [117, 118], the jet area (A) [119], jet p_T and η . The pileup offset corrections, defined as the mean value of the difference between the p_T of the reconstructed jet in events with and without pileup contamination, for AK5 CHS jets as a function of the corrected jet p_T and η are shown in Fig. 6.16, estimated for typical 2012 (8 TeV) conditions with an average number of additional pileup interactions $\langle \mu \rangle = 20$. The typical offset correction for a AK5 jet without CHS is 0.75 for a corrected jet p_T of 30 GeV, while a correction of 0.85 is obtained for AK5 CHS jets with same p_T value. This indicates that CHS removes approximately half of this offset before jet clustering by matching tracks to pileup vertices, reducing the residual

offset correction. Roughly one third of the remaining pileup is from PF charged hadrons that have not been matched to good pileup vertices, and much of the rest is from PF photons.

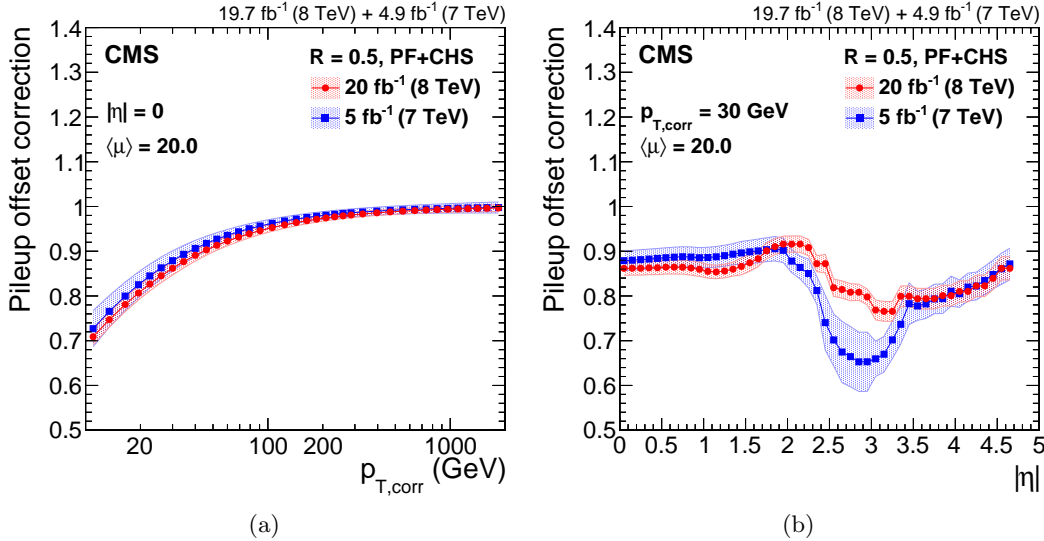


Figure 6.16: Pileup offset correction for AK5 CHS jets estimated for the typical 2012 condition of $\langle\mu\rangle = 20$. Corrections are shown for jets at $|\eta| = 0$ as a function of the corrected jet p_T (a), and for jets with $p_T = 30$ GeV as a function of the jet $|\eta|$ (b) [115].

Secondly, a simulation driven jet energy response correction is applied. The detector simulation takes into account effects due to energy lost when traversing the detector material, particle conversions, and a detailed detector geometry. In this step the aim is to correct for non-uniformities in the different CMS subdetectors, by comparing the reconstructed jet p_T to the particle-level one using simulated events only. The corrections are derived as a function of jet p_T and η and make the response uniform over these two variables. The simulated particle response corrections are summarized in Fig. 6.17 for 7 and 8 TeV data. The response is quite flat at $p_T > 50$ GeV, where the competing effects of increasing calorimeter response and falling tracking efficiency within the jet core compensate each other. In the barrel and endcap regions, the corrections rise with $|\eta|$, due to the increasing amount of material located in front of the calorimeters, which leads to effects such as an increased rate of nuclear interactions in the tracker. The corrections are higher around $|\eta| = 1.3$ and 3.0 due to the degradation of the response in the transition regions.

Finally data-driven residual corrections are applied to correct for any measurable difference between the detector simulation and the jets measured in data. This correction is done in two steps. At first, an additional correction for the non homogeneous response of the detector with η is derived from dijet events, in which the p_T response of a probe jet, outside the barrel region, is balanced to the one in the reference tag region ($|\eta| < 1.3$) as a function of the average p_T of the dijet system. Only events with back-to-back dijets and little additional activity in the event are used, to avoid any impact from unbalanced events. The jet energy is calibrated as a function of transverse momentum using a combination of $Z(\rightarrow \ell\ell) + \text{jet}$, $\gamma + \text{jet}$, and multijet events for jets in the reference barrel region ($|\eta| < 1.3$). The basic idea, in all the considered topologies, is to exploit the transverse momentum balance between the jet to be calibrated and a well reconstructed and calibrated reference object (Z or γ). The jet energy response is studied using two approaches. In one method the jet response is evaluated by comparing the reconstructed jet momentum ($p_{T,\text{jet}}$) directly to the momentum of the reference object ($p_{T,\text{ref}}$), while the second, more advanced, method takes into account

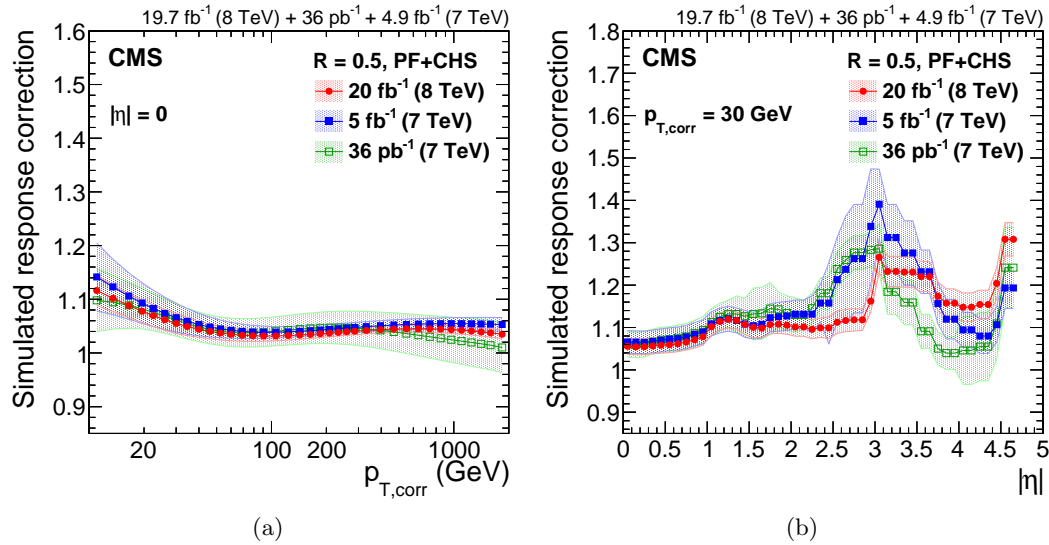


Figure 6.17: Detector response correction factors for AK5 CHS jets estimated for the 8 TeV data collected in 2012. Corrections are shown for jets at $|\eta| = 0$ as a function of the corrected jet p_T (a), and for jets with $p_T = 30$ GeV as a function of the jet $|\eta|$ (b) [115].

the missing energy measured in the calorimeters to balance the reference object and jet momenta. In this method the additional event activity is taken into account by the missing energy. Therefore, additional jets in the event have only a small impact on the measurement. The residual corrections are summarized in Fig. 6.18 for 8 TeV data. The residual response corrections are less than 3% in the barrel, less than 10% in the endcaps, and about 10% in the forward detector.

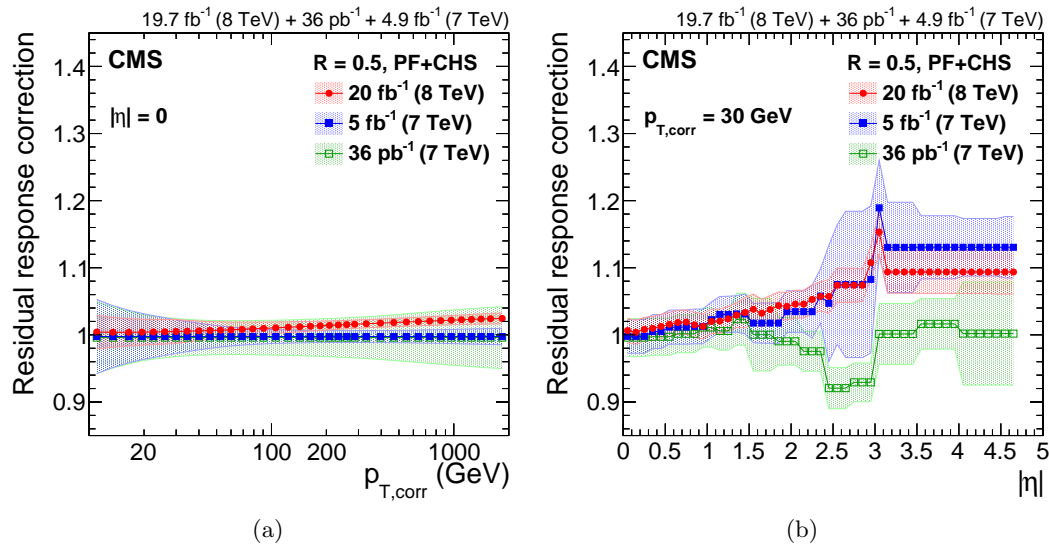


Figure 6.18: Residual data/simulation response correction factors for AK5 CHS jets for the 8 TeV data collected in 2012. Corrections are shown for jets at $|\eta| = 0$ as a function of the corrected jet p_T (a), and for jets with $p_T = 30$ GeV as a function of the jet $|\eta|$ (b) [115].

The fully calibrated PF jets are finally obtained in both data and simulation by multiplying all the above correction factors to the raw jet p_T as follows:

$$p_{T,\text{corr}} = p_{T,\text{raw}} \times C_{\text{pu}}(p_{T,\text{raw}}, \eta, \rho \cdot A) \times C_{\text{sim}}(C_{\text{pu}} \cdot p_{T,\text{raw}}, \eta) \times C_{\text{res}}(C_{\text{pu}} \cdot C_{\text{sim}} \cdot p_{T,\text{raw}}, \eta) \quad (6.2)$$

where C_{pu} represents the pileup correction, C_{sim} is the simulated response correction and C_{res} is the global residual correction applied only on jets in data. Figure 6.19 shows the overall uncertainty on the corrections to the jet energy scale for AK5 and AK4 CHS jets for 8 and 13 TeV data, respectively. In both cases, the final uncertainties are below 3% across the phase space of this analysis.

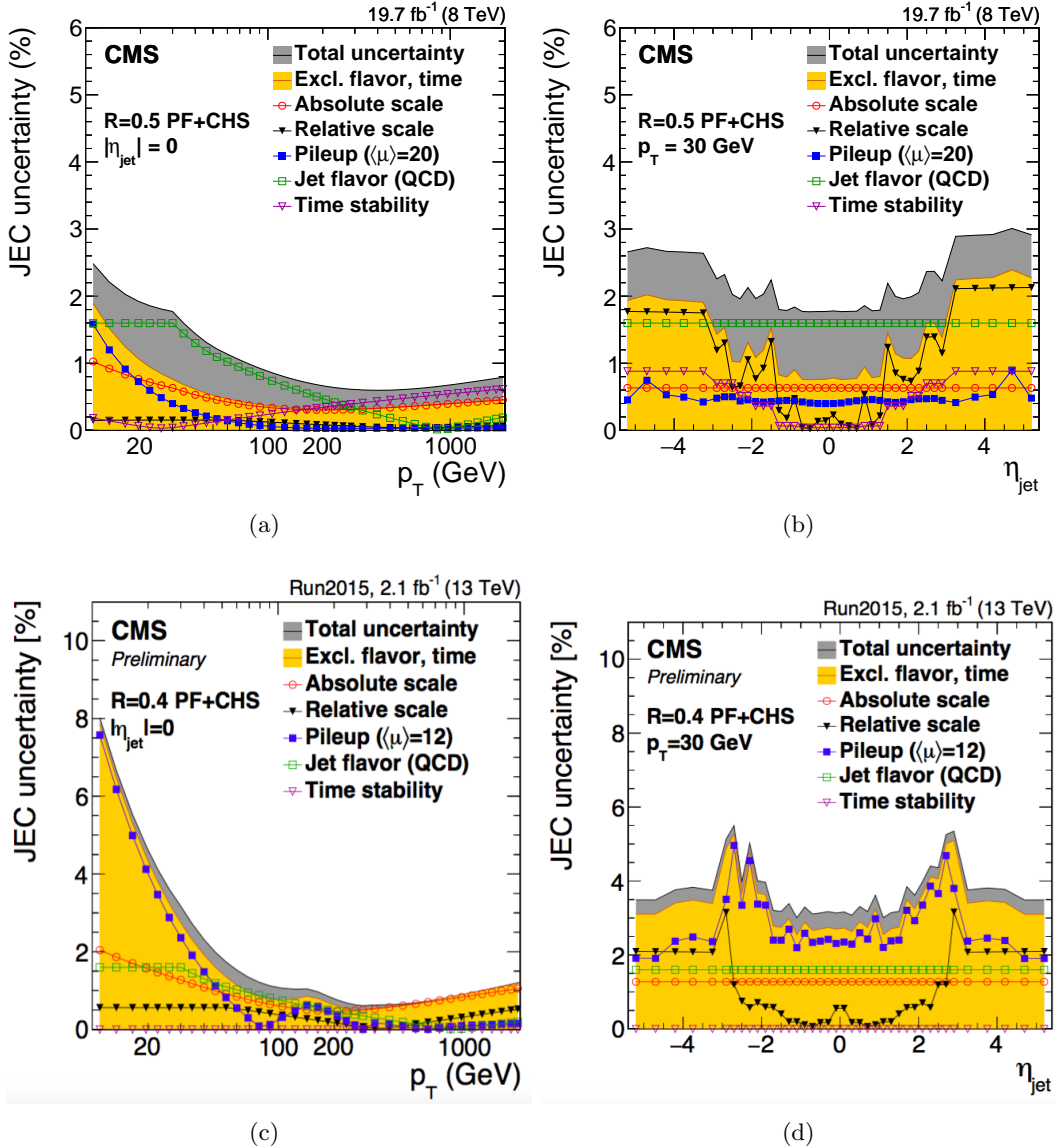


Figure 6.19: Summary of jet energy scale systematic uncertainties for the 8 TeV data collected in 2012 for AK5 CHS jets (upper plots) and for the 13 TeV data collected in 2015 for AK4 CHS jets (lower plots). Uncertainties are shown for jets at $|\eta| = 0$ as a function of the corrected jet p_T (left), and for jets with $p_T = 30$ GeV as a function of the jet $|\eta|$ (right) [115, 120].

The energy resolution of jets is relatively poor compared to the resolution of other physics objects (electrons, muons, photons), and the biases caused by jet resolution smearing

is important for steeply falling spectra and for resonance decays. Hence, calibrations are evaluated to correct the jet energy resolution in addition to the corrections to the jet energy scale described above. The measurements are performed with methods which are extensions of the methods used for measuring jet energy scales, but instead of looking at the mean of the response distribution, the width is the interesting parameter. Furthermore, corrections have to compensate for effects that do not produce an overall shift in the mean, but that can widen the distribution. As shown in Fig. 6.20, the jet energy resolution in data is worse than in the simulation by 10–20% depending on η , and the jets in simulation need to be smeared accordingly.

2690

Jets used in this analysis are requested to pass loose identification criteria, in order to reject spurious jet-like features originating from isolated noise patterns in the calorimeters or the tracker. The efficiency of these requirements is above 99% for real jets [121].

For the 8 TeV data analysis described in this work, all AK5 and CA8 jets must have corrected $p_T > 30 \text{ GeV}$ and $> 200 \text{ GeV}$, respectively, and $|\eta| < 2.4$ to be considered in the subsequent steps of the analysis. Furthermore, the AK5 and CA8 jets are required to be separated from any well-identified muon or electron (Sections 6.3 and 6.2) by $\Delta R > 0.3$ and > 0.8 , respectively. This requirement is applied to clean the jet collection used in the analysis from leptons clustered in jets. The AK5 jets are required to be separated from the CA8 jet representing the $V \rightarrow q\bar{q}^{(\prime)}$ candidate by $\Delta R > 0.8$ since an overlap is expected between the two reconstructions. Finally, CA8 jets are not used in the analysis if their pseudorapidity falls in the region $1.0 < |\eta| < 1.8$, thus overlapping the barrel-endcap transition region of the silicon tracker. In fact, in Run 1 it has been found that in this region, ‘noise’ can arise when the tracking algorithm reconstructs many fake displaced tracks associated with the jet. This issue in the reconstruction has been studied in details in the context of this work. The studies, presented and discussed in Appendix A, resulted in the choice of the η region to be excluded. In particular, the simulation does not sufficiently describe the full material budget of the tracking detector in that region, thus it does not accurately describe this effect. Without this requirement, a bias can be introduced in the b tagging, jet substructure and missing energy information, making this analysis systematically prone to that noise. As a consequence of these results, other analyses involving similar kinematic cuts and identification algorithms have been affected [122]. The same selections are applied for AK4 and AK8 jets in the 13 TeV data analysis, except for the fiducial cut on the η of the large-cone jet since the aforementioned reconstruction issue has been fixed for Run 2.

6.4.3 Identification of b jets

The identification of jets originating from b quarks (“b jets”) is one of the key ingredients of the analysis described in this work, which aims at isolating events of new physics with H bosons decaying to $b\bar{b}$. The ability to identify b jets (“b tagging”) plays a crucial role in reducing background coming from processes involving jets from gluons and light-flavor quarks (u, d, s), and from c quark fragmentation.

Identifying b jets relies on the properties of the weak decay and fragmentation of the b hadrons formed from the original b quarks. The most important property is the relatively long lifetime of b hadrons of about 1.5 ps ($c\tau \equiv 450\mu\text{m}$) corresponding to a flight distance that is observable with high resolution tracking detectors. A b hadron with $p_T = 50 \text{ GeV}$ propagates, on average, over almost half a centimetre ($Lc \sim \gamma\tau$) before decaying. As shown in Fig. 6.21, this leads to secondary vertices displaced from the primary event vertex and charged particle tracks incompatible with the primary vertex with sizeable impact parameter. In addition, b hadrons have a large mass and large multiplicity of charged particles in the

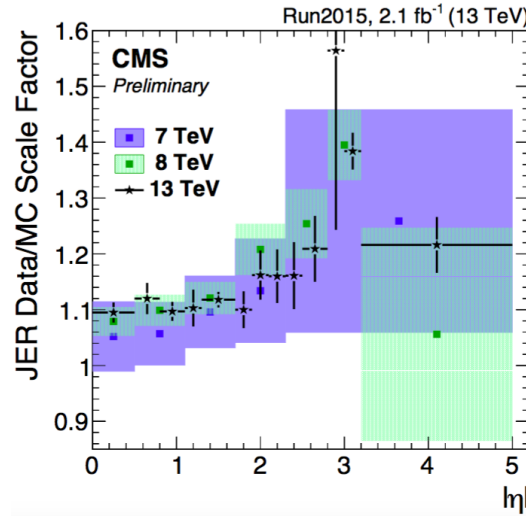


Figure 6.20: Data-to-simulation scale factors for the jet p_T resolution for AK5 CHS jets as a function of $|\eta|$ determined from 8 TeV data collected in 2012, and for AK4 CHS jets in 13 TeV data collected in 2015 [120].

final state (about five charged particles on average per b hadron decay). Because of the hard b-fragmentation function, the b hadron in a b jet carries a large fraction of the jet energy. Since b and c hadrons may decay semileptonically, in about 20% (per lepton species) of the cases an electron or muon is produced inside a b jet, if both direct and cascade decays are taken into account.

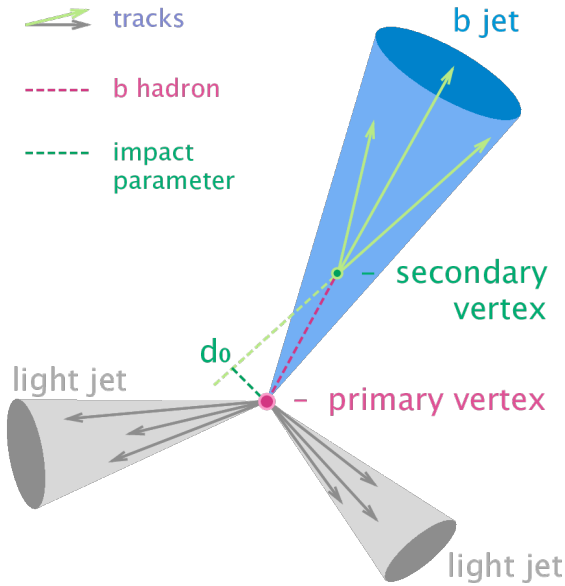


Figure 6.21: Representation of a b hadron decay and reconstructed b jet in the transverse plane.

A variety of algorithms have been developed in CMS [123] that, starting from jets and charged tracks, identify b jets exploiting the b hadron properties described above. Only the tracking detectors offer the spatial resolution needed to measure the properties of b hadron decays such as their long flight path. Efficient track reconstruction, and in particular precise

2738 spatial reconstruction close to the interaction point, is thus the key ingredient. Some of these
 2739 algorithms use just a single observable, while others combine several of these objects to achieve
 2740 a higher discrimination power. Each of these algorithms yields a single discriminator value
 2741 for each jet. The minimum thresholds on these discriminators define loose (“L”), medium
 2742 (“M”), and tight (“T”) operating points with a misidentification probability for light-flavor
 2743 jets of 10%, 1%, and 0.1%, respectively, at an average jet p_T of about 80 GeV.

2744 The jets used for b tagging are reconstructed with the PF algorithm and calibrated as
 2745 described in Section 6.4.2. A sample of well-reconstructed tracks of high purity inside the jet
 2746 is selected as input to each of the b tagging methods. In addition to the selection applied in
 2747 the iterative tracking procedure described in Section 6.1.1, specific requirements are imposed:

- 2748 • the fraction of misreconstructed or poorly reconstructed tracks is reduced by requiring
 $p_T > 1 \text{ GeV}$;
- 2750 • at least 8 tracker hits (including pixel) must be associated with the track;
- 2751 • at least 2 hits are required in the pixel system since track measurements in the innermost
 2752 layers provide most of the discriminating power;
- 2753 • the normalised χ^2 is required to be < 5 to ensure a good-quality fit;
- 2754 • the absolute value of the transverse and longitudinal impact parameter of the track must
 2755 be < 0.2 and $< 17 \text{ cm}$, respectively, to reject charged particle tracks having their origin
 2756 from sources with large displacement from the primary vertex (e.g. photon conversions
 2757 and nuclear interactions in the beam pipe or the first layers of the pixel detector);
- 2758 • tracks are associated to jets in a cone $\Delta R < 0.3$ around the jet axis, where the jet axis
 2759 is defined by the primary vertex and the direction of the jet momentum;
- 2760 • in order to reject tracks from pileup the distance to jet axis, defined as the distance of
 2761 closest approach of the track to the axis, is required to be $< 700 \mu\text{m}$;
- 2762 • the point of closest approach between the track trajectory and the jet axis, must be
 2763 within 5 cm of the primary vertex.

2764 Two algorithms for reconstructing secondary vertices are exploited. For the first algorithm,
 2765 the tracks associated to jets and fulfilling the above selection requirements are used in the
 2766 *adaptive vertex reconstruction* (AVR) algorithm [124] based on the adaptive vertex fitter
 2767 described in Section 6.1.1. This is the secondary vertex reconstruction algorithm used for b
 2768 tagging methods in CMS during Run 1. A number of selection criteria are applied to remove
 2769 vertices that are less likely to originate from a b hadron decay.

- 2770 • at least 2 tracks must be associated to the secondary vertex;
- 2771 • the fraction of tracks shared with the primary vertex is required to be $< 65\%$;
- 2772 • the distance between the primary vertex to the secondary vertex in the transverse plane,
 2773 the 2D flight distance, must be in the range 0.1–25 mm;
- 2774 • the 2D flight distance divided by its uncertainty or so-called 2D flight distance signifi-
 2775 ance has to be > 3 ;
- 2776 • the invariant mass of charged particles associated to the vertex is required to be
 2777 $< 6.5 \text{ GeV}$ and not compatible with the mass of the K_S^0 hadron in a window of 50 MeV;

- 2778 • the angular distance ΔR between the jet axis and the secondary vertex flight direction
 2779 is required to be less than the jet distance parameter;

2780 In contrast to the AVR algorithm, the *inclusive vertex finder* (IVF) [125] is not seeded
 2781 from tracks associated to the reconstructed jets. The IVF algorithm uses as input the
 2782 collection of reconstructed tracks in the event and looser quality criteria are applied. The
 2783 selected tracks are then used to identify clusters of nearby tracks based on their minimum
 2784 distance and the angles between them. The clusters are fitted with the adaptive vertex fitter
 2785 and a cleaning procedure is applied. At this stage, tracks can appear in multiple vertices and
 2786 therefore, one of the vertices is removed based on the number of shared tracks and distance
 2787 between the vertex and another one. Furthermore, tracks in the secondary vertex compatible
 2788 with the primary vertex are removed. When there are at least 2 tracks associated to the
 2789 secondary vertex after the track arbitration, the vertex is refitted and selection criteria similar
 2790 to the case of the AVR vertices are applied.

2791 The efficiency to reconstruct a secondary vertex for b (c) jets using the IVF algorithm is
 2792 about 10% (15%) higher compared to the efficiency to reconstruct a secondary vertex with
 2793 the AVR algorithm. However, for light-flavour jets the probability to find a secondary vertex
 2794 also increases by about 8%. Independently of the jet flavour, around 60% of the jets with an
 2795 AVR vertex also have an IVF vertex.

2796 In this analysis the *Combined Secondary Vertex* (CSV) b tagging algorithm is used, which
 2797 combines the information of displaced tracks with the information of secondary vertices
 2798 associated to the jet. This allows the algorithm to avoid limitations due to inefficiencies in
 2799 the secondary vertex reconstruction. Jets are divided in three vertex-dependent exclusive
 2800 categories: the presence of a reconstructed secondary vertex; at least two tracks with impact
 2801 parameter significance larger than 2; none of the previous. The following set of variables with
 2802 high discriminating power and low correlations are considered:

- 2804 • the secondary vertex category;
 2805 • the 2D flight distance significance of the secondary vertex;
 2806 • the number of tracks in the jet
 2807 • the number of tracks associated to the secondary vertex;
 2808 • the secondary vertex mass;
 2809 • the ratio of the energy carried by tracks at the vertex with respect to all tracks in the
 2810 jet;
 2811 • the η of the tracks at the vertex with respect to the jet axis;
 2812 • the 2D impact parameter significance of the first track that raises the invariant mass
 2813 above the charm threshold of 1.5 GeV when subsequently summing up tracks ordered
 2814 by decreasing impact parameter significance;
 2815 • the 3D signed impact parameter significance for each track in the jet.

2816 Two likelihood ratios are built from these variables used to discriminate between b and c
 2817 jets and between b and light-flavor jets and combined with prior weights of 0.25 and 0.75,
 2818 respectively. Figure 6.22(a) shows the distribution of the CSV discriminator value in a
 2819 multijet sample for 8 TeV data and for simulation, for jets clustered with the AK5 algorithm.

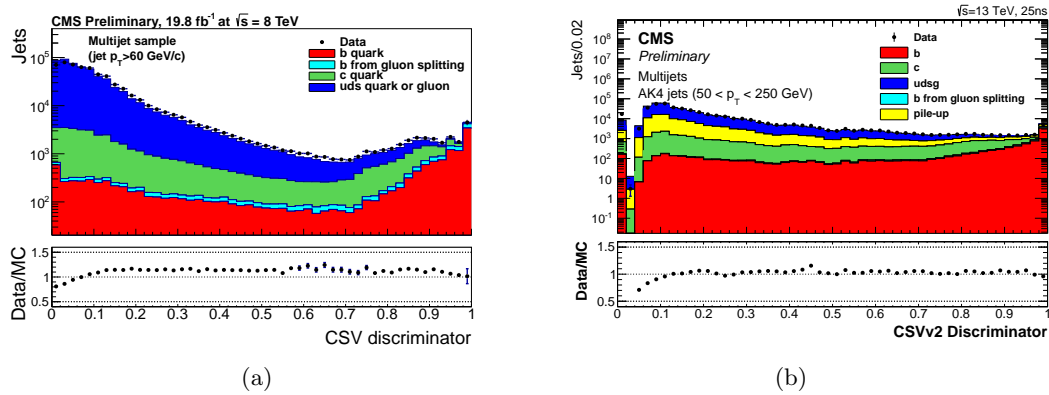


Figure 6.22: (a) Distribution of the CSV discriminator value in a multijet sample for data collected at 8 TeV and for simulation [126], for jets reconstructed with the AK5 algorithm. (b) Distribution of the CSVv2 discriminator value in a multijet sample for data collected at 13 TeV and for simulation, for jets reconstructed with the AK4 algorithm [127].

The CSV algorithm was further optimized for Run 2 and the new version is referred to as CSV version 2 (CSVv2) [127]. The main differences with respect to the Run 1 version of the CSV algorithm are the different vertex reconstruction algorithm used, the number of input variables and the way those are combined. As in the previous version, the input variables are combined using a multivariate technique. However, the method previously used, limited the amount of input variables since correlation between those could not be taken into account properly. In addition, the secondary vertex information is obtained with the IVF method described above. Figure 6.22(b) shows the distribution of the CSVv2 discriminator value in a multijet sample for 13 TeV data and for simulation, for jets clustered with the AK4 algorithm.

The performance of the CSVv2 tagger is presented in Fig. 6.23 as the b jet identification efficiency versus the misidentification probability for jets in simulated $t\bar{t}$ events requiring jet $p_T > 30$ GeV. A comparison is shown with the Run 1 version of the CSV algorithm trained for 8 TeV pp collisions using AK5 jets. The absolute improvement of the CSVv2 algorithm with respect to the CSV is of the order of 2 to 4% in b jet identification efficiency when comparing at the same misidentification probability for light-flavour jets. The improvement of using IVF vertices with respect to using AVR vertices in the CSVv2 algorithm is of the order of 1 to 2%.

The value of the discriminator threshold for the b tagging algorithms used in this analysis and the corresponding efficiencies are presented in Table 6.13. In this analysis the medium working point is used to identify and reject $t\bar{t}$ events where a real b jet is expected in addition to the large-cone jet used to reconstruct the $V \rightarrow q\bar{q}^{(\prime)}$ or $H \rightarrow b\bar{b}$ candidate, representing instead the signal. The same b tagging algorithm but together with the loose working point is used to identify whether the CA8 jet comes from a H boson decaying into bottom quarks, as described in Section 7.3.

The mismodelling of the b tagging variables in simulation is taken into account by reweighting simulation event-by-event with the ratio of the b tagging efficiency in data and simulation, determined in a sample enriched with b jets and depending on the jet p_T and η . The correction factors as a function of the b jet p_T are shown in Fig. 6.24(a) and 6.24(b) for the CSVM and CSVv2M operating points respectively, as measured in 8 and 13 TeV data. In a similar way, correction factors are also derived and applied to correct the misidentification

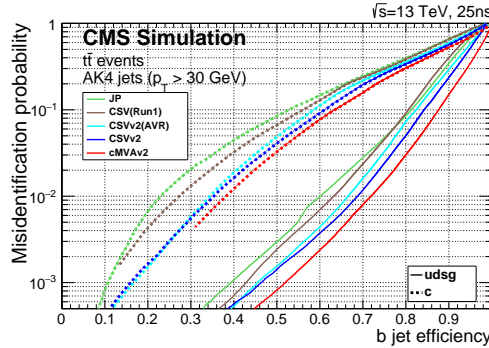


Figure 6.23: Performance of the CSVv2 algorithm showed as the probability for non-b jets to be misidentified as b jet as a function of the efficiency to correctly identify b jets. The improvement of this algorithm with respect to the Run 1 version is also shown [127].

Table 6.13: B taggers and discriminator threshold used in CMS for Run 1 and Run 2 and corresponding efficiency for b jets with $p_T > 30$ GeV in simulated $t\bar{t}$ events.

Algorithm	operating point	discriminator value	b tagging efficiency (%)
CSV (Run 1)	CSVL	0.244	80
	CSVM	0.679	64
	CSVT	0.898	42
	CSVv2L	0.460	83
	CSVv2M	0.800	69
	CSVvsT	0.935	49

2851 probability in simulation. These factors are shown in Fig. 6.25(a) and 6.25(b) as a function
 2852 of the jet p_T for the CSVM and CSVv2M operating points.

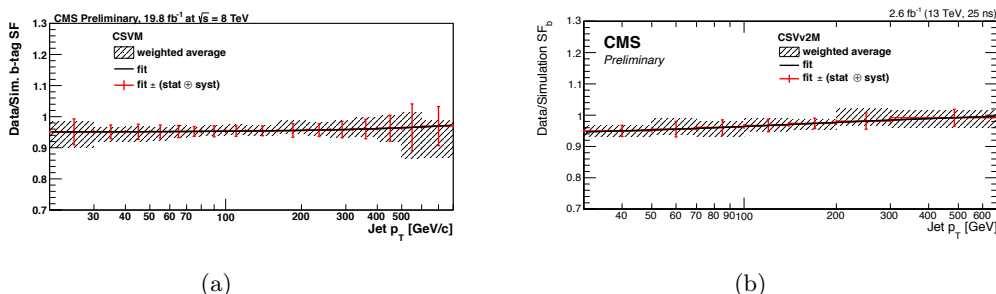


Figure 6.24: Data-to-simulation correction factors for the b tagging efficiency for the CSVM (a) and CSVv2M (b) algorithms as a function of the b jet p_T as measured in 8 and 13 TeV data [126, 127].

6.5 Missing transverse energy

2853 CMS is a full coverage hermetic detector which identifies and reconstructs almost all stable
 2854 or long-lived particles produced in pp collisions. The only exceptions are neutrinos and
 2855 hypothetical neutral weakly interacting particles. Although these particles do not leave a

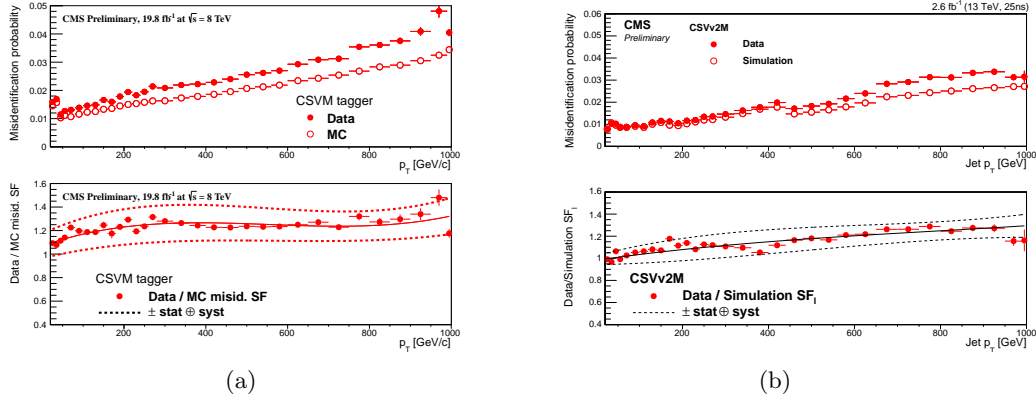


Figure 6.25: Data-to-simulation correction factors for the misidentification probability for the CSVM (a) and CSVv2M (b) algorithms as a function of the jet p_T as measured in 8 and 13 TeV data [126, 127].

signal in the detector, their presence can be inferred from the momentum imbalance in the transverse plane, a quantity known as missing transverse momentum and denoted by \vec{p}_T^{miss} .

The standard method available in CMS for the reconstruction of \vec{p}_T^{miss} uses the PF algorithm [128]. The PF \vec{p}_T^{miss} is used in this analysis along with PF jets and it is calculated as the negative vector sum of the transverse momenta of all reconstructed PF candidates in a given event

$$\vec{p}_T^{\text{miss}} = - \sum_i^N \vec{p}_{T,i}. \quad (6.3)$$

Its magnitude is referred to as missing transverse energy and denoted by E_T^{miss} . The E_T^{miss} is an important variable in many searches for physics beyond the standard model such as the ones described in this thesis where a real highly energetic neutrino is expected in the final state. In addition, the precise measurement of E_T^{miss} plays a crucial role for measurements of standard model physics involving W bosons and top quarks. The \vec{p}_T^{miss} reconstruction is sensitive to pileup, detector malfunctions and to various reconstruction effects. A precise calibration of all reconstructed physics objects is therefore crucial for its performance. The level of mismeasurement is significantly reduced after jet energy calibration, described in Section 6.4.2. A correction to the \vec{p}_T^{miss} is derived by propagating the jet energy scale corrections as described in the following.

The raw missing transverse momentum can be written as:

$$\vec{p}_T^{\text{miss,raw}} = - \sum_i^{N_{\text{jets}}} \vec{p}_{T,i}^{\text{raw}} - \sum_i^{N_{\text{uncl}}} \vec{p}_{T,i}, \quad (6.4)$$

where the first and second sum runs over the p_T of the PF candidates clustered as jets and unclustered, respectively, and the superscript “raw” indicates the uncorrected value. The correction to the \vec{p}_T^{miss} is then obtained by replacing the first sum with the vector sum of the transverse momenta of the jets to which jet energy scale corrections (JEC) are applied:

$$\vec{C}_T^{\text{JEC}} = \sum_i^{N_{\text{jets}}} \vec{p}_{T,i}^{\text{raw}} - \sum_i^{N_{\text{jets}}} \vec{p}_{T,i}^{\text{JEC}}, \quad (6.5)$$

where the sum is performed over all jets with corrected $p_T > 10$ GeV.

Another type of correction is derived and applied to correct for a modulation in ϕ in the \vec{p}_T^{miss} present not only in data but also in simulation. The distribution of genuine \vec{p}_T^{miss} is instead independent of ϕ because of the rotational symmetry of the collisions around the beam axis. The possible causes of the modulation include imperfect detector alignment, inefficiencies, a residual p_T dependence of the calibration, and a shift between the center of the detector and the beam line. The correction for this effect can be expressed as a shift in the \vec{p}_T^{miss} components along the x and y detector coordinates, which increases approximately linearly with the number of reconstructed vertices. This correlation is used for a correction procedure as follows

$$\vec{E}_{T,x}^{\text{miss},\phi\text{corr}} = \vec{E}_{T,x}^{\text{miss,raw}} - (c_{x_0} + c_{x_s} N_{\text{vtx}}), \quad \vec{E}_{T,y}^{\text{miss},\phi\text{corr}} = \vec{E}_{T,y}^{\text{miss,raw}} - (c_{y_0} + c_{y_s} N_{\text{vtx}}), \quad (6.6)$$

where the coefficients are determined separately for data and simulated events.

The distributions of the PF E_T^{miss} , obtained after applying all the corrections described above, in $Z \rightarrow \mu^+\mu^-$, $Z \rightarrow e^+e^-$, and prompt photon events are presented in Fig. 6.26 as measured in 8 TeV data and for simulation. Good agreement between data and simulation is observed in all distributions.

These events contain no genuine \vec{p}_T^{miss} , and thus a balance exists between the well-measured vector boson transverse momentum, denoted as \vec{q}_T , and the hadronic recoil, denoted as \vec{u}_T , which dominates the \vec{p}_T^{miss} measurement. The q_T can therefore be used as a reference to measure the scale and resolution of \vec{p}_T^{miss} . The hadronic recoil can be projected to the axis defined by q_T , yielding two signed components, parallel (u_{\parallel}) and perpendicular (u_{\perp}) to this axis. The parallel component is typically negative as the observed hadronic system is usually in the hemisphere opposite the boson. The scalar quantity $-\langle u_{\parallel} \rangle / \vec{q}_T$ is referred to as the \vec{p}_T^{miss} response. The response curves, extracted from the data as a function of the vector boson boost \vec{q}_T , are shown in Fig. 6.27(a), where deviations from unity indicate a bias on the hadronic recoil energy scale which is fully recovered for $\vec{q}_T > 40$ GeV. The resolution curves, $\sigma(u_{\parallel})$ and $\sigma(u_{\perp})$ as a function of q_T , are shown in Fig. 6.27(b) and 6.27(c), respectively, for each control sample. The resolution increases with increasing q_T , while the data and simulation curves are in good agreement for each control sample.

2906

6.6 $W \rightarrow \ell\nu$ reconstruction

2908 The identified muon or electron (see Section 6.2.3 and 6.3.3) is associated with the $W \rightarrow \ell\nu$
 2909 candidate. The \vec{p}_T of the undetected neutrino is assumed to be equal to the \vec{p}_T^{miss} . The
 2910 longitudinal momentum of the neutrino (p_z) is obtained by solving a quadratic equation that
 2911 sets the $\ell\nu$ invariant mass to the known W boson mass [10]:

$$M_W^2 = m_\ell^2 + 2(E_\ell E_\nu - p_{x_\ell} p_{x_\nu} - p_{y_\ell} p_{y_\nu} - p_{z_\ell} p_{z_\nu}) = (80.4)^2 \quad (6.7)$$

2912 In the case of two real solutions, the one with the smaller absolute value is chosen. If the
 2913 discriminant becomes negative, or equivalently the W boson transverse mass M_T is larger
 2914 than M_W used in the constraint, the solutions have an imaginary part. This happens because
 2915 of the finite resolution of E_T^{miss} . Several schemes exist to deal with this situation. One
 2916 technically simple method consists of taking the real part of the complex solutions but it
 2917 leads to the wrong W boson mass. This method is used for the reconstruction of the $W \rightarrow \ell\nu$
 2918 candidate in the 13 TeV data analysis described in this work. A second method has been

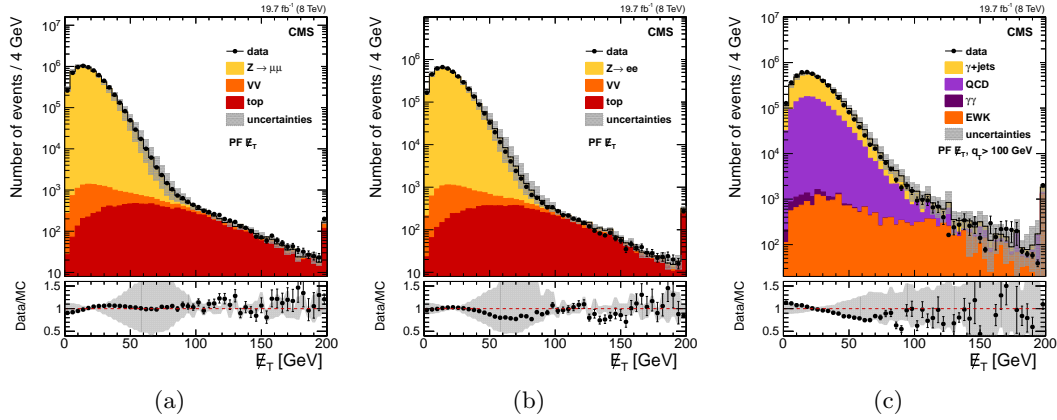


Figure 6.26: The PF E_T^{miss} distribution in $Z \rightarrow \mu^+\mu^-$ (a), $Z \rightarrow e^+e^-$ (b), and prompt photon (c) events for 8 TeV data and for simulation. The points in the lower panel of each plot show the ratio between data and simulation describing their agreement [129].

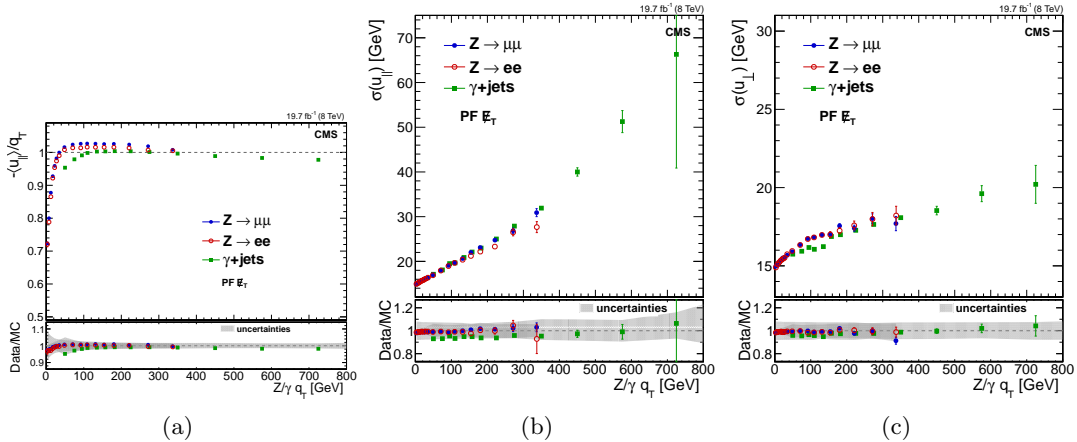


Figure 6.27: (a) Response curves for PF \vec{p}_T^{miss} in events with a Z-boson or prompt photon. Also shown are the resolution curves of the parallel (b) and perpendicular (b) recoil components as a function of the $Z/\gamma q_T$. In each plot the upper frame shows the response in 8 TeV data, while the lower one shows the ratio between data and simulation. [129].

studied, which eliminates the imaginary component by modifying the components of the missing transverse energy such to give $M_T = M_W$, still respecting equation 6.7 [130]. This method is used in the 8 TeV data analysis for the reconstruction of the $W \rightarrow \ell\nu$ candidate and for the reconstruction of the mass of the leptonically decaying top quark in $t\bar{t}$ events. The performance of the two methods are equivalent in terms of resolution of the reconstructed diboson or top quark invariant mass.

The four-momentum of the neutrino is used to reconstruct the four-momentum of the $W \rightarrow \ell\nu$ candidate. The same procedure holds also for the cases where the W boson decays to $\tau\nu$ and the τ decays to one muon or electron and two neutrinos. In this case, the \vec{p}_T^{miss} represents the \vec{p}_T of the three-neutrino system.

Identification of highly boosted W/Z → q \bar{q} ^(') and H → b \bar{b}

2932

2933 Large-cone jets (Section 6.4), also referred to as “fat jets”, are used to reconstruct the W
 2934 jet, Z jet, and H jet candidates resulting after the hadronization of the two quarks from the
 2935 decay of highly boosted W, Z, and Higgs boson, respectively. For the resonance mass range
 2936 considered in this search, the two quarks from the V or Higgs boson decay are separated by a
 2937 small angle, resulting in the detection of a single “merged” jet after hadronization, instead
 2938 of two separated jets. To discriminate against multijet background comprising of QCD jets
 2939 originated from quark or gluon fragmentation, the analysis exploits both the reconstructed
 2940 jet mass, which is required to be close to the boson mass, and the jet substructure arising
 2941 from the two jet cores that correspond to the two high- p_T decay quarks. The techniques
 2942 used to identify jets arising from the merged decay products of a single V or Higgs boson are
 2943 referred to as “V tagging” or “H tagging”, respectively. They employ novel jet substructure
 2944 algorithms, which are described in Section 7.1. The features of the V tagging algorithm
 2945 are described in Section 7.2 and its performance in both data and simulation are discussed.
 2946 Finally, in Section 7.3, an algorithm tuned to the specific properties of the Higgs boson decay
 2947 into a bottom quark-antiquark pair is presented.

7.1 Jet substructure observables

7.1.1 Pruned jet mass

The bulk of the signal jet mass arises from the kinematics of the two jet cores that correspond
 to the two decay quarks. In contrast, the QCD jet mass arises mostly from large-angle and
 soft quark or gluon radiation. As a first step in exploring potential substructure, the jet
 constituents are subjected to a jet grooming algorithm that improves the resolution in the jet
 mass and reduces the effect of pileup [114, 131]. The goal of jet grooming is to recluster the
 jet constituents, while applying additional requirements that eliminate soft, large-angle QCD
 radiation. This procedure shifts the jet mass of QCD jets to smaller values, while maintaining
 the mass for signal jets close to the boson mass. Furthermore, soft contributions from the
 underlying event and pileup, usually present in all jets, are removed. Different jet grooming
 algorithms have been explored at CMS and their performance on jets in multijet processes has
 been studied in detail [114, 131]. In this analysis, the *jet pruning* algorithm [132, 133] is used,
 as it was found to provide the best discrimination against QCD background as discussed in
 Ref. [114, 131].

Jet pruning reclusters each fat jet starting from all its original constituents, through the
 implementation of the CA algorithm, but applying two additional conditions beyond those
 given in 6.1. In particular, the softer of the two particles i and j to be merged is removed
 when the following conditions are met:

$$z_{ij} \equiv \frac{\min(p_{Ti} + p_{Tj})}{p_{Ti} + p_{Tj}} < z_{cut}, \quad \Delta R_{ij} > D_{cut} \equiv \alpha \frac{m_j}{p_T} \quad (7.1)$$

where p_{Ti} and p_{Tj} are the momenta of the particles i and j , m_j and p_T are the mass and transverse momentum of the originally-clustered jet, and z_{cut} and α are parameters of the algorithm, chosen to be 0.1 and 0.5, respectively. The resulting jet is the *pruned jet*. The pruned jet mass, m_{jet} , is computed from the sum of the four-momenta of the constituents that survive the pruning; it is then corrected by the same factor used to correct the jet p_T (Section 6.4). Figure 7.1(a) illustrates the effect of pruning on AK8 jets: the m_{jet} spectrum of the W jet candidate from the decay of highly boosted and longitudinally polarized W bosons is shown together with the distribution in m_{jet} for the simulated background of W+jets. Dashed and solid lines correspond to the distributions before and after the application of the pruning algorithm, respectively. Fully merged jets reconstructed from the W boson decay generate a distinctive peak around the W boson mass, which is narrowed by the pruning, while background jets acquire a smaller mass on average, enhancing the discrimination. Figure 7.1(b) compares the distributions in m_{jet} for W, Z and H jet candidates from the decay of highly boosted W, Z and Higgs bosons, respectively. The distribution in m_{jet} for the W+jets background is also shown. Not-full-merged signal jets give rise to a small peak at low masses.

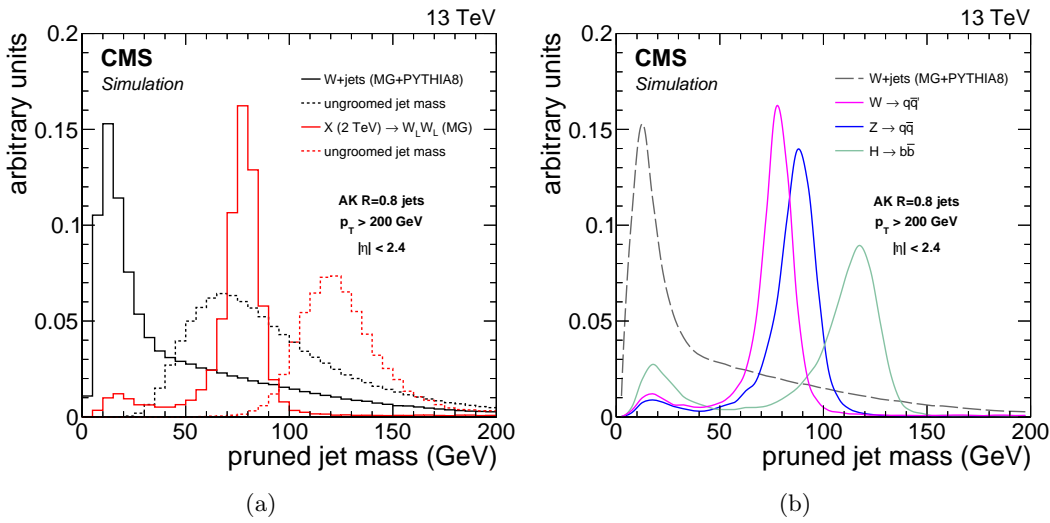


Figure 7.1: (a) Distribution in pruned jet mass m_{jet} for simulated events of highly boosted W bosons and inclusive QCD jets expected in the W+jets process. The ungroomed jet mass is shown as dotted lines to illustrate the effect of pruning. MG denotes the MADGRAPH generator. (b) Comparison of the distributions in m_{jet} for simulated events of highly boosted V and Higgs bosons.

7.1.2 N-subjettiness

In addition to the pruned jet mass, additional information about the jet shape is used to discriminate the signal against QCD jets. A generalized jet shape observable called *N-subjettiness* [134] has shown the best performance in terms of the required signal and background discrimination [114]. This observable takes advantage of the multi-body kinematics in the decay pattern of boosted hadronic objects and define a measure, τ_N , to quantify the compatibility of the jet clustering with the hypothesis that exactly N subjets are present. The

2991 constituents of the jet before the pruning procedure are reclustered using the k_T algorithm
 2992 (Section 6.4), until N joint objects (subjets) remain in the iterative combination procedure of
 2993 the algorithm. The observable τ_N is then defined as

$$\tau_N = \frac{1}{d_0} \sum_k p_{T,k} \min\{\Delta R_{1,k}, \Delta R_{2,k}, \dots, \Delta R_{N,k}\}, \quad (7.2)$$

2994 where k runs over the constituents of the jet, and the distances $\Delta R_{n,k}$ are calculated
 2995 relative to the axis of the n th subjet. The normalization factor d_0 is taken as

$$d_0 = \sum_k p_{T,k} R_0, \quad (7.3)$$

2996 where R_0 is the characteristic jet radius used in the original jet clustering algorithm. The
 2997 subjet axes are obtained by running the exclusive k_T algorithm [110], and reversing the last
 2998 N clustering steps. The variable τ_N quantifies the compatibility of the jet clustering with
 2999 the hypothesis that exactly N subjets are present. Jets with $\tau_N \approx 0$ have all their radiation
 3000 aligned with the candidate subjet directions and therefore have N (or fewer) subjets. Jets
 3001 with $\tau_N \gg 0$ have a large fraction of their energy distributed away from the candidate subjet
 3002 directions and therefore have at least $N + 1$ subjets. The ratio between 2-subjettiness and
 3003 1-subjettiness, $\tau_{21} = \tau_2/\tau_1$, is found to be a powerful discriminant between jets originating
 3004 from hadronic V decays and from gluon and single-quark hadronization. Jets from $V \rightarrow q\bar{q}^{(\prime)}$
 3005 decays in signal events are characterized by lower values of τ_{21} relative to QCD background.
 3006 Figure 7.2 shows the N -subjettiness ratio τ_{21} distribution for W jets and QCD jets after
 3007 requiring $60 < m_{\text{jet}} < 100$ GeV, demonstrating its discrimination power after the pruned jet
 3008 mass selection.

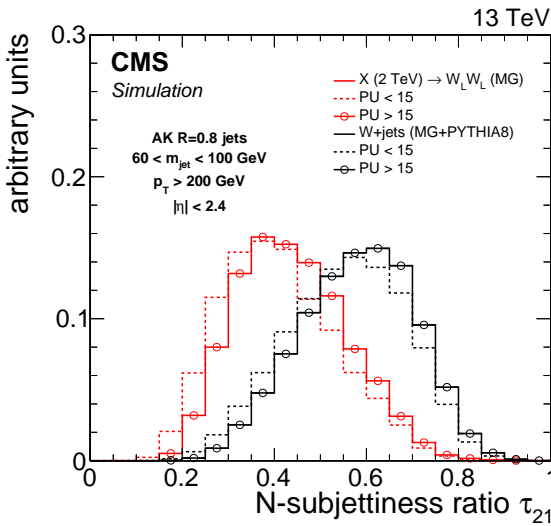


Figure 7.2: Distribution in N-subjettiness ratio τ_{21} for simulated events of highly boosted and longitudinally polarized W bosons and inclusive QCD jets expected in the W+jet process. The distributions are shown after a selection on the pruned jet mass requiring $60 < m_{\text{jet}} < 100$ GeV. The histograms are the expected distributions after full CMS simulation with pileup corresponding to an average number above and below 15 interactions.

3009 7.2 The V tagging algorithm

3010 The jet substructure observables described in the previous section are employed for identifying,
 3011 or “tagging”, W and Z jets (“V jets”). The V tagging of the jets is obtained combining
 3012 selections on both the pruned jet mass m_{jet} and N-subjettiness ratio τ_{21} observables.

3013 The selection criteria have been optimized in the context of searches for resonances
 3014 decaying into diboson in the $\ell\nu + \text{jet}$ and dijet final states [86, 135, 136]. The optimization,
 3015 based on simulation, aims at maximizing the analysis sensitivity and it leads to slightly
 3016 different working points for each analysis. In particular, the baseline selection values have
 3017 been changed from Run 1 to Run 2. Typical signal efficiencies and mistagging rates of QCD
 3018 jets obtained, respectively, from simulations and measurements with 8 and 13 TeV data are
 3019 summarized in Table 7.1, for jets with $p_T = 500$ GeV. The $\ell\nu q\bar{q}$ analysis described in this
 3020 work makes use of a looser τ_{21} working point of 0.6 resulted from an optimization which takes
 3021 into account signal efficiency and background rejection over a large jet p_T range. In fact,
 3022 this channel is characterized by a low background rate and a τ_{21} selection providing a higher
 3023 signal efficiency over the whole jet p_T range is therefore preferred.

3024

Table 7.1: Typical selection criteria for V tagging used in Run 1 and Run 2. The corresponding signal efficiency for W jets and mistagging rate of QCD jets are also reported for jets with $p_T = 500$ GeV, obtained from 8 and 13 TeV data and from simulation.

Data sets	V tagging selections	signal efficiency	mistagging rate
8 TeV	$60 < m_{\text{jet}} < 100$ GeV $\tau_{21} < 0.5$	0.65	0.04
13 TeV	$65 < m_{\text{jet}} < 105$ GeV $\tau_{21} < 0.45$	0.55	0.03
	$65 < m_{\text{jet}} < 105$ GeV $\tau_{21} < 0.6$	0.76	0.05

3025 The V tagging performance at 8 TeV has been studied in detail in Ref. [114]. From
 3026 simulation studies it is observed that the efficiency of the m_{jet} selection increases with p_T up
 3027 to about 600 GeV since at higher p_T the showers from the W decay quarks are more likely
 3028 to be reconstructed within a single fat jet. Above 600 GeV, the efficiency begins to decrease
 3029 as a function of jet p_T , since at very large values the PF candidate reconstruction degrades
 3030 in resolving the jet substructure, and the pruning algorithm therefore removes too large a
 3031 fraction of the jet mass. For Run 2, the PF reconstruction has been optimized by exploiting
 3032 the full potential of the CMS ECAL granularity to resolve jet substructure and a constant
 3033 efficiency is maintained up to at least $p_T = 2.5$ TeV [137, 138].

3034 The efficiency of the additional τ_{21} selection also drops as a function of p_T , thus a fixed
 3035 working point will degrade the efficiency with increasing p_T . However, the same efficiency
 3036 at an equivalent background rejection rate can be reached by adjusting the τ_{21} selection as
 3037 a function of p_T . This possibility has not been explored yet in any of the searches which
 3038 employ V tagging.

3039 The efficiency of the V tagging selection as a function of the number of reconstructed
 3040 primary vertices (PV) has also been studied [138]. It is observed that the efficiency of the
 3041 m_{jet} selection is constant as a function of PV, whereas the additional τ_{21} selection efficiency
 3042 drops from 60% at 0 PV to 40% at 30 PV. However, the mistagging of the background also
 3043 decreases with pileup for the same selection, yielding similar discrimination. Efficiency and
 3044 mistagging rate are affected by pileup in the same way, since additional pileup shifts the τ_{21}

3045 distribution towards higher values (towards background like) for both signal and background
 3046 (Fig. 7.2). Therefore, the same signal efficiency can be reached at the same background
 3047 rejection rate for up to 30 reconstructed vertices by merely adjusting the τ_{21} selection.

3048 An important factor that influences the V tagging performance is the polarization of the
 3049 reconstructed V bosons. In fact, the pruned jet mass selection is less efficient for transversely
 3050 polarized (V_T) V bosons. This can be explained by a higher asymmetry in the p_T of the two
 3051 quarks from the V_T boson decay, such that the pruning algorithm in a considerable fraction
 3052 of events rejects the particles from the lower p_T quark and yields a much lower jet mass.
 3053 In addition, the ΔR separation between the partons for pure longitudinally polarized (V_L)
 3054 V bosons is smaller on average than for V_T bosons and is more likely to be accepted by a
 3055 large-cone jet. In the analysis presented in this work only V_L bosons are considered.
 3056

3057 This analysis relies on the modelling of the jet substructure variables m_{jet} and τ_{21} in
 3058 simulation. The data/simulation discrepancies in m_{jet} and τ_{21} can bias the signal efficiency
 3059 estimated from simulated samples. Therefore, the modelling of signal efficiency is cross-
 3060 checked in a signal-free sample with jets having characteristics that are similar to those
 3061 expected for a genuine signal [138]. A pure sample of high- p_T W bosons, that decay to quarks
 3062 and are reconstructed as a single jet, is obtained selecting $t\bar{t}$ and single top quark events.
 3063 Scale factors for the τ_{21} selection efficiency are extracted by estimating the selection efficiency
 3064 on both data and simulation for the pure W jet signal. This is achieved by subtracting the
 3065 background contribution. The generated W boson in the $t\bar{t}$ simulation provides a model
 3066 of the contribution from the W jet peak in the pruned jet mass. The contribution from
 3067 combinatorial background is derived from $t\bar{t}$ simulation as well. This signal plus background
 3068 model is fitted directly in the distributions of data and in their simulation.

3069 The pruned jet mass distribution of events that pass and fail the τ_{21} selection are fitted
 3070 simultaneously to extract the selection efficiency on the pure W jet component. The ratio of
 3071 data and simulation efficiencies are taken as the scale factor to correct the efficiency of the
 3072 τ_{21} selection. Figure 7.3 shows the fits obtained with 13 TeV data for the $\tau_{21} < 0.6$ selection.
 3073 The extracted scale factor is 1.01 ± 0.03 and it is used in the $\ell\nu q\bar{q}$ analysis to correct the
 3074 total signal efficiency and the VV background normalization predicted by the simulation.
 3075 The quoted uncertainty includes two systematic effects. One comes from the modelling of the
 3076 nearby jets and p_T spectrum in $t\bar{t}$ MC events, obtained by comparing the selection efficiency
 3077 estimated from LO and NLO $t\bar{t}$ simulation. The other is due to the choice of the models
 3078 used to fit signal and background. The quadratic sum of these systematic uncertainties is
 3079 found to be smaller than half of the statistical uncertainty on the scale factor. An additional
 3080 uncertainty is calculated to account for the extrapolation of the scale factor from $t\bar{t}$ events
 3081 with an average jet $p_T \sim 200$ GeV to higher momenta. This is estimated from the difference
 3082 between PYTHIA8 and HERWIG++ [139] showering models resulting in an uncertainty of
 3083 $4.53\% \times \ln(p_T/200\text{ GeV})$.

3084 The peak position in the W jet mass and its resolution are also extracted to obtain
 3085 data-to-simulation corrections on the pruned jet mass listed in Table 7.2, as obtained from
 3086 13 TeV data and simulation. The quoted uncertainties are statistical. The W jet mass scale
 3087 in data is $\approx 1\%$ smaller than in simulation while its resolution is found to be larger by about
 3088 5%. In the simulation m_{jet} must therefore be shifted and smeared by the above quantities to
 3089 correct for the difference between data and simulation.

3090 The mass peak position is slightly shifted relative to the W boson mass. The shift is found
 3091 to be primarily due to extra radiation in the W jet from the nearby b quark, and additional
 3092 effects are due to the presence of the extra energy deposited in the jet cone from pileup, un-
 3093 derlying event, and initial-state radiation not completely removed in the jet pruning procedure.

3094

Because the kinematic properties of W jets and Z jets are very similar, the same corrections are also used when the V jet is assumed to arise from a Z boson.

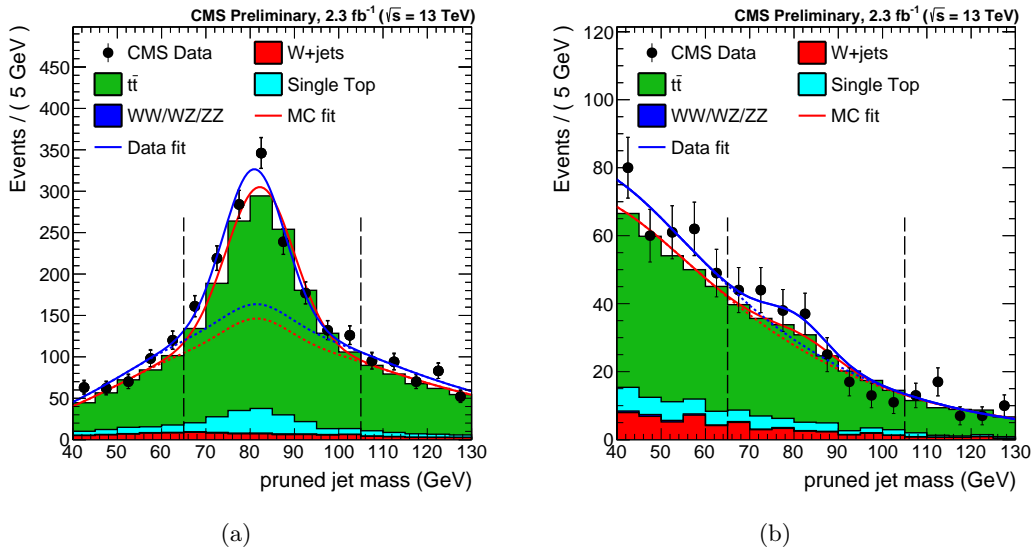


Figure 7.3: Distribution in pruned jet mass for events that (a) pass and (b) fail the $\tau_{21} < 0.6$ selection in the $t\bar{t}$ control sample. The results of the fits to data and simulation are indicated, respectively, by the solid and long-dashed line. The background components of the fit are shown as dashed-dotted and short-dashed lines.

Table 7.2: W jet mass peak position and resolution, as extracted from top quark enriched sample in 13 TeV data and from simulation [114].

	m_{jet} [GeV]	Standard deviation [GeV]
Data	84.1 ± 0.4	8.4 ± 0.6
Simulation	82.7 ± 0.3	7.6 ± 0.4

3097 7.3 The H tagging algorithm

As discussed in the previous sections boosted V bosons are reconstructed using jet substructure methods through the V tagging algorithm, providing large discrimination against multijet backgrounds. However, if one or more of the decay products is a b quark, adding b jet identification (Section 6.4) along with jet substructure information can significantly improve the sensitivity of these methods.

Two different approaches to identify boosted $H \rightarrow b\bar{b}$ candidates have been explored and used at CMS [126]:

- application of b tagging to the fat jet (“fat jet b tagging”)
 - application of b tagging to the subjets reconstructed within the fat jet (“subjets b tagging”)

Both approaches are based on the standard b tagging algorithms which take advantage of the tracking and vertexing information and are designed to identify jets from single b quarks.

As described in Section 6.4, the b tagging procedure starts with an association of tracks to jets, based on the angular distance between the tracks and the jet axis. The default b tagging algorithms use the selection $\Delta R < 0.3$. However, when applying this to a large-cone jet of size $R = 0.8$, the criteria is suboptimal. Hence, to apply b tagging to fat jets, this angular distance is enlarged to $\Delta R < 0.8$. For the application of b tagging to subjets, the angular distance remains at the default value of $\Delta R < 0.3$.

3116

The H tagging technique starts requiring that the pruned jet mass of the H jet candidate lies in a window around the Higgs boson mass (Fig. 7.1(b)), as this requirement rejects a large fraction of QCD background as demonstrated in the previous sections. The subjets are then obtained by reversing the last step of the pruning recombination algorithm described in Section 7.1.1. In addition to the jet mass requirement, the b tagging is applied either to the whole fat jet or to the two subjets, where both subjets are required to pass the same selection on the CSV discriminator. The b tagging efficiency and misidentification probability of QCD jets after applying the selection $75 < m_{\text{jet}} < 135 \text{ GeV}$ are shown in Fig. 7.4. The subjet b tagging outperforms the fat jet tagging for most of the phase space.

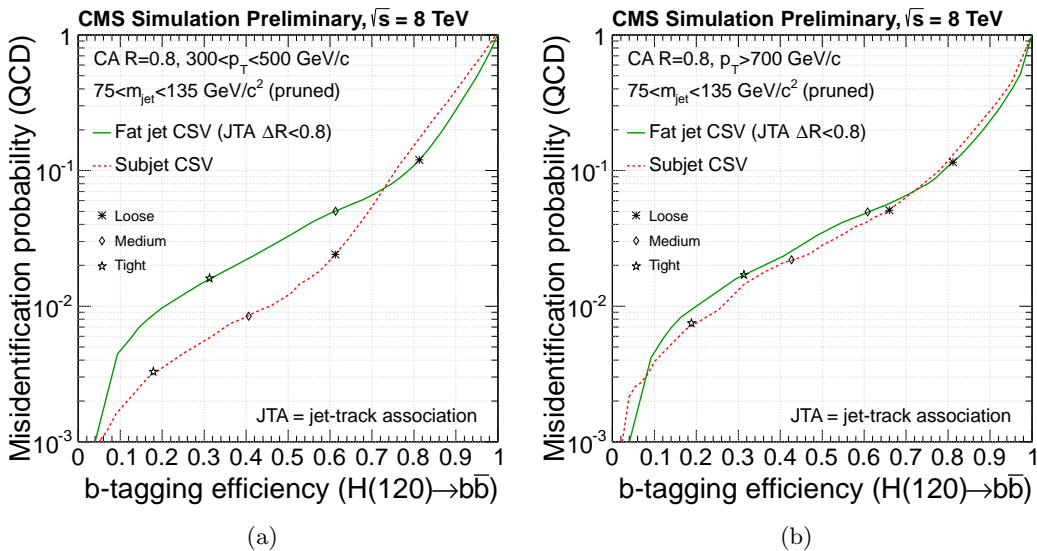


Figure 7.4: Misidentification probability as a function of b tagging efficiency for boosted $H \rightarrow b\bar{b}$ jets and inclusive QCD jets for the CSV algorithm applied to CA8 jets and pruned subjets for jets with (a) $300 < p_T < 500 \text{ GeV}/c$ and (b) $p_T > 700 \text{ GeV}/c$. Loose, medium, and tight operating points of the CSV discriminator are indicated [126].

The H tagging efficiency obtained combining the requirement on the pruned jet mass ($75 < m_{\text{jet}} < 135 \text{ GeV}$) and the subjet b tagging at the CSVL operating point is between 40 and 50% for a H jet p_T range spanning from 300 GeV to 1 TeV, with a suppression of QCD background to about 0.4%.

3130

The use of a fixed-size jet-track association cone inevitably leads to track sharing between the subjets of the jets once their angular separation becomes comparable or smaller than the size of the association cone. For boosted H jets the fraction of shared tracks, defined as the ratio of the number of tracks within $\Delta R < 0.3$ from more than one subjet and the number of all tracks within $\Delta R < 0.3$ from any of the subjets, ranges from a few percent at a jet p_T of 400 GeV and increases to 40% at a jet p_T of 700 GeV and to 80% at a jet p_T of

3137 1 TeV. Because of track sharing, the b tagging probabilities for individual subjets deteriorate
 3138 at large jet p_T and the subjet b tagging performance approach the fat jet b tagging one as
 3139 can be seen in Fig. 7.4. The loss in efficiency is then recovered applying the two approaches
 3140 depending on the ΔR between the two subjets. In particular, the analysis involving boosted
 3141 Higgs bosons such as the one presented in this work apply subjet b tagging and fat jet b
 3142 tagging if $\Delta R > 0.3$ and < 0.3 , respectively. The distribution of the angular separation ΔR
 3143 of the two subjets reconstructed within the fat jet for different jet p_T ranges in simulated
 3144 events of highly boosted Higgs bosons decaying to $b\bar{b}$, is shown in Fig. 7.5.

3145 In this analysis a requirement on the pruned jet mass of the reconstructed H jet candidate
 3146 given by $110 < m_{\text{jet}} < 135$ GeV is applied. The m_{jet} window is chosen such that a contamina-
 3147 tion from possible signals with boosted V jets in the Higgs boson mass region is minimized.
 3148 The b tagging is performed with the algorithm described above using the loose working point
 3149 of the CSV discriminant. The total H tagging efficiency for these selections is about 35% for
 3150 jet p_T of about 1 TeV with a mistagging probability below 1%.

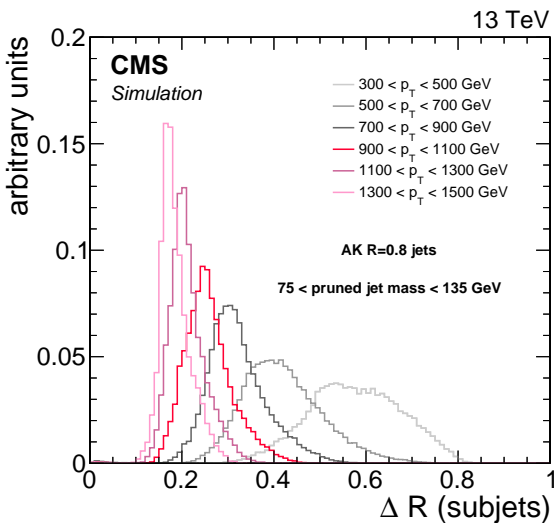


Figure 7.5: Distributions of the angular separation ΔR of the two subjets reconstructed within the fat jet for simulated events of highly boosted Higgs bosons decaying to $b\bar{b}$. The distributions are compared for different ranges of the H jet p_T .

3151 The validation of b tagging in boosted H jets is performed selecting events containing jets
 3152 from gluon splitting to $b\bar{b}$ ($g \rightarrow b\bar{b}$) in which the b quarks hadronize inside the fat jet [126].
 3153 To enrich a sample of fat jets in $g \rightarrow b\bar{b}$ component, used as an analogue of boosted $H \rightarrow b\bar{b}$
 3154 jets, the fat jets are required to be double-muon-tagged with both subjets matched to distinct
 3155 muon candidates within a cone of size $\Delta R < 0.4$. This sample is used to study the modelling
 3156 of b tagging efficiencies in boosted $H \rightarrow b\bar{b}$ topologies. The scale factors, given by the ratio
 3157 between the efficiencies measured in data and simulation, are found to be in good agreement
 3158 with those measured in the standard, non-boosted topologies, indicating that the simulation
 3159 reproduces the b tagging performance in boosted and non-boosted environments equally well.
 3160 These scale factors are used in the analysis to reweight the simulated events.

3161 The discrepancy between data and simulation in the m_{jet} distribution for V jets is well
 3162 estimated using the pure sample of merged W jets provided by lepton+jet $t\bar{t}$ events as
 3163 described in the previous section (Table 7.2). On the contrary, a pure source of high- p_T H
 3164 bosons is not available to validate the H mass tagging selection. An uncertainty in the m_{jet}
 3165 selection for H jets is therefore assigned by evaluating the discrepancies between different

3166 showering algorithms in handling hadronically decaying W and H bosons. In particular, the
3167 different m_{jet} windows for W and H jets are applied, and the ratios R_{PYTHIA} and R_{HERWIG} of
3168 the corresponding efficiencies calculated for the PYTHIA and HERWIG showering algorithms,
3169 respectively. The double ratio $R_{\text{PYTHIA}}/R_{\text{HERWIG}}$ provides the required uncertainty and it is
3170 estimated to be 2.6%.

Analysis strategy

3171

3172

3173

3174 This chapter describes in details the strategy followed in this search, that starting from the
 3175 physics objects and identification algorithms described in the previous chapters, leads to
 3176 the final results of the analysis. Although preliminary selections on the objects expected in
 3177 the final state have already been discussed, tighter requirements and a categorization of the
 3178 events are applied as described in Section 8.1 to maximize the analysis sensitivity to the
 3179 signals under study. The final discriminating observable used to search for the signal is the
 3180 invariant mass of the diboson system. In fact, a possible signal would appear as a localized
 3181 excess of data on the top of a smooth background. An accurate description of the expected
 3182 background and signal distributions is therefore fundamental. A background estimation
 3183 method for the main W+jets component, which makes use of data in sideband regions is used
 3184 and described in Section 8.2. Another important source of background is represented by top
 3185 quark production, which is estimated from data in a dedicated control region as discussed in
 3186 Section 8.3. The background model together with the signal model presented in Section 8.4
 3187 is used to perform a maximum likelihood fit of the data in the statistical analysis. The
 3188 systematic uncertainties in the signal and background predictions discussed in Section 8.5 are
 3189 treated as nuisance parameters in the statistical interpretation. Finally, Section 8.6 describes
 3190 the standard procedure for the statistical test of the new signal hypothesis commonly used
 3191 by LHC experiments and originally employed for the Higgs boson search. The final results
 3192 are presented in the next chapters.

3193 8.1 Event selection and categorization

3194 Events are selected online with triggers requiring either one muon or electron (Sections 6.2.2
 3195 and 6.3.2). Several requirements are then applied offline to the selected events to enhance
 3196 the analysis sensitivity as described in the following.

3197

3198 The two analyses described in this work feature the same selection strategy on the leptonic
 3199 part of the final state. Both analyses require exactly one muon or one electron satisfying
 3200 certain p_T and η requirements and passing the high- p_T lepton identification criteria described
 3201 in Sections 6.3.3 and 6.2.3. As summarized in Tables 8.1 and 8.2, the only difference is in the
 3202 p_T threshold of the lepton which is higher for the 13 TeV data analysis to match the increase
 3203 in the trigger threshold. The offline reconstructed p_T of the electron must be greater than
 3204 90 (120) GeV for the 8 (13) TeV data analysis, where the trigger reaches the plateau. This
 3205 is required in order to avoid any bias on the distributions due to the turn-on of the trigger
 3206 efficiency curve and its description in simulation. Reconstructed electrons must have $|\eta| < 2.5$
 3207 and also be located outside of the overlap region between the ECAL barrel and endcaps,
 3208 because the reconstruction of an electron object in this region is not optimal. In a similar
 3209 way, the offline reconstructed p_T of the muon must be greater than 50 (53) GeV for the 8
 3210 (13) TeV analysis, and within $|\eta| < 2.1$ as a consequence of the trigger criteria. Events with
 3211 additional well-identified muons and/or electrons are rejected to avoid contamination from
 3212 events containing $Z \rightarrow \ell\ell$ decays.

3213

Table 8.1: Summary of the final selection for the 8 TeV data analysis in the $\ell\nu b\bar{b}$ final state.

Selection	Value
Lepton selection	
Electron	$p_T > 90 \text{ GeV}$ $ \eta < 2.5$ except [1.44, 1.57] range
Muon	$p_T > 50 \text{ GeV}$ $ \eta < 2.1$
AK5 jet selections	
Jet p_T	$p_T > 30 \text{ GeV}$
Jet η	$ \eta < 2.4$
E_T^{miss} selections	
E_T^{miss} (electron channel)	$E_T^{\text{miss}} > 80 \text{ GeV}$
E_T^{miss} (muon channel)	$E_T^{\text{miss}} > 40 \text{ GeV}$
Boson selections	
$W \rightarrow \ell\nu$	$p_T > 200 \text{ GeV}$
$H \rightarrow b\bar{b}$ (CA8 jet)	$p_T > 200 \text{ GeV}$ $ \eta < 2.4$ except [1.0, 1.8] range
Back-to-back topology	$\Delta R(\ell, H_{b\bar{b}}) > \pi/2$ $\Delta\phi(H_{b\bar{b}}, p_T^{\text{miss}}) > 2$ $\Delta\phi(H_{b\bar{b}}, W_{\ell\nu}) > 2$
Diboson invariant mass	$m_{WH} > 0.7 \text{ TeV}$
H tagging selections	
Pruned jet mass	$110 < m_{\text{jet}} < 135 \text{ GeV}$
Combined b-tagging cut	2 CSVL b-tagged subjets if $\Delta R(\text{subjets}) > 0.3$ 1 CSVL b-tagged CA8 jet if $\Delta R(\text{subjets})$
$t\bar{t}$ rejection	
B-tag veto	no CSVM b-tagged AK5 jet within $\Delta R(H_{b\bar{b}}, AK5) = 0.8$
Top quark mass veto	$m_{\text{top}}^l < 120 \parallel m_{\text{top}}^l > 240$ $m_{\text{top}}^h < 160 \parallel m_{\text{top}}^h > 280$

3214 The requirements $E_T^{\text{miss}} > 40$ and $> 80 \text{ GeV}$ are applied, respectively, in the muon and
 3215 electron channels. The threshold is higher in the electron channel to further suppress the larger
 3216 background from multijet processes expected at low values of E_T^{miss} due to jets misidentified
 3217 as electrons. This background is expected to be negligible in the muon channel, for which a
 3218 lower E_T^{miss} threshold can be used to preserve a higher efficiency for a low-mass signal. The
 3219 identified lepton and the E_T^{miss} are used to reconstruct the $W \rightarrow \ell\nu$ candidate as described in
 3220 Section 6.6, which is required to have $p_T > 200 \text{ GeV}$.

3221 A different strategy is instead used in the two analyses, for the hadronic part of the final
 3222 state. As described in Section 6.4, the CA8 and AK8 algorithms are used to reconstruct
 3223 the H and V jet candidates in the 8 and 13 TeV analysis, respectively. In both cases the jet
 3224 is required to have $p_T > 200 \text{ GeV}$ and $|\eta| < 2.4$. For CA8 jets, the pseudorapidity region
 3225 $1.0 < |\eta| < 1.8$ is excluded corresponding to the barrel-endcap transition region of the silicon
 3226 tracker where the reconstruction of tracks is not optimal (Section 6.4.2). The probability of
 3227 signal events with jets outside this region is 80% (92%) for a resonance mass of 1.0 (2.5) TeV.
 3228 The 8 TeV analysis aims at isolating events with a high- p_T Higgs boson decaying to $b\bar{b}$

3229

Table 8.2: Summary of the final selection for the 13 TeV data analysis in the $\ell\nu q\bar{q}$ final state.

Selection	Value
Lepton selection	
Electron	$p_T > 120 \text{ GeV}$ $ \eta < 2.5$ except $[1.44, 1.57]$ range
Muon	$p_T > 53 \text{ GeV}$ $ \eta < 2.1$
AK4 jet selections	
Jet p_T	$p_T > 30 \text{ GeV}$
Jet η	$ \eta < 2.4$
E_T^{miss} selections	
E_T^{miss} (electron channel)	$E_T^{\text{miss}} > 80 \text{ GeV}$
E_T^{miss} (muon channel)	$E_T^{\text{miss}} > 40 \text{ GeV}$
Boson selections	
$W \rightarrow \ell\nu$	$p_T > 200 \text{ GeV}$
$V \rightarrow q\bar{q}$ (AK8 jet)	$p_T > 200 \text{ GeV}$ $ \eta < 2.4$
Back-to-back topology	$\Delta R(\ell, V_{q\bar{q}}) > \pi/2$ $\Delta\phi(V_{q\bar{q}}, \vec{p}_T^{\text{miss}}) > 2$ $\Delta\phi(V_{q\bar{q}}, W_{\ell\nu}) > 2$
Diboson invariant mass	$m_{WW} > 0.7 \text{ TeV}$
V tagging selections	
Pruned jet mass	$65 < m_{\text{jet}} < 105 \text{ GeV}$
2- to 1-subjettiness ratio	$\tau_{21} < 0.6$
m_{jet} categories	
WW-enriched	$65 < m_{\text{jet}} < 85 \text{ GeV}$
WZ-enriched	$85 < m_{\text{jet}} < 105 \text{ GeV}$
$t\bar{t}$ rejection	
B-tag veto	no CSVM b-tagged AK5 jet within $\Delta R(V_{q\bar{q}}, AK5) = 0.8$

and the H tagging algorithm described in Section 7.3 is applied. The H tagging requires the selected CA8 jet to have pruned mass in the range $110 < m_{\text{jet}} < 135 \text{ GeV}$. Furthermore, the subjets are required to be b-tagged with the CSVL algorithm if their angular distance $\Delta R < 0.3$. Otherwise, b tagging is applied to the whole CA8 jet using the same algorithm.

The 13 TeV analysis is instead focused on events with a high- p_T V boson decaying to $q\bar{q}$ and the V tagging algorithm described in Section 7.3 is applied in this case. The pruned jet mass window is shifted down to the V boson mass, requiring the selected AK8 jet to have pruned mass in the range $65 < m_{\text{jet}} < 105 \text{ GeV}$. Furthermore, the V jet is required to have $\tau_{21} < 0.6$. Finally, the V jet is deemed a W-boson candidate if its pruned mass falls in the range 65–85 GeV, while it is deemed a Z-boson candidate if it falls in the range 85–105 GeV instead. This categorization has been added on the top of the V tagging requirements on the m_{jet} to enhance discrimination between resonances with different charge and spin. Indeed, the first category, referred to as “WW-enriched”, has a higher sensitivity for resonances such as the neutral spin-2 graviton or the neutral spin-1 Z' decaying to WW, where a W jet is expected. The second category, referred to as “WZ-enriched”, is instead optimized for resonances such as the charged spin-1 W' decaying to WZ, where a Z jet is expected.

3246

In addition, there are specific topological selection criteria chosen for both the analyses. It is required that the two V bosons from the decay of a massive resonance are approximately back-to-back: the ΔR between the lepton and the signal jet is greater than $\pi/2$; the $\Delta\phi$ between the vector \vec{p}_T^{miss} and the signal jet, as well as between the $W \rightarrow \ell\nu$ and signal jet candidates, are both greater than 2 radians.

To reduce the level of the $t\bar{t}$ background, events with one or more reconstructed AK5 (or AK4) jets, not overlapping with the signal jet candidate are analyzed: if one or more of these jets is b-tagged with the CSV algorithm, the event is rejected. For the 8 TeV analysis additional selections are applied to further reduce contamination from $t\bar{t}$ background. In fact, the b tagging requirements in this analysis enhance the contribution from top quark production where real b jets are present. A leptonically decaying top quark candidate mass m_{top}^l is reconstructed from the lepton, E_T^{miss} , and the closest AK5 jet to the lepton using the method described in Section 6.6. A hadronically decaying top quark candidate mass m_{top}^h is also reconstructed, from the H jet candidate and the closest AK5 jet. Events with $120 < m_{\text{top}}^l < 240$ GeV or $160 < m_{\text{top}}^h < 280$ GeV are rejected. The chosen windows around the top quark mass are the result of an optimization carried out in this analysis, taking into account the asymmetric tails at larger values due to combinatorial background.

3264

According to the above description of the final selections, the event categorization is based on 2 orthogonal classes of events for the 8 TeV data analysis in the $\ell\nu b\bar{b}$ final state, depending on the lepton flavour (muon or electron), and on 4 orthogonal classes of events for the 13 TeV data analysis in the $\ell\nu q\bar{q}$ final state, depending on the lepton flavour and on the pruned jet mass category (WW or WZ).

The two boson candidates are combined into a diboson candidate, with presence of signal then inferred from the observation of localized excesses in the $m_{\ell\nu+\text{jet}}$ distribution. When several diboson resonance candidates are present in the same event, only the one with the highest p_T V or H jet is kept for further analysis.

The reconstructed invariant mass of the resonance is required to be at least 0.7 TeV.

3275

The distributions in p_T and N-subjettiness ratio τ_{21} distributions for the V jet candidate in the $\ell\nu q\bar{q}$ channel is shown in Fig. 8.1, after requiring $65 < m_{\text{jet}} < 105$ GeV, for both simulation and 13 TeV data. Figure 8.2 shows the distribution in p_T for the H jet candidate after requiring $40 < m_{\text{jet}} < 110$ GeV, for both simulation and 8 TeV data.

3280 8.2 W+jets background estimate with α ratio method

3281 The $m_{\ell\nu+\text{jet}}$ distribution observed in data is dominated by SM background processes where
 3282 single quark or gluon jets are falsely identified as W or H jets. The dominant process
 3283 is inclusive W boson production. Since both normalization and shape discrepancies are
 3284 visible between data and simulation (Figures 8.1 and 8.2), a data driven method has been
 3285 developed to estimate this background component, as described in the following. Sub-dominant
 3286 backgrounds include $t\bar{t}$, single top quark, and non resonant diboson SM production, which are
 3287 estimated from simulation, after applying correction factors for residual data-to-simulation
 3288 disagreement measured in control samples selected in data.

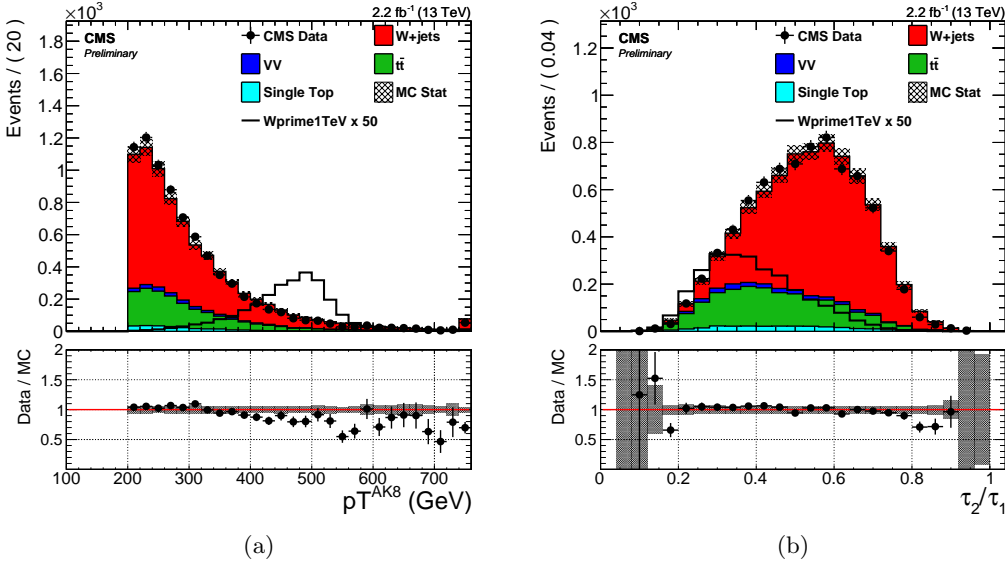


Figure 8.1: Distributions in p_T (a) and N-subjettiness ratio τ_{21} (b) for the V jet candidate obtained requiring $65 < m_{jet} < 105$ GeV after merging muon and electron channels. The SM diboson, $t\bar{t}$, and single top quark backgrounds are taken from simulation and are normalized to the integrated luminosity of the 13 TeV data sample. The $W+jets$ background is rescaled to match the number of events in data.

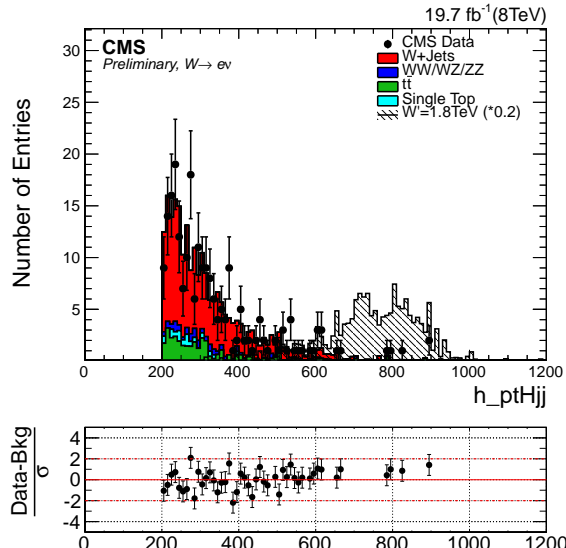


Figure 8.2: Distributions in p_T for the H jet candidate obtained requiring $40 < m_{jet} < 110$ GeV for events in the muon channel. The SM diboson, $t\bar{t}$, and single top quark backgrounds are taken from simulation and are normalized to the integrated luminosity of the 8 TeV data sample. The $W+jets$ background is rescaled to match the number of events in data.

3289 8.2.1 Background estimation procedure

3290 The $W+jets$ background is estimated through the so called α *ratio* method. This method
 3291 assumes that the correlation between m_{jet} and $m_{\ell\nu+jet}$ for the dominant $W+jets$ background
 3292 can be adequately modelled by simulation. A signal-depleted control region (sideband) is
 3293 defined by requiring the mass of the V or H jet to lie below or above the nominal selection;

the $m_{\ell\nu+\text{jet}}$ distribution observed in this region is then extrapolated to the nominal region through a transfer function estimated from simulation. Other minor sources of background, such as $t\bar{t}$, single top quark, and SM diboson production, are estimated using simulated events after applying correction factors based on control regions in data, as described in Sections 7.2 and 8.3. The sideband region is defined around the jet mass window that represents the analysis signal region (Section 8.1). The lower and upper sidebands for the two analyses are summarized in Table 8.3. For the 13 TeV analysis a “gap” is introduced between the signal region and the upper sideband, since the range defined by $105 < m_{\text{jet}} < 135$ might include contribution from signals with highly Lorentz-boosted Higgs bosons in the final state. Since these types of searches at 13 TeV [140] have been performed simultaneously with the one described in this work, this region has been discarded to avoid introducing a bias in the shape and normalization extrapolation due to a possible signal. On the other hand, the lower sideband of the 8 TeV $\ell\nu b\bar{b}$ analysis includes the region where signals from highly Lorentz-boosted V bosons might occur. In fact, this analysis has been performed after the search for WV resonances in the semi-leptonic final state at 8 TeV disclosed the signal region, where no deviation from the predicted SM background have been observed [135].

Table 8.3: Sideband regions used in the two analyses to estimate the contribution from the main W+jets background.

m_{jet} sideband	final state	
	$\ell\nu b\bar{b}$	$\ell\nu q\bar{q}$
Low sideband (LSB)	40–110 GeV	40–65 GeV
High sideband (HSB)	135–150 GeV	135–150 GeV

8.2.2 Extraction of the W+jets normalization

The overall normalization of the W+jets background in the signal region is determined from a fit to the m_{jet} distribution in the lower and upper sidebands of the data. The analytical form of the fitting function is chosen from simulation studies, as are the contributions from minor backgrounds. A summary of the empirical functional forms used to parametrize each background contribution are listed in Table 8.4, and defined as follows:

$$\begin{aligned}
 F_{\text{Exp}}(x) &= e^{cx} \\
 F_{\text{ErfExp}}(x) &= e^{cx} \cdot \frac{1 + \text{Erf}((x - a)/b)}{2} \\
 F_{\text{ExpGaus}}(x) &= c_0 \cdot e^{cx} + c_1 \cdot \text{Gaus}(x, x_1, \sigma_1) \\
 F_{\text{4Gaus}}(x) &= c_1 \cdot \text{Gaus}(x, x_1, \sigma_1) + c_2 \cdot \text{Gaus}(x, x_2, \sigma_2) + c_3 \cdot \text{Gaus}(x, x_3, \sigma_3) + c_4 \cdot \text{Gaus}(x, x_4, \sigma_4) \\
 F_{\text{ErfExp2Gaus}}(x) &= e^{cx} \cdot \frac{1 + \text{Erf}((x - a)/b)}{2} + c_1 \cdot \text{Gaus}(x, x_1, \sigma_1) + c_2 \cdot \text{Gaus}(x, x_2, \sigma_2)
 \end{aligned} \tag{8.1}$$

Table 8.4: Summary of the empirical functional forms used to fit the m_{jet} spectra of each background component in the two analyses.

Final state	W+jets	$t\bar{t}$	single top quark	diboson
$\ell\nu b\bar{b}$	$F_{\text{ErfExp}}(x)$	$F_{\text{Exp}}(x)$	$F_{\text{Exp}}(x)$	$F_{\text{ExpGaus}}(x)$
$\ell\nu q\bar{q}$	$F_{\text{ErfExp}}(x)$	$F_{\text{ErfExp2Gaus}}(x)$	$F_{\text{ExpGaus}}(x)$	$F_{\text{4Gaus}}(x)$

Figure 8.3 shows the functional forms listed in Table 8.4 for the $\ell\nu q\bar{q}$ channel, after fitting the simulation data of each background component, demonstrating that the chosen functions well reproduce the expected m_{jet} spectra.

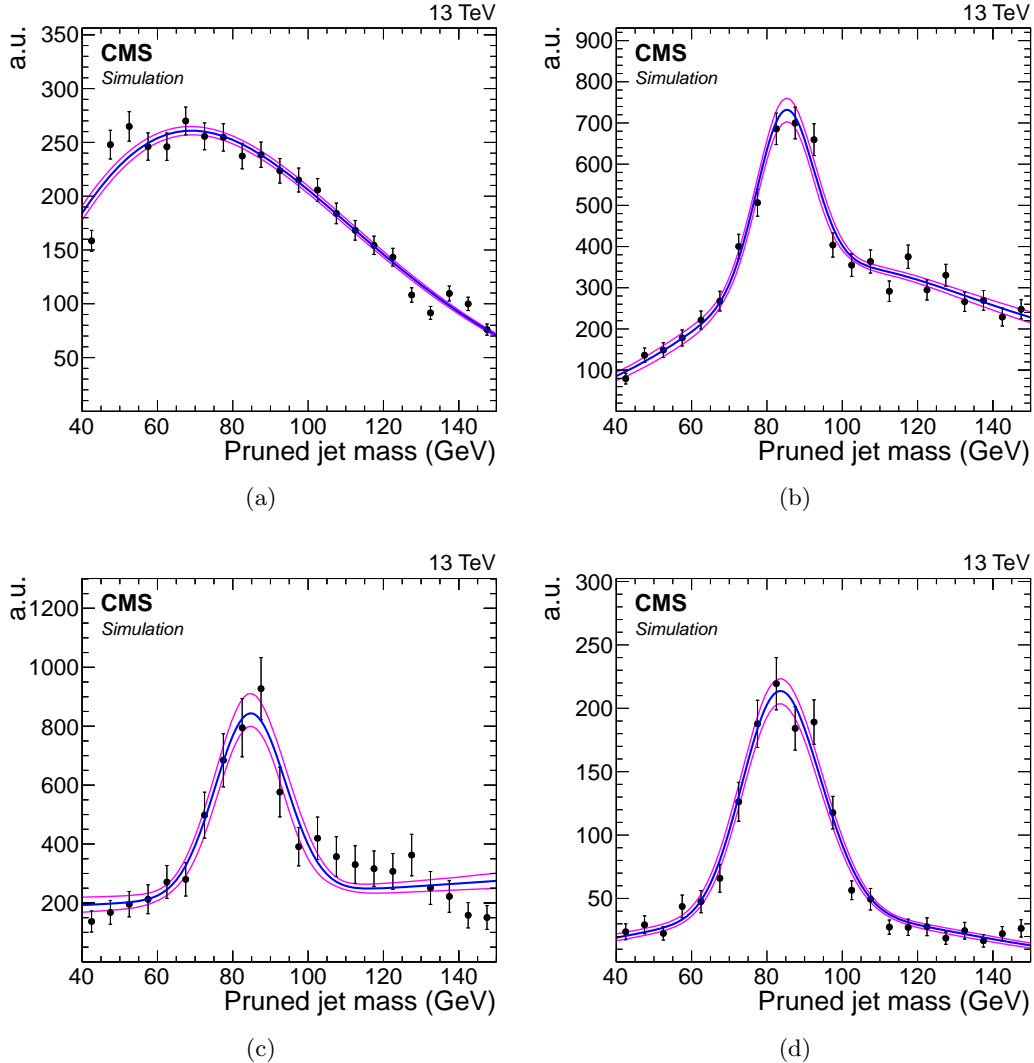


Figure 8.3: Functional forms describing the m_{jet} spectra for each background contribution after fitting the simulation data. (a) W+jets. (b) $t\bar{t}$. (c) Single top quark. (d) Diboson.

3319 The results of this fit procedure to extract the W+jets normalization are shown in Fig. 8.4
 3320 and 8.5 for the $\ell\nu b\bar{b}$ and the $\ell\nu q\bar{q}$ channel, respectively. The factors for correcting the
 3321 simulated W-peak position and resolution to represent the observed data, taken from the top
 3322 quark enriched control sample as described in Section 7.2, are included in the m_{jet} spectra of
 3323 Fig. 8.5.

3324 8.2.3 Extraction of the W+jets shape

3325
 3326 The form of the $m_{\ell\nu+\text{jet}}$ distribution for the W+jets background in the signal region
 3327 (SR) is determined from the lower m_{jet} sideband, through the transfer function $\alpha_{\text{MC}}(m_{\ell\nu+\text{jet}})$
 3328 obtained from the W+jets simulation, and defined as:

$$\alpha_{\text{MC}}(m_{\ell\nu+\text{jet}}) = \frac{F_{\text{MC},\text{SR}}^{\text{W+jets}}(m_{\ell\nu+\text{jet}})}{F_{\text{MC},\text{SB}}^{\text{W+jets}}(m_{\ell\nu+\text{jet}})}, \quad (8.2)$$

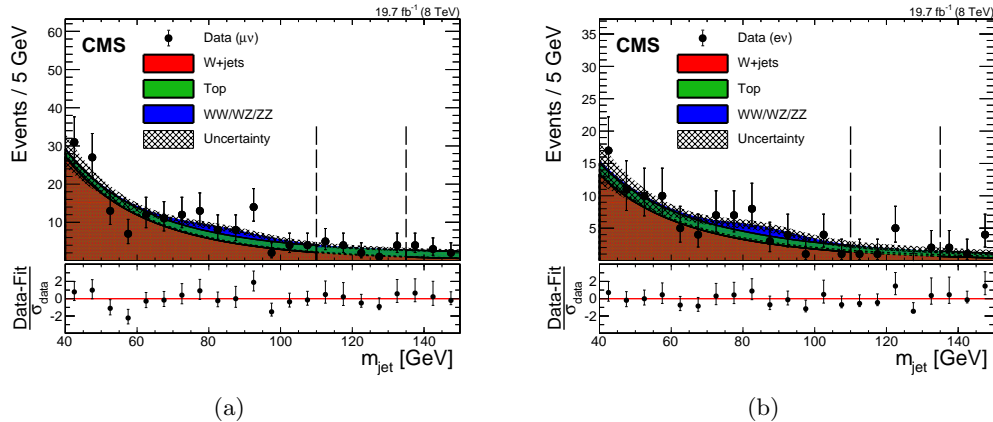


Figure 8.4: Distributions in pruned jet mass m_{jet} in the muon (a) and electron (b) channels for the $\ell\nu b\bar{b}$ analysis at 8 TeV. All selections are applied except the requirement on the m_{jet} signal window. The signal region lies between the dashed vertical lines. The hatched region indicates the statistical uncertainty of the fit. At the bottom of each plot, the bin-by-bin fit residuals, $(N_{\text{data}} - N_{\text{fit}})/\sigma_{\text{data}}$, are shown.

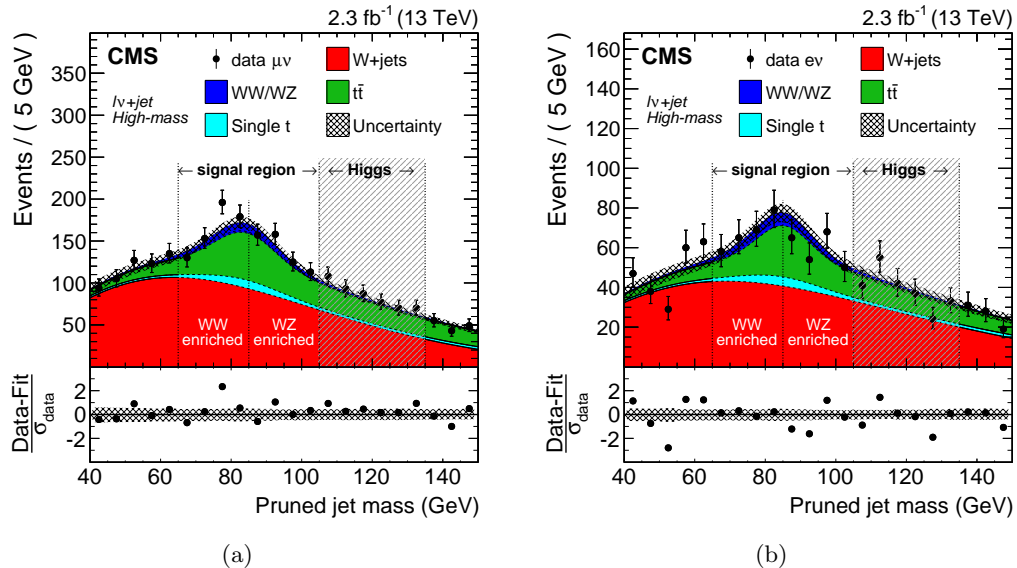


Figure 8.5: Distributions in pruned jet mass in the muon (a) and electron (b) channels for the $\ell\nu q\bar{q}$ analysis at 13 TeV. All selections are applied except the requirement on the m_{jet} signal window. The signal regions and m_{jet} categories of the analysis are indicated by the vertical dotted lines. The shaded m_{jet} region 105–135 GeV is not used in the analysis. At the bottom of each plot, the bin-by-bin fit residuals, $(N_{\text{data}} - N_{\text{fit}})/\sigma_{\text{data}}$, are shown together with the uncertainty band of the fit normalized by the statistical uncertainty of data, σ_{data} .

where $F_{\text{MC,SB}}^{\text{W+jets}}$ and $F_{\text{MC,SR}}^{\text{W+jets}}$ are the probability density functions used to describe the simulated $m_{\ell\nu+\text{jet}}$ spectrum in the lower m_{jet} sideband and signal region, respectively. The upper m_{jet} sideband is not considered since the W+jets shape is different here compared to what expected in the lower sideband. Furthermore, the upper sideband suffers from a larger $t\bar{t}$ background contamination.

Since the lower sideband region does not represent a perfectly pure sample of W+jets events in data, the presence of minor backgrounds is subtracted from the observed diboson

3336 invariant mass distribution to obtain an estimation of the W+jets contribution in the sideband
 3337 control region of the data, $F_{\text{data,SB}}^{\text{W+jets}}(m_{\ell\nu+\text{jet}})$.

3338 The $m_{\ell\nu+\text{jet}}$ range used in the estimate of the background distribution determines the
 3339 region of masses probed by these searches. This range is chosen to ensure a smoothly falling
 3340 background spectrum, and therefore far enough from the kinematic turn-on at low masses
 3341 generated by the acceptance selections, allowing for a good stability and a robust control of
 3342 the background estimation. For this reason the low edge of the range is chosen at 0.7 TeV
 3343 while the high edge is chosen such that it is not too far from the last value where data are
 3344 still present. Therefore, the fits are performed in the range $0.7 < m_{\ell\nu+\text{jet}} < 4$ TeV for the
 3345 13 TeV analysis, while at 8 TeV no data are present above $m_{\ell\nu+\text{jet}} \approx 3$ TeV and the chosen
 3346 range is therefore $0.7 < m_{\ell\nu+\text{jet}} < 3$ TeV.

3347 To describe the smoothly falling W+jets background distribution, a parametrization of
 3348 the form of a leveled exponential is adopted, defined as

$$F_{\text{ExpTail}}(x) = e^{-\frac{x}{a+bx}}. \quad (8.3)$$

3349 This functional form is found to adequately describe the simulation in both the signal
 3350 region and the low sideband as demonstrated in Fig. 8.6. Tests are performed with alternative
 3351 functional forms, and the background prediction is found to agree with the one of the default
 3352 function within the uncertainties. The minor background contributions are parametrized
 3353 with a simple exponential functional form, except for the diboson contribution for which the
 3354 $F_{\text{ExpTail}}(x)$ defined above is used.

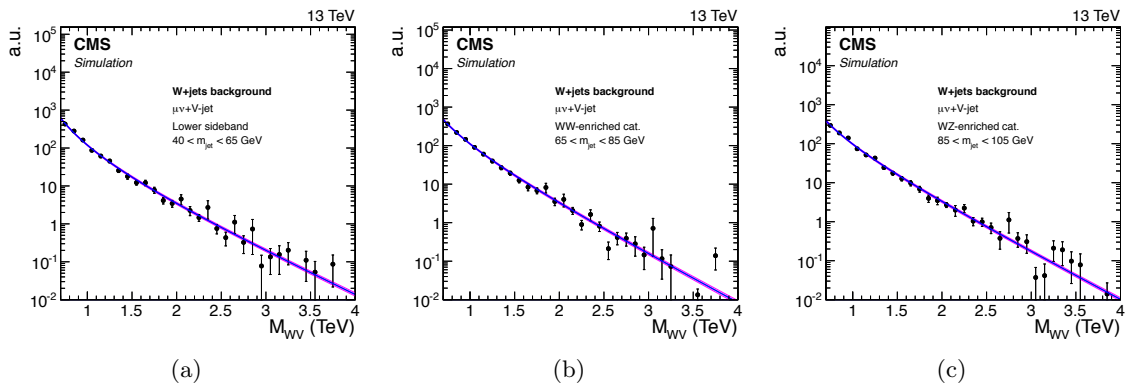


Figure 8.6: Functional form describing the diboson invariant mass spectrum of the W+jets background after fitting the simulation data. The distributions for the lower m_{jet} sideband (a), and the WW-enriched (b) and WZ-enriched (c) signal regions of the $\ell\nu q\bar{q}$ analysis are shown.

3355 For the $\ell\nu q\bar{q}$ analysis, the α_{MC} is computed independently for the two WW- and WZ-
 3356 enriched categories, which are therefore treated as two different signal regions. Figure 8.7
 3357 shows the α_{MC} for the two categories, obtained from a simultaneous fit of W+jets simulated
 3358 data in the lower sideband and in the signal region defined by the category using the
 3359 parametrization in Eq. 8.3. The blue and the red lines represent the probability density
 3360 functions describing the W+jets background with m_{jet} in the lower sideband and signal region,
 3361 respectively, and given by the leveled-exponential function of Eq. 8.3. A simultaneous fit is
 3362 performed of the two distributions, where the parameters used to model the distribution in
 3363 the signal region are correlated with the ones used to model the distribution in the sideband.
 3364 The transfer function α_{MC} is shown as a solid black line, while the dark (light) shaded
 3365 region corresponds to the 1σ (2σ) statistical uncertainty of the fit. These uncertainties only
 3366 represent the uncertainty in the modelling of the W+jets distribution. The bands have a

size of approximately zero around 2 TeV as the α_{MC} is the ratio of two probability density functions which have to cross in order to conserve the total probability. Similar results are obtained for the $\ell\nu b\bar{b}$ analysis.

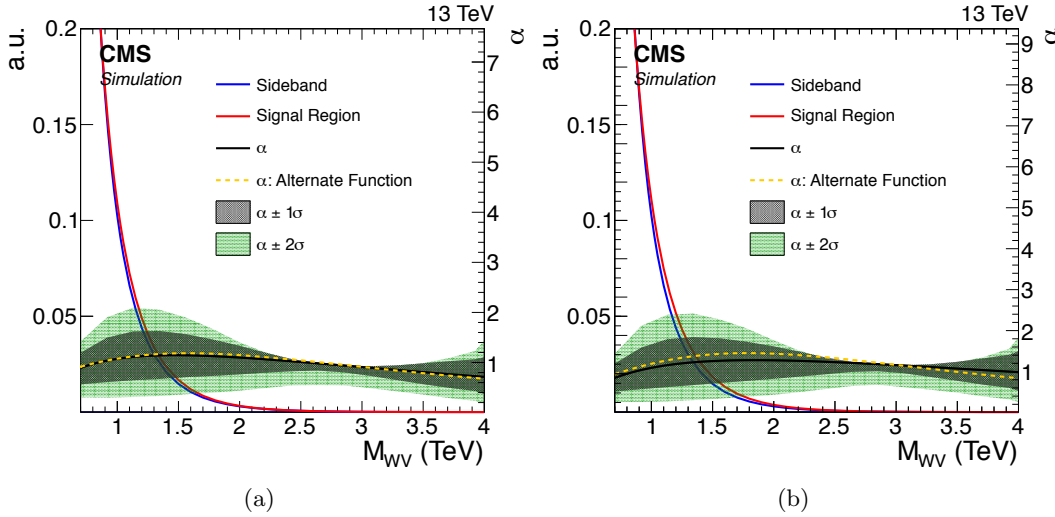


Figure 8.7: The transfer functions α_{MC} from the lower m_{jet} sideband to the signal region defined by the WW-enriched (a) and WZ-enriched (b) category of the $\ell\nu q\bar{q}$ analysis. The dark and light shaded areas represent the statistical uncertainty of the fit. The blue and the red lines represents the probability density functions describing the W+jets background with m_{jet} in the lower sideband and signal region, respectively. The α_{MC} obtained fitting the W+jets with and alternative function is shown as yellow line.

In Fig. 8.8, the result of the fit to the $m_{\ell\nu+jet}$ distribution of the data with m_{jet} in the lower sideband is shown for the electron and muon channels of the $\ell\nu q\bar{q}$ analysis. From this fit, an estimation of $F_{data,SB}^{W+jets}(m_{\ell\nu+jet})$ is obtained. Finally, the W+jets background distribution in the signal region is then extrapolated by rescaling $F_{data,SB}^{W+jets}$ by α_{MC} . The minor backgrounds are then added to the W+jets background to obtain the total SM prediction in the signal region, which is given by

$$N_{SR}^{bkg}(m_{\ell\nu+jet}) = N_{SR}^{W+jets} \times \alpha_{MC}(m_{\ell\nu+jet}) \times F_{data,SB}^{W+jets}(m_{\ell\nu+jet}) + \sum_k N_{SR}^k \times F_{MC,SR}^k(m_{\ell\nu+jet}). \quad (8.4)$$

In the above equation, the sum runs over the products of the normalization $N_{MC,SR}^k$ and probability density function $F_{MC,SR}^k$ of each minor background contribution k , while N_{SR}^{W+jets} and $F_{data,SB}^{W+jets}$ represent the normalization and probability density function of the W+jets background derived from data as described previously in this chapter. The transfer function α_{MC} accounts for small kinematic differences between the signal and the sideband regions.

Results of the final background extraction in the signal region will be presented in Chapters 9 and 10 or the $\ell\nu b\bar{b}$ and $\ell\nu q\bar{q}$ analysis, respectively.

8.2.4 Validation of the α method

To test the validity and the robustness of the data driven method used to estimate the W+jets contribution and described previously in this section, a closure test is performed. In this test, the background is extracted to a signal free control region that allows to check the compatibility with data for both the distribution and normalization. In order to achieve this,

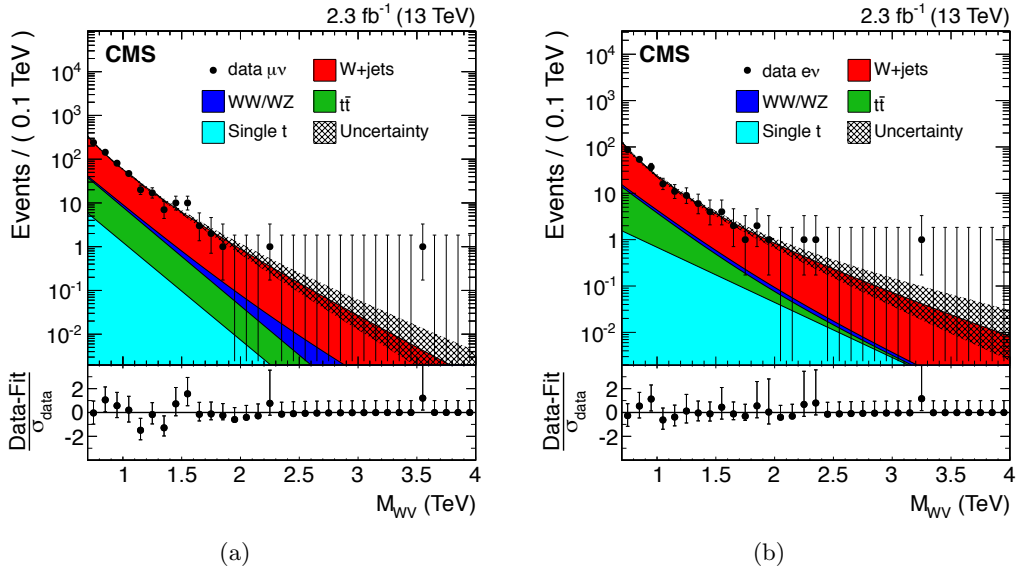


Figure 8.8: Results of the fit to the m_{WV} distribution of the data with m_{jet} in the lower sideband to estimate $F_{\text{data,SB}}^{\text{W+jets}}$ for both muon (a) and electron (b) channels of the $\ell\nu q\bar{q}$ analysis. Minor backgrounds are estimated from simulation, while the W+jets contribution is the result of the fit to the data.

3388 the low mass sideband defined in Table 8.3 is divided into two regions: $40 < m_{jet} < 55 \text{ GeV}$,
 3389 referred to as “region A”, is used as sideband, while $55 < m_{jet} < 65 \text{ GeV}$, referred to as
 3390 “region B”, is used as signal region. The W+jets background normalization is then predicted
 3391 in region B by performing a fit to the m_{jet} distribution of the data in region A and in the
 3392 upper sideband (Table 8.3), while its distribution in $m_{\ell\nu+jet}$ is extrapolated in region B with
 3393 a fit of the data in region A and a suitable transfer function α_{MC} . In this test, the α_{MC} is
 3394 defined as the ratio between the simulated W+jets background distributions in $m_{\ell\nu+jet}$ in
 3395 region B and A.

3396 An example of the result of this test is presented in the following for the muon channel in
 3397 the $\ell\nu q\bar{q}$ analysis.

3398 Figure 8.9(a) shows the transfer function α_{MC} obtained from a simultaneous fit of
 3399 W+jets simulated events in the region A and in the region B, using the leveled-exponential
 3400 parametrization defined in Eq. 8.3. In Fig. 8.9(b), the result of the fit to the $m_{\ell\nu+jet}$
 3401 distribution of the data with m_{jet} in the lower sideband is shown, where the W+jets shape is
 3402 modelled through the same leveled-exponential function.

3403 Finally, Fig. 8.10 shows a comparison between the total predicted background, obtained
 3404 through Eq. 8.4, and the data inside the signal free region B. A good agreement is found over
 3405 the whole $m_{\ell\nu+jet}$ range. The test has been performed for both lepton flavours for the $\ell\nu q\bar{q}$
 3406 analysis, as well as for the $\ell\nu b\bar{b}$ analysis where slightly different definitions for region A and
 3407 B are used. In all the cases, consistency between the predicted background and the data is
 3408 observed, thus validating the proposed strategy for the W+jets background estimation.

3409 8.3 Modelling of top quark production

3410 The backgrounds from $t\bar{t}$ and single top quark production in both analysis channels are esti-
 3411 mated from data-based correction factors in the normalization of the simulation. A top quark
 3412 enriched control sample is selected by applying all the analysis requirements except that the

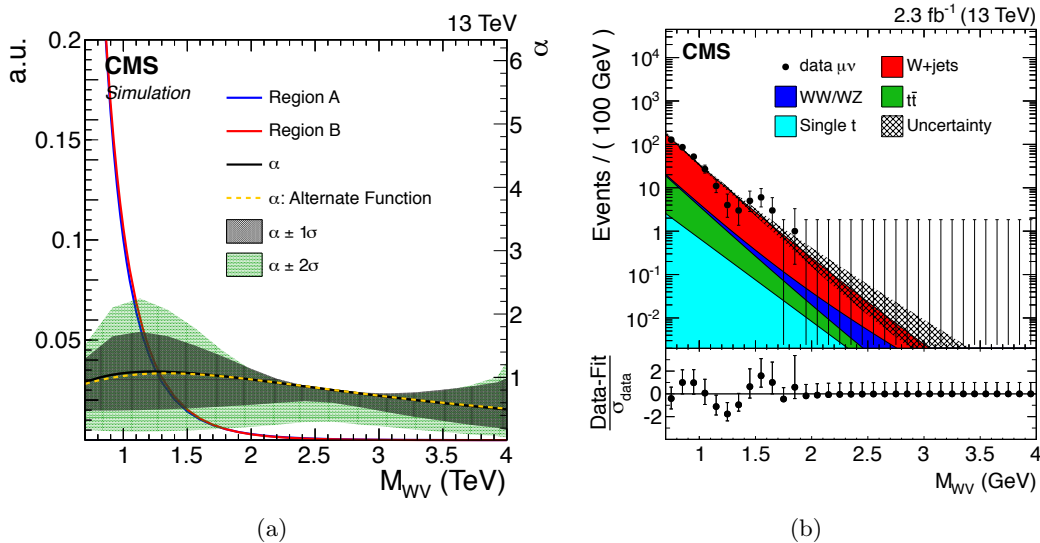


Figure 8.9: (a) The transfer function α_{MC} obtained by simultaneously fitting the diboson invariant mass distributions of simulation data inside the sideband (A) and signal region (B). (b) Diboson invariant mass distribution for events with $40 < m_{jet} < 55 \text{ GeV}$ (A). The W+jets shape is fitted, after subtracting contaminations from minor backgrounds, by means of a leveled-exponential function.

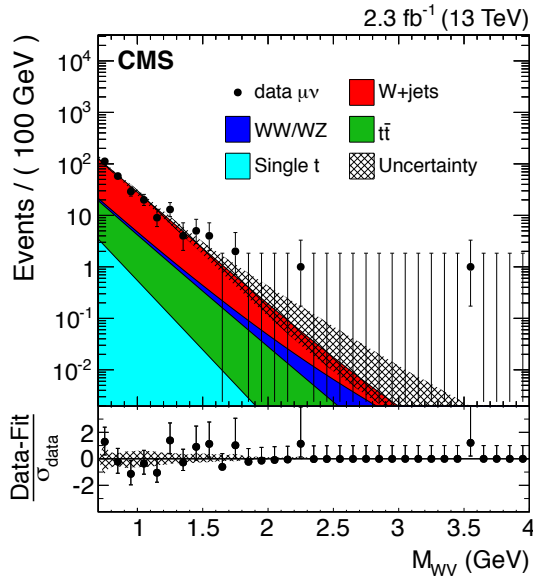


Figure 8.10: Distributions in diboson invariant mass for data and the expected backgrounds for events inside the pruned mass region defined by $55 < m_{jet} < 65 \text{ GeV}$ (B). The W+jets background distribution is extracted using events within $40 < m_{jet} < 55 \text{ GeV}$ (A).

3413 b jet veto is inverted by requiring, instead, at least one b-tagged AK4 (or AK5) jet in the event.

3414

3415 For the $\ell\nu q\bar{q}$ channel, the comparison between data and simulation yields normalization
 3416 correction factors for $t\bar{t}$ and single top quark background processes evaluated in the pruned
 3417 jet mass signal region $65 < m_{jet} < 105 \text{ GeV}$. The measured correction factors are $0.87 \pm$
 3418 0.04 and 0.83 ± 0.07 for the muon and electron channel, respectively, where the quoted
 3419 uncertainty is only statistical. The disagreement is consistent with the difference between

3420 NLO and NNLO shape prediction for large top quark p_T [141].

3421
 3422 For the $\ell\nu b\bar{b}$ channel, a unique correction factor is calculated with a simultaneous fit
 3423 to number of data events in the muon and electron channels in the pruned jet mass region
 3424 $40 < m_{\text{jet}} < 150 \text{ GeV}$. The difference in normalization between data and simulation is found
 3425 to be $4.6 \pm 5.6\%$, where the quoted uncertainty is only statistical.

3426
 3427 These scale factors include both the W boson signal and the combinatorial components
 3428 mainly due to events where the extra b jet from the top quark decay is in the proximity of
 3429 the W, and are used to correct the normalization of the $t\bar{t}$ and single top quark simulated
 3430 background predictions in the signal regions. The relative uncertainties are used to quantify
 3431 the uncertainty in the $t\bar{t}$ and single top quark background normalization.

3432 The m_{jet} distribution in the top quark enriched sample for the 13 TeV data $\ell\nu q\bar{q}$ analysis
 3433 and for simulation is shown in Fig. 8.11(a), while Fig. 8.11(b) shows the τ_{21} distribution. The
 3434 same distribution is also shown for the $\ell\nu b\bar{b}$ analysis channel in Fig. 8.12, where 8 TeV data
 3435 and simulation are compared. In all cases, the m_{jet} spectrum shows a clear peak for events with
 3436 a W boson decaying to hadrons, including the combinatorial background, while a reasonable
 3437 agreement between the shapes in data and simulation is observed. Comparisons of data
 3438 and simulation are also shown in Fig. 8.13 for other distributions such as the reconstructed
 3439 $m_{\ell\nu+\text{jet}}$, as well as m_{top}^l and m_{top}^h . In the latter a clear peak at the top quark mass is visible.

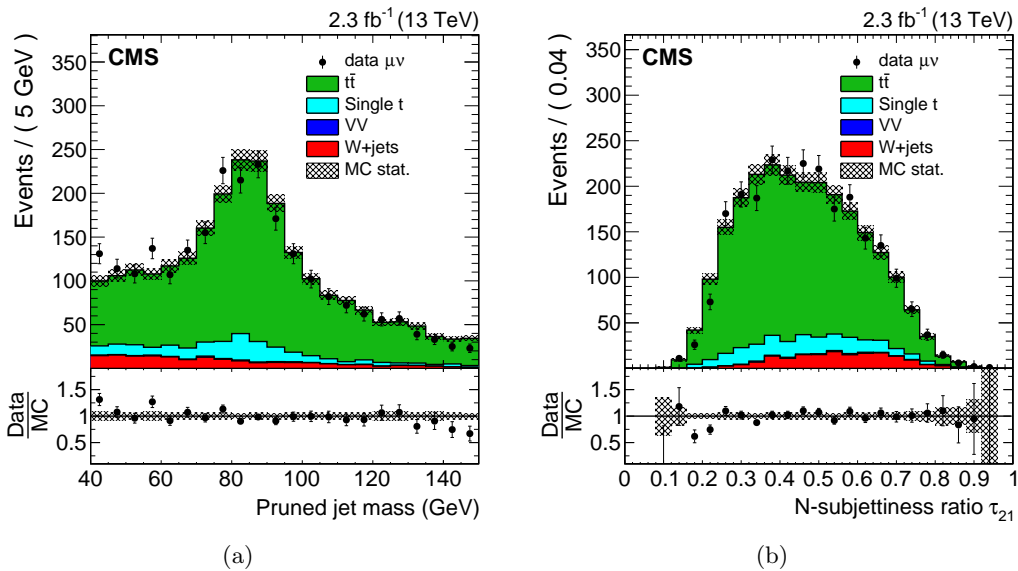


Figure 8.11: Distributions in the N-subjettiness ratio τ_{21} (a) and pruned jet mass m_{jet} (b) from the top quark enriched control sample in the muon channel of the $\ell\nu q\bar{q}$ analysis. The $t\bar{t}$ background is rescaled such that the total number of background events matches the number of events in 13 TeV data.

3440 8.4 Signal modeling

3441 The potential discovery and exclusion power of these analyses rely on the ability of finding a
 3442 local enhancement on the top of a smoothly falling background. This is achieved through
 3443 an unbinned likelihood fit of the signal + background model to the reconstructed diboson
 3444 invariant mass, which depends on the accurate description of the signal shape.

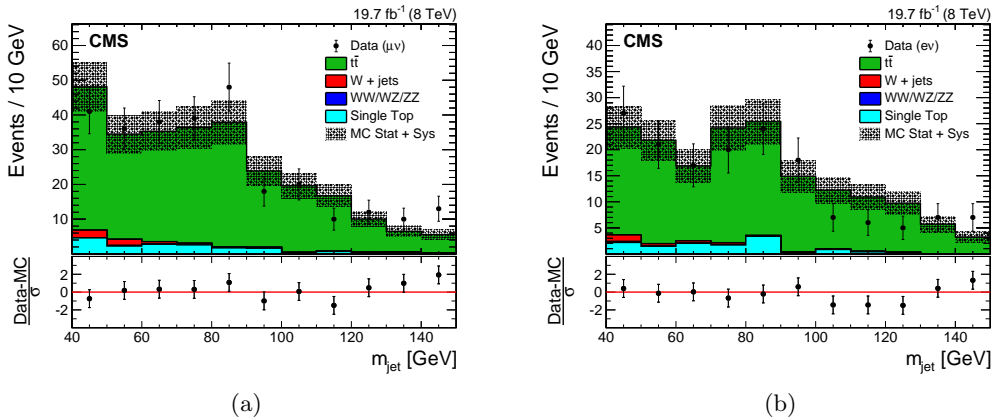


Figure 8.12: Distributions in pruned jet mass m_{jet} in the top quark enriched control sample in the electron (a) and muon (b) channels of the $\ell\nu b\bar{b}$ analysis. The hatched region indicates the overall uncertainty in the background. In the lower panels, the bin-by-bin residuals, $(\text{Data} - \text{MC})/\sigma$ are shown, where σ is the sum in quadrature of the statistical uncertainty of the 8 TeV data, the simulation, and the systematic uncertainty in the $t\bar{t}$ background.

An analytical parametrization of the signal shape is chosen such that it well reproduces the simulated resonance distributions. As stated in Section 5.2.1, simulated signal events are generated with a resonance natural width sufficiently small compared to the detector resolution. This makes the model used for generating the events dependent only on the detector effects on the signal shape, allowing a model independent search for narrow resonances where only the detector resolution has to be described. A double-sided Crystal-Ball (CB) function [142] (i.e. a Gaussian core with power law tails on both sides) is found to well serve this purpose. To take into account differences between muon and electron momentum resolutions, the signal invariant mass distribution is parametrized separately in the two lepton flavor categories.

Figure 8.14 shows examples of the fitted signal distribution through a CB function, for several signal benchmarks and in different m_{jet} categories of the $\ell\nu q\bar{q}$ analysis. Similar results are obtained for the W' signal used in the $\ell\nu b\bar{b}$ analysis.

Because of the limited number of available simulated samples, a linear interpolation is performed for each parameter of the CB function between the shapes obtained for some reference mass points, in order to extrapolate the distribution for intermediate values of the resonance mass. The resolution of the reconstructed diboson invariant mass is given by the width of the Gaussian core and it ranges between 7 and 4% depending on the resonance mass, as summarized in Fig. 8.15. The resolution is dominated by the jet and $E_{\text{T}}^{\text{miss}}$ contributions.

The signal selection efficiency, evaluated for each category, is defined as the number of selected signal events over the number of generated ones, which include all the possible lepton flavours (e , μ and τ). As shown in Fig. 8.16 the efficiency for a Z' or bulk graviton signal in the WW-enriched category is ≈ 2 times larger compared to a W' signal. On the other hand, the efficiency for a W' signal in the WZ-enriched category is ≈ 4 times larger compared to a Z' or bulk graviton signal. For both categories and for each signal hypothesis the efficiency is smaller compared to the large m_{jet} window used for V tagging. However, the resulting loss in sensitivity in each of the category is recovered with a combination of the two m_{jet} categories which allows the use of all the available data. With this solution the discrimination between the two type of signals is maximized together with a gain in sensitivity of 10–20% depending on the resonance mass.

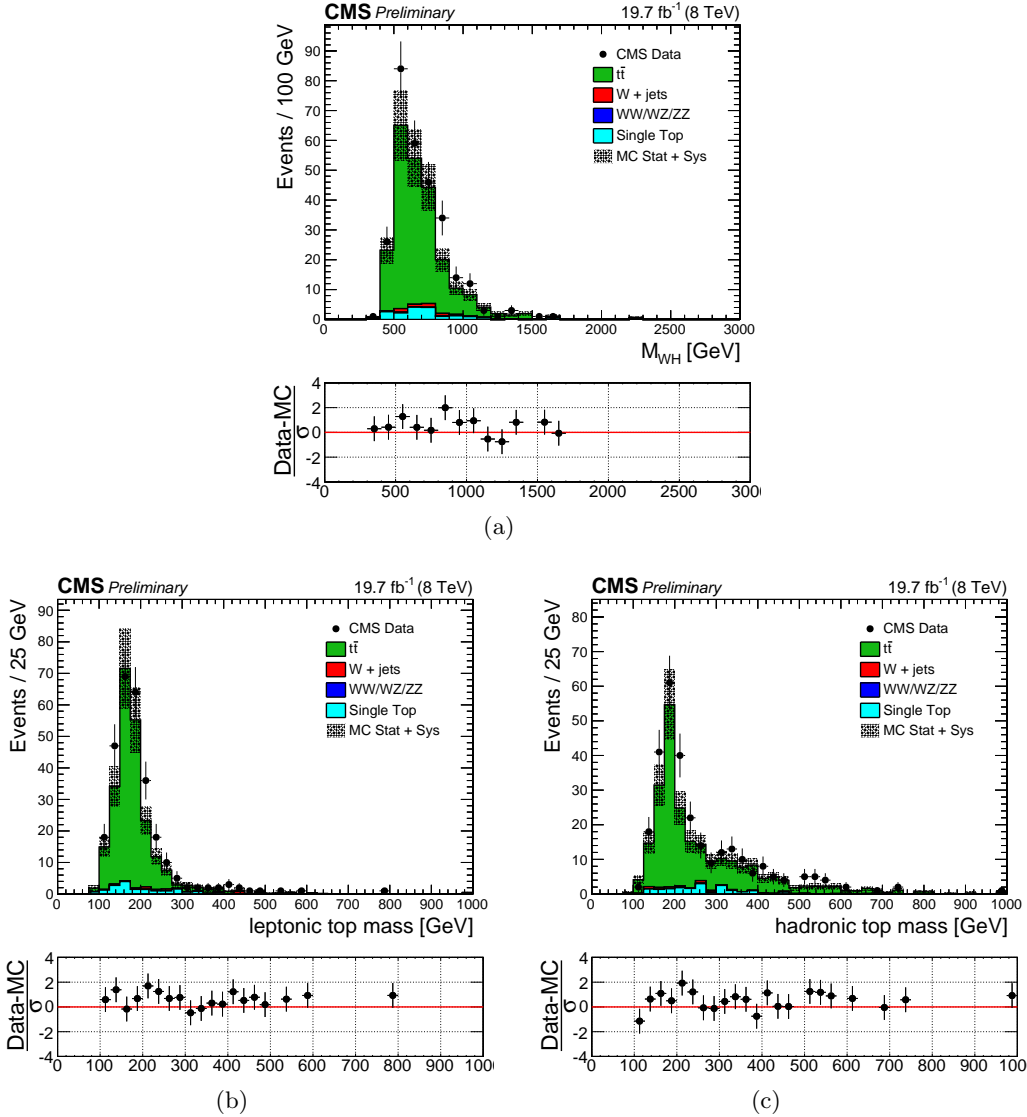


Figure 8.13: Distributions for 8 TeV data and for simulation in m_{WH} (a), m_{top}^l (b) and m_{top}^h (c) in the top quark enriched control sample for the muon channel of the $\ell\nu b\bar{b}$ analysis.

3475 A linear interpolation of the signal efficiency is performed between the values obtained for
 3476 some reference mass points in order to extrapolate the efficiency for intermediate resonance
 3477 masses for which a simulated sample is not available. The efficiency for the electron channel
 3478 is lower compared to the muon channel over most of the phase space due to the tighter
 3479 requirements on the electron p_T and E_T^{miss} . This effect is less visible in the $\ell\nu b\bar{b}$ channel
 3480 (Fig. 8.17) where the electron selections are less strict. For all cases, at low masses the
 3481 efficiency increases with the resonance mass because of the increase in the acceptance of the
 3482 lepton, E_T^{miss} and m_{WV}/m_{WH} selections together with the inefficiency of the jet algorithms in
 3483 reconstructing the merged jet for a low boosted V boson (Fig. 6.13). At larger resonance
 3484 masses the efficiency slightly decreases due to τ_{21} selection inefficiency for very high p_T V
 3485 jets, as described in Section 7.2. For the electron channel this effect is compensated by a
 3486 larger increase in the lepton selection acceptance, resulting in a nearly flat efficiency at high
 3487 resonance masses. Similar considerations hold for the efficiency in the $\ell\nu b\bar{b}$ channel shown in
 3488 Fig. 8.17.

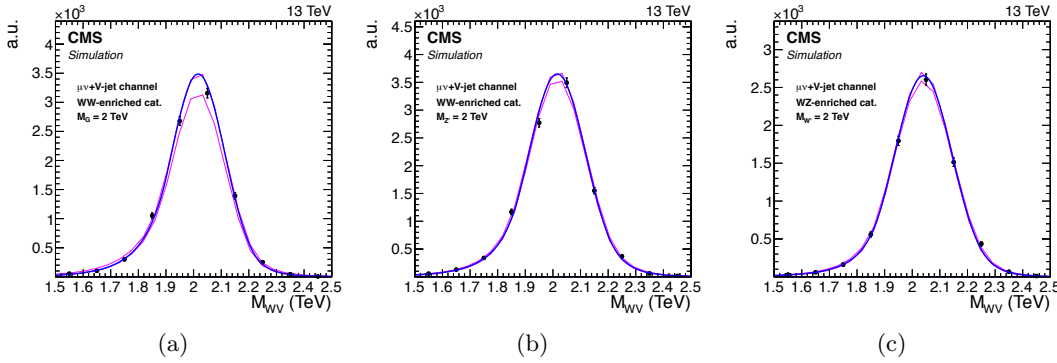


Figure 8.14: Modeling of the reconstructed signal distribution with a double-sided Crystal Ball function, for different signal benchmarks and in different m_{jet} categories of the $\ell\nu q\bar{q}$ analysis: bulk graviton (a) and Z' (b) signals in the WW-enriched category; (c) W' signal in the WZ-enriched category. In all cases, a signal sample with a generated mass of 2 TeV is considered.

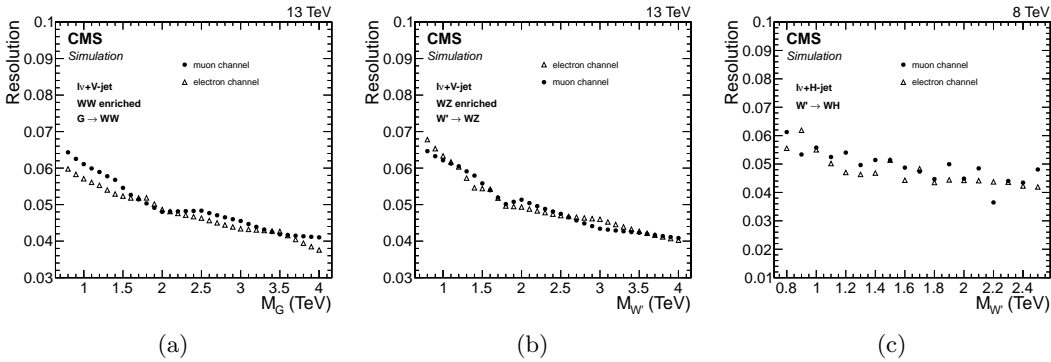


Figure 8.15: Relative resolution of the fitted signal distribution as given by the width of the Gaussian core, as a function of the generated resonance mass for different signal benchmarks and for the two analysis: bulk graviton (a) and W' (b) signals in the WW-enriched and WZ-enriched category, respectively, of the $\ell\nu q\bar{q}$ analysis; (c) W' signal for the $\ell\nu b\bar{b}$ analysis.

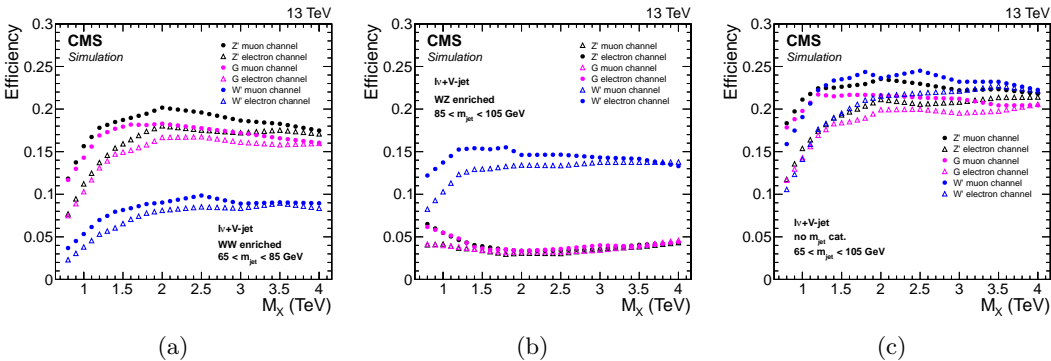


Figure 8.16: Signal efficiency in the $\ell\nu q\bar{q}$ analysis channel as a function of the generated resonance mass for all signal benchmarks and for different m_{jet} selection: (a) WW-enriched category; (b) WZ-enriched category; (c) $65 < m_{\text{jet}} < 105 \text{ GeV}$.

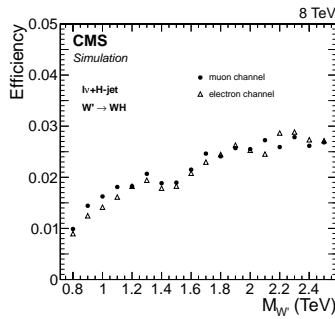


Figure 8.17: Signal efficiency in the $\ell\nu b\bar{b}$ analysis channel as a function of the generated W' mass.

3489 8.5 Systematic uncertainties

3490 This section describes the systematic uncertainties in the signal and background predictions
 3491 affecting both the normalizations and the $m_{\ell\nu+\text{jet}}$ distributions. The uncertainties described
 3492 below are included as nuisance parameters in the calculation of the limits on the cross section
 3493 as well as of the p-values of potential excesses of events observed in the data.

3494 8.5.1 Systematic uncertainties in the background estimation

3495 The uncertainty in the $W+\text{jets}$ background normalization is mainly due to the uncertainties
 3496 in the parameters extracted from the fit of the data in the pruned jet mass sideband. This
 3497 contribution is statistical in nature since it depends on the amount of data in the m_{jet} sideband
 3498 regions, and it is evaluated varying the fit parameters from the final fit values by random
 3499 amounts sampled from the covariance matrix. Alternative parametrizations of the $W+\text{jets}$
 3500 m_{jet} distribution have been studied and the differences with respect to the results obtained
 3501 with the chosen default function taken into account by adding this effect in quadrature to
 3502 the pure statistical contribution. This contribution is found to constitute up to 15% of the
 3503 total uncertainty. The total uncertainty on the $W+\text{jets}$ yields remains below 10% in the $\ell\nu q\bar{q}$
 3504 channel, while uncertainties above 40% are obtained for the $\ell\nu b\bar{b}$ channel where the amount
 3505 of data in the sidebands is largely reduced by the tight b tagging requirements.

3506 As described in Section 8.2.3 the extrapolated background shape in the signal region is
 3507 computed from the product of $F_{\text{data},\text{SB}}^{\text{W+jets}}$ and α_{MC} . Thus, the shape uncertainty comes from
 3508 both uncertainties in the $W+\text{jets}$ $m_{\ell\nu+\text{jet}}$ shape obtained from the fit of the data in the lower
 3509 m_{jet} sideband region and in the modelling of the transfer function α_{MC} . Both contributions
 3510 are mainly statistical in nature, as they are driven by the available amount of data in the
 3511 sideband and by the number of simulated $W+\text{jets}$ events passing the analysis requirements,
 3512 respectively. These effects are estimated from the covariance matrix of the fit and included in
 3513 the final limit and p-value calculations after a procedure which diagonalizes the matrix to
 3514 decorrelate the fitted parameters. In this procedure, the new parameters are defined in such a
 3515 way to be centered at zero and with error equal to unity. The background fit parameterization
 3516 is then redefined as a function of these new, uncorrelated parameters. This new fit function
 3517 together with the uncertainties in the fitted parameter is used to describe the background
 3518 distribution in the limit and p-value calculations explained in Section 8.6.

3519 Additionally, the α_{MC} (Fig. 8.7) is affected by variations due to the choice of the para-
 3520 metrization used to model the $W+\text{jets}$ distribution. Previous studies showed that addi-
 3521 tional variations of about the same size are due to the use of different parton showering
 3522 algorithms [135]. This effect has been evaluated comparing the α obtained with simulated
 3523 samples with parton showering implemented through HERWIG++ and PYTHIA. All these

variations are found to be equal or slightly smaller than the statistical uncertainties on the α , and hence the associated systematic effect is taken into account by enlarging the errors on the decorrelated fit parameters by a factor $\sqrt{2}$. This is sufficiently conservative to cover all the shape variations. In a similar way, variations in the $F_{\text{data,SB}}^{\text{W+jets}}$ due to the same effects, are as well taken into account.

The uncertainties in the W+jets normalization are treated as uncorrelated among the different lepton flavor channels and m_{jet} categories. While the uncertainties in the W+jets distribution are uncorrelated among electron and muon channels, a partial correlation among m_{jet} categories is defined according to the following scheme:

- uncertainties in the $F_{\text{data,SB}}^{\text{W+jets}}$ parameters are correlated;
- uncertainties in the α_{MC} parameters are uncorrelated.

This solution takes into account the fact that in the different m_{jet} categories the same data in the sideband are used to estimate the W+jets distribution, while the transfer function is used to predict the shape in the two orthogonal signal regions defined by the categories.

The systematic uncertainty in the normalization of the $t\bar{t}$ /single top quark backgrounds is driven by the uncertainties in the data-to-simulation scale factors estimated in the top quark enriched control sample (Section 8.3). In the $\ell\nu q\bar{q}$ channel these uncertainties are measured to be 4.6% and 8.4% in the muon and electron channel, respectively. For the $\ell\nu b\bar{b}$ channel, this uncertainty amounts to 5.6%. For the single top quark background an additional systematic uncertainty related to the cross section calculations is assigned to be 15% and 5%, for the 8 and 13 TeV data analysis respectively [143, 144].

The $t\bar{t}$ background distribution in $m_{\ell\nu+\text{jet}}$ is taken from simulation and this choice is found to be reasonable given the agreement between data and simulation in the top quark enriched control sample (Fig. 8.13(a)). However, previous studies [135] showed that variations in the shape occur due to the choices of regularization or factorization scales (varied up and down by a factor of 2), to the matching scales in the MADGRAPH simulation, and to different generators (MADGRAPH or POWHEG). These effects are covered by enlarging the errors on the decorrelated fit parameters for the $t\bar{t}$ distribution by a factor of 2.

The systematic uncertainties in the diboson background normalization is due to the uncertainty in the inclusive cross sections, which are assigned to be 10% [145] and 3% [146] for the 8 and 13 TeV data analysis, respectively. For the $\ell\nu q\bar{q}$ channel, the uncertainty in the diboson background normalization is as well due to the uncertainty of 3% in the measured data-to-simulation scale factors for the V tagging efficiency derived in the top quark enriched control sample (Section 7.2).

Additional sources of systematic uncertainties in the background normalization are due to the uncertainty in the integrated luminosity, and in the measured data-to-simulation scale factors for the efficiency of lepton trigger and identification, described in the following section.

A summary of the systematic uncertainties in the normalization of the predicted background is provided in Tables 8.5 and 8.6 for the $\ell\nu q\bar{q}$ and $\ell\nu b\bar{b}$ analysis channel, respectively.

8.5.2 Systematic uncertainties in the signal prediction

Systematic uncertainties affecting the predicted signal efficiency (or normalization) and $m_{\ell\nu+\text{jet}}$ distribution arise from several sources as described in the following and summarized

Source	W+jets	t <bar>t</bar>	single top quark	diboson
Integrated luminosity		2.6%	2.6%	2.6%
Cross section	-	-	15%	10%
Data-driven prediction	42% (μ) / 59% (e)	5.6%	5.6%	-
Lepton trigger (μ/e)	-	1% / 1%	1% / 1%	1% / 1%
Lepton identification (μ/e)	-	1% / 3%	1% / 3%	1% / 3%

Table 8.5: Summary of the systematic uncertainties in the normalization of the predicted background in the $\ell\nu b\bar{b}$ analysis at 8 TeV.

Source	W+jets	t <bar>t</bar>	single top quark	diboson
Integrated luminosity		2.7%	2.7%	2.7%
Cross section	-	-	5%	3%
V-tagging efficiency	-	-	-	3%
Data-driven prediction	5–9%	5–8%	5–8%	-
Lepton trigger (μ/e)	-	1% / 1%	1% / 1%	1% / 1%
Lepton identification (μ/e)	-	1% / 3%	1% / 3%	1% / 3%

Table 8.6: Summary of the systematic uncertainties in the normalization of the predicted background in the $\ell\nu q\bar{q}$ analysis at 13 TeV.

3569 in Tables 8.7 and 8.8. The effect of each source is evaluated for each considered simulated
 3570 signal hypothesis as a function of the resonance mass.

3571

3572 One of the primary sources affecting the signal normalization for the $\ell\nu q\bar{q}$ channel is due
 3573 to uncertainties in data-to-simulation scale factors for the V tagging efficiency, derived from
 3574 the top quark enriched control sample as described in Section 7.2. These uncertainties include
 3575 separately the uncertainty of 3% on the scale factor measured in tt events with an average p_T
 3576 ≈ 200 GeV, and the uncertainty due to the extrapolation of the scale factor to higher momenta,
 3577 which is assigned to be 6–10% depending on the signal mass. Additional uncertainties are
 3578 assigned due to the pruned jet mass scale and resolution measured in tt events (Table 7.2).
 3579 These are computed by rescaling or smearing the m_{jet} value according to the uncertainties in
 3580 the respective m_{jet} scale or resolution. The selection efficiencies are recalculated on these
 3581 modified events, with the resulting changes taken as systematic uncertainties that depend on
 3582 the resonance mass.

3583 In a similar way, systematic uncertainties are assigned in the $\ell\nu b\bar{b}$ channel due to the
 3584 uncertainty in the H tagging efficiency. This contribution arises from both uncertainties in
 3585 the data-to-simulation scale factors for b-tagged jet identification efficiency (Section 6.4.3)
 3586 and for the efficiency of the m_{jet} selection for H jets. The first is obtained by varying the
 3587 b-tagging scale factors within the associated uncertainties and amounts to 2–8% depending
 3588 on the signal mass. The second is evaluated by considering the uncertainties in the m_{jet} scale
 3589 and resolution measured in tt events for W jets, additionally accounting for the difference
 3590 in fragmentation of light quarks and b quarks, which amounts to 2.6% (Section 7.3). The
 3591 systematic uncertainty in the mass tagging efficiency is found to be 2–10%, depending on the
 3592 signal mass.

3593 The accuracy on energy and momentum measurements for leptons and jets represents an
 3594 important source of systematic uncertainties in the signal efficiency. In particular, the muon
 3595 momentum scale and resolution, the electron energy scale and resolution, and the jet energy

scale and resolution are considered. The event selection is applied to the signal samples after varying the lepton four-momenta within one standard deviation of the corresponding uncertainty in the muon momentum scale [103] or electron energy scale [147], or applying an appropriate Gaussian momentum/energy smearing in case of resolution uncertainties. The same procedure is also applied for the jet four-momenta using the corresponding energy scale and resolution uncertainties. In this process, variations in the lepton and jet four-momenta are propagated consistently to the \vec{p}_T^{miss} vector. The signal efficiency is then recalculated using modified lepton and jet four-momenta separately for each source of systematic uncertainties. The largest relative change in the signal efficiency compared to the default value is taken as the systematic uncertainty for that specific source. The induced relative migration among V jet mass categories is evaluated for the $\ell\nu q\bar{q}$ channel, but do not affect the overall signal efficiency. The muon, electron, and jet uncertainties are assumed to be uncorrelated. Finally, the resulting changes on the reconstructed resonances are propagated on the reconstructed $m_{\ell\nu+\text{jet}}$ signal distribution, resulting in a small effect on both peak position and width of the Gaussian core.

The systematic uncertainties in the lepton trigger, identification, and isolation efficiencies are derived using a dedicated T&P analysis in $Z \rightarrow \ell^+ \ell^-$ events. For both analysis channels, an uncertainty of 1% is assigned to the trigger efficiency for both lepton flavors, while for lepton identification and isolation efficiency, the systematic uncertainty is estimated to be 1% for the muon and 3% for electron flavors.

The 2.7% and 2.6% uncertainty in the integrated luminosity affects to the normalization of both signal and backgrounds in the $\ell\nu q\bar{q}$ and $\ell\nu b\bar{b}$ channel, respectively, as obtained in measurements performed for the 2015 and 2012 data taking periods [148, 149].

For the $\ell\nu q\bar{q}$ channel, uncertainties on the signal yield due to variations in the parton distribution function and the choice of factorization (μ_f) and renormalization (μ_r) scales are also taken into account. The PDF uncertainties are evaluated using the NNPDF 3.0 [68] PDF set. The uncertainty related to the choice of μ_f and μ_r scales is evaluated following the proposal in Refs. [150, 151] by varying the default choice of scales in the following 6 combinations of factors: $(\mu_f, \mu_r) \times (1/2, 1/2), (1/2, 1), (1, 1/2), (2, 2), (2, 1)$, and $(1, 2)$. The uncertainty in the signal cross section from the choice of PDFs and of factorization and renormalization scales ranges from 4 to 77%, and from 1 to 22%, respectively, depending on the resonance mass, particle type and its production mechanism. For the $\ell\nu b\bar{b}$ channel, only the impact of the proton PDF uncertainties on the signal efficiency is evaluated with the PDF4LHC prescription [152, 153], using the MSTW2008 [154] and NNPDF 2.1 [155] PDF sets. This effect is found to be $< 0.5\%$.

Finally, the systematic uncertainty due to the modelling of pileup is estimated by reweighting the signal simulation samples such that the distribution of the number of interactions per bunch crossing is shifted according to the uncertainty in the inelastic proton-proton cross section compared with that found in data. This contribution is found to be 0.5% in both channels.

8.6 Testing for a new resonance hypothesis

The purpose of this analysis is to infer a constraint on the existence of a new resonance decaying into diboson for a set of different signal mass hypotheses. The comparison between the diboson invariant mass distribution observed in data and the SM background prediction is used to check for the presence of the new resonance. A hypothesis test is built to decide

Table 8.7: Summary of the systematic uncertainties in the signal prediction for the $\ell\nu b\bar{b}$ analysis channel and their impact on the event yield in the signal region and on the reconstructed m_{WH} shape (mean and width) for both muon and electron channels.

Source	Relevant quantity	Uncertainty (%)
Lepton trigger (μ/e)	Signal yield	1 / 1
Lepton identification (μ/e)	Signal yield	1 / 3
Lepton p_T scale (μ/e)	Signal yield	1 / 0.5
Lepton p_T resolution (μ/e)	Signal yield	0.1 / 0.1
Jet energy scale	Signal yield	1–3
Jet energy resolution	Signal yield	0.5
Integrated luminosity	Signal yield	2.6
Pileup	Signal yield	0.5
PDFs	Signal yield	< 0.5
H jet mass tagging efficiency	Signal yield	2–10
H jet b tagging efficiency	Signal yield	2–8
Jet energy scale	Resonance shape (mean)	0.5
Jet energy scale	Resonance shape (width)	4
Jet energy resolution	Resonance shape (mean)	0.2
Jet energy resolution	Resonance shape (width)	4
Lepton p_T resolution	Resonance shape (mean)	0.1
Lepton p_T resolution	Resonance shape (width)	1.2
Lepton p_T scale	Resonance shape (mean)	0.7
Lepton p_T scale	Resonance shape (width)	2.5

3643 between a null hypothesis given by the predicted SM background only, against an alternative
 3644 hypothesis which includes both background as well as the sought after signal. In principle
 3645 one can either test the background-only hypothesis and exclude it if there is a large deviation
 3646 of the data from the SM background prediction, or test the signal hypothesis and exclude it
 3647 if there is a large deviation of the data from the expected signal model. In particular, if no
 3648 significant deviation from the SM background prediction is observed in data, compatible with
 3649 the signal hypothesis, an upper limit on production cross section of such signal is usually
 3650 set, up to a certain degree of belief. The CMS community has agreed upon a procedure for
 3651 computing upper limits, which is based on the modified frequentist method, often referred
 3652 to as CL_s . While a detailed description of this method can be found in Refs. [156, 157], the
 3653 basic ingredients will be summarized Section 8.6.1. A description of the procedure followed
 3654 to quantify an excess of events is provided in Section 8.6.3. A summary of the final results
 3655 will be given in the next chapter.

3656 8.6.1 Limit setting procedure

3657
 3658 The procedure to establish the exclusion of a given signal hypothesis is based on a
 3659 frequentist significance test which uses a log-likelihood ratio as a test statistic. In order to
 3660 construct the test statistic a likelihood function is defined as

$$\mathcal{L}(\text{data}|\mu, \theta) = \text{Poisson}(\text{data}|\mu \cdot s(\theta) + b(\theta)) \cdot p(\tilde{\theta}|\theta). \quad (8.5)$$

3661 In this definition, s and b denote the expected signal and background event yields,
 3662 respectively, which, before the scrutiny of the observed data entering the statistical analysis,

Table 8.8: Summary of the systematic uncertainties in the signal prediction for the $\ell\nu q\bar{q}$ analysis and their impact on the event yield in the signal region and on the reconstructed m_{W^*} shape (mean and width) for both muon and electron channels. The last uncertainty results in migrations between event categories, but does not affect the overall signal efficiency.

Source	Relevant quantity	Uncertainty (%)
Lepton trigger (μ/e)	Signal yield	1 / 1
Lepton identification (μ/e)	Signal yield	1 / 3
Lepton p_T scale (μ/e)	Signal yield	0.7 / 0.2
Lepton p_T resolution (μ/e)	Signal yield	0.1 / 0.1
Jet energy and m_{jet} scale	Signal yield	0.2–4
Jet energy and m_{jet} resolution	Signal yield	0.1–2
Integrated luminosity	Signal yield	2.7
Pileup	Signal yield	0.5
PDFs (W')	Signal yield	4–19
PDFs (Z')	Signal yield	4–13
PDFs (G_{bulk})	Signal yield	9–77
(μ_f and μ_r) scales (W')	Signal yield	1–14
(μ_f and μ_r) scales (Z')	Signal yield	1–13
(μ_f and μ_r) scales (G_{bulk})	Signal yield	8–22
V tagging efficiency	Signal yield	3
V tagging p_T -dependence	Signal yield	6–10
Jet energy scale	Resonance shape (mean)	1.3
Jet energy scale	Resonance shape (width)	3
Jet energy resolution	Resonance shape (mean)	0.1
Jet energy resolution	Resonance shape (width)	3
Lepton p_T resolution	Resonance shape (mean)	0.1
Lepton p_T resolution	Resonance shape (width)	0.1
Lepton p_T scale	Resonance shape (mean)	0.1
Lepton p_T scale	Resonance shape (width)	0.5
Jet energy and m_{jet} scale	Migration	2–24

3663 are subject to multiple uncertainties that are treated by introducing nuisance parameters
 3664 θ , so that signal and background expectations depend on these parameters as $s(\theta)$ and $b(\theta)$.
 3665 The exclusion of a signal hypothesis is generally expressed as an upper limit on the *signal*
 3666 *strength modifier* μ which scales the cross section used as input in the evaluation of the
 3667 expected signal yields. With this definition, the likelihood represents the Poisson probability
 3668 of observing a certain amount of data when the expected yield is $\mu \cdot s(\theta) + b(\theta)$ and given
 3669 the probability $p(\tilde{\theta}|\theta)$ of measuring a value $\tilde{\theta}$ for the nominal nuisance parameter θ . Note
 3670 that, in this likelihood definition, “data” stands for a generic dataset, either experimental or
 3671 a pseudo-data generated randomly.

3672 The likelihood can be either binned or unbinned. In the first case the function $\text{Poisson}(data|\mu \cdot$
 3673 $s + b)$ in Eq. 8.5 is the product of Poisson probabilities for observing n_i events in each bin i
 3674 of the signal+background model

$$\prod_i \frac{(\mu s_i + b_i)^{n_i}}{n_i!} e^{-(\mu s_i + b_i)}. \quad (8.6)$$

3675 For the unbinned case each event enters the calculation as follows

$$k^{-1} \prod_i (\mu S f_s(x_i) + B f_b(x_i)) e^{-(\mu S + B)}, \quad (8.7)$$

3676 where k is the number of events, $f_s(x)$ and $f_b(x)$ are the probability density functions of
 3677 signal and background of the observable x , while S and B are the total event rates expected
 3678 for signal and background. In this analysis the unbinned form for the likelihood is used,
 3679 where the observable x coincides with the reconstructed diboson invariant mass.

3680

3681 To compare the compatibility of the data with the background-only and signal+background
 3682 hypotheses, where the prediction for the signal is allowed to be scaled by some factor μ , the
 3683 test statistic \tilde{q}_μ is constructed based on the profile likelihood ratio as

$$\tilde{q}_\mu = -2 \ln \frac{\mathcal{L}(\text{data}|\mu, \hat{\theta}_\mu)}{\mathcal{L}(\text{data}|\hat{\mu}, \hat{\theta})}, \quad \text{with} \quad 0 \leq \hat{\mu} \leq \mu. \quad (8.8)$$

3684 Here $\hat{\theta}_\mu$ denotes the value of θ that maximizes the likelihood for the hypothesized μ , i.e. it
 3685 is the conditional maximum-likelihood (ML) estimator of θ (and thus is a function of μ). The
 3686 procedure of refitting the nuisance parameters to maximize the likelihood for each possible
 3687 value of the parameter of interest μ , is usually referred to as “profiling”. The denominator is
 3688 the maximized (unconditional) likelihood function, i.e., $\hat{\mu}$ and $\hat{\theta}$ are the global maximum of
 3689 the likelihood. The presence of the nuisance parameters broadens the profile likelihood as a
 3690 function of μ relative to what one would have if their values were fixed. This reflects the loss
 3691 of information about μ due to the systematic uncertainties. Higher values of \tilde{q}_μ correspond to
 3692 increasing incompatibility between the data and the hypothesized signal of strength μ . The
 3693 lower constraint for $\hat{\mu}$ in the denominator excludes the possibility of negative signal yields.
 3694 The upper constraint is introduced to avoid that data with $\hat{\mu} > \mu$ (upward fluctuations) are
 3695 considered as representing less compatibility with μ than what obtained with data.

3696 The observed value of the test statistic, $\tilde{q}_\mu^{\text{obs}}$ for the given signal strength modifier μ under
 3697 test is computed, as well as the nuisance parameters $\hat{\theta}_0^{\text{obs}}$ and $\hat{\theta}_\mu^{\text{obs}}$ maximizing the likelihood
 3698 under the background-only and signal+background hypothesis, respectively. Furthermore,
 3699 the probability density functions of the chosen test statistic \tilde{q}_μ under the signal+background
 3700 hypothesis, $f(\tilde{q}_\mu|\mu, \hat{\theta}_\mu^{\text{obs}})$, and the background-only hypothesis, and $f(\tilde{q}_\mu|0, \hat{\theta}_0^{\text{obs}})$, are con-
 3701 structed by means of ensembles of MC pseudo-experiments generated according to the same
 3702 Poisson probabilities used to build the likelihood. In this process the nuisance parameters
 3703 are fixed to the values $\hat{\theta}_0^{\text{obs}}$ and $\hat{\theta}_\mu^{\text{obs}}$ obtained by fitting the observed data.

3704 Using the $f(\tilde{q}_\mu|0, \hat{\theta}_0^{\text{obs}})$ and $f(\tilde{q}_\mu|\mu, \hat{\theta}_\mu^{\text{obs}})$ distributions, two p-values are computed

$$\begin{aligned} p_\mu &\equiv \text{CL}_{s+b} = P(\tilde{q}_\mu \geq \tilde{q}_\mu^{\text{obs}} | \mu s(\hat{\theta}_\mu^{\text{obs}}) + b(\hat{\theta}_\mu^{\text{obs}})) = \int_{\tilde{q}_\mu^{\text{obs}}}^{+\infty} f(\tilde{q}_\mu|\mu, \hat{\theta}_\mu^{\text{obs}}) d\tilde{q}_\mu \\ p_0 &\equiv \text{CL}_b = P(\tilde{q}_\mu \geq \tilde{q}_\mu^{\text{obs}} | b(\hat{\theta}_0^{\text{obs}})) = \int_{\tilde{q}_\mu^{\text{obs}}}^{+\infty} f(\tilde{q}_\mu|0, \hat{\theta}_0^{\text{obs}}) d\tilde{q}_\mu. \end{aligned} \quad (8.9)$$

3705 The two probabilities are shown in the example in Fig. 8.18(a). In the classical frequentist
 3706 approach, the level of agreement between the data and hypothesized μ is evaluated by using
 3707 the CL_{s+b} probability only, and one says that the hypothesized signal μ is excluded at 95%
 3708 CL if $\text{CL}_{s+b} \leq 0.05$.

3709 However, such a definition has a caveat. If the distributions of the test statistic for the
 3710 signal+background and background-only hypotheses have a not negligible overlap as in the
 3711 plot (c) of Fig. 8.18(b), the experiment would tend to exclude the hypothesized signal μ even

if the experiment in this case has little sensitivity to discriminate it against the background. In fact, in this case the experimental data are highly contaminated with background and a statement about the signal would be a mistake of interpretation. To prevent the inference of a signal in such cases, the so-called modified frequentist approach has been introduced at the time of LEP [156, 157]. In this approach, the level of agreement between the data and hypothesized μ is evaluated by using instead the quantity

$$\text{CL}_s = \frac{\text{CL}_{s+b}}{\text{CL}_b}, \quad (8.10)$$

and the hypothesized signal μ is excluded at 95% confidence level (CL) if $\text{CL}_s \leq 0.05$. It is straightforward to see from plot (a) of Fig. 8.18(b) that, if the distribution of the test statistic for the signal+background hypothesis is well separated from the background-only distribution, then $\text{CL}_s \sim \text{CL}_{s+b}$ and there is no risk of misinterpretation.

In order to quote, as conventionally done, 95% CL observed upper limits, the full procedure is iterated for different values of μ , until $\text{CL}_s = 0.05$ is found. This value of μ is denoted as $\mu_{95\%}$, and one can infer that the hypothesized resonance $X \rightarrow WV/VH$ with a cross section μ -times larger than the one predicted by some specific theoretical model σ_{th} used as input to the statistical analysis, is excluded at 95% CL. In this analysis, model-independent limits on the cross section are set by rescaling the $\mu^{95\%} = \sigma_{95\%}/\sigma_{th}$ by the input cross section in order to obtain $\sigma_{95\%}$.

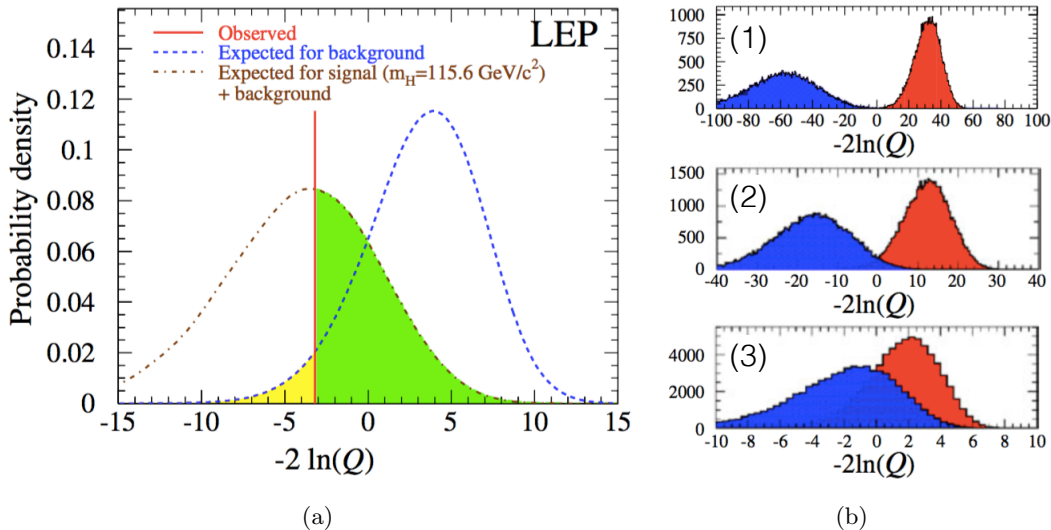


Figure 8.18: (a) Distributions of the test statistic Q (defined in the text as \tilde{q}_μ) for the combined Higgs search at LEP for the background (right) and signal+background hypotheses (left) for $m_H = 115.6$ GeV. The light grey region to the left of the observation is $1 - \text{CL}_b$ and the dark grey region to the right of the observation is CL_{s+b} . (b) Illustration of the evolution of the test statistic distributions with falling search sensitivity from (1) to (3) [156].

In addition to the observed upper limit derived from the actual data distribution, it is important to study also the expected limit given the observed data. In fact, the expected limit quantifies the sensitivity of the experiment independent from statistical fluctuations in the data. In order to compute the median-expected upper limit, and the associated $\pm 1\sigma$ and $\pm 2\sigma$ bands, a large set of background-only pseudo-experiments is generated and, for each of them, the $\mu_{95\%}$ is calculated. From the cumulative distribution of $\mu_{95\%}$, the median value is taken as the expected limit, while the $\pm 1(2)\sigma$ uncertainty bands on the expected limits are

3736 extracted from the values of the 16% (2.5%) and 84% (97.5%) quantiles.

3737 8.6.2 The asymptotic approximation

3738 In order to compute CL_s the probability density functions of the test statistics are required.
 3739 In particular, one needs the probability density functions $f(\tilde{q}_\mu|\mu')$, where $\mu' = 0$ or $\mu' = \mu$,
 3740 which are obtained from MC pseudo-experiments requiring very expensive computational
 3741 resources. An approximation for the CL_s method, valid in the large sample limit, also referred
 3742 to as “asymptotic approximation” has been proposed in Ref. [158] and it is briefly described
 3743 in the following.

3744

3745 By using the Wald approximation [159] the desired distribution $f(\tilde{q}_\mu|\mu')$ can be obtained
 3746 by expressing the test statistic given by the log-likelihood ratio as

$$\tilde{q}_\mu = \frac{(\mu - \hat{\mu})^2}{\sigma^2} + \mathcal{O}(1/\sqrt{N}), \quad (8.11)$$

3747 where $\hat{\mu}$ follows a Gaussian distribution with a mean μ' and standard deviation σ , and
 3748 N represents the data sample size. For large data samples ($N \rightarrow \infty$), the $\mathcal{O}(1/\sqrt{N})$ can
 3749 be neglected and it can be shown [160] that the distribution $f(\tilde{q}_\mu|\mu')$ of the test statistic
 3750 \tilde{q}_μ follows a *noncentral chi-square* distribution for one degree of freedom with noncentrality
 3751 parameter

$$\Lambda = \frac{(\mu - \mu')^2}{\sigma^2}. \quad (8.12)$$

3752 For the special case $\mu' = \mu$ one has $\Lambda = 0$ and the test statistic is distributed as a
 3753 chi-square for one degree of freedom. For the general case in which $\mu' \neq \mu$, the standard
 3754 deviation σ of $\hat{\mu}$ has to be evaluated, which depends on the MLE estimator of the nominal
 3755 nuisance parameters. The evaluation of σ is greatly simplified considering a special, artificial
 3756 data set, referred to as the “Asimov data set”, where all statistical fluctuations are suppressed
 3757 and the estimators for all parameters are replaced by their expectation values as follows:

$$\hat{\mu} = \mu' \quad \text{and} \quad \hat{\theta} = \theta. \quad (8.13)$$

3758 With these assumptions the test statistic $\tilde{q}_{\mu,A}$ for the Asimov dataset is given by

$$\tilde{q}_{\mu,A} \approx \frac{(\mu - \mu')^2}{\sigma^2} = \Lambda. \quad (8.14)$$

3759 From the Asimov data set one therefore obtains an estimate of the noncentrality parameter
 3760 Λ that characterizes the distribution $f(\tilde{q}_\mu|\mu')$. Equivalently, the above equation can be used
 3761 to obtain the variance σ^2 which characterizes the distribution of $\hat{\mu}$, namely,

$$\sigma_A^2 = \frac{(\mu - \mu')^2}{\tilde{q}_{\mu,A}}, \quad (8.15)$$

3762 so that the distribution obtained by using σ_A^2 has a median given by the corresponding
 3763 Asimov value $\tilde{q}_{\mu,A}$. Using these formulae, asymptotic relations are derived which are easily
 3764 solved for the observed upper limits with the CL_s method, as well as for the expected median
 3765 and error bands.

8.6.3 Quantifying an excess of events

The presence of the signal is quantified by the background-only p-value, i.e. the probability for the background to fluctuate and give an excess of events as large or larger than the observed one. As for the upper limits, this evaluation requires defining a test statistic and the construction of its probability density function. For a given resonance mass hypothesis M_X , the test statistic used in this case is \tilde{q}_0 , defined as

$$\tilde{q}_0 = -2 \ln \frac{\mathcal{L}(\text{data}|0, \hat{\theta}_0)}{\mathcal{L}(\text{data}|\hat{\mu}, \hat{\theta})}, \quad \text{with } \hat{\mu} \geq 0. \quad (8.16)$$

The probability density function $f(\tilde{q}_0|0, \hat{\theta}_0^{\text{obs}})$ is built by generating MC pseudo-experiments under the assumption of the background-only hypothesis. From this distribution, the p-value corresponding to a given experimental observation \tilde{q}_0^{obs} is evaluated:

$$p_0 = P(\tilde{q}_0 \geq \tilde{q}_0^{\text{obs}} | b(\hat{\theta}_0^{\text{obs}})) = \int_{\tilde{q}_0^{\text{obs}}}^{+\infty} f(\tilde{q}_0|0, \hat{\theta}_0^{\text{obs}}) d\tilde{q}_0. \quad (8.17)$$

This probability is converted into a *significance*, also referred to as *Z value*, as follows

$$Z = \Phi^{-1}(1 - p_0). \quad (8.18)$$

A significance of 5σ , corresponding to a p-value of 2.87×10^{-7} , is conventionally used in high energy physics to claim a discovery, and 3σ for an evidence.

It can be demonstrated that in the asymptotic approximation (Section 8.6.2), the likelihood ratio test statistic \tilde{q}_0 follows a chi-square distribution for one degree of freedom, and a fair estimate of the p-value and of the significance can be obtained from the observed value \tilde{q}_0^{obs} itself, without the need for generating pseudo-data, as follows

$$p_0 = \frac{1}{2} [1 - \text{erf}(\sqrt{\tilde{q}_0^{\text{obs}}}/2)] \quad (8.19)$$

$$Z = \sqrt{\tilde{q}_0^{\text{obs}}}.$$

The p-value discussed above is evaluated at a fixed resonance mass M_X and can be referred to as a *local p-value*. In this search, a scan is performed over a wide range of resonance mass hypotheses with the aim of finding the minimum local p-value, which describes the probability of a background fluctuation for that particular resonance mass hypothesis. However, it is important to distinguish the probability of finding a fluctuation in some particular location from the probability of finding such a fluctuation anywhere else in the spectrum. The former is associated to the so called *local significance*, whereas the latter is referred to as the *global significance*. The fact that the global significance is usually smaller than the largest local one is often referred to as the “look-elsewhere effect” (LEE). As demonstrated in Ref. [161], the global and local p-values are related to each other by a multiplicative factor, usually referred to as “trial factor”, proportional to the number of independent search regions. In the asymptotic approximation the trial factor grows linearly with the local significance, through a proportional constant that is related to the ratio between the mass range under consideration divided by its resolution. In particular, it can be shown that

$$\text{trial\#} = \frac{p_{\text{global}}}{p_{\text{local}}} \approx \frac{1}{3} \frac{\text{mass range}}{\text{mass resolution}} Z_{\text{local}}. \quad (8.20)$$

The trial factor is best estimated through MC methods as it will be shown in Section 9.2. However, a good agreement with the equation above is obtained.

3799

3800

3801

3802

Results of the search for $\text{WH} \rightarrow \ell\nu b\bar{b}$ resonance

As for all the data analyses carried out by the LHC experiment collaborations, the ones described in this work have been performed “blind”, meaning that the observed data in the signal region are not used in the optimization of the analysis strategy. The various steps involved in the analysis procedures are first carefully scrutinized by the collaboration and it is only after the sign-off that the signal region is unblinded. The results of the unblinding are put through further scrutiny by the collaboration before are made public.

The final results of the analysis performed with 8 TeV data and focused on the search for a heavy charged resonance decaying into W and Higgs bosons in the $\ell\nu b\bar{b}$ final state, are presented and discussed in this chapter. The final observed m_{WH} spectrum is used to check for the presence of a new resonance. In particular, a search is conducted for local enhancement in the m_{WH} distribution, which might be due to a signal. As described in the following, since no significant excesses are found, upper limits are set on the production cross section of the new resonance.

9.1 Final m_{WH} distribution

The predicted number of background events in the signal region after the inclusion of all backgrounds is summarized in Table 9.1 and compared with observations. The yields are quoted in the range $0.7 < m_{\text{WH}} < 3$ TeV. The expected background is derived with the sideband procedure described in Section 8.2. The uncertainties in the background prediction from data are statistical in nature, as they depend on the number of events in the sideband region. The muon channel has more expected background events than the electron channel owing to the lower $E_{\text{T}}^{\text{miss}}$ requirement and its worse mass resolution at high p_{T} .

Table 9.1: Observed and expected yields in the signal region together with statistical uncertainties.

	$e\nu + \text{H-jet}$	$\mu\nu + \text{H-jet}$
Observed yield	9	16
Expected total background	11.3 ± 3.1	14.9 ± 3.1
W+jets	4.7 ± 2.9	7.0 ± 3.1
Top	6.3 ± 1.1	7.3 ± 0.4
VV	0.4 ± 0.1	0.6 ± 0.2

Figure 9.1 shows the final observed m_{WH} spectra after all selection criteria have been applied. The highest mass event is in the electron category and has $m_{\text{WH}} \approx 1.9$ TeV. The observed data and the predicted background in the muon channel agree. In the electron channel, an excess of three events is observed with $m_{\text{WH}} > 1.8$ TeV, where about 0.3 events are expected, while in the muon channel no events with $m_{\text{WH}} > 1.8$ TeV are observed, where about 0.3 events are expected.

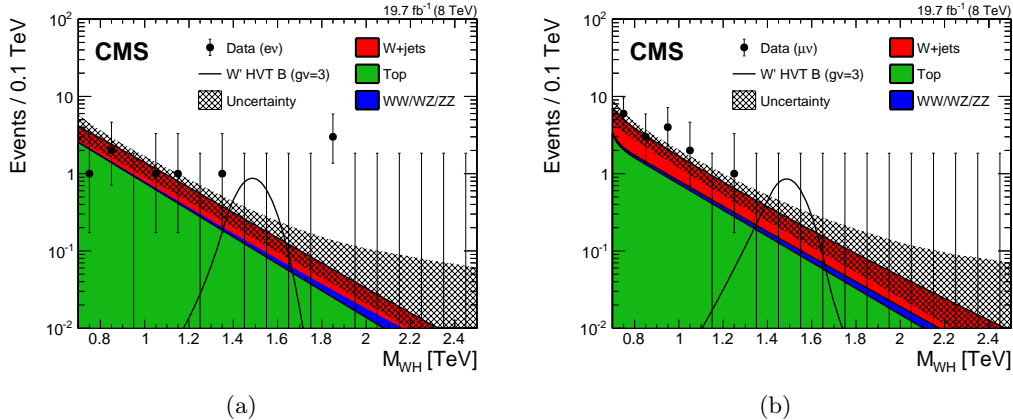


Figure 9.1: Final distributions in m_{WH} for data and expected backgrounds for electron (a) and muon (b) categories. The 68% error bars for Poisson event counts are obtained from the Neyman construction [162]. The hatched region indicates the statistical uncertainty of the fit combined with the systematical uncertainty in the shape. This figure also shows a hypothetical W' signal with mass of 1.5 TeV, normalized to the cross section predicted by the HVT model B with parameter $g_V = 3$ as described in Section.

9.2 Significance of the data

A comparison between the m_{WH} distribution observed in data and the largely data-driven background prediction is used to test for the presence of a resonance decaying into WH. As described in Section 8.6, the statistical test is performed based on a profile likelihood discriminant for an unbinned shape analysis. Systematic uncertainties in the signal and background prediction are treated as nuisance parameters and profiled in the statistical. Uncertainties in the background yield are constrained using log-normal priors, while Gaussian priors are used for uncertainties in the signal and background shape parameters. Uncertainties in the signal yield are not included in the computation of the p-value. Systematic uncertainties in the signal and background yields are treated as nuisance parameters and profiled in the statistical interpretation using log-normal priors. The local significance of the observations is evaluated in the context of the described statistical test, under the assumptions of a narrow resonance decaying into the WH final state and lepton universality for the W boson decay, by combining the two event categories. Correlations arising from the uncertainties common to both channels are taken into account. The result is shown in Fig. 9.2. The highest local significance of 2.2 standard deviations is found for a resonance mass of 1.8 TeV, driven by the excess in the electron channel described in the previous section. The corresponding local significance for a resonance of 1.8 TeV in the electron channel is 2.9 standard deviations, while in the muon channel there is no significance.

Taking into account the look-elsewhere effect (Section 8.6.3), the local significance of 2.9 standard deviations can be translated into a global significance value by computing the trial factor as given by Eq. 8.20. Considering the mass range 0.8–2.5 TeV and an average mass resolution of 100 GeV, a trial factor of ≈ 16.4 is obtained. The factor, when multiplied by the local p-value, gives a global significance of 1.9 standard deviations when searching for resonances over the full mass range and across two channels. In order to cross check this final value, the LEE is also estimated by means of background-only pseudo-experiments. The relation between the global and local significances obtained with this method is shown in Fig. 9.3, and it agrees with the calculation performed with the trial factor. It can be concluded that the results are thus statistically compatible with the SM expectation within 2

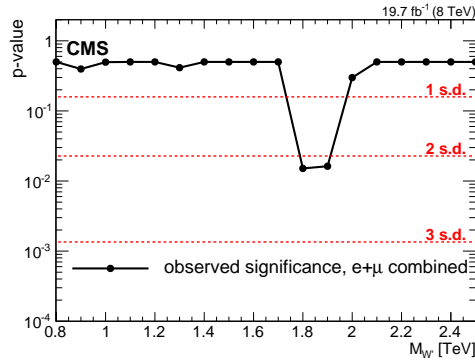


Figure 9.2: Local p-value of the combined electron and muon data as a function of the W' boson mass, probing a narrow WH resonance.

3860 standard deviations.

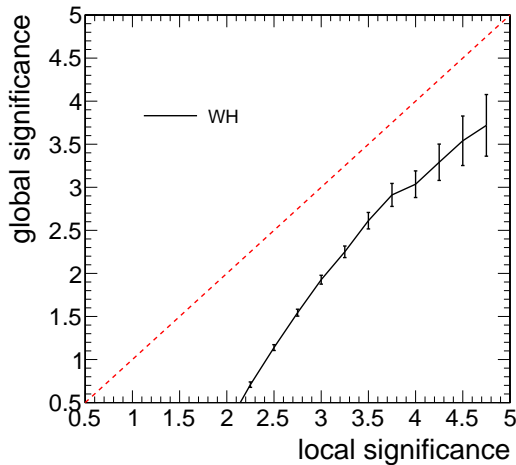


Figure 9.3: Global significance as a function of the local significance which corresponds to the maximal significance in the m_{WH} range 0.8–2.5 TeV in the two categories. The global significance is estimated with a frequentist approach using background-only pseudo-experiments and corresponds to the fraction of toys (translated from a p-value to significance) with at least a certain local significance in the m_{WH} range in the two categories.

3861 9.3 Cross section limits

3862 Since no excesses with significance larger than three standard deviations are observed, upper
 3863 limits are set on the production cross section of the new resonance following the modified-
 3864 frequentist CL_s method described in Section 8.6. Exclusion limits can be set as a function of
 3865 the W' resonance mass, under the narrow-width approximation. The results are interpreted
 3866 in the HVT model B and in the context of the little Higgs model.

3867

3868 Figure 9.4 shows the expected and observed exclusion limits at 95% CL on the product of
 3869 the W' production cross section and the branching fraction of $W' \rightarrow WH$ for the electron and
 3870 muon channels separately, and for the combination of the two. The limits are compared with
 3871 the prediction of the two theoretical models. For the combined channels, the observed and

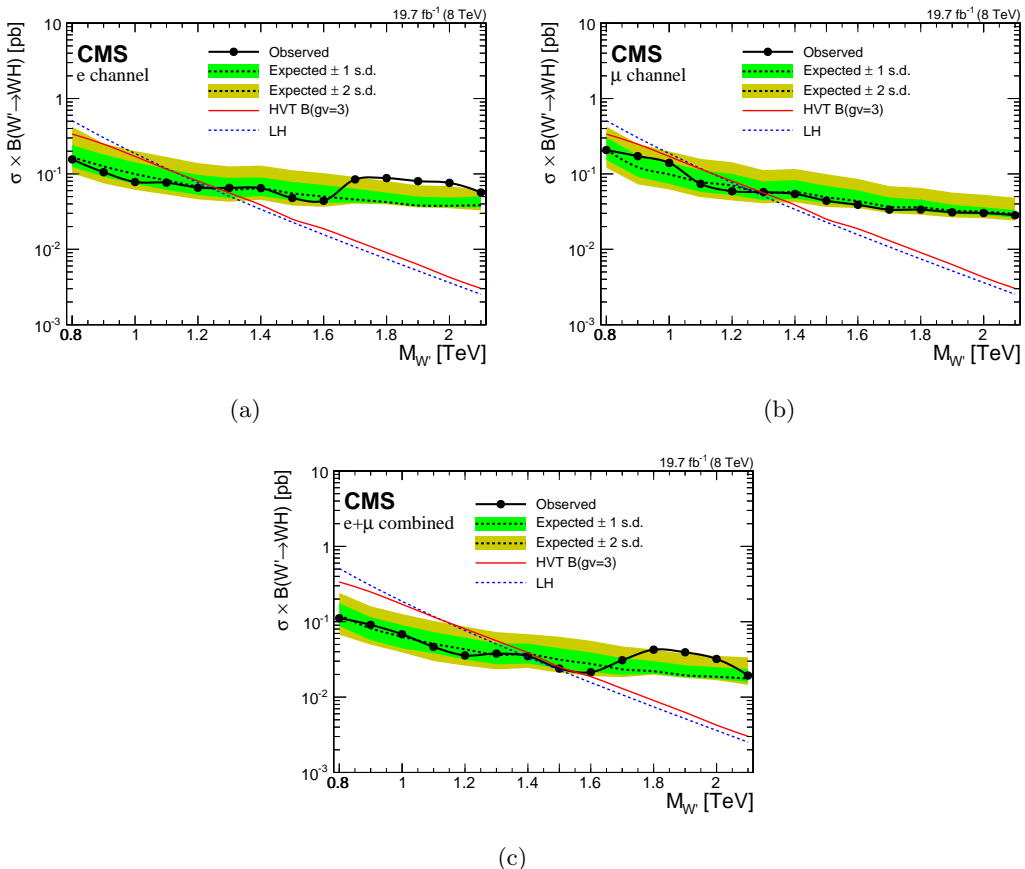


Figure 9.4: Observed (solid) and expected (dashed) upper limits at 95% CL on the product of the W' production cross section and the branching fraction of $W' \rightarrow WH$ for electron (a) and muon (b) channels, and the combination of the two channels (c). The products of cross sections and branching fractions for W' production in the LH and HVT models are overlaid.

expected lower limits on the W' mass are 1.4 TeV in the LH model and 1.5 TeV in the HVT model B. For the electron (muon) channel, the observed and expected lower limits on the W' mass are 1.2 (1.3) TeV in the LH model and 1.3 (1.3) TeV in the HVT model B.

These results are finally combined with other searches for heavy resonances decaying into diboson performed with pp collisions at 8 and 13 TeV as described in Chapter 11.

Results of the search for WW and WZ → $\ell\nu q\bar{q}$ resonances

3880

3881 In this chapter, the final results of the analysis performed with 13 TeV data and focused
 3882 on the search for a heavy resonances decaying into a pair of vector bosons (WW/WZ) in
 3883 the $\ell\nu q\bar{q}$ final state, are presented and discussed. Following the same strategy as for the
 3884 8 TeV data analysis described in the previous chapter, the final m_{WV} spectrum observed in
 3885 data is used to check for the presence of a new resonance. No excess with significance larger
 3886 than three standard deviations are observed and upper limits are set on the production cross
 3887 section of such resonances under a variety of signal benchmarks by combining all the event
 3888 categories.

3889 10.1 Final m_{WV} distribution

3890 The final m_{WV} spectra observed in data and for the background predicted with the α ratio
 3891 method (Section 8.2) for all event categories are shown in Fig. 10.1. The observed data and
 3892 the predicted background are found to well agree. The highest mass events are at $m_{WV} =$
 3893 2.95 and 3.15 TeV for the muon and electron category, respectively.

3894 10.2 Significance of the data and cross section limits

3895 The highest significance of 1.8σ is observed for a bulk graviton signal hypothesis with a
 3896 mass of 2.9 TeV. Since no excesses with significance larger than three standard deviations
 3897 are observed, upper limits are set on the production cross section of the new resonance by
 3898 combining all event categories. The asymptotic approximation of the CL_s criterion described
 3899 in Section 8.6 is followed. The exclusion limits computed with this approach are found to agree
 3900 with the results obtained using the modified frequentist prescription. Systematic uncertainties
 3901 are treated as nuisance parameters in the statistical interpretation using log-normal, and they
 3902 are profiled following the frequentist convention as discussed in Section 8.6.

3903

3904 Exclusion limits are set in the context of the bulk graviton model and of the HVT Models
 3905 A and B, under the assumption of a natural width negligible compared to the experimental
 3906 resolution. Figure 10.2 shows the resulting 95% CL expected and observed exclusion limits
 3907 on the signal cross section as a function of the resonance mass for all signal hypotheses. The
 3908 limits are compared with the product of cross section and branching fraction ($\sigma \times \mathcal{B}$) to WW
 3909 for a bulk graviton with $k/\tilde{M}_{Pl} = 0.5$, and with $\sigma \times \mathcal{B}$ for WZ and WW for spin-1 particles
 3910 predicted by the HVT Models A and B. In this context, a scenario is considered, where the
 3911 W' and Z' bosons are expected to be degenerate in mass (triplet hypothesis). In addition,
 3912 the statistical interpretation is provided in a scenario where only a charged (W') or a neutral
 3913 (Z') resonance is expected at a given mass (singlet hypothesis).

3914 In the narrow-width bulk graviton model, the sensitivity of the search is not large enough
 3915 to set mass limits, however, cross sections are excluded in the range 0.007–0.4 pb. For HVT

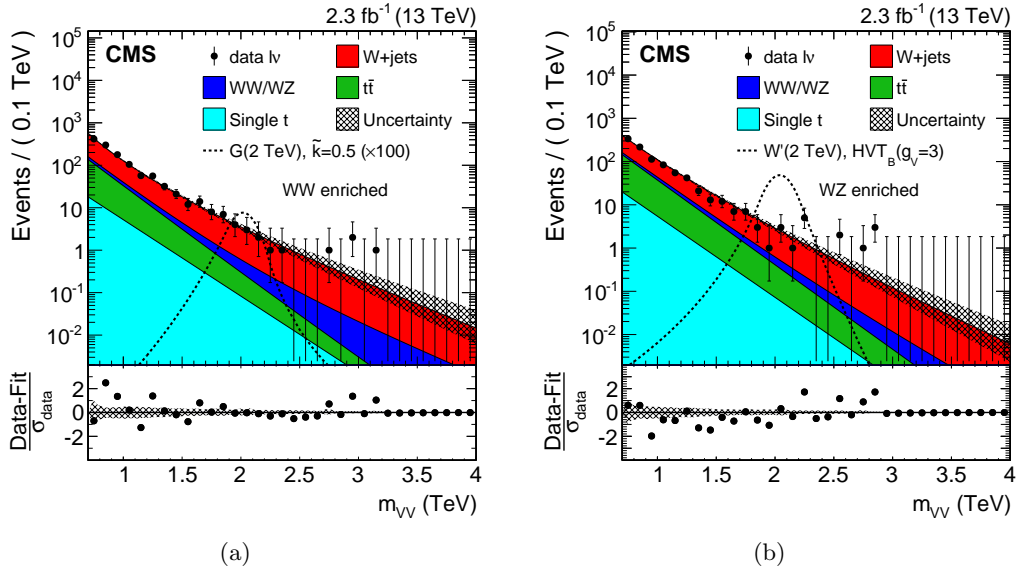


Figure 10.1: Final $m_{W'}$ distributions for data and expected backgrounds obtained combining muon and electron channels in the WW-enriched (a) and WZ-enriched (b) signal regions. In each plot the solid curve represents the background estimation provided by the α ratio method. The hatched band includes both statistical and systematic uncertainties. The data are shown as black points. At the bottom of each plot are the bin-by-bin fit residuals, $(N_{\text{data}} - N_{\text{fit}})/\sigma_{\text{data}}$, shown together with the uncertainty band of the fit normalized by the statistical uncertainty of data, σ_{data} . The distributions for a bulk graviton and for a W' signal are also shown with black dashed lines.

Model A (B), the data exclude singlet W' resonances with masses < 1.6 (1.9) TeV and Z' resonances with masses below < 1.5 (1.6) TeV. Under the triplet hypothesis, spin-1 resonances with masses < 1.9 and < 2 TeV are excluded for HVT Models A and B, respectively.

These results supersede the ones obtained analyzing 8 TeV data, where the lower mass limit of 1.5 TeV for a W' in the context of the HVT model B is reached (Fig. 9.4). However, the most stringent limits are obtained in the final combination of these results with other searches for heavy resonances decaying into diboson with 8 and 13 TeV data, as described in Chapter 11.

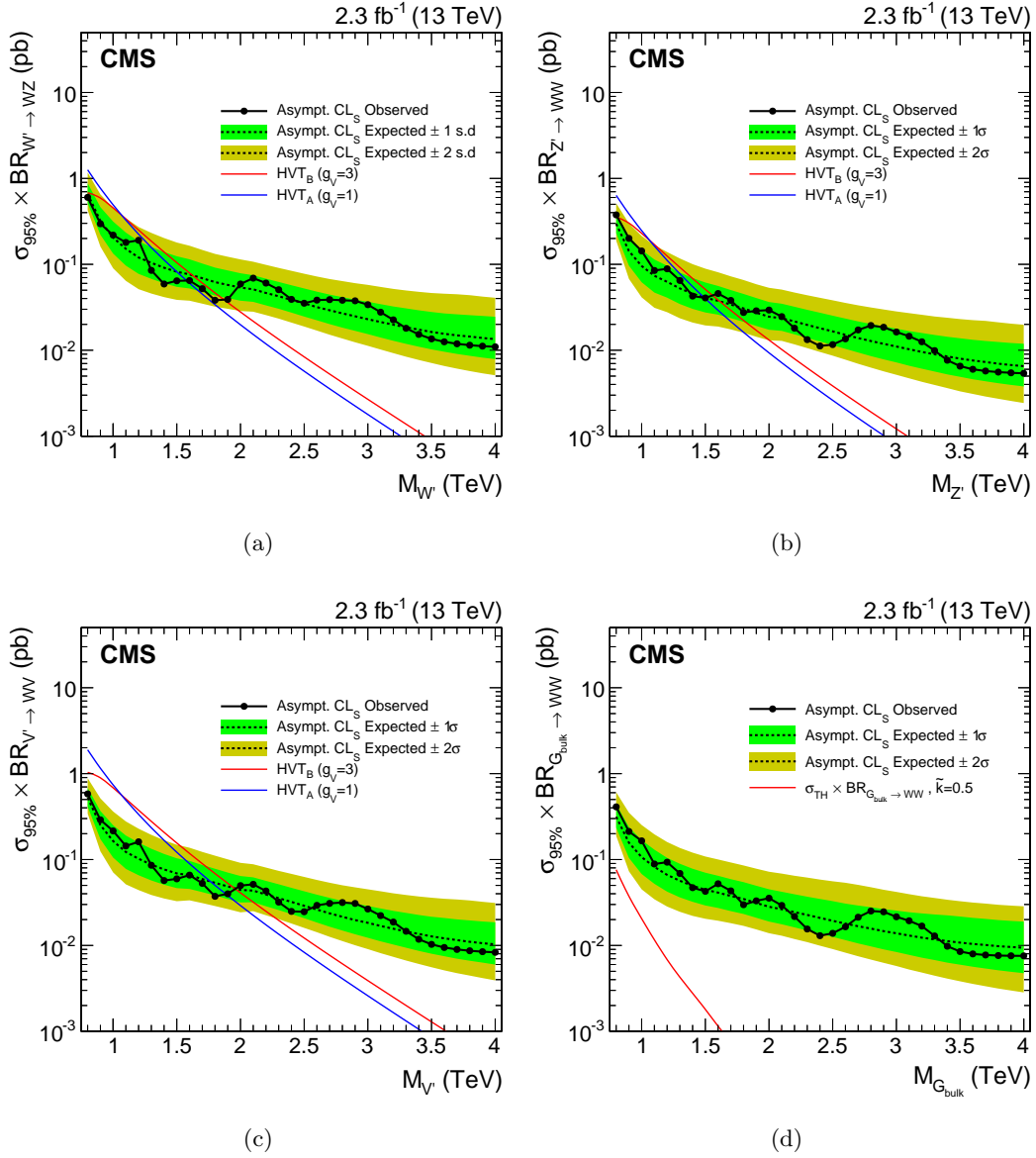


Figure 10.2: Observed (black solid) and expected (black dashed) 95% CL upper limits on the production of a narrow-width resonance decaying to a pair of vector bosons for different signal hypotheses. In the upper plots, limits are set in the context of a spin-1 charged W' (a) and neutral Z' (b) resonances, and compared with the prediction of the HVT Models A and B. (c) Limits are set in the same model under the triplet hypothesis (W' and Z'). (d) Limits are set in the context of a bulk graviton with $k/\bar{M}_{\text{Pl}} = 0.5$ and compared with the prediction.

3924

3925

3926

3927

Combination of searches for diboson resonances at $\sqrt{s} = 8$ and 13 TeV

3928

In addition to the analyses described in this work, several similar searches for narrow-width massive resonances decaying to pairs of W, Z, and Higgs bosons in various final states have been performed with the CMS experiments in both LHC Run 1 and Run 2 [86, 135, 136, 140, 163–166]. As these searches have individually very similar sensitivity to benchmark physics scenarios of interest, a statistical combination to maximize the overall sensitivity is performed and presented in this chapter. Furthermore, the combination of these analyses is fundamental to fully understand the compatibility of the excess observed in the $\ell\nu b\bar{b}$ final state at $m_{\text{WH}} = 1.8$ TeV as discussed in Chapter 9. The interest in this excess was further enhanced by the observation of an excess at the same diboson invariant mass values by the ATLAS experiment in the all-hadronic final state [167].

3939

The analyses taken into account in the statistical combination are based on pp collision data collected by the CMS experiment during 2012 and 2015 at $\sqrt{s} = 8$ TeV and 13 TeV, corresponding to an integrated luminosity of 19.7 fb^{-1} and $2.3\text{--}2.7 \text{ fb}^{-1}$, respectively. Analyses with all-leptonic, semi-leptonic, and all-jets final states are considered. This includes the decay into charged leptons (ℓ) and neutrinos (ν) of W and Z bosons, as well as reconstructed jets containing the decay products of hadronically decaying W or Z bosons. The latter are labeled as q \bar{q} final states that include $W \rightarrow q\bar{q}' \rightarrow \text{jet}$ and $Z \rightarrow q\bar{q} \rightarrow \text{jet}$. For Higgs bosons, hadronic decays labeled as b \bar{b} or q \bar{q} q \bar{q} final states referring to $H \rightarrow b\bar{b}$ or $H \rightarrow WWq\bar{q}'q\bar{q}'$ are considered.

3949

Altogether, results are combined corresponding to the following final states: $\ell\nu q\bar{q}$ (13 TeV, this work) [86], q \bar{q} q \bar{q} (13 TeV) [86], $\ell\ell b\bar{b}/\ell\nu b\bar{b}/\nu\nu b\bar{b}$ (13 TeV) [140], $3\ell\nu$ (8 TeV) [164], $\ell\nu q\bar{q}$ (8 TeV) [135], $\ell\ell q\bar{q}$ (8 TeV) [135], q \bar{q} q \bar{q} (8 TeV) [136], $\ell\nu b\bar{b}$ (8 TeV, this work) [165], q \bar{q} b \bar{b} /6q (8 TeV) [163], q $\bar{q}\tau\tau$ (8 TeV) [166]. As for the analyses described in this thesis, also the other searches feature a similar experimental signature given by highly boosted bosons in the final state. Therefore, all these analyses exploit same V tagging and H tagging algorithms to help resolve jet decays of massive bosons and achieve large suppression of SM backgrounds.

3956

The results are interpreted in the context of the BSM models described in Section 2.3 and summarized in Table 4.1, namely, heavy vector triplet and singlet models predicting W' and Z' bosons, and the bulk graviton model. Combined cross section limits as a function of resonance mass are obtained. This work represents the first combined search for high mass resonances with both WW/WZ and WH/ZH signatures.

3961

This chapter is organized as follows. A summary of the analyses entering the combination is given in Section 11.1. The combination procedure is described in Section 11.2, and finally the results are presented and discussed in Section 11.3.

3964 11.1 Inputs to the combination

3965 A statistical combination is carried out of searches for new heavy resonances that are performed
 3966 on top of the steeply falling invariant mass distribution of two reconstructed W, Z or Higgs
 3967 bosons. Various decay modes of these bosons are considered. The $Z \rightarrow \ell\ell$ candidates are
 3968 reconstructed from electron and muon candidates, while $W \rightarrow \ell\nu$ candidates are reconstructed
 3969 from identified muons or electrons with the method described in Section 6.6, which makes use
 3970 of the missing transverse momentum under the constraint that the $\ell\nu$ invariant mass is equal
 3971 to the known W-boson mass. The $H \rightarrow \tau\tau$ candidates are reconstructed from electron, muon
 3972 and hadronically-decaying τ candidates in combination with missing transverse momentum.
 3973 The $W \rightarrow q\bar{q}'$, $Z \rightarrow q\bar{q}$, $H \rightarrow b\bar{b}$ and $H \rightarrow q\bar{q}'q\bar{q}'$ candidates are reconstructed with jet
 3974 algorithms with a distance parameter of 0.8 (CA for the 8 TeV data analyses, AK for the
 3975 13 TeV analyses).

3976 All analyses are focused on high mass resonances which decay in highly boosted W/Z/H
 3977 bosons. Hence, their decay products are reconstructed close-by in angle, requiring the special
 3978 reconstruction techniques already described previously in this thesis. For highly boosted
 3979 W/Z/H bosons decaying to electron, muon and τ candidates, identification and isolation
 3980 requirements are adapted such that the nearby reconstructed leptons do not reduce the
 3981 identification efficiency.

3982 For highly boosted V bosons decaying to quark anti-quark pairs, the V algorithm described
 3983 in Section 7.2 is applied. In the 8 TeV data analyses, a V jet candidate is identified if its
 3984 pruned mass, m_{jet} , falls in a range around the W or Z mass. In the 13 TeV data analyses,
 3985 two distinct categories enriched in W or Z bosons are defined by two exclusive ranges in m_{jet}
 3986 as described in Section 8.1. In the 8 TeV data analyses the sensitivity is further enhanced
 3987 by distinguishing two categories, a low purity (LP) and a high purity (HP) one based on
 3988 the τ_{21} variable. This same strategy is follow in the dijet 13 TeV analysis. Although the HP
 3989 category dominates the total sensitivity of the analyses, the LP category is retained, since for
 3990 large masses of a new resonance it provides improved signal efficiency with only moderate
 3991 background contamination.

3992 Higgs-boson identification is similarly performed using a pruned jet mass window around
 3993 the Higgs mass together with b-tagging algorithms applied to the H jet or to its subjets as
 3994 described in Section 7.3. To distinguish $H \rightarrow WW \rightarrow q\bar{q}'q\bar{q}'$ jets from background, a similar
 3995 technique as V tagging is applied using the τ_{42} ratio. The selection efficiencies for each signal
 3996 and channel are summarized in Table 11.1.

3997 In all-jets final states, the background dominated by QCD multijets production is estimated
 3998 with a fit of signal+background to the data, where the background is described by a smooth
 3999 functional form. In semi-leptonic final states, the dominant backgrounds from V+jets
 4000 production are estimated using data in m_{jet} sidebands with the method described in Section 8.2.
 4001 In all-leptonic final states, the dominant background from standard model diboson production
 4002 is estimated using simulated events.

4003 More details are given in the following for the analyses where not all signal models
 4004 presented in the combination were originally considered.

4005 11.1.1 Reinterpretations

4006 In the searches for new heavy resonances decaying into a pair of vector bosons (WW, ZZ or
 4007 WZ) in the semi-leptonic ($\ell\nu q\bar{q}$ and $\ell\ell q\bar{q}$) final states [135] with pp collision data collected at
 4008 $\sqrt{s} = 8$ TeV, exclusion limits at 95% CL have been set on the production cross section of
 4009 a bulk graviton. The results were published with a parametrization for the reconstruction
 4010 efficiency as a function of W and Z boson kinematics, enabling a reinterpretation in the

Table 11.1: Summary of signal efficiencies in analysis channels for models with a 2 TeV resonance. For analyses that define high-purity (HP) and low-purity (LP) categories, both efficiencies are quoted in the form HP/LP. Signal efficiencies are given in percent, and include the SM branching fractions of the bosons to the final state in the analysis channel, effects from detector acceptance, as well as reconstruction and selection efficiencies. Values are not indicated for signals for which the analysis channel has no sensitivity.

Channel	Efficiency [%]							
	W'		HVT		Z'		RS bulk	
	WZ	WH	WW	ZH	WW	G _{bulk}	ZZ	
3ℓν (8 TeV)	0.6	-	-	-	-	-	-	-
ℓℓq̄q̄ (8 TeV)	1.1	-	-	0.2	-	-	3.0/1.0	-
ℓνq̄q̄ (8 TeV)	4.8	-	9.4	-	10.6/7.1	-	-	-
q̄qq̄q̄ (8 TeV)	5.9/5.5	0.8/0.7	5.7/5.3	0.8/0.7	3.8/3.1	-	5.7/4.2	-
ℓνbb̄(8 TeV)	-	0.9	-	-	-	-	-	-
q̄q̄τ̄τ̄ (8 TeV)	-	1.2	-	1.3	-	-	-	-
q̄q̄bb̄/6q̄ (8 TeV)	-	3.0/1.8	-	1.7/1.1	-	-	-	-
ℓνq̄q̄ (13 TeV)	10.2	1.7	19.4	-	18.1	-	-	-
q̄q̄q̄q̄ (13 TeV)	9.7/12.3	1.8/2.5	8.2/10.6	1.9/2.6	8.7/12.4	-	11.0/13.5	-
ℓℓbb̄ (13 TeV)	-	-	-	1.5	-	-	-	-
ℓνb̄b̄ (13 TeV)	-	4.0	-	-	-	-	-	-
ννb̄b̄ (13 TeV)	-	-	-	4.2	-	-	-	-

4011 context of neutral and charged the spin-1 resonances as predicted by HVT models. The
 4012 reinterpretation in the context of this model is obtained by rescaling the bulk graviton signal
 4013 efficiencies by scale factors taking into account the different kinematics of W and the Z bosons
 4014 from W' and Z' production compared to the graviton production. The scale factors have
 4015 been derived for each mass point by means of the tables published in Ref. [135]. Since the
 4016 efficiency parametrization is restricted to the HP category of the analyses, the LP category is
 4017 not used for the W' and Z' interpretations of these channels. The m_{jet} window that defines
 4018 the signal regions of the analysis channels is such that the ℓνq̄q̄ channel is sensitive to both
 4019 the charged and neutral resonance predicted by HVT models. This is taken into account in
 4020 the statistical combination.

4021 The searches for new heavy resonances decaying into a pair of vector bosons (WW, ZZ
 4022 or WZ) in the semi-leptonic (ℓνq̄q̄ and ℓℓq̄q̄) [86, 135, 135], and all-hadronic (q̄q̄q̄q̄)
 4023 final states [86, 136] at 8 and 13 TeV, are also sensitive to WH and ZH signatures, since a small
 4024 fraction of jets initiated by Higgs bosons have a pruned jet mass in the range considered
 4025 to identify W or Z bosons. These searches were therefore re-interpreted with WH and ZH
 4026 signals to profit from this additional signal sensitivity. The additional signal efficiencies for
 4027 those signals are indicated in Table 11.1.

4028 The search for resonances in the q̄q̄τ̄τ̄ final state [163] was optimized for a resonance
 4029 Z' decaying into Z and a Higgs boson. However, given the large m_{jet} window ($65 < m_{\text{jet}} <$
 4030 105 GeV) used to identify the hadronically decaying Z boson, this analysis channel is also
 4031 sensitive to the production of the charged spin-1 W' resonance decaying into W and Higgs
 4032 bosons as predicted in HVT models. This overlap is also taken into account in the statistical
 4033 combination.

4034 11.2 Combination procedure

4035 In all the analysis channels a search is performed for a peak on top of the falling background
 4036 distribution in the diboson invariant mass by means of a maximum likelihood fit to the data.
 4037 As done for the main analyses described in this work (Section 8.6), the likelihood function
 4038 is maximized to obtain the best fit of the signal strength modified μ for each signal and
 4039 resonance mass hypothesis. The function is constructed from the reconstructed diboson
 4040 invariant mass distribution observed in data, the background prediction, and the signal
 4041 resonance shape to test for the presence of a new resonance decaying to two bosons. For
 4042 the $3\ell\nu$, $q\bar{q}q\bar{q}$, $q\bar{q}b\bar{b}/6q$, and $q\bar{q}\tau\tau$ analyses, the likelihood function is computed using events
 4043 binned as a function of reconstructed diboson invariant mass as in Equation 8.6. For the
 4044 remaining analyses ($\ell\nu q\bar{q}$, $\ell\ell q\bar{q}$, $\ell\nu b\bar{b}$), the functional form for an unbinned likelihood is
 4045 similarly defined using functional forms that describe the shape of the reconstructed diboson
 4046 invariant mass for background and signal resonance as given by Equation 8.7.

4047 The treatment of the background in the maximum likelihood fit depends on the analysis
 4048 channel. In the $q\bar{q}q\bar{q}$ and $q\bar{q}b\bar{b}/6q$ analyses, the background fit function parameters are left
 4049 floating in the maximum likelihood fit, such that the background prediction is simultaneously
 4050 obtained with the signal μ for every hypothesis. The remaining analyses ($\ell\nu q\bar{q}$, $\ell\ell q\bar{q}$, $\ell\ell b\bar{b}$,
 4051 $\ell\nu b\bar{b}$, $\nu\nu b\bar{b}$) follow the same procedure as for the analyses described in this work: the
 4052 background is estimated using data sidebands and uncertainties related to its parametrized
 4053 shape are treated as nuisance parameters constrained with Gaussian probability density
 4054 functions in the maximum likelihood fit. Except for the cases described in Section 11.1, which
 4055 have been found to be negligible, selection are exclusive. The combined likelihood is then
 4056 obtained from the product of the likelihoods of each individual analysis channel.

4057 The asymptotic approximation of the CL_s criterion (Section 8.6.2) is used with the test
 4058 statistic given by Eq. 8.8 to set upper limits on the cross section for resonance production.
 4059 When combining 8 and 13 TeV analyses, limits are set on the signal scale factor μ taking into
 4060 account the production cross section ratio evaluated from theory between 8 TeV and 13 TeV.

4061 The dominant sources of systematic uncertainties are treated as nuisance parameters
 4062 constrained with a log-normal probability density function. All nuisance parameters are
 4063 profiled following the frequentist convention discussed in Section 8.6. When the likelihoods
 4064 of multiple analyses channels are combined, the correlation of systematic effects across
 4065 analysis channels is taken into account by categorizing the uncertainties into fully correlated
 4066 (associate to same nuisance parameter) and fully uncorrelated (associate to different nuisance
 4067 parameters). Table 11.2 summarizes which uncertainties are treated as correlated among 8
 4068 and 13 TeV analyses, electron and muon channels, HP and LP categories and W, Z and Higgs
 4069 enriched categories in the combination. Further categorisation within individual analyses are
 4070 described therein.

4071 The most important and only nuisance parameters treated as correlated between 8 and
 4072 13 TeV analyses are those related to the PDFs and the choice of factorization (μ_f) and
 4073 renormalization (μ_r) scales used to estimate the signal cross sections. They have been re-
 4074 evaluated for this combination for both 8 and 13 TeV analyses, estimating the full impact on
 4075 the expected signal yield rather than the impact on only the signal acceptance. The PDF
 4076 uncertainties are evaluated using the NNPDF 3.0 [68] PDFs. The uncertainty related to the
 4077 choice of μ_f and μ_r scales is evaluated following the proposal in Refs. [150, 151] by varying
 4078 the default choice of scales in the following 6 combinations of factors: $(\mu_f, \mu_r) \times (1/2, 1/2)$,
 4079 $(1/2, 1)$, $(1, 1/2)$, $(2, 2)$, $(2, 1)$, and $(1, 2)$. The experimental uncertainties are all treated as
 4080 uncorrelated between 8 and 13 TeV. At 13 TeV the systematic uncertainties are dominated by
 4081 the statistical uncertainty of the datasets used to evaluate scale factors applied to the signal

Table 11.2: Correlation of systematic uncertainties in the signal prediction across analyses. A “yes” signifies 100% correlation, and “no” means uncorrelated. The asterisk indicates information based on distribution and on yields.

Source	Information	Analyses			
		8 and 13 TeV	e and μ	HP and LP	W-, Z-, and H-enriched
Lepton trigger	yield	no	no	yes	yes
Lepton identification	yield	no	no	yes	yes
Lepton momentum scale	yield*	no	no	yes	yes
Jet energy scale	yield*	no	yes	yes	yes
Jet energy resolution	yield*	no	yes	yes	yes
Jet mass scale	yield	no	yes	yes	yes
Jet mass resolution	yield	no	yes	yes	yes
b tagging	yield	no	yes	yes	yes
W tagging τ_{21} (HP/LP)	yield	no	yes	yes	yes
Integrated luminosity	yield	no	yes	yes	yes
Pileup	yield	no	yes	yes	yes
PDF	yield	yes	yes	yes	yes
μ_f and μ_r scales	yield	yes	yes	yes	yes

4082 simulation to reproduce data.

4083 11.3 Results

4084 In this section the combination of the individual analysis channels described in Section 11.1
 4085 is presented, for each of the signal hypothesis described in Section 2.3. For each channel the
 4086 95% CL exclusion limits on the signal strength modifier $\mu = \sigma_{95\%}/\sigma_{\text{theory}}$ are presented.

4087 11.3.1 Limits on W' and Z' singlets

4088 Figures 11.1(a) and 11.1(b) show the comparison and combination of the results obtained in
 4089 the 8 and 13 TeV searches for a W' singlet resonance for model A and model B, respectively.
 4090 The 95% CL exclusion limits on the signal strength in the resonance mass range $0.6 < m_{W'} <$
 4091 4 TeV for model A and $0.8 < m_{W'} < 4$ TeV for model B are shown. Table 11.3 summarizes
 4092 the resulting resonance mass exclusion limits. Below resonance mass values of about 1.4
 4093 TeV, the $3\ell\nu$ channel at 8 TeV is most sensitive. At higher masses, the $q\bar{q}q\bar{q}$ search at 13
 4094 TeV dominates the sensitivity. The overall sensitivity benefits from the combination up to
 4095 resonance masses of about 2 TeV, lowering the cross section exclusion limit by up to a factor
 4096 1/3 when comparing to the most sensitive single channel. Above masses of 2 TeV the 8 TeV
 4097 channels do not add any significant contribution compared to the $q\bar{q}q\bar{q}$ search at 13 TeV. The
 4098 observed mass limit is not affected by the combination compared to that obtained from the
 4099 13 TeV searches. However, the expected mass limit is slightly improved from 2.3 to 2.4 TeV.

Table 11.3: Exclusion lower limits at 95% CL for resonant contributions in HVT models A and B.

model	Observed limit (TeV)	Expected limit (TeV)
Singlet W' (model A)	2.3	2.1
Singlet Z' (model A)	2.2	2.0
Triplet W' and Z' (model A)	2.4	2.4
Singlet W' (model B)	2.3	2.4
Singlet Z' (model B)	2.3	2.1
Triplet W' and Z' (model B)	2.4	2.6

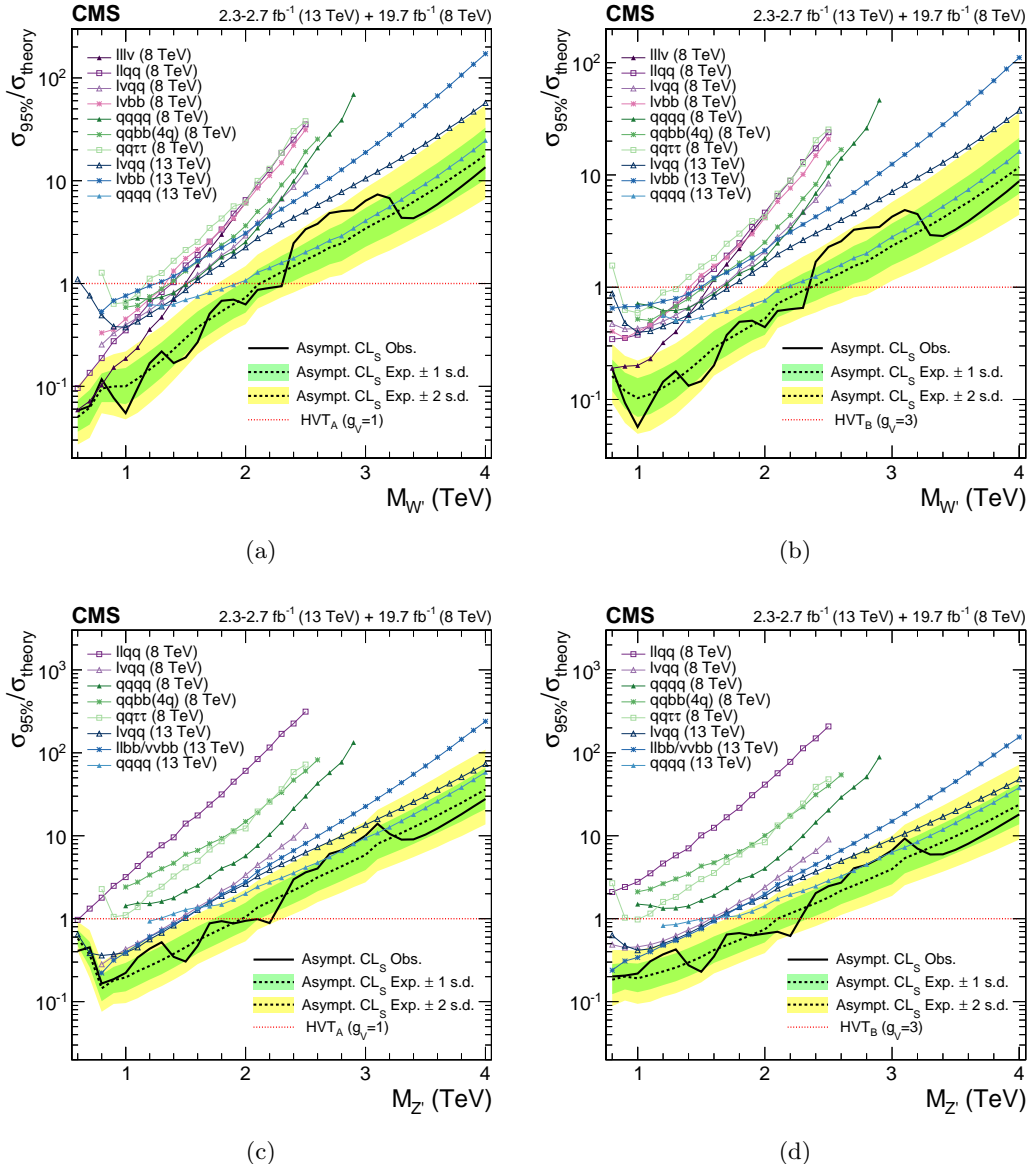


Figure 11.1: Exclusion limits at 95% CL on the signal strength for (top) $W' \rightarrow WZ/WH$ and (bottom) $Z' \rightarrow WW/ZH$ in (left) HVT model A and (right) HVT model B as a function of the resonance mass obtained by combining the 8 and 13 TeV diboson searches. In each of the plots the different colored lines correspond to the searches entering the combination.

Figures 11.1(c) and 11.1(d) show the comparison and combination of the results obtained in the 8 and 13 TeV searches for a Z' singlet resonance for model A and model B, respectively. The $\ell\nu q\bar{q}$ channel at 8 TeV and the $q\bar{q}q\bar{q}$, $\ell\nu q\bar{q}$, $\ell\ell b\bar{b}/\nu\nu b\bar{b}$ channels at 13 TeV dominate the sensitivity over the whole range, with 8 and 13 TeV analyses giving almost equal contributions for masses below 2 TeV. Above this value, the sensitivity is mainly driven by the 13 TeV analyses. Under this signal hypothesis the sensitivities reached by the 8 and 13 TeV channels are similar at low resonance masses. As for the W' case, the mass limit is not affected by the combination compared to what is obtained from the 13 TeV searches.

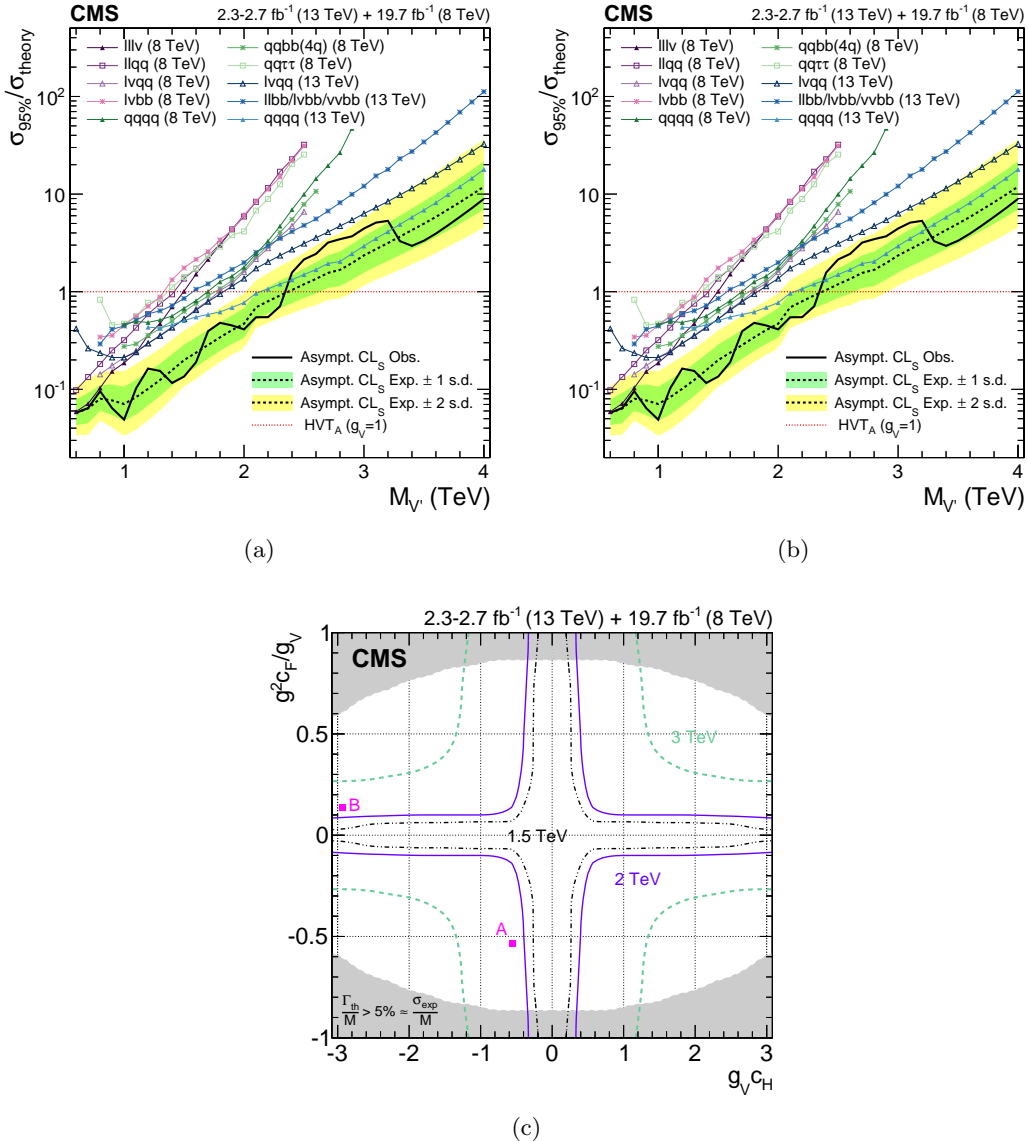
4108 11.3.2 Limits on heavy vector triplet V' 

Figure 11.2: Exclusion limits at 95% CL on the signal strength in (a) HVT model A and (b) HVT model B as a function of the resonance mass obtained by combining the 8 and 13 TeV diboson searches. In both plots the different colored lines correspond to the searches entering the combination. (c) Exclusion regions in the plane of the HVT-model couplings ($g_V c_H$, $g^2 c_F/g_V$) for three resonance masses, 1.5, 2, and 3 TeV, where g denotes the weak gauge coupling. The points A and B of the benchmark models used in the analysis are also shown. The boundaries of the regions outside these lines that are excluded by this search are indicated by the solid and dashed lines. The areas indicated by the solid shading correspond to regions where the resonance width is predicted to be more than 7% of the resonance mass and the narrow-resonance assumption is not satisfied.

4109 Figures 11.2(a) and 11.2(b) shows the comparison and combination of the results obtained
 4110 in the 8 and 13 TeV searches for a heavy vector triplet scenario. As for the W' and Z' cases,
 4111 the observed mass limit of 2.4 TeV obtained combining 8 and 13 TeV searches is determined
 4112 by the 13 TeV channels.

4113 In Fig. 11.2(c), a scan of the coupling parameters and the corresponding observed 95% CL

exclusion contours in the HVT model from the combination of the 8 and 13 TeV analyses are shown. The parameters are defined as $g_{\text{VC}} \text{H}$ and $g^2 c_F / g_V$, in terms of the coupling strengths (Section 2.3.3) of the new resonance to the Higgs boson and to fermions. The range of the scan is limited by the assumption that the new resonance is narrow. A contour is overlaid, representing the region where the theoretical width is larger than the experimental resolution of the searches, and hence where the narrow-resonance assumption is not satisfied. This contour is defined by a predicted resonance width of 5%, corresponding to the narrowest resonance mass resolution of the considered searches.

11.3.3 Limits on bulk graviton

Figure 11.3 shows the comparison and combination of the results obtained in the 8 and 13 TeV VV searches in the bulk graviton scenario with $k/\bar{M}_{Pl} = 0.5$. The sensitivity is mainly driven by the 13 TeV $q\bar{q}q\bar{q}$ and $\ell\nu q\bar{q}$ channels. Under this signal hypothesis, the sensitivity reached by the 13 TeV searches supersedes the 8 TeV combination down to very low resonance masses (0.7 TeV), since this signal is produced via gluon-fusion in contrast to the HVT resonances produced via $q\bar{q}$ annihilation. Hence, the contribution given by 8 TeV channels is less significant with respect to the spin-1 resonance hypotheses. The combination yields the most stringent signal strength limits on narrow bulk graviton resonances ($k/\bar{M}_{Pl} = 0.5$) to date in the mass range from 0.6 to 4 TeV.

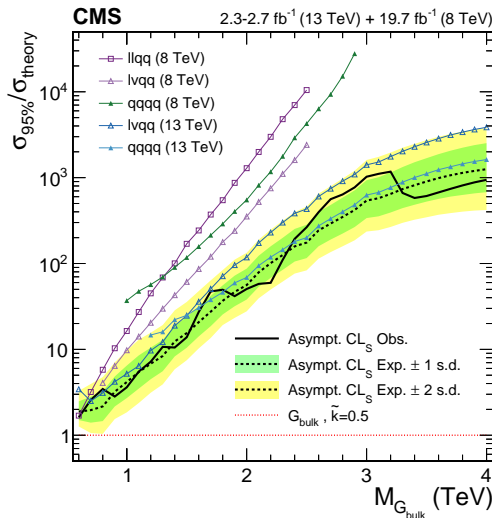


Figure 11.3: Exclusion limits at 95% CL on the signal strength as a function of the resonance mass obtained by combining the 8 and 13 TeV diboson searches in the bulk graviton scenario with $k/\bar{M}_{Pl} = 0.5$. The different colored lines correspond to the searches entering the combination.

11.3.4 Significance at 2 TeV

ATLAS reported an excess in the all-hadronic $VV \rightarrow q\bar{q}q\bar{q}$ search corresponding to a local significance of 3.4σ for a W' resonance with a mass of 2 TeV [167]. For CMS, the largest deviation of 2.2σ has been observed in the semi-leptonic $WH \rightarrow \ell\nu b\bar{b}$ search described in this work (Chapter 9). The combined significance of the 8 and 13 TeV CMS searches in the range 1.8–2.0 TeV is here evaluated and showed in Figure 11.4 for a W' hypothesis.

Combining all 8 TeV VH searches in the W' hypothesis, the local significance of the excess at 1.8 TeV is slightly reduced to 2.1σ . Combining all 8 TeV VV and VH searches,

it is increased back to 2.2σ , since the VV searches observed a small deviation in the same resonance mass range. However, in combination with the 13 TeV VV and VH searches, the overall significance at 1.8 TeV is reduced to 0.8σ . This remains the largest significance for the overall combination of 8+13 TeV searches considering all signal hypothesis over the mass range 1.8–2.0 TeV, thus not supporting the excesses observed in the two individual channels in 8 TeV data.

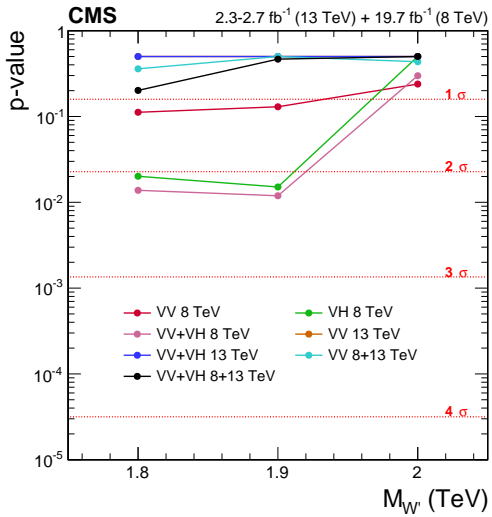


Figure 11.4: Local p-values of the excesses observed in the resonance mass range 1.8–2 TeV in the various combinations of searches for a W' hypothesis.

Conclusions

4149 A search for new massive resonances decaying into a pair of vector bosons (WW/WZ) or
 4150 into a W boson and a Higgs boson (WH) in semi-leptonic final states has been presented.
 4151 In particular two analyses and a statistical combination with previous searches have been
 4152 described.

4153 The first analysis is performed with pp collision data at $\sqrt{s} = 8$ TeV collected in 2012, and
 4154 is focused on the final state given by the W boson decay to $\ell\nu$, with $\ell = \mu$ or e, and the Higgs
 4155 boson decay to a pair of bottom quarks. The second analysis is performed with pp collision
 4156 data at $\sqrt{s} = 13$ TeV collected in 2015, and also in this case a final state is considered given
 4157 by the $W \rightarrow \ell\nu$ decay together with the decay of the second boson into quarks, where the
 4158 second boson (V) can be either a W or a Z.

4159 In both analyses, each event is reconstructed as a leptonic W boson candidate recoiling
 4160 against a jet with mass compatible with the Higgs or V boson mass for the $\ell\nu b\bar{b}$ or $\ell\nu q\bar{q}$
 4161 analysis channel, respectively. Specialized methods, referred to as V tagging and H tagging,
 4162 are exploited to help resolve jet decays of massive bosons and achieve large suppression of
 4163 background from the W+jets process. In particular, the H tagging algorithm combines jet
 4164 substructure information with identification techniques based on the peculiarities of b jets.

4165 In the $\ell\nu b\bar{b}$ analysis channel, no excess of events above the standard model prediction
 4166 is observed in the muon channel, while an excess with a local significance of 2.9 standard
 4167 deviations is observed in the electron channel at $m_{WH} \approx 1.8$ TeV. Taking into account the
 4168 look-elsewhere effect, the results are statistically compatible with the standard model within
 4169 2 standard deviations. In the context of the little Higgs and the heavy vector triplet models,
 4170 upper limits at 95% CL are set on the W' production cross section in a range from 100 to
 4171 10 fb for masses between 0.8 and 2.5 TeV, respectively. Within the little Higgs model, a lower
 4172 limit on the W' mass of 1.4 TeV has been set. A heavy vector triplet model that mimics the
 4173 properties of composite Higgs models has been excluded up to a W' mass of 1.5 TeV.

4174 These results are improved by the limits set by the analysis in the $\ell\nu q\bar{q}$ final state. No
 4175 evidence for a signal is found in this search with new 2015 data, and the result is interpreted
 4176 as an upper limit on the production cross section of a narrow-width resonance as a function
 4177 its mass, in the context of several benchmark models for spin-1 and spin-2 resonances. In
 4178 particular, for the same heavy vector triplet model as mentioned above the data exclude a
 4179 W' resonance with masses < 1.9 TeV.

4180 However, the best results are provided by a statistical combination of all searches performed
 4181 in CMS with 8 and 13 TeV data for massive resonances decaying to pairs of W, Z, and Higgs
 4182 bosons in various final states. The results are interpreted in the context of heavy vector
 4183 singlet and triplet models predicting a W' and a Z' decaying to WZ, WH, WW, and ZH and
 4184 a model with a bulk graviton that decays into WW and ZZ. The combined significance of a
 4185 potential resonances at 1.8–2.0 TeV has been evaluated and has been found to be 0.8 standard
 4186 deviations for the hypothesis of a W', thus the excesses observed in the $\ell\nu b\bar{b}$ channel in
 4187 8 TeV data is not supported. The combination yields mass limits at the 95% CL on spin-1
 4188 resonance in the range 2.2–2.4 TeV, depending on the specific benchmark. The most stringent
 4189 cross section limits on a narrow-width bulk graviton resonance with $\tilde{k} = 0.5$ to date are set
 4190 in the mass range from 0.6 to 4 TeV.

4191

Part II

4192

Calibration and upgrade of the CMS pixel barrel detector

4193

Introduction

4197 The extremely high particle fluxes at small distances from the interaction point require the
 4198 innermost tracking layers to be composed of pixel devices delivering spatial information
 4199 with high resolution. Over the full acceptance of the CMS detector, the silicon pixel system
 4200 provides two or more hits per track, which allow secondary vertices to be reconstructed
 4201 for tagging long-lived objects, like b or c quarks and τ -leptons, and to distinguish them
 4202 from a large background of light quark and gluon jets. It is also an important detector for
 4203 identifying the primary vertex, and separating it from dozens of additional pileup vertices.
 4204 Hence, this detector plays a special role in the physics analyses described in this thesis. In
 4205 fact, its performance has a large impact on the identification of b-quark jets as well as on jet
 4206 substructure observables, being the latter highly dependent on pileup. The pixel detector
 4207 consists of central barrel layers (BPix) and forward disks (FPix). This part of the thesis is
 4208 dedicated to different aspects of the BPix system, including its calibration and upgrade.

4210 The pixel detector was installed in 2008 and showed an excellent performance during
 4211 the first period of data taking at the LHC (2010–2012). During the first long shut-down of
 4212 the machine (2012–2015), that allowed to increase the center-of-mass energy of the collisions
 4213 to 13 TeV, the detector was extracted for repair and re-installed into CMS, and successfully
 4214 continued taking data throughout the first two years of LHC Run 2 (2015–2016). The excellent
 4215 performance of the BPix at the re-start of collisions have been made possible by the efforts
 4216 spent during LS1 in recovering the broken channels as well as in re-calibrating the detector
 4217 after the radiation damage suffered during Run 1.

4218 The current planning for the LHC and injector chain foresees other two long shut-downs,
 4219 LS2 and LS3 (Fig. 13.1). In the period through LS2 (2019–2020), the injector chain will be
 4220 improved, and during LS3 (2024–2026) the LHC itself will be upgraded with new components
 4221 to optimize the bunch overlap at the interaction region. Further upgrades are foreseen beyond
 4222 2030.

4223 The present pixel detector was originally designed for a luminosity of $1 \times 10^{34} \text{ cm}^{-2} \text{ s}^{-1}$
 4224 and a pileup of 25 in LHC collisions with 25 ns bunch spacing. These parameters have already
 4225 been exceeded in 2016, when collisions at 13 TeV happened at instantaneous luminosities
 4226 up to $1.5 \times 10^{34} \text{ cm}^{-2} \text{ s}^{-1}$ with an average pileup of 25 [54]. Based on the excellent LHC
 4227 performances to date, it can be anticipated that the peak luminosity will keep increasing
 4228 until 2018 reaching values up to $1.7\text{--}1.8 \times 10^{34} \text{ cm}^{-2} \text{ s}^{-1}$, and beyond these after LS2. Thus,
 4229 starting from 2017 the CMS experiment must be prepared to operate with an average pileup
 4230 of 50 as a baseline, with the possibility that it may be significantly higher (up to 100) if
 4231 collisions will happen at 50 ns bunch spacing after LS2. In order to maintain efficient and
 4232 robust tracking at CMS, the pixel detector will be replaced with an upgraded pixel system,
 4233 referred to as *Phase 1 pixel upgrade*, in the LHC winter shutdown 2016/2017. The design
 4234 of the upgraded detector allows to cope with the aforementioned harsh conditions expected
 4235 at the LHC in the upcoming years. A more complex upgrade step is planned for the LS3
 4236 and referred to as *Phase 2 upgrade*. It will include deeper changes in the whole CMS, among
 4237 which a complete substitution of the entire tracker detector system.

4238 The Phase 1 pixel detector is expected to be operative up to the Phase 2 upgrade, around

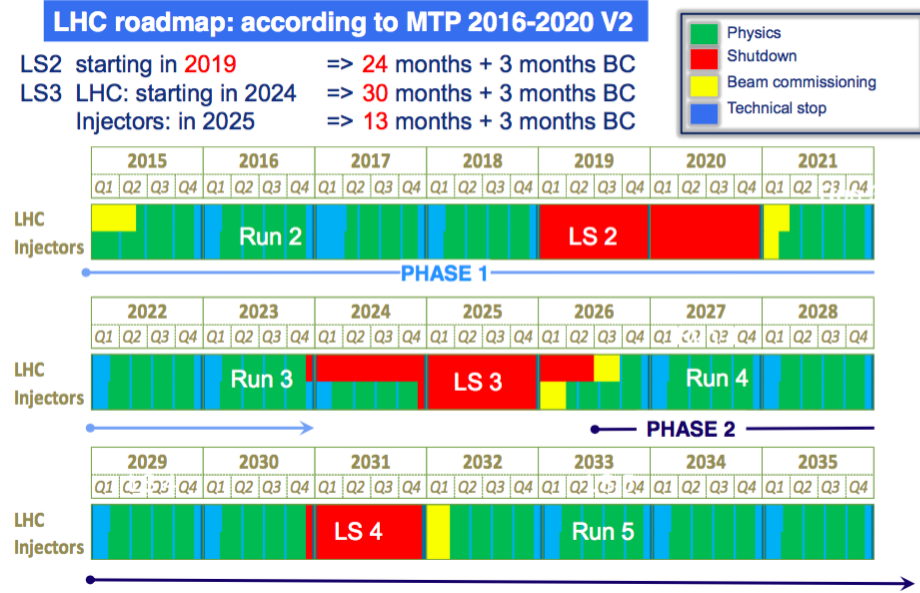


Figure 13.1: The outline LHC schedule up to 2035 as officially approved in June 2015 [168].

4239 2023. During the planned 5 years of operation before LS3, the LHC is expected to deliver
 4240 about 500 fb^{-1} . The proposed Phase 1 upgrade system has been designed and tested to be
 4241 operative up to this target, with the only exception of the innermost layer. In fact, the
 4242 estimated hadron fluence that will be accumulated in the innermost pixel layer is too high for
 4243 the pixel sensor, thus a replacement of the innermost barrel layer is planned after 250 fb^{-1} .

4244 The Phase 1 pixel upgrade project is now at its last stage of assembly and testing of the
 4245 entire system. A test stand has been setup at the University of Zurich (UZH) in 2014 and
 4246 was operated until the end of 2016. It has been fundamental to test the performance of the
 4247 complete upgraded BPix system and gain experience in its operation. This activity is crucial
 4248 in view of the success of the installation and commissioning of the new detector planned for
 4249 the beginning of March 2017, as well as for excellent and stable performance during its first
 4250 year of data-taking.

4251 This part of the thesis is organized as follows. First, a description of the design and
 4252 functionality of the present BPix detector is given in Chapter 14. The work carried out
 4253 during LS1 aimed at optimizing the detector for LHC Run 2 is discussed in Chapter 15.
 4254 The same chapter also includes details on the operations conducted during its re-installation
 4255 into CMS and commissioning. Chapter 16 provides an overview of the design and features
 4256 of the upgraded BPix system. In this chapter, a section is dedicated to the description
 4257 of the test stand at UZH which I contributed to setup. The last section focuses on the
 4258 development of new tests and procedures to be used during the upgraded detector assembly
 4259 and commissioning.

The CMS pixel barrel detector

4263

4264 This chapter provides an introduction to the design and functionality of the present CMS
 4265 pixel barrel detector. It was developed, designed and built at the Paul Scherrer Institute
 4266 (PSI) in cooperation with the Eidgenössische Technische Hochschule Zurich (ETH) and
 4267 the University of Zurich (UZH). Section 14.1 gives an overview of the detector design and
 4268 mechanical structure, followed by a description of the detector module and its main building
 4269 blocks (Section 14.2). In Section 14.3, the detector readout and control system are described.
 4270 The last section provides an introduction to the structure and functionality of the pixel online
 4271 software (POS) used for controlling and calibrating the detector. The detector calibration
 4272 and its performance at the re-start of collisions in 2015 are discussed in the next chapter.

4273 14.1 Design

4274 The CMS BPix detector [169] consists of three cylindrical layers at mean radii of 4.4, 7.3
 4275 and 10.2 cm from the center of the detector and with a length of 53 cm. A three dimensional
 4276 representation of the detector can be seen in Fig. 14.1(a). The layers are composed of 768
 4277 modular detector units that consist of thin segmented silicon sensors, with a pixel size of
 4278 $100 \times 150 \mu\text{m}^2$ providing about 48 million readout channels. The pixels are almost square
 4279 shaped in order to achieve a similar track resolution in both the $r\phi$ and z direction.

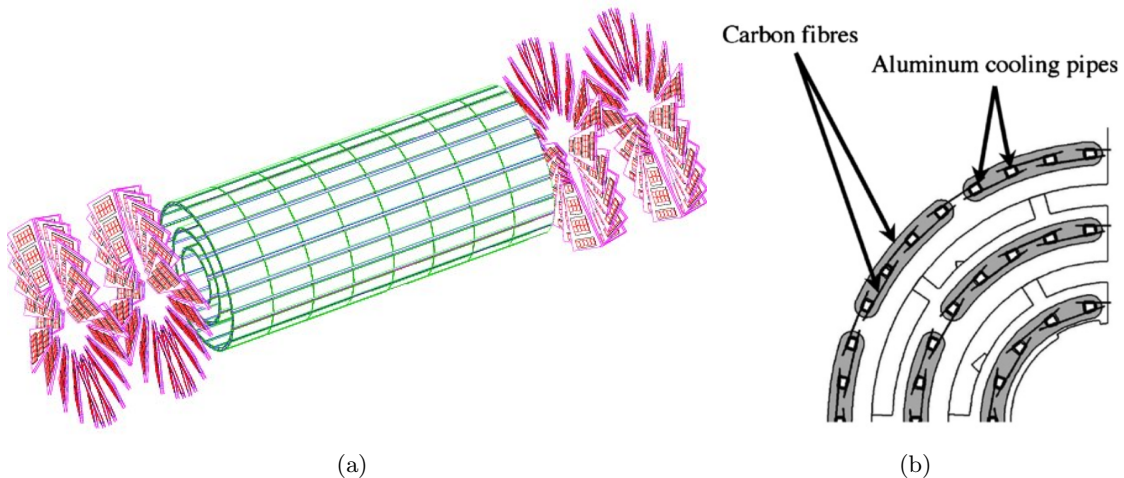


Figure 14.1: (a) Layout of the CMS pixel detector with three barrel layers (green) and two forward disks at each endcap (red). (b) Detailed view in $r\phi$ of the geometric layout.

4280 Sets of 8 modules are screwed on 0.25 mm thin carbon fibre ladders that are glued to
 4281 aluminum cooling pipes with 0.3 mm wall thickness. The cylindrical shape of the barrel is
 4282 achieved by assembling several ladders on each layer half shell. The three half shells are then
 4283 mounted together at the end flange building up half of the BPix detector. The total number
 4284 of ladders per half shell is 10 for layer 1, 16 for layer 2 and 22 for layer 3. To guarantee full

4285 spatial coverage ladders are mounted with overlap on alternating sides of the cooling tubes.
 4286 This is shown in Fig. 14.1(b). The resulting two detector parts are mechanically separated
 4287 and the half shells are joined together with special ladders equipped with half modules. The
 4288 overall layout results in 96 half modules and 672 full modules.

4289 The BPix detector is connected to four 2.2 m-long half cylinders (supply tubes) that carry
 4290 the services along the beam pipe, accommodate the cooling lines and house the electronics for
 4291 detector readout and control. The supply tubes are a complex system in design as well as in
 4292 production due to the thin radial shell thickness (1–2 cm), the large number of circuits, plugs
 4293 and sensors, the fine wires and thin printed circuit boards that are assembled. The detector
 4294 and the supply tubes are connected via a six layer printed circuit board (PCB) which is
 4295 mounted on the detector end flange and distributes the power and the control signals to the
 4296 individual modules. The final BPix system consists of two independent half cylinders placed
 4297 at $+x$ (inner) and $-x$ (outer) coordinates, with each half shell connected to two supply tubes
 4298 placed at $+z$ and $-z$ coordinates.

4299 A liquid cooling system based on C_6F_{14} is used to cool down the sensors and the electronics.
 4300 The cooling plant is located outside the CMS detector and the fluid is guided along the
 4301 ladders inside the aluminum pipes (Fig. 14.1(b)).

4302 14.2 Detector modules

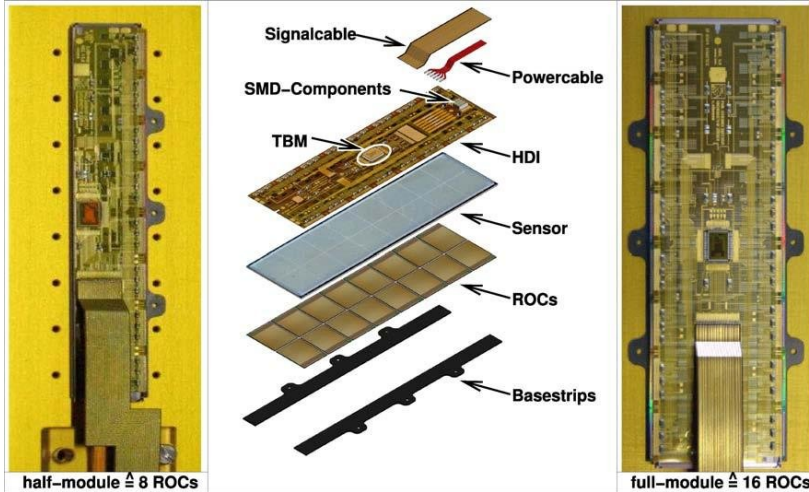
4303 The BPix modules are made of a thin, segmented silicon sensor [170] with a dimension of
 4304 $66.6 \times 18.6 \text{ mm}^2$ that enables the detection of particles that pass through it by measuring
 4305 the ionization charge that they produce. The charge measurement is performed by readout
 4306 chips (ROCs) [171] that are connected to the sensor using the bump-bonding technique with
 4307 Indium solder. Full modules consist of two rows of 8 ROCs, while half modules use a smaller
 4308 sensor with 1×8 ROCs. Each ROC has a size of $7.9 \times 9.8 \text{ mm}^2$ and reads a matrix of 4160
 4309 pixel readout channels. Table 14.1 summarizes the configuration of full and half modules
 4310 on the three different BPix detector layers. The ROCs are wire-bonded to a three-layer
 4311 high-density interconnect (HDI) flex printed circuit glued onto the backside of the sensor. A
 4312 token bit manager (TBM) chip [172], mounted on the top of the HDI, controls the readout of
 4313 the ROCs, receives all external control signals, and distributes them to the ROCs. Base-strips
 4314 made of $250 \mu\text{m}$ thick silicon nitride (Si_3N_4) are glued underneath the ROCs allowing the
 4315 module to be mounted on the mechanical support structure. A power cable consisting of 6
 4316 copper coated aluminum wires is soldered to the HDI and brings analog, digital and high
 4317 voltage to the module. The control and readout signals are sent through a two layer Kapton
 4318 signal cable which is wire-bonded to the HDI. Additionally, the HDI distributes the signals
 4319 and the voltages to the ROCs. The signal cables from the modules are plugged into the end
 4320 flange that exists on both sides of the barrel and connects the three layers to the detector
 4321 supply tubes. The modules are attached to cooling frames, with the cooling tubes being an
 4322 integral part of the mechanical structure. The size of a full module is $66.6 \times 26 \text{ mm}^2$ and the
 4323 weight is up to 3.5 g depending on the length of the signal and power cables. The average
 4324 power consumption of a full module is 2 W. A view of each component of the BPix module is
 4325 shown in Fig. 14.2.

4326 14.2.1 Sensor

4327 The sensor is made from a n -type silicon wafer with a thickness of $285 \mu\text{m}$. Charged particles
 4328 that travel through the sensor material leave electron-hole pairs as the result of multiple
 4329 interactions with the atoms in the material. For charged particles at intermediate energies

Table 14.1: Number of modules, readout chips and pixel channels for the three detector layers.

radius (cm)	full modules #	half modules #	ROCs #	pixels (10^6)
4.4	128	32	2304	9.6
7.3	224	32	3840	16.0
10.2	320	32	5376	22.4
Total	672	96	11520	48

**Figure 14.2:** Picture of a BPix half module (left) and full module (right). In the center, the components of the module are shown. From top to bottom: the Kapton signal cable, the power cable, the HDI with the TBM, the silicon sensor, the 16 ROCs and the base strips [173].

4330 (0.1 $\leq \beta\gamma \leq 1000$), the average energy loss dE in a thickness dx of material is described by
 4331 the *Bethe-Bloch formula*

$$-\left\langle \frac{dE}{dx} \right\rangle = 4\pi N_A r_e^2 m_e c^2 z^2 \frac{Z}{A} \frac{1}{\beta^2} \left[\frac{1}{2} \ln \frac{2m_e c^2 \beta^2 \gamma^2 W_{\max}}{I^2} - \beta^2 - \frac{\delta(\beta\gamma)}{2} \right]. \quad (14.1)$$

4332 In the above equation, N_A is the Avogadro's number, r_e the classical electron radius,
 4333 m_e the electron mass, z the charge of the particle, Z (A) the atomic number (mass) of the
 4334 material ($Z = 14$ and $A = 28.1$ u for silicon), W_{\max} the maximum energy transfer to an
 4335 electron in a single collision, I the mean excitation energy, and δ a density effect correction.
 4336 At a particle velocity $\beta \approx 0.96$ ($\beta\gamma \approx 3$) a broad minimum is reached. At higher energies
 4337 the logarithmic term leads to a slow rise again, which is eventually canceled by the density
 4338 correction. A particle with an energy loss in the minimum is called a minimum ionizing
 4339 particle (MIP).

4340 The energy loss in a finite medium is subject to statistical fluctuations well described by
 4341 a *Landau distribution* (Fig. 14.3). If a particle is not stopped in the medium, the energy loss
 4342 (and therefore the number of charge carriers) varies around the peak of the distribution (most
 4343 probable value or MPV). In rare but measurable cases (δ -rays or δ -electrons), the transferred
 4344 energy is large, so that these cases are responsible for the asymmetric long tail towards high
 4345 charge deposits. Due to this tail the most probable value of energy transfer is about 30%
 4346 lower than the average value. For a MIP crossing the sensor at an angle of 90° the most

probable number of electron-hole pairs generated in $1\text{ }\mu\text{m}$ of silicon is 76. Therefore, a MIP generates a signal of about 22,500 electron-hole pairs (MPV).

4349

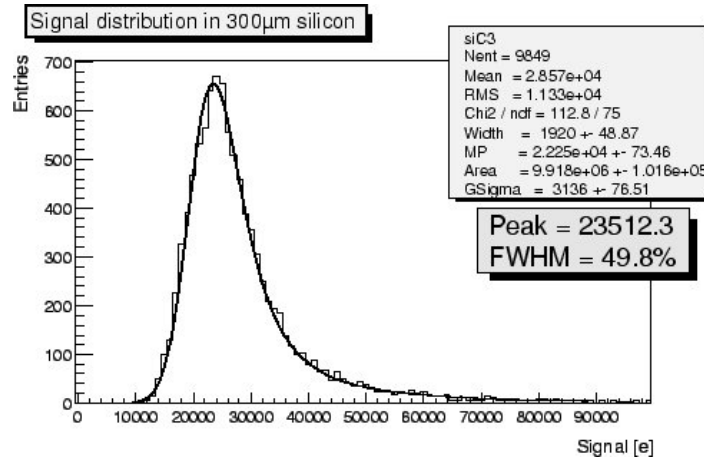


Figure 14.3: Measured MIP signal distribution in a Silicon detector of $300\text{ }\mu\text{m}$ thickness.

4350 The silicon sensor used for the CMS pixel detector adopts a double sided n^+ -in- n design:
 4351 pixels consist of high dose n^+ implants on a high resistance n substrate. The backside of
 4352 the substrate is p-doped, therefore the p-n junction is placed on this side of the sensor. A
 4353 cross-section of the sensor is shown in Fig. 14.4. If the junction is reverse biased, a depletion
 4354 zone forms that extends towards the pixel implants. In this zone, an electric field is established
 4355 that allows ionization charge to drift. Electrons drift toward n^+ implants while holes drift
 4356 toward the back of the sensor. In Fig. 14.4, the bulk of the silicon is p-type because of the type
 4357 inversion occurring in the bulk after prolonged exposure to high fluences of radiation. In fact,
 4358 the effective concentration of impurities gradually decreases with exposure, until a transition
 4359 to the other type material behavior occurs. At this stage, the depletion zone grows
 4360 from the pixel implants toward the back of the sensor, enabling the collection of electrons
 4361 even when the sensor is only partially depleted. Extremely high operating voltages can
 4362 therefore be avoided, reducing the problems of leakage currents and high-voltage breakdowns.
 4363 Furthermore, the double-sided processing of n^+ -in- n detectors allows a guard ring concept
 4364 which keeps all sensor edges at ground potential and avoids the risk of disruptive discharges
 4365 to the very closely spaced ROCs.

4366 Additional processing is needed on the readout side to electrically isolate the n^+ implants
 4367 from each other. The electron accumulation layer induced by ionizing radiation otherwise
 4368 tends to short-circuit the pixel implants. A moderated p-spray technique is used, which
 4369 consists of a medium dose p-type Boron implants.

4370

4371 The position resolution of single-pixel hits is given by the pixel pitch divided by the $\sqrt{12}$.
 4372 However, the spatial resolution can be improved exploiting charge sharing among adjacent
 4373 pixels. A group of pixels collecting a signal from the same particle is usually called “cluster”.
 4374 Significant charge sharing is a consequence of the Lorentz drift in the strong magnetic field
 4375 of 3.8 T inside CMS. In fact, charge carriers released by the ionizing particle in the silicon
 4376 sensor do not follow the electric field lines to the collection electrodes, but are deflected by
 4377 the Lorentz force (Fig. 14.4). Furthermore, the readout of the pulse height allows for an
 4378 interpolation of the amounts of collected charge for each of the pixels in the cluster. This
 4379 effect influenced the choice of the barrel pixel size which have been optimized to achieve

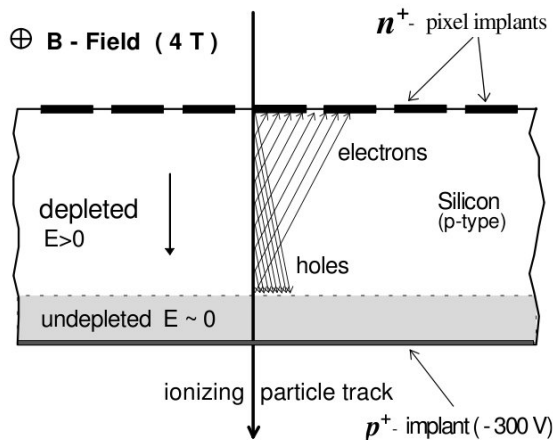


Figure 14.4: Illustration of a charged particle crossing a sensor of the CMS pixel detector. The charge carriers produced by the passage of the ionizing particle are collected at the high dose n^+ implants.

optimal spatial resolution. Two-pixel clusters and the interpolation allow a much better resolution, limited only by fluctuations of the charge deposition. Since division of the signal charge among more than two pixels increases the data rate and reduces the signal charge per pixel without an improvement of the resolution, an ideal choice of the pixel size in the direction perpendicular to the magnetic field ($r\phi$) is therefore given by the length over which charges are spread when they reach the surface of the sensor. For a $\sim 300\text{ }\mu\text{m}$ sensor thickness and a Lorentz angle of 28° this amounts to $\sim 150\text{ }\mu\text{m}$. A slightly smaller size of $100\text{ }\mu\text{m}$ was chosen to maintain charge sharing, and hence resolution, after irradiation. The area of a pixel must also be large enough to accommodate the readout electronics. With one dimension fixed by the Lorentz drift, this leads to a more or less quadratic shape of $100\text{ }\mu\text{m}(r\phi) \times 150\text{ }\mu\text{m}(z)$, resulting in comparable resolution in both directions. The typical pixel resolutions are $9\text{ }\mu\text{m}$ in $r\phi$ and $24\text{ }\mu\text{m}$ in z (Section 15.5).

14.2.2 Readout chip

The readout chip is responsible for measuring the charge deposited by a particle in the sensor's pixel. It amplifies and samples the signal with a time resolution of 25 ns, which is the time between two LHC bunch crossings. The pixel hit information has to be stored on-chip during the CMS Level-1 trigger latency of $3.2\text{ }\mu\text{s}$ after which they are either read out or discarded. Each pixel sensor is connected via a bump bond to its own readout circuit on the ROC, referred to as *Pixel Unit Cell* (PUC). The PUCs are arranged in 26×80 double columns. Each double column represents an independent readout unit controlled by a circuit sitting in the column periphery. The ROC periphery controls the PUC, buffers data and houses global functions common to all pixels.

To control and optimize the readout, 26 digital-to-analog converters (DAC) can be programmed using a serial protocol similar to I²C modified to operate at 40 MHz.

The PUC can receive a signal either through a charge deposition in the sensor or by injecting a calibration signal. Within the PUC, the signal is first passed through a two stage pre-amplifier/shaper system to a comparator where zero-suppression is performed. It compares the shaper output to a threshold value which is programmed by a DAC distributed globally to all pixels. Since variations of the threshold of the individual pixels caused by

4409 transistor mismatch, voltage drops or preamplifier gain variations can lead to an increased
 4410 noise rate, each pixel has a 4-bit DAC to trim the threshold. Furthermore, a mask bit allows
 4411 to disable noisy pixels. When the rising edge of the signal has passed the threshold, the
 4412 signal height is sampled after some delay and stored in the sample-and-hold capacitance until
 4413 the readout mechanism is started from the periphery. During this time the pixel becomes
 4414 insensitive.

4415 Since the L1 trigger latency time in CMS is $3.2\ \mu\text{s}$ (128 bunch crossings), the information
 4416 of a hit pixel, including the associated bunch crossing number and the analog pulse height
 4417 signal, can not be kept on the pixel itself during this time without introducing a significant
 4418 inefficiency. In the *Column Drain Architecture* chosen for the CMS pixel readout, all pixel
 4419 hits occurring in a pixel double column are immediately and quickly copied into the column
 4420 periphery in order to free the pixels for the next hit. In this case the probability of having
 4421 a second hit in the pixel during the latency is significantly reduced. Each double column
 4422 informs the column periphery immediately of any hits that have been occurred by sending to
 4423 the periphery a current with adjustable intensity. The column periphery writes the value
 4424 of the bunch crossing counter into a time stamp buffer and initiates a token scan of the
 4425 double column passing a readout token from cell to cell. Once the hit pixel is found, in
 4426 the readout block of the PUC the token signal initiates the transfer of pixel address and
 4427 analog pulse-height information, which are stored in a data buffer located in the periphery
 4428 waiting for the L1 trigger. The hit pixels remain inactive until their hit information has been
 4429 transferred. The double column periphery verifies the trigger by comparing the time stamp
 4430 with a counter running behind the bunch crossing counter by the trigger delay. In case of
 4431 agreement the column is set into readout mode and the data acquisition is stopped, otherwise
 4432 the data are discarded. When the readout token arrives at the double column periphery the
 4433 validated data are sent to the chip periphery and the double column is reset. The ROCs are
 4434 read out serially via a 40 MHz analog link.

4435 A picture of the BPix readout chip is shown in Fig. 14.5.

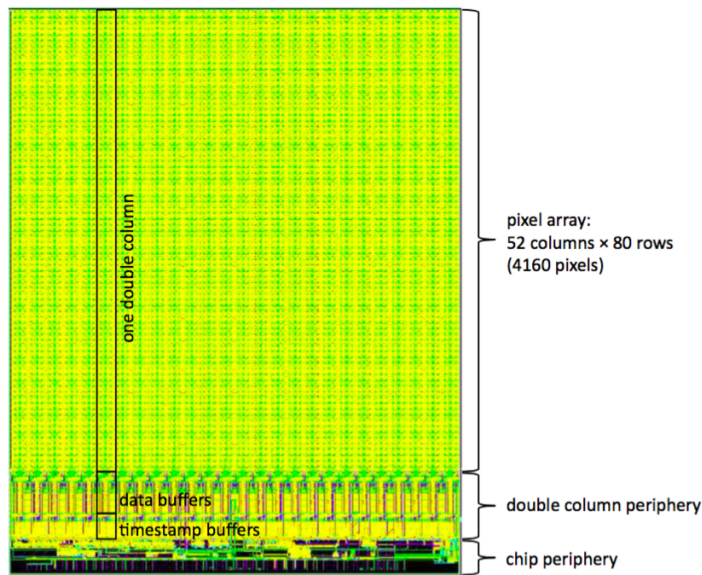


Figure 14.5: Picture of the CMS pixel readout chip showing the three main building blocks: double column, double column periphery and chip periphery [50].

4436 14.2.3 Token bit manager

4437 A token bit manager chip is wire-bonded to the HDI and controls the readout of the ROCs. It
 4438 serves as an interface for data acquisition and programming and is responsible to synchronize
 4439 the readout of the ROCs on the module. For each incoming L1 trigger, the TBM sends a
 4440 token in a fixed order from chip to chip, and waits until the token returns from the last chip
 4441 in the chain. The chip that has the token transmits all hits for a given trigger and then
 4442 passes the token to the next chip. Upon the arrival of the token, each ROC sends a three
 4443 clock cycle header. While the header is transmitted, the token is passed through the chip
 4444 looking for a double column with validated hits belonging to that token. The length of the
 4445 header is sufficient for the token to skip all 26 double columns if no triggered hits were present
 4446 and to be passed on to the next chip with the right timing. Triggers and readout tokens
 4447 are both counted and hits are only readout when the token number matches the readout
 4448 number. It must be ensured that exactly one token for every trigger is issued and that there
 4449 is never more than one. The ROCs in the module are either serviced by a single token that
 4450 sequentially passes through all the 16 chips, or a second channel in a dual TBM chip is used
 4451 such that the ROCs are divided into two groups of eight. This method is employed for the
 4452 two innermost layers of the detector which experiences higher hit rates per module than the
 4453 others. It requires two separate buses for the readout of the two groups of ROCs, and the
 4454 data streams are also individually transmitted through two separate readout links for the
 4455 data acquisition. The TBM multiplexes the signal from the ROCs, adds a header and a
 4456 trailer to the data stream and drives the signal through the readout link. In addition, the
 4457 TBM distributes the L1 trigger and the clock to the ROCs. The header contains an event
 4458 number and the trailer a status information, such as the stack overflow warning.

4459 The TBM keeps track of triggers arriving while the token is still under way with a trigger
 4460 stack of 32 entries that is filled each time a trigger arrives and reduced every time a token
 4461 returns. In case of a stack overflow, the TBM withholds the incoming triggers from the ROCs
 4462 until the stack is reduced. It notifies the data acquisition that events have become lost in
 4463 this case. The TBM chip also includes a communication component called the HUB which
 4464 serves as a port for programming commands sent from the DAQ.

4465 14.3 Detector readout and control

4466 A schematic drawing of the pixel readout and control systems is shown in Fig. 14.6. The path
 4467 on the right shows the readout part of the system. Signals from a group of ROCs are amplified
 4468 and converted into a 40 MHz analog optical signal in the analog opto-hybrid circuits mounted
 4469 on the supply tube. Optical fibers allow the data to be transferred over approximately 60 m
 4470 distance to the underground counting room, where a VME front-end driver unit (FED) [174]
 4471 digitizes the signal, builds event fragments and sends them to the DAQ. The signal path in
 4472 the middle shows the fast detector control link. In the counting room, the control signals
 4473 are driven by front-end control (FEC) units [175] which are used to program the detector
 4474 modules. The signals enter the supply tubes through optical fibers to be converted in digital
 4475 opto-hybrid circuits. Several other electronic devices are needed by the system and are placed
 4476 on the supply tubes. Some of these components need to be programmed. This happens
 4477 through a dedicated slow control link corresponding to the signal path on the left. Also
 4478 shown in Fig. 14.6 is the Timing Trigger and Control (TTC) [176] system which distributes
 4479 the clock and trigger signals to all detector components. The individual electronic devices of
 4480 the detector readout and control system are described in more detail in the following.

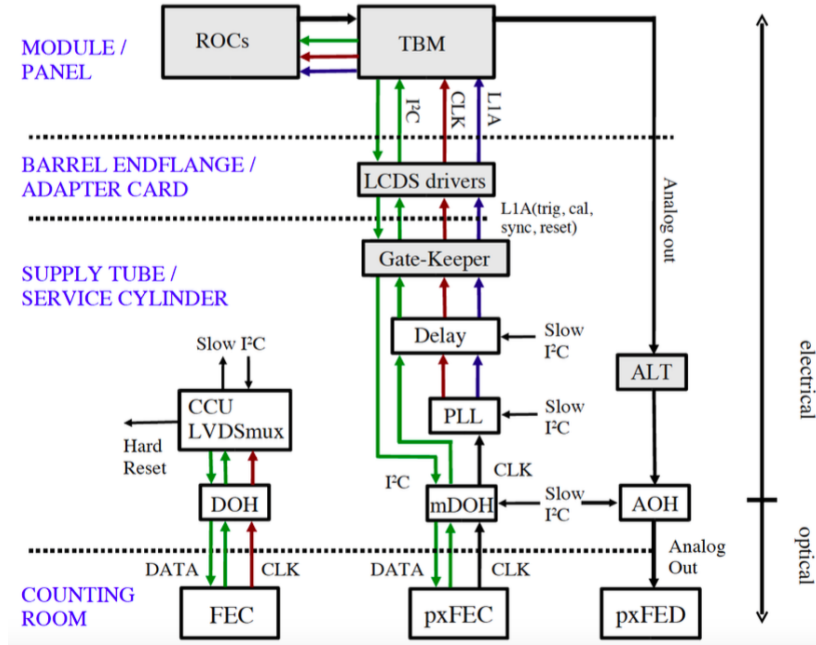


Figure 14.6: Overview of the BPix readout and control system [177].

14.3.1 Readout of the analog signal

An example of an analog readout signal from a module with a single pixel hit is shown in Fig. 14.7. The TBM header uses eight clock cycles and starts with three ultra black levels (UBL). An UBL is simply a large negative signal level well outside of the range of pixel data. The three UBLs are followed by a black level (BL), which defines the zero level of the differential analog signal. The four remaining clock cycles encode an 8-bit event number. The minimal readout of each ROC starts with an UBL, a BL and a level called last DAC which represents the value of the most recently programmed DAC. A pixel hit adds a block of six clock cycles to the ROC minimal readout: two for the double-column address, three for the row address, and one for the pulse height. In order to speed up the transmission of digital pixel hit information while maintaining the global 40 MHz clock, the pixel addresses are not sent in a common binary fashion, but the available signal amplitude is divided into six possible analog levels (2.5 bits/clock). The readout is terminated by the TBM trailer, containing two UBLs, two BLs, and four clock cycles with the TBM status information.

The data stream which contains all hit information belonging to a single trigger is sent out by the TBM through the module Kapton cable. The Kapton cable consists of differential analog lines separated by quiet lines from the lines for the fast digital signals. The analog signals are split from the digital signals on the end flange boards that drive the signals to the PCB on which the analog optical hybrids (AOHs) [178] are plugged. The electric analog signals are amplified in an Analog Level Translator (ALT) chip and converted into 40 MHz analog optical signals in the AOHs. Each AOH is equipped with 6 lasers with adjustable gain and threshold, which drive the signal through optical fibers to the front-end drivers.

A total of 32 FED modules, located in the underground counting room, receive the data packets. They convert the signals from optical to electrical, perform the digitization at the LHC frequency, and decode the pixel hit information. The pixel FED also builds event fragments and sends them to the CMS central DAQ system. It is a 9 U VME module designed at HEPHY Vienna that includes optical receivers, ADCs and several FPGAs for

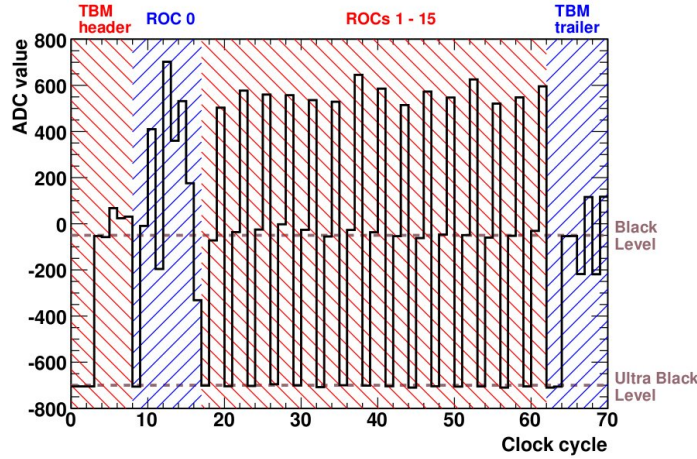


Figure 14.7: Analogue readout of a pixel module with one hit in ROC 0.

4508 signal processing.

4509 A FED has three opto-receiver devices each of which has twelve input channels where
 4510 the fibers terminate. Each input channel is equipped with a 10-bit ADC. The ADC has a
 4511 clock with adjustable phase w.r.t. the global clock in steps of 1.6 ns to select the optimum
 4512 digitization sampling point for each input. A programmable offset voltage can be set for each
 4513 optical input in order to compensate for bias shifts in the analog signal. An additional, single
 4514 optical input receives TTC signals such as clock, trigger and reset. Each channel has a 1k
 4515 words 32-bit data buffer (FIFO1) which stores the digitized module signal (Fig. 14.7). The
 4516 data package from four or five (depending on the location) FIFO1 channels are collected in a
 4517 FIFO2 with a size of 8k words and a width of 64 bits plus 4 control bits. During the data
 4518 transfer to FIFO2 the input event number is compared with that of the CMS TTC system.
 4519 The data of all FIFO2 memories are collected by two final memories (FIFO3) of 8k words
 4520 each over two buses of 64+4 bits at 40 MHz. Four front FPGAs, each handling 9 inputs,
 4521 house FIFO1 and FIFO2 buffers, while a center FPGA houses the FIFO3 where the whole
 4522 event fragment is built, together with the S-link connection to the central DAQ. The FED
 4523 can also be operated in a transparent mode making unprocessed ADC output data available
 4524 for calibration and testing purpose.

4525 14.3.2 Detector control and programming

4526 The detector control and programming is performed through front-end control modules (pixel
 4527 FECs or pxFECs) located in the underground counting room. The function of the pixel
 4528 control system is to send the 40 MHz clock, the trigger and control signals (e.g. resets) to the
 4529 front-end electronics, and to program all front-end devices (TBMs and ROCs). All the signals
 4530 are sent through optical fibers and converted to electrical signals by digital optical hybrids
 4531 (DOHs) [178] mounted on the supply tube before forwarding them to the pixel modules. A
 4532 DOH is connected to four optical fibers, two for receiving and two for sending signals. The
 4533 LHC 40 MHz clock and trigger information is encoded in one signal which is sent over a
 4534 single fiber to the DOH. A modified version of the common I²C protocol has been developed
 4535 to cope with the required volume of the data that have to be downloaded to configure the
 4536 detector modules. The main modifications include the increase of the clock speed to 40 MHz
 4537 and dropping the requirement of an acknowledge signal. Each DOH contains two laser drivers
 4538 and two PIN diodes. The DOH is mounted on the digital opto-board together with other

4539 electronic devices needed by the system. In particular, a phase-locked loop (PLL) chip [179] is
4540 used to split the clock from the trigger, and the Delay25 chips [180] adjust the relative phases
4541 of all control signals. The Gate-Keeper chip converts the LVDS signals used by PLLs and
4542 Delay25s to low current differential signals (LCDS) used by the pixel front-end chips. Finally,
4543 the LCDS-driver chips mounted on the end flange PCB are used to drive the signals on the
4544 Kapton cables to each detector module. In addition, these chips are used to compensate the
4545 signal phases for the different Kapton cable lengths.

4546

4547 The electronics on the supply tubes (DOHs, PLLs, Delay25s, AOHs, and so on) have to be
4548 controlled and programmed. This is achieved through a system of four CCU (Communication
4549 and Control Unit) boards equipped with 9 CCU chips each [181]. This is indicated in Fig. 14.6
4550 as “slow I²C”, since the standard I²C protocol is implemented for this task. The boards are
4551 mounted on the supply tubes and each of them supervises one quarter of the detector.

4552

4553 The slow control links are implemented as a ring architecture. A ring consists of 9 CCUs,
4554 two optical drivers and receivers that bring clock, trigger and control data to the CCUs,
4555 and a front-end controller (tracker FEC or tkFEC) which provides the communication with
4556 the CCUs and the programming signals. Each CCU distributes the digital control and
4557 programming signals to a set of individual boards forming one readout sector of the detector.
4558 A CCU chip supports two I²C channels to communicate with the front-end electronics, and
4559 three PIA channels to generate the necessary signals to reset the circuits and the ROCs of
4560 one sector. Eight CCUs are used for the control of the eight sectors in which each supply tube
4561 is divided, the ninth CCU is a dummy chip used for redundancy. Since a large number of
4562 front-end channels depend on the same control link, a very high reliability of the system is of
4563 utmost importance. A CCU failure leads to a loss of communication to all electronics attached
4564 to it. A redundancy scheme based on doubling signal paths and bypassing of interconnection
4565 lines, between the CCUs and between the CCUs and the FEC, is supported. The dummy
4566 CCU allows to mitigate a single DOH failure. The CCU is equipped with two DOHs which
4567 form separated control rings and thus ensure a high operational reliability. The DOHs on the
4568 CCU board are programmed by the first two CCU chips.

4568 14.3.3 Supply tubes

4569 As mentioned previously in this chapter, the readout and control circuits of the pixel detector
4570 are integrated on four supply tube half cylinders. In addition, the supply tubes bring the
4571 power and cooling lines to the detector. A schematic view of a supply tube is shown in
4572 Fig. 14.8. A supply tube is divided into 8 sectors which contain the power lines and electronics
4573 of two readout groups, one serving the modules of the first two layers, the other serving the
4574 modules of the third layer. One sector includes an analog opto-board with six AOHs, a digital
4575 opto-board with two DOHs, two PLL chips, two Delay25 chips and two Gate-Keeper chips.
4576 A total of 192 AOHs and 72 DOHs are used for the pixel barrel detector. For each sector, 44
4577 optical fibers drive the communication with the front-end modules, 36 for the analog readout
4578 and 8 for the digital control. The CCU board is placed in the central sector of the supply
4579 tube.

4580

4581 The stability of the analog signal is strongly affected by the temperature dependence
4582 of the AOHs. A shift of 50 ADC counts is observed in the level of the analog signal for a
4583 temperature variation of the AOH of 1° C. The FED is able to internally correct for a drift
4584 within a temperature range of ±2° C. Consequently, the temperature of the AOHs has to be
4585 controlled within a very narrow range in order to assure a stable operation of the detector.
4586 The barrel pixel supply tubes are equipped with a total of 124 temperature sensors and
4587 8 humidity sensors. The temperature sensors are placed on the CCU boards, the analog

4587 opto-board and on the supply tube cooling lines.

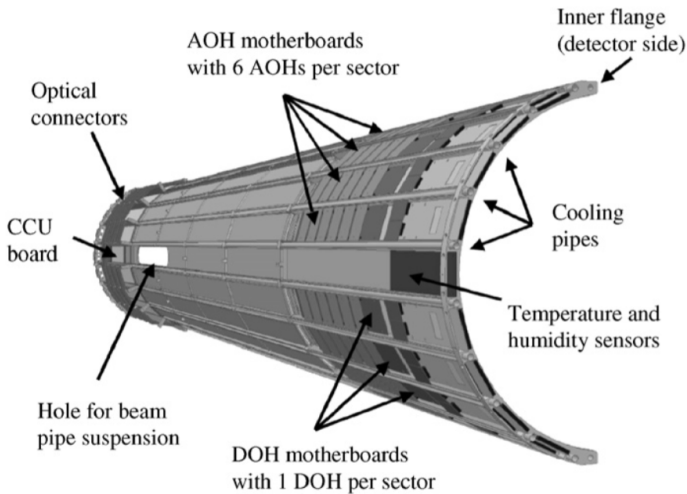


Figure 14.8: Layout of a BPix supply tube [169].

4588 14.4 Pixel online software

4589 The pixel online software [182] is the framework used for controlling and calibrating the
 4590 CMS pixel detector and that runs on the PCs of the CMS control room at LHC-P5. Its
 4591 main functionalities are to configure the detector, perform calibrations, analyze calibration
 4592 data and monitor the detector during data taking. The pixel online software is based on
 4593 the XDAQ toolkit [183] and is written in C++. It has a very complex structure built from
 4594 a large number of different applications and packages. The dependencies among the main
 4595 applications and packages is presented in Fig. 14.9. The top level application is represen-
 4596 ted by the `PixelSupervisor` which is responsible for the overall coordination of the pixel
 4597 DAQ. Its main function is to coordinate the activities of the other supervisors, particularly
 4598 during configuration and calibration. It is also responsible for updating the configuration
 4599 database with new settings obtained by calibrations. Among the other supervisors there
 4600 is the `PixelFECSupervisor` that controls the pxFECs and is responsible for loading the
 4601 configuration parameters for the ROCs and TBMs from the configuration database and
 4602 programming those parameters into the detector. Similarly, the `PixelTKFECSupervisor`
 4603 controls the tkFECs and the initialization of all the electronics placed on the supply tubes.
 4604 The `PixelFEDSupervisor` controls the FEDs. An additional supervisor is included in the
 4605 software to control the pixel TTC module used for trigger and timing. Among other things
 4606 the TTC module is used during calibrations to generate triggers. The various supervisors
 4607 run as independent processes, or even on different computers. Therefore, in order to com-
 4608 municate with each other they must exchange messages on the network. This is done using
 4609 the XML-based SOAP (Simple Object Access Protocol) protocol. A set of classes such
 4610 as `PixelFEDIInterface`, `PixelFECInterface`, and `FECSoftware`, provides the direct com-
 4611 munication between the supervisors and the VME hardware via Hardware Access Library
 4612 (HAL) [184].

4613 A function manager acts as an interface between the global run control (Run Control and
 4614 Monitoring System or RCMS) and POS. It is a JAVA application that basically passes the
 4615 state machine of CMS (Halted, Running, Configured, and so on) to the `PixelSupervisor`

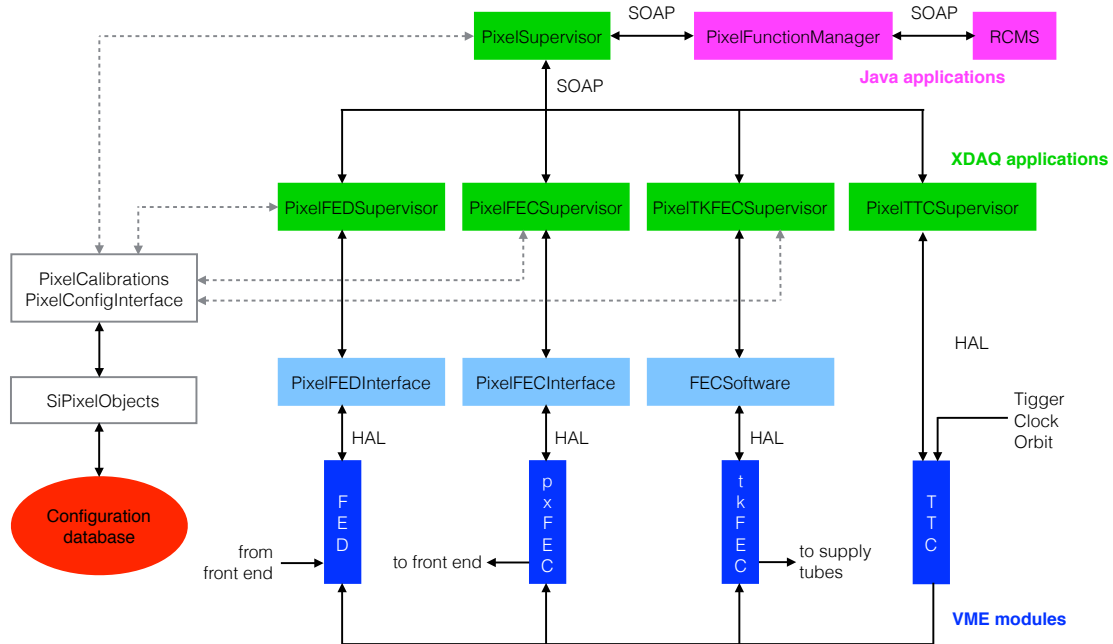


Figure 14.9: Illustration of the dependencies among the main applications and packages implemented in the pixel online software.

4616 which then forwards state requests to the underlying supervisors to carry out the different
 4617 tasks needed in state transitions of the run control.

4618 Another key element of the software is represented by the `PixelConfigInterface` package
 4619 which provides access methods for retrieving and storing configuration data. Several different
 4620 classes are available in the `SiPixelObjects` package, each responsible for storing a specific
 4621 set of detector settings as well as the configuration needed by the calibration code (e.g.,
 4622 which detector parameter to scan and its range). For instance, the `PixelNameTranslation`
 4623 class translates from the naming scheme used to label each individual ROC to the hardware
 4624 addresses used by both the FEC and the FED to identify a specific ROC. Similarly, the
 4625 `PixelDACSettings` and `PixelTBMSettings` classes store, respectively, the DAC settings for
 4626 all ROCs on one module and the settings for one TBM. The `PixelSupervisor` features a
 4627 web GUI that can be accessed as an html page. It displays information about the current
 4628 configuration, or if it is not configured it allows the user to select a possible configuration
 4629 from a list and configure the detector using that choice. The GUI is also used to run and
 4630 monitor the detector calibrations. The calibration routines are implemented in independent
 4631 and separate classes contained in the `PixelCalibrations` package. The description of the
 4632 detector calibration procedures is presented in the following chapter.

Optimization and commissioning for LHC Run 2

4636

4637 The CMS pixel detector was designed to cope with the high radiation environment of LHC and
 4638 to operate with the highest performance even after the accumulation of significant radiation
 4639 doses. Nevertheless, radiation damage affects hit efficiency and resolution and hence, it is
 4640 necessary to monitor its effects during operation. As described in this chapter, throughout
 4641 Run 1, re-calibrations of the detector have been performed to compensate for these effects
 4642 and recover full performance.

4643 During LS1, both BPix and FPix were extracted from CMS for maintenance with the
 4644 purpose to recover broken channels. In this period, the calibration procedure has been
 4645 exercised and improved in view of commissioning and operation for Run 2.

4646 The pixel detector has been operated with a coolant temperature of 7.4 °C in 2008–2011
 4647 and 0 °C in 2012, which for the pixel sensors translates to values of about 10 °C higher. In
 4648 order to limit the impact of radiation damage, during Run 2 the detector has been operated
 4649 at much lower temperature, down to -10 °C. This has been made possible thanks to a
 4650 major effort during the long shut-down to implement a tracker wide sealing that ensures
 4651 minimal humidity levels. The flow of dry gas into the tracker volume was increased and a new
 4652 safety system was developed that shuts down the detector safely in case a sudden increase
 4653 of temperature, electric current or humidity is detected. During LS1, the pixel detector
 4654 functionalities at very low temperature have been checked and its (temperature dependent)
 4655 settings re-calibrated to allow for optimal operations under such conditions. This activity,
 4656 described in the following, have been crucial to achieve a quick and reliable re-installation
 4657 and commissioning for Run 2, as well as for stable and excellent operations during 2015 and
 4658 2016.

4659 15.1 Effects of radiation damage in LHC Run 1

4660 One of the first visible effect of radiation is the increase of the sensor leakage current with
 4661 integrated luminosity, due to damages in the silicon bulk. The most fundamental type of bulk
 4662 radiation damage is a defect, produced by the displacement of an atom of the semiconductor
 4663 material from its normal lattice site. The vacancy left behind, together with the original
 4664 atom now at an interstitial position, constitutes a trapping site for normal charge carriers.
 4665 The formation of mid-gap states facilitates the transition of electrons from the valence to the
 4666 conduction band leading to an increase of the leakage current in the depletion region. The
 4667 primary defects caused by irradiation are not stable but able to move through the crystal. As
 4668 result of this diffusion process, there is the possibility of combination of more complex defects.
 4669 This process is called *annealing*, with a beneficial part reducing the damage and a reverse
 4670 one degrading macroscopic sensor properties, called *reverse annealing*. During beneficial
 4671 annealing, with a time constant of a few days at room temperature, the leakage current
 4672 decreases, while later it rises due to reverse annealing process until it finally saturates at a
 4673 value which is significantly above the initial level. At temperatures below 0 °C however, both

4674 effects can be frozen and the detector current remains constant. Thus, irradiated detectors
 4675 should be operated and stored at low temperature, while it is favorable to shortly expose
 4676 them to room temperature to take advantage of the beneficial annealing.

4677 Figure 15.1 shows the increase of the leakage current for the pixel barrel layers measured
 4678 from readings of the high voltage power supplies as a function of the integrated luminosity
 4679 and of time in 2011-2012. The damage was only partially recovered by beneficial annealing
 4680 that took place during a longer shut-down after about 6 fb^{-1} and a shorter technical stop after
 4681 about 13 fb^{-1} delivered integrated luminosity. Between the end of 2011 and the beginning
 4682 of 2012 the operating temperature was decreased from 7.4°C to 0°C achieving a reduction
 4683 in leakage current by a factor two and preventing reverse annealing which would eventually
 4684 require too high depletion voltages. The data are compared to a parametrization that accounts
 4685 for accumulated damage and for annealing, whose input is the fluence as predicted by a
 4686 model of the CMS detector. The overall trend of the measurements is in agreement with this
 4687 model except for the normalization. The reasons for this discrepancy in scale remain under
 4688 investigation, with possibilities including uncertainties in the operational temperature and
 4689 incorrect inputs to the model of the CMS detector.

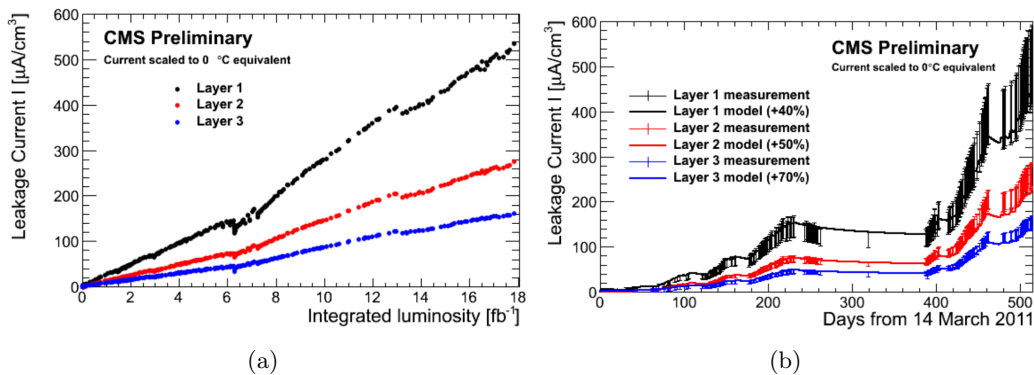


Figure 15.1: Leakage current scaled to 0°C operational temperature for the barrel layers as a function of the integrated luminosity (a) and time (b) in 2011-2012 [185].

4690 The depletion voltage was also monitored during operations. With irradiation, defects
 4691 with a negative space charge are generated throughout the bulk leading to variations in
 4692 the effective doping concentration. When starting with n-type bulk, the effective doping
 4693 concentration decreases because of the negatively charged defects until the bulk is transformed
 4694 into an effective p-type. This process, called *type inversion*, happens at a relatively low dose
 4695 of several $10^{12} n_{eq}/\text{cm}^2$ (neutron equivalent fluence) [186]. As a consequence of this space
 4696 charge sign inversion, the depletion zone now expands from the n^+ pixel implants towards
 4697 the p-type back. The depletion voltage scales with the bulk doping concentration: it initially
 4698 decreases reaching a minimum at the inversion point, and then rises with the effective bulk
 4699 doping concentration.

4700 A dedicated scan of the bias voltage was performed several times per year, by varying the
 4701 detector bias voltage from 0 V to the normal operating value of 150 V, and measuring
 4702 the single hit efficiency. The results of the hit efficiency measurements for the innermost
 4703 barrel layer between 2011 and the beginning of 2013 are shown in Fig. 15.2(a). The bias
 4704 voltage that is needed to reach a depletion depth corresponding to full hit efficiency decreases
 4705 with irradiation at first, then increases as expected due to the aforementioned changes in
 4706 the effective doping. The dependence of the voltage needed to achieve full hit efficiency on
 4707 the integrated luminosity is shown in Fig. 15.2(b) for the barrel layers and endcap disks.

4708 The presence of a minimum for the layer 1 and layer 2 is evidence for type inversion occurrence.

4709

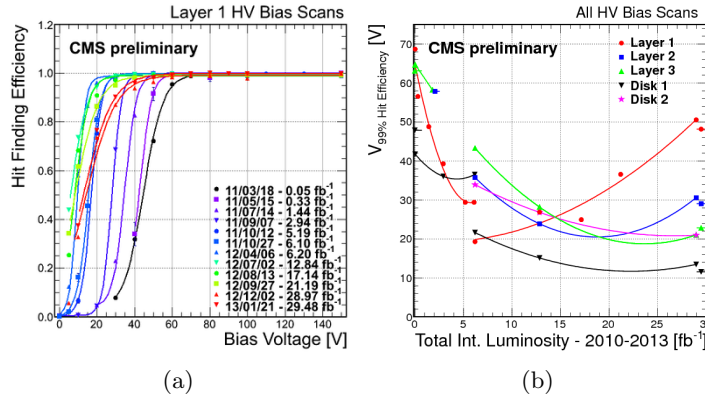


Figure 15.2: (a) Scans of the bias voltage performed on the innermost barrel layer. (b) Bias voltage corresponding to full single hit efficiency for all barrel layers and forward disks as a function of the integrated luminosity delivered in Run 1 [57].

4710 The evolution of the pixel threshold (Fig. 15.3(a)) and the analog current (Fig. 15.3(b))
 4711 was also frequently monitored in Run 1, and an increase of both parameters with integrated
 4712 luminosity was observed. The possible explanation for these changes is the radiation damage
 4713 in the bad-gap reference voltage circuit, which would shift all voltage settings inside the ROC.
 4714 Because of the described effect, a re-calibration of the analog voltage and the pixel threshold
 4715 during technical stops was necessary to recover the optimal ROC performance.

4716 The pixel hit resolution also exhibits a slow degradation with integrated luminosity as
 4717 shown in Fig. 15.4. The two points of improvement correspond to re-calibrations of the pixel
 4718 threshold.

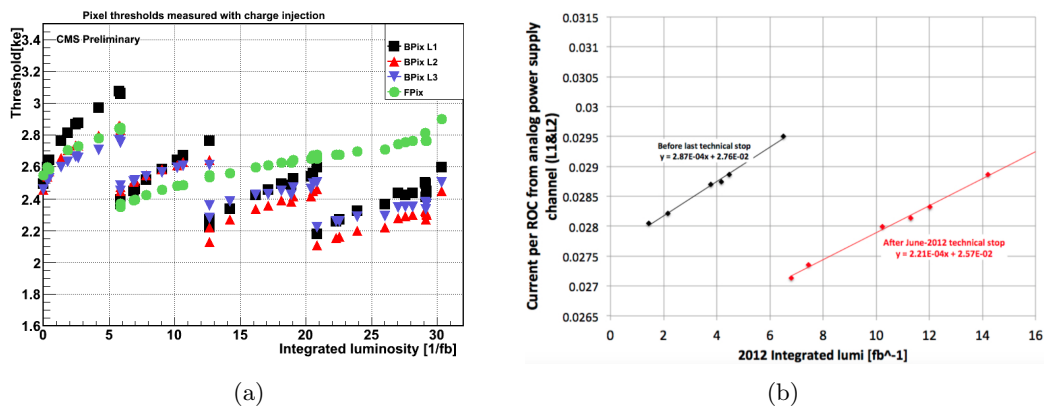


Figure 15.3: (a) Average pixel threshold in units of 1 ke for the barrel layers and forward disks, and
 (b) average analog current per ROC drawn by the power supply for BPix layers 1 and 2, as a function
 of the integrated luminosity delivered in Run 1 [57].

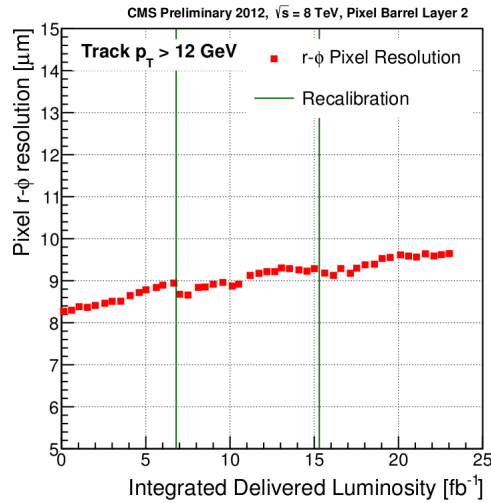


Figure 15.4: Single hit resolution for barrel layer 2 in the $r\phi$ plane as a function of the integrated luminosity delivered in Run 1 [57].

4719 15.2 Optimization for LHC Run 2

4720 In Summer 2013, after the first LHC run, the BPix and FPix detectors were extracted
 4721 from CMS, and throughout LS1 they were kept in a refrigerated, climate-controlled room
 4722 environment (Fig. 15.5) located at the CMS experimental site, LHC-P5. The BPix was
 4723 maintained in two cold boxes in a laboratory with repair workbenches, and all the electronics
 4724 and computers necessary to control and readout the detector for maintenance and tests.



Figure 15.5: Barrel pixel detector temporarily installed in the clean room at LHC P5.

4725 At the end of Run 1, the fraction of operational channels in the barrel pixel detector was
 4726 97.7% and the long shut-down was used to recover the faulty channels. The main reasons

were broken wire-bond connections between the ROC and the HDI as well as issues with the lasers on few AOHs. Furthermore, some modules had an old ROC design, which caused operational problems, and were therefore disabled. Replacements were attempted only for the barrel layer 3 outer shell, since the other layers and the inner shell of layer 3 were considered too risky to touch without breaking further parts. The defects in layer 3 made up 52% of the faulty channels. Two AOHs were found with disconnected wire bonds between the laser and the AOH PCB, and they were also replaced. Figure 15.6 shows pictures from the laboratory in LHC-P5 during this operation. In order to proceed with the replacement one of the two cold boxes was opened and the half shell of interest extracted using a support equipped with rails. The shields covering the AOHs were unscrewed and all the AOHs of the sector in the outside direction had to be unplugged in order to replace the two malfunctioning ones. Before restoring the detector in its original position inside the box, the two new AOHs were tested by checking with the oscilloscope the variations in the optical output when changing the laser bias settings with commands sent through the tkFEC. The same tests were performed for the other functioning AOHs that had to be unplugged to perform the replacement. It was found that during the operation, two additional AOHs were damaged and they had to be replaced as well.

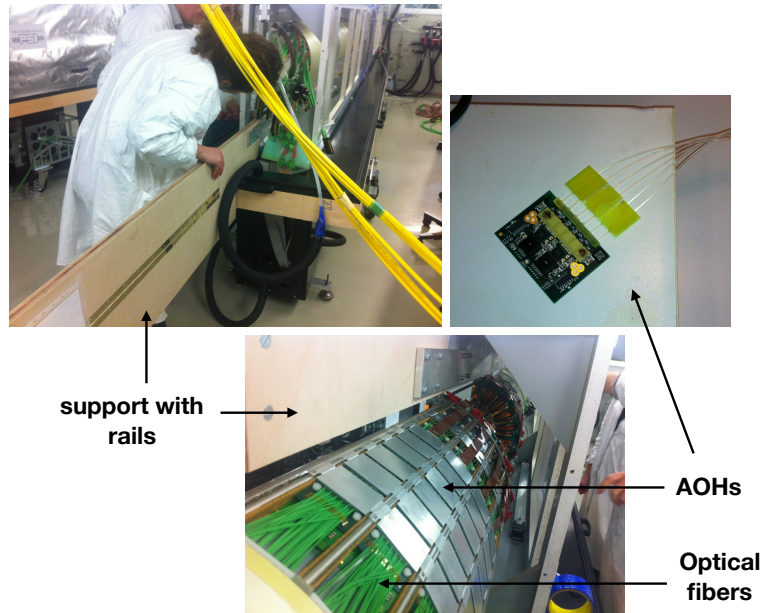


Figure 15.6: Pictures of the operations conducted in the clean room at LHC-P5 to replace the broken AOHs. The support with rails used to extract one half shell from the box is visible. The AOHs are mounted on the supply tube and covered by metal shields. A picture of an AOH is shown on the top right.

There was, however, a serious incident in mid-August 2014. After having replaced a BPix module, tests of the corresponding quadrant showed severe damage: 55 new unresponsive modules were found. It was decided to take that part of the detector to PSI for further tests and repairs. Shorts were discovered at the ROCs and in several modules between the TBM and cable pads. Eventually, the detector was repaired within three months using 40 new modules and 19 repaired ones. The shorts were suspected to be caused by humidity due to unobserved condensation in the cold box. After being repaired, the functionalities of the new modules were successfully confirmed and at the end of LS1 the good detector fraction was 99%.

4753 Part of the time available during LS1 have been employed to exercise and improve
4754 calibration procedures in view of commissioning and operations for Run 2. An overview of
4755 the calibration procedure is given in the following.

4756 15.3 Overview of pixel calibrations

4757 Detector functionality and performance depend on proper calibrations of readout chain
4758 parameters. Most of these parameters are quite stable unless major changes occur, such as
4759 the detector operating temperature. Other parameters are more sensitive to environmental
4760 variations. For these parameters a re-calibration on a regular basis was necessary during
4761 Run 1 operations.

4762 Further expertise in the calibration procedure was achieved during LS1 and it has been
4763 fundamental for the re-commissioning of the detector to prepare it for a successful data-taking
4764 in 2015–2016. In addition, the detector was fully re-calibrated at low temperature after
4765 re-installation. As for Run 1, in these two years, re-calibrations have been performed during
4766 technical stops, and in particular in mid-2016 when the analog current drawn by the ROCs of
4767 the innermost layer reached critical values ($\approx 6\text{ A}$) that led to the trip of the power supplies
4768 in several occasions.

4769 The calibrations are performed with POS which was installed and run on the computers
4770 available in the clean room. There are a large number of different calibration tasks that need
4771 to be executed sequentially and sometimes iterated. While a detailed description of each
4772 calibration as well as the implementation in POS can be found in Ref. [182], an overview of
4773 the most important steps is given in the following. The calibration process consists first of a
4774 part where the readout chain settings are adjusted. It is meant to put the detector in a state
4775 in which it can correctly reconstruct hits and involves tuning of the settings of the FED, of
4776 the electronic components placed on the supply tubes, as well as the threshold and timing
4777 settings of the ROCs, which are controlled by programmable DACs (Section 14.2.2). In the
4778 second part of the process the pulse height information is optimized. The steps involved here
4779 are lengthy and require several iterations to reach the target signal rise speed as well as the
4780 lowest practical value for the threshold of each ROC. In the final step, an optimization of the
4781 analog signal response is performed. Most of the calibrations produce directly new optimal
4782 settings which can then be used in subsequent runs. Other calibrations write binary data
4783 files which have to be analyzed offline, these include the pixel alive test, the threshold and
4784 noise measurement and the gain calibration.

4785 15.3.1 Adjustment of readout chain settings

4786 1) Delay25 chip

4787 As described in Section 14.3 (Fig. 14.6), the LHC clock, L1 trigger and programming signals
4788 are transmitted from the pxFEC placed in the underground counting room to the detector
4789 through fibers. The optical signals are first converted into digital signals by the DOH to be
4790 then sent to the detector through the Delay25, PLL and Gate-Keeper chips integrated in the
4791 same digital circuit. The clock and trigger are encoded as a single signal transmitted using
4792 one single fiber. As schematically illustrated in Fig. 15.7, this signal is decoded by the PLL
4793 chip and sent via two separate lines, LHC clock (CLK) and Calibrate/Trigger/Reset (CTR),
4794 through the Delay25 chip to the BPix modules. In addition, the CLK signal is split in the
4795 Gate-Keeper chip and one line (RCK) is returned and sent back to the pxFEC through the
4796 Delay25 chip. The digital programming and control data (SDA) also goes through the Delay25
4797 and Gate-Keeper chips. If the gate is open the SDA is transmitted to the BPix modules

4798 which sends the acknowledge signal (RDA) back, otherwise the data packet is returned in the
 4799 Gate-Keeper.

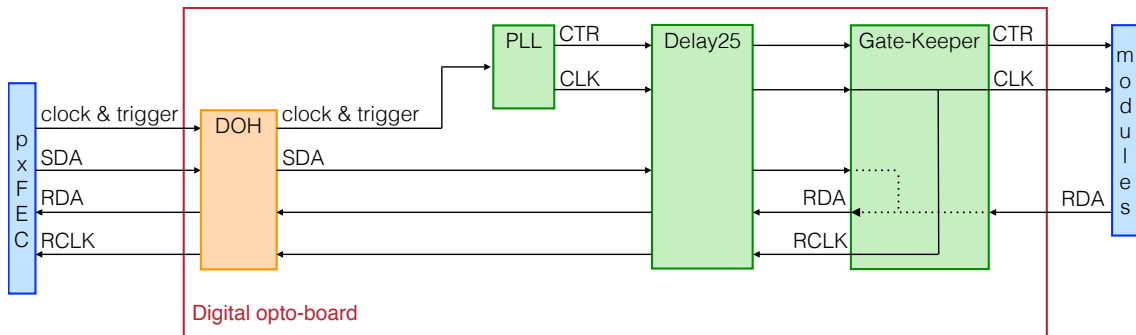


Figure 15.7: Diagram illustrating the functionality of the BPix digital circuit.

4800 The SDA signal can only be decoded by the TBM if it is in phase with the CLK signal.
 4801 The purpose of the Delay25 chip is to adjust the timing between the two lines to make this
 4802 communication work. Hence, a calibration is performed where the delays for the SDA and
 4803 RDA lines are scanned and for each set of values commands are sent to the TBM and the
 4804 return status in the pxFEC is checked. The main output from this calibration is new SDA and
 4805 RDA delay settings. If the calibration converges the old settings stored in the configuration
 4806 database are updated with the new ones. An example of the scan is shown in Fig. 15.8 for
 4807 one module. The set of values chosen by the algorithm is indicated with a red point and
 4808 corresponds to a region where the communication between the TBM and the pxFEC has
 4809 been established for each trial.

4810 This calibration is fundamental to ensure correct communication with the pxFEC, but
 4811 once the settings are found they do not need to be readjusted often.

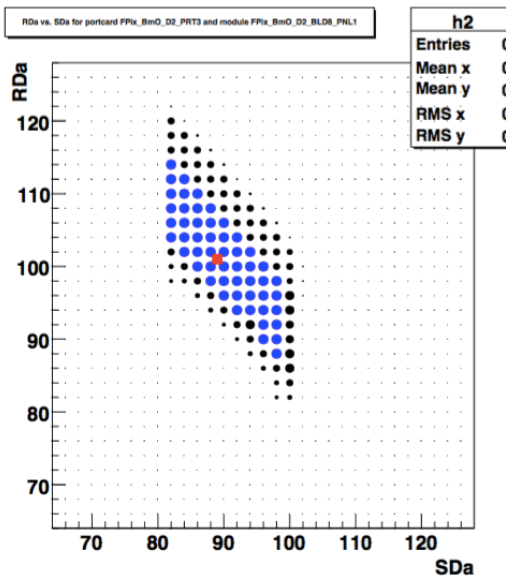


Figure 15.8: Example of output of the Delay25 calibration for one module. For each set of SDA and RDA delay settings the communication with the TBM is checked. The blue dots indicates areas with 100% communication efficiency. The black dots indicated partial efficiency where larger dots have higher efficiency. The red square indicates the point chosen by the algorithm.

4812 2) FED receiver offset

4813 This calibration adjusts the individual offsets included in each input channel of the FED such
 4814 that the baseline of the analog signal (black level) is tuned to be near a given target value,
 4815 normally 450 ADC counts, which is near the midpoint of the dynamic range of the ADC. The
 4816 main output consists of new FED parameters that, if satisfactory, are used to update the
 4817 previous settings. This calibration is performed often because the AOH is very temperature
 4818 sensitive. Already 1 °C temperature change shifts the signal by 50 ADC counts (out of 1024).
 4819 The pixel FED automatically corrects for baseline shifts during a run but it is important to
 4820 start with a uniform baseline distribution. The baseline calibration adjusts each optical input
 4821 to be ± 5 ADC counts from the target value. During normal LHC operations it is performed
 4822 at least once a day during the LHC fills.

4823 The calibration also produces an output file with the analog signal for each module where
 4824 its several components are visible, namely the TBM header and trailer, and each ROC header
 4825 (Fig. 15.9). It runs quickly and provides an information on the data buffer for each FED
 4826 channel. It is therefore very useful as a debugging tool since it provides a feedback on the
 4827 basic functionalities of optical links, AOHs, TBMs and ROCs, needed to assess the status of
 4828 the detector.

4829 If this step fails to converge, for instance when part of the analog signal is not visible,
 4830 a calibration can be run that adjusts the timing of the signal digitization in the FED by
 4831 changing the phase of the ADC clock. This calibration is usually very stable, and needs to
 4832 be repeated only when the FEDs, fibers, or other parts of the detector are touched, or if
 4833 modifications of the fine phase of the global clock occur.

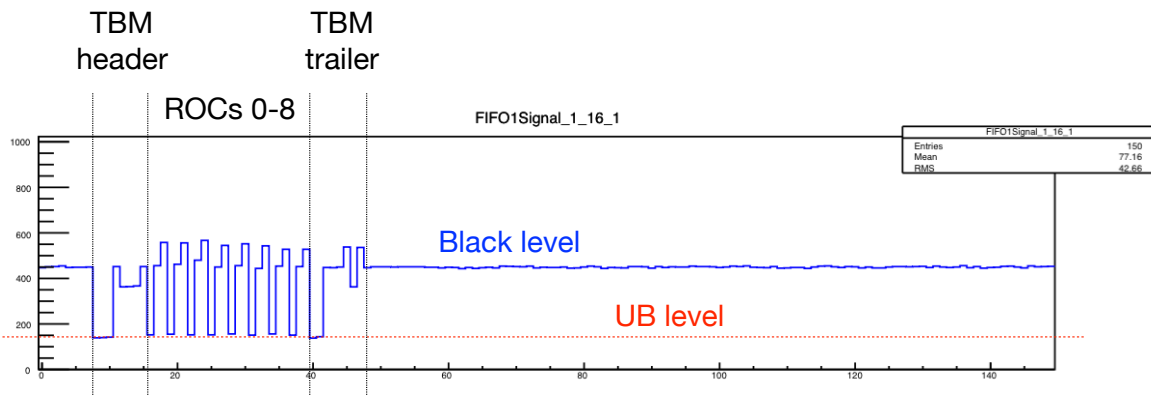


Figure 15.9: Example of analog signal from the TBM displayed at the end of the FED baseline calibration. The FED parameters are adjusted to center the baseline (or black level) in the middle of the FED ADC range.

4834 3) AOH bias and gain

4835 Each AOH is equipped with 6 lasers for which the bias and the gain can be adjusted
 4836 individually. The optical fibers connected to the lasers are combined in groups of 12 and each
 4837 of them is connect to one FED channel. The AOH bias is a setting that controls the laser
 4838 bias current and hence, the amount of light (optical power) sent to the FED. The optical
 4839 power, and hence the ADC counts in the FED, increases with the laser bias setting. As

4840 shown in Fig. 15.10, at low values of the bias, the black (BL) and ultra black (UBL) levels
 4841 are unaffected, so that there is no separation between the two. At some threshold, the BL
 4842 begins to increase approximately linearly, followed by the UBL at a higher laser bias value
 4843 and with about the same slope.

4844 The maximum BL-UBL separation depends on the TBM settings discussed in the next
 4845 section, and it is low if these parameters are configured to low values. In fact, the BL is
 4846 independent on these settings, whereas the linear rise of the UBL begins at a later point
 4847 if the configured values in the TBM are higher. As a consequence, the BL-UBL difference
 4848 saturates at a higher laser bias value. The goal of the AOH bias calibration is to determine
 4849 a laser bias setting for each FED channel that is just high enough to saturate the BL-UBL
 4850 difference. The calibration measures this difference, using the levels from the TBM header
 4851 and trailer, as a function of the laser bias. It is important, though, that during this scan
 4852 the TBM settings are set to reasonable values, at least as high as they will be set in later
 4853 calibrations and physics runs. Otherwise, the laser bias value determined from the saturation
 4854 point will be too low.

4855 Temperature variations alter the response of the AOH, essentially shifting the curves in
 4856 Fig. 15.10 to the left or right by 4 bias counts for 5 °C variation. In order to provide a margin
 4857 of error for these variations, the optimal laser bias setting is chosen by the calibration to be
 4858 4 counts higher than the saturation value. This offset can be externally configured before
 4859 running the calibration.

4860 It is also important that the laser bias is not too high to avoid that the signal moves
 4861 out of the dynamic range of the FED. In the last part of the AOH bias calibration a coarse
 4862 baseline adjustment is performed to bring the black level into the target range by re-adjusting
 4863 the FED optical receiver offsets and laser bias settings. In this step the AOH bias is not
 4864 decreased below the saturation value unless it is absolutely necessary. The main output of
 4865 the calibration is a new configuration for the AOH bias and FED offset values that puts all
 4866 FED baselines near the center of the dynamic range, with laser bias values that allow for
 4867 a large BL-UBL separation. After the AOH bias calibration, the FED baseline calibration
 4868 should be run to obtain a finer adjustment of the baseline (using the freedom to move each
 4869 channel offset).

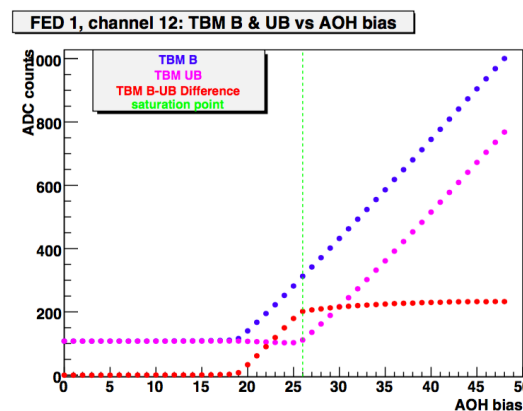


Figure 15.10: Black and ultra black levels as a function of the AOH laser bias. An optimal value for this parameter is found at the saturation value of the BL-UBL separation.

4870 The gain is a setting for each AOH laser that can accept just 4 possible values (0, 1, 2,
 4871 3). This setting does not affect the black level, whereas it scales the size of deviations from
 4872 the BL expanding or shrinking the signal. Larger settings correspond to larger deviations

4873 and hence, to a larger BL-UBL separation. Although the adjustment of TBM and ROC
4874 parameters will be the primary method for tuning the UBL to the optimal value, the aim of
4875 this calibration is to set the laser gain at the lowest level that will allow the TBM UBL to
4876 be sufficiently low for an optimal readout of the signal. In fact, too high laser gain values
4877 will increase the power drawn and they are intended to be used to compensate for radiation
4878 damage over time. The optimal laser gain setting is chosen as the lowest value that provides
4879 an UBL below a user-defined threshold.

4880 4) TBM and ROC ultra black levels

4881 With the black level set at about 450 ADC counts by the FED baseline calibration and
4882 automatic correction, the next step consists in a fine adjustment of the TBM and ROC ultra
4883 black levels. First, the TBM settings are calibrated to set the TBM header and trailer UBL
4884 to a value of about 250 ADC counts. There are three registers on the TBM affecting the
4885 UBL, where higher configured values correspond to lower UBL and hence, larger BL-UBL
4886 separation. Furthermore, two of them affect also the signal from the ROCs. A simultaneous
4887 scan of all three registers is usually performed. Although higher settings generally provide
4888 lower ultra black levels, at very high values the UBL may actually increase. Thus, if the
4889 calibration finds multiple settings that give the target UBL, it will choose the lower ones.

4890 Dual TBMs represent a special case. The two channels on a dual TBM share the same
4891 registers, so that they cannot be adjusted independently to tune both ultra black levels at the
4892 target value. In this case, the settings are optimized such that one channel is at the target
4893 UBL, and the other is below.

4894 A second calibration is run that sets the ultra black level for each ROC equal to the
4895 corresponding TBM's UBL. There are two DAC settings on the ROC which affect the UBL,
4896 and higher configured values correspond to lower UBL (and larger BL-UBL separation).

4897 These calibrations have to be repeated every time the previous steps 2 and 3 are run and
4898 modify the correlated parameters.

4900 5) Threshold and charge injection delay

4901 The rest of the calibrations require the use of the charge injection feature of the ROC. For
4902 the injected charge to be readout as a hit, it has to cross the comparator threshold and be
4903 validated by the trigger (which involves the timing of the injection). Thus, a calibration is
4904 first run that aims at finding the settings for each ROC for the comparator threshold and
4905 for the delay at which the charge is injected into the pixels. It is meant at quickly finding a
4906 working point in which the injected test charge can be read out. The amplitude of the injected
4907 signal is set by programming the corresponding DAC register (V_{cal}). Since these settings are
4908 common to all pixels in a ROC, only few cells can be enabled for this calibration. A 2D scan
4909 of the threshold and delay settings is performed: for each pair of values, a defined number of
4910 triggers are sent and for each of them the event is readout from FIFO1 or FIFO3 to verify
4911 that the hits have been collected for each ROC. The settings are changed by programming
4912 the corresponding DAC registers, V_{cThr} and $CalDel$.

4913 It has to be mentioned that the $CalDel$ setting is only relevant for calibration data taken
4914 with charge injection. For real data, only the trigger delay has to be known and programmed
4915 into the so called *WBC* register of each ROC. The trigger delay basically sets the bunch
4916 crossing in which data is read out and is estimated from the known cable/fiber lengths and
4917 delays introduced by the electronics.

4918 An example of $VcThr$ versus $CalDel$ scan is shown in Fig. 15.11(a). For large $VcThr$
 4919 values, which correspond to low thresholds, a large number of pixel fire due to noise such
 4920 that to block a double column. For lower values, hits are collected in the $CalDel$ range
 4921 that corresponds to the WBC used. The curve bends to smaller delay values as the $VcThr$
 4922 decreases. The explanation for this behavior is illustrated in Fig. 15.11(b). Since a low $VcThr$
 4923 value corresponds to a higher threshold, the signal reaches the threshold later and hence a
 4924 smaller delay is needed for the signal, i.e. the signal is injected earlier.

4925 At the end of the calibration an optimal set of values is chosen in the region where the
 4926 efficiency for detecting a pixel hit is 100%. The optimal working point is also chosen such
 4927 that it is sufficiently far away from the noise level.

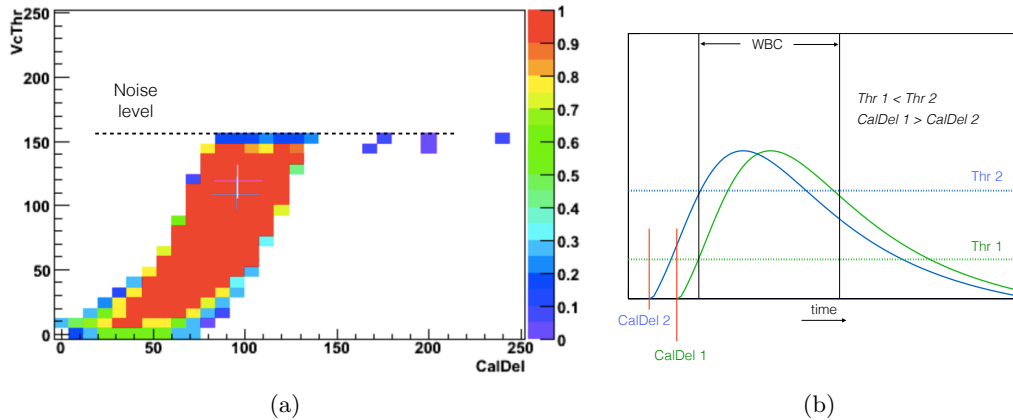


Figure 15.11: (a) Efficiency for detecting a hit as a function of the comparator threshold ($VcThr$) and delay ($CalDel$) settings for one ROC. Large values of $VcThr$, corresponding to a low threshold, generate much noise that saturates the digital circuit and no hits are detected. The optimal point is indicated in black while the blue point indicates the old settings. For small values of $VcThr$ the signal reaches the threshold later and hence a smaller delay is needed for the signal. This behavior is illustrated in (b).

4928 6) Address levels

4929 The row and column address of the hit pixel is encoded in 6 discrete analog levels (Section
 4930 14.3.1) which have to be well separated for being correctly decoded by the FED. The
 4931 position of the address levels is determined by measuring the levels of all pixels in a ROC
 4932 and overlaying them in a histogram. Pixels are scanned to make sure that combinations of
 4933 address levels that could potentially cause problems are probed, such as transitions from
 4934 high to low levels and vice versa. An example of the results is shown in Fig. 15.12, where the
 4935 six peaks corresponding to the six address levels can be seen. The separation between the
 4936 levels is good and the decoding limits are chosen in the center between to neighboring peaks
 4937 to be then downloaded to the FED. The separation can mainly be affected by dirty optical
 4938 connectors and poor light transmission, or by large temperature changes not compensated by
 4939 the automatic baseline correction. Hence, during stable running conditions this calibration is
 4940 run once every few days.

4941 7) Pixel alive test

4942 In this test, the functionality of each pixel in a ROC is checked by verifying that it responds
 4943 to an injected calibration signal above threshold. Charge is injected in each pixel several

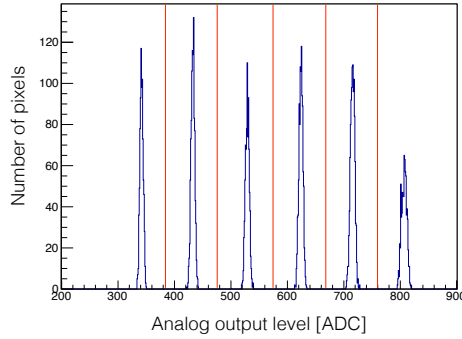


Figure 15.12: Address levels of all pixels in a ROC as received by the FED. The red lines are the separation limits used for the decoding of the pixel addresses in the FED.

times and the number of output signals is recorded. The pixel is fully working if all signals are registered; the pixel is defective, if no output signal is registered at all. The data are then analyzed offline to produce an efficiency map that displays the efficiency for each pixel. Examples of the results for two ROCs are shown in Fig. 15.13. For the case on the left all cells are functioning, whereas on the right an example is shown of a ROC with a large number faulty pixels.

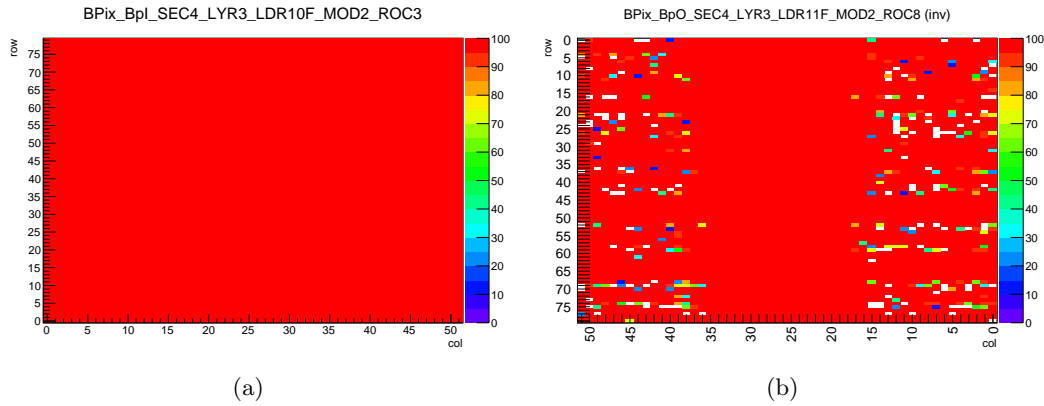


Figure 15.13: Examples of pixel alive test results for two ROCs: (a) all cells are functioning and (b) a large number of pixels are broken.

4950 8) Measurement of threshold and noise

4951 This is the last step of the calibration chain aimed at verifying and adjusting the basic
 4952 functionality of the detector. At this stage it is important to perform a measurement of the
 4953 threshold and noise of each pixel, which will be afterwards optimized in the second part of the
 4954 procedure as described in the next section. In fact, the detection thresholds are an important
 4955 parameter of the pixel detector since they influence the hit position resolution (Fig. 15.4).

4956 The thresholds are measured through the so called “S-curve” scan, which provides the
 4957 pixel response efficiency as a function of the amplitude of the injected test charge (V_{cal}),
 4958 varied from 0 to its maximum. The V_{cal} value where the signal shows 50% efficiency is

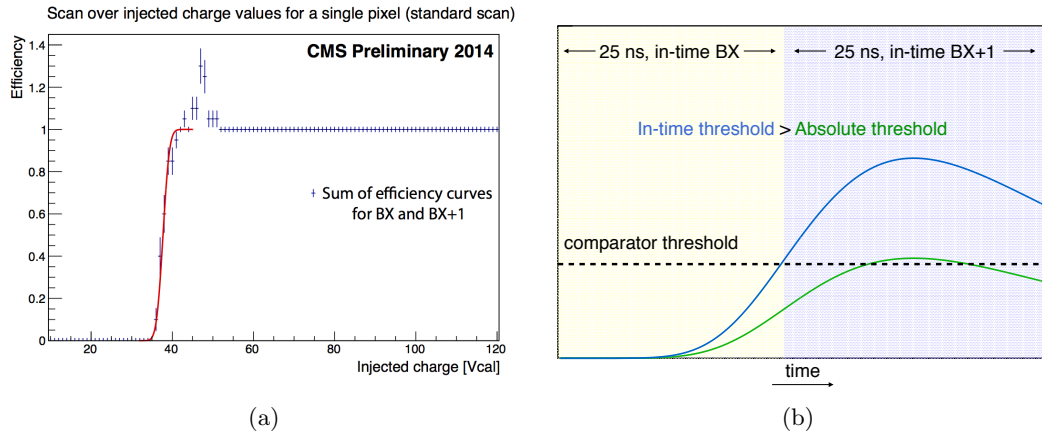


Figure 15.14: (a) Single pixel efficiency curve determined performing a scan over injected signal amplitudes (V_{cal}). The curve is the result of the sum of efficiency curves for the in-time bunch crossing (BX) and the following one (BX+1). Points exceeding the 100% efficiency are due to statistical fluctuations of the two curves in the turn-on region. The effect on the fit is negligible. (b) Diagram illustrating the difference between in-time and absolute thresholds due to the finite rise-time of the signals.

4959 defined as the threshold. As for the pixel alive test, the data are analyzed offline to produce
 4960 the final results. An example of such scan is shown in Fig. 15.14(a) for a test conducted in
 4961 the clean room at a temperature of -15 °C.

4962
 4963 The finite rise-time of the signal complicates the threshold measurement. One should
 4964 distinguish the *absolute threshold* defined as the comparator level above which the signal is
 4965 accepted and the pixel hit is available for readout, and the *in-time threshold* where the signal
 4966 is fast enough to be correctly labeled by the right bunch crossing. The difference between
 4967 the two is due to *time-walk* and is related to the speed of the pixel amplifier. The absolute
 4968 threshold is relevant when discussing noise and cross-talk, that is the optimum conditions
 4969 under which the ROC still works. It also determines the pixel detector hit occupancy. The
 4970 in-time threshold determines the lowest amplitude signals useful for hit reconstruction and
 4971 affects the position resolution. Both thresholds can be measured using the S-curve method:
 4972 for the in-time measurement the *WBC* (or trigger delay) is set to the nominal value; for the
 4973 absolute threshold measurement the *WBC* is shifted down by one unit making the readout
 4974 of the lowest amplitude (i.e. slowest) signal possible. By definition the in-time threshold is
 4975 higher than the absolute. This behavior is illustrated in Fig. 15.14(b).

4976
 4977 The noise can also be measured with the S-curve method since it is proportional to the
 4978 width of the region where the signal efficiency rises from 0 to 100%. Both noise and threshold
 4979 are measured in V_{cal} units, representing the parameter which determines the magnitude of
 4980 the injected charge. The calibration of the V_{cal} unit itself was done during module testing
 4981 using data from X-ray sources of known energies, and it varies from pixel to pixel and from
 4982 ROC to ROC. On the average, one V_{cal} unit corresponds to 65.5 electrons, representing
 4983 the slope of the calibration curve, whereas the average offset is -414 electrons. However, the
 4984 spreads of the two distributions are rather large, the slope parameter has an RMS of 9 and
 4985 the RMS of the offset is about 570 [187].

4986 Running this method for the whole detector is very time consuming. Instead, for each ROC

4987 the thresholds and noise are measured using only 81 pixels, which was found to be sufficient to
 4988 determine the average values. The results of the noise and threshold measurements performed
 4989 in 2015 during commissioning for Run 2 will be discussed in Section 15.4.

4990 15.3.2 Optimization of the pulse height information

4991 1) Signal rise speed

4992 The in-time threshold depends on the amount of time-walk introduced in the amplification
 4993 and shaping that occur before the signal reaches the comparator. The speed of the pixel
 4994 amplifier is controlled by *Vana*, a 8-bit DAC that regulates the voltage applied to the analog
 4995 part of the ROC, which can be varied in the range from 800 to 1,300 mV. The *Vana* has to be
 4996 optimized such that a compromise is obtained between the desire to minimize the time-walk
 4997 and the need to keep the current drawn by the analog part of the ROC, or analog current,
 4998 at a reasonable level. During module testing the optimal *Vana* setting was determined for
 4999 each BPix ROC by measuring directly the analog current drawn by the ROC, and then
 5000 choosing the value that corresponds to 26–28 mA. In fact, this value for the current has been
 5001 found optimal to avoid exceeding the limit of the power supply. Nevertheless, the radiation
 5002 damage affects the ROC analog current and a re-calibration is necessary during operations
 5003 (Fig. 15.3(b)).

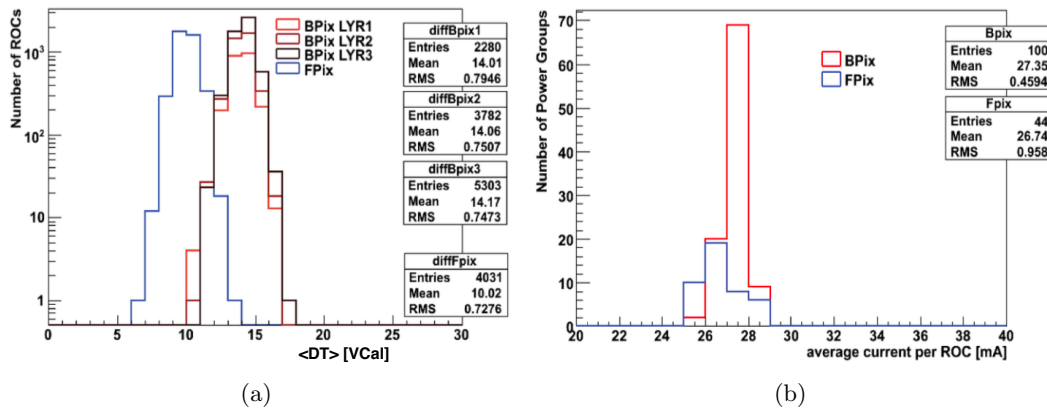


Figure 15.15: (a) Final distributions in DT obtained at the end of the optimization of the signal rise speed in 2012 for each barrel pixel layer and for FPix . The target DT value is chosen to reach an average analog current per ROC of 26–28 mA (b).

5004 Once the detector is fully assembled, it is no longer possible to access the value of the
 5005 analog current for each ROC, since at this stage the only available information is the total
 5006 current drawn from a single power supply, which services more than one-hundred ROCs.
 5007 Thus, a procedure has been developed in the past to optimize *Vana* that does not make use of
 5008 this information. The analog current can indeed be directly related to the time-walk, whose
 5009 value DT can be obtained by the difference between the in-time and absolute thresholds. The
 5010 higher *Vana*, the faster is the detector (smaller DT), but also the higher the current drawn
 5011 by the ROC. The target value of DT is then chosen such that the average analog current per
 5012 ROC in each power group is near the optimal value of 26–28 mA. However, the correct target
 5013 for DT depends on radiation damage and temperature, so that a fixed number to target
 5014 cannot be given. Instead, one should tune the target based on the average analog current
 5015 per ROC as read from the power supply. Figure 15.15 shows the DT distributions for both

5016 BPix and FPix measured in 2012, as well as the corresponding average analog current per
 5017 ROC. For BPix, a target DT value of 14 V_{cal} was found to be sufficient to reach the optimal
 5018 current.

5019 In order to optimize the DT, the calibration is implemented as an iterative procedure,
 5020 which makes use of the in-time and absolute threshold measurements given by the S-curve
 5021 method. It has been found from calibrations performed during Run 1 that the relation
 5022 $\Delta(DT) = DT - DT_{target} \simeq \Delta V_{ana}$ holds [188]. Using this relation, the new V_{ana} settings
 5023 are computed for each iteration and then downloaded to the ROCs for the next iteration.
 5024 In each iteration, the absolute threshold and charge injection timing has to be re-calibrated
 5025 (step 5 in Section 15.3.1) because of their dependence on V_{ana} . Figure 15.16 illustrates the
 5026 evolution of the V_{ana} settings with the iterations showing how these converge to the value
 5027 corresponding to the target DT.

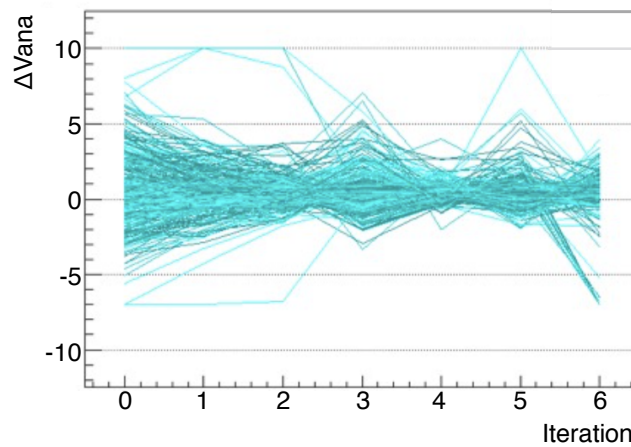


Figure 15.16: Example of optimization of the signal rise speed obtained from tests conducted in the clean room during LS1. The evolution of the V_{ana} settings for some ROCs with the iterations is shown and illustrates how these converge to the values corresponding to the target DT.

5028 2) Threshold minimization

5029 This step is meant to set the threshold of each ROC at the lowest practical value, so that
 5030 the threshold is low enough to detect low amplitude signals and ensure high hit resolution,
 5031 but above the noise level. The procedure for minimizing the threshold starts setting a large
 5032 value of the comparator threshold (for instance 50 V_{cal}) in each ROC such that it is above
 5033 the level of noise. The threshold is then lowered by 2 units and a pixel alive test or S-curve
 5034 is run to check whether a ROC is failing because the threshold is too low and noise occurs.
 5035 The procedure is iterated until all ROCs reach the minimum achievable value. For each
 5036 iteration the charge injection timing has to be re-optimized as well. Several scripts have been
 5037 implemented during LS1 to automatize this time consuming procedure. An example of the
 5038 results from tests conducted in the clean room during LS1 is shown in Fig. 15.17. The final
 5039 threshold and noise distributions for the whole detector obtained with this method before
 5040 the start of data-taking in 2015 are discussed in Section 15.4.

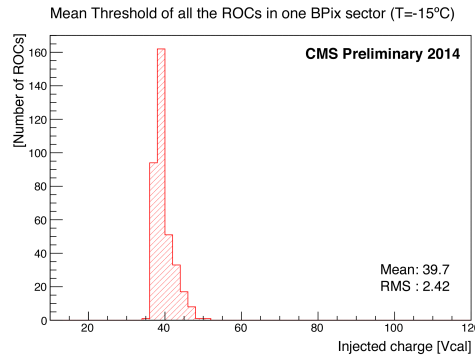


Figure 15.17: Distribution of the minimized thresholds for all the ROCs in one BPix sector. The measurement was performed at -15°C coolant temperature in the clean room during LS1.

3) Analog signal response calibration

The final part of the calibration procedure is aimed at maximizing the range and linearity of the detector. In fact, the hit position is interpolated from the charge information of all pixels in a cluster. For a precise position resolution it is therefore crucial to know for each pixel the exact response curve (or pixel gain) that converts the analog pulse height (in ADC counts) into the corresponding charge. The response curve is measured by injecting signals with increasing amplitudes to each pixel and measuring the analog pulse height. Before this calibration, the linearity of the response curve is optimized by adjusting few DAC registers in the ROC. The linearity is required for two reasons. On one hand the non-linear behavior in the low range does not allow to reconstruct the charge of the signal, on the other hand fewer parameters have to be stored in the data base. The *VhldDel* register controls the delay that is applied to each pulse before its height is sampled and stored in the sample and hold capacitance until the readout mechanism is started from the periphery. The supply voltage of the sample and hold circuit is regulated by the *Vsf* register.

Figure 15.18 shows the pulse height as a function of *VhldDel* settings at low, medium, and high values of *Vsf*, for a fixed injected signal amplitude. A good *Vsf* value is one for which this curve rises and then falls so that the pulse heights at the two endpoints (lowest and highest *VhldDel*) are equal. The figure also includes a plot of these endpoints as a function of *Vsf*; the rightmost intersection point is the *Vsf* value chosen. Low values of *Vsf*, below ~ 90 are discarded because they are found to be not optimal for a correct readout. After choosing the *Vsf* value, *VhldDel* is set to the value that maximizes the pulse height.

Several ROC DAC settings also affect the scaling of the pulse height signal that is sent out to the FED. The difference in recorded pulse height between a small and large amount of collected charge should be preferably large. However, the pulse height signal should not go too low to be confused with the UB level, nor too high to exceed the FED's dynamic range. Hence, a calibration is run to optimize these settings as well.

After these fine adjustments, the measurement of the response curve for each pixel is performed. For each pixel about 30 charge values are injected. During the scan, the acquired data is stored in binary files and is later analyzed offline. All pixels have to be calibrated, therefore, the procedure is time consuming and takes about 8 hours for the whole detector. An example of such measurement for one pixel is shown in Fig. 15.19. For comparison, an example exhibiting a non-linear behavior for a non optimal *Vsf* setting is also shown. The saturation in the high range is less important since it occurs for charges of more than 30-40 ke.

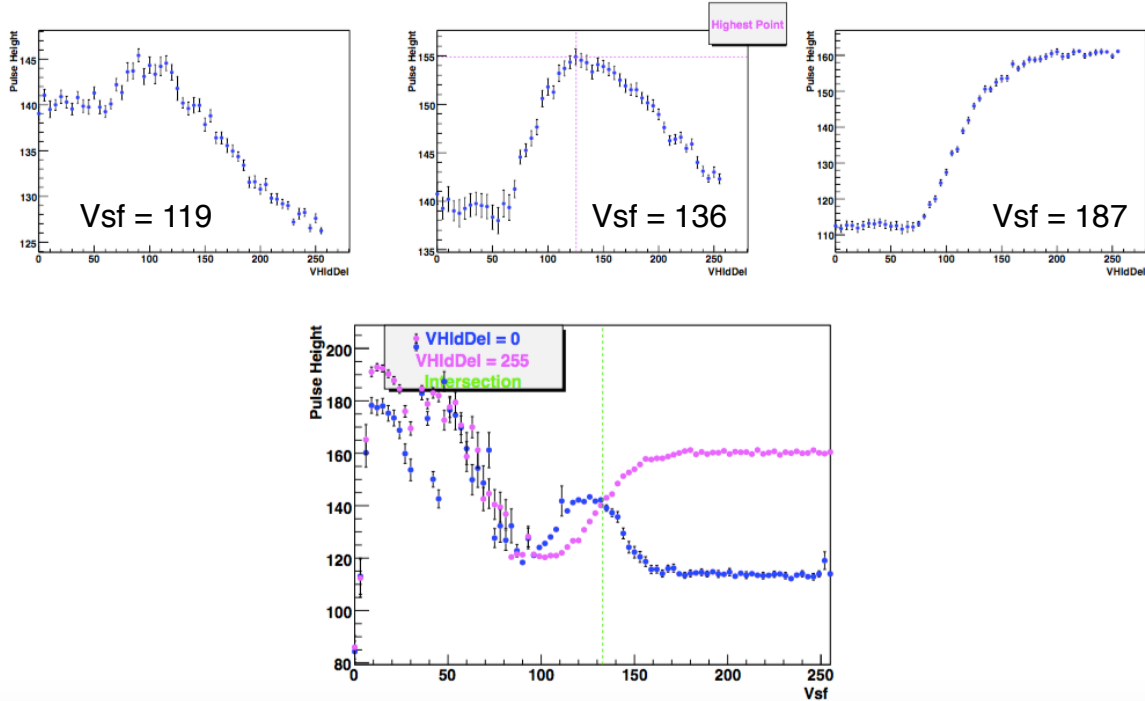


Figure 15.18: Top row: pulse height as a function of $VhldDel$ for low, medium, and high values of Vsf . As Vsf increases, the right endpoint shifts to the right. The best Vsf value is the one for which the pulse heights measured at the extremes of the $VhldDel$ range are equal. Bottom plot: pulse height at the extremes, as a function of Vsf . Low values of Vsf are discarded because not optimal.

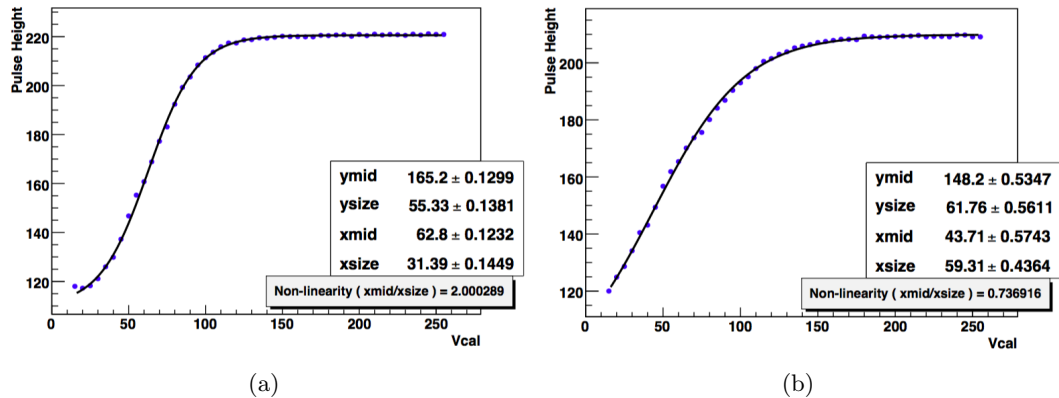


Figure 15.19: Examples of pixel response curve (gain calibration) representing the scan of the pulse height as a function of $Vcal$. The scan on the left presents poor linearity as performed for a not optimal value of Vsf .

5075

The pixel response curves are parametrized with the following function:

$$PH = f(Vcal) = y_{mid} + y_{size} \cdot \tanh\left(\frac{Vcal - x_{mid}}{x_{size}}\right), \quad (15.1)$$

5076

where PH is the recorded pulse height, (x_{mid}, y_{mid}) is the point at the center of the quasi-linear rise region of the hyperbolic tangent, x_{size} and y_{size} are the horizontal and vertical

5077

scales of the quasi-linear region, respectively. If $x_{mid}/x_{size} \approx 1$, the response curve is linear in the whole region of interest. Thus, the linear region below the saturation is parametrized by only the slope (gain) and offset (pedestal) of a linear fit. These parameters are then used in the data reconstruction. The results of the gain calibration performed for the whole detector before the start of data-taking in 2015 are discussed in Section 15.4.

15.4 Re-commissioning for LHC Run 2

The barrel pixel detector was installed back into CMS on 8th December 2014. The operations, described in Section 15.4.1, were coordinated by the PSI and UZH teams (Fig. 15.20), and were completed in only 5 days. After that, the FPix detector was also installed following a similar check out procedure as for BPix so that most work was already completed before Christmas. The full pixel detector was re-commissioned in January 2015 within about a fortnight using the procedure described in the previous section. Section 15.4.2 presents the results of the detector calibrations performed for the whole detector at low temperature after the installation. Finally, in Section 15.5, the detector performance at the beginning of the LHC Run 2 are discussed.

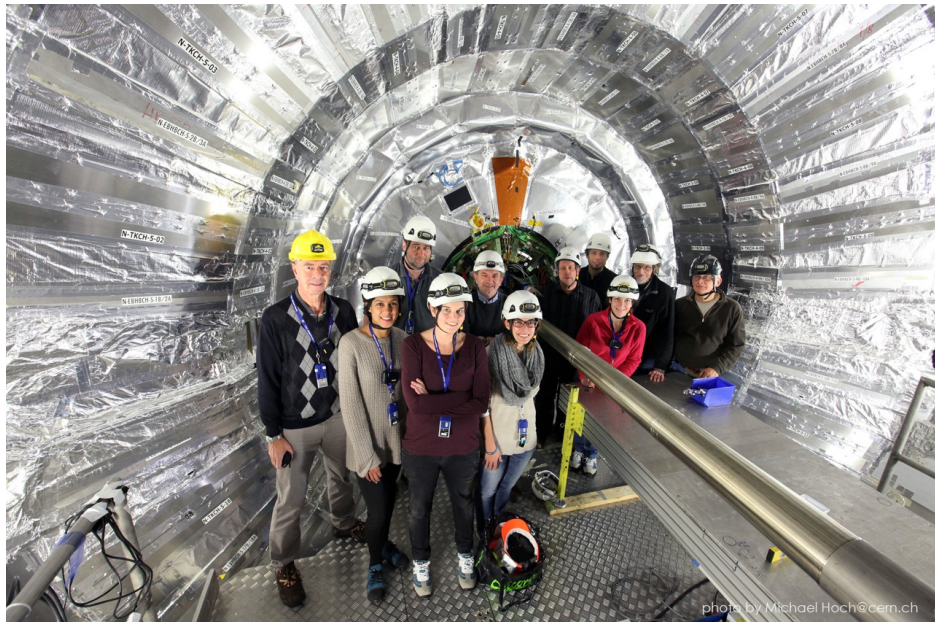


Figure 15.20: Pictures taken on the CMS underground platform after the re-installation of the barrel pixel detector in December 2014. The operations were coordinated by the PSI and UZH teams.

15.4.1 Installation into CMS

The barrel pixel detector re-installation into CMS took place only three months later than originally planned due to the incident mentioned in the previous section. Particular care was given to the centering of the detector with respect to the new beam pipe, required for the upgraded pixel detector planned for Spring 2017 (Chapter 16), since before it had been slightly shifted irradiating one side stronger than the other. Figure 15.21 shows pictures taken on the CMS underground platform illustrating the operations conducted in the first two days. The first day, each half of the detector was moved inside a transport box from the

5101 clean room and lowered down to the cavern through the main shaft. A system with rails on
 5102 top and bottom inside CMS had been designed to insert the pixel detector and the supply
 5103 tubes along the beam pipe. The transport box with the detector was lifted to the insertion
 5104 table and the rail system inside the box was joint with the rail system inside CMS using
 5105 temporary extension rails. In this way, the detector could slide out of the transport box into
 5106 its final position. The following day, all cooling loops, power cables and fibers were connected,
 5107 and first attempts to power the detector and to test a sector were made. A picture of the
 5108 detector in the final position with all power and control cables and optical fibers connected is
 5109 shown in Fig. 15.22.

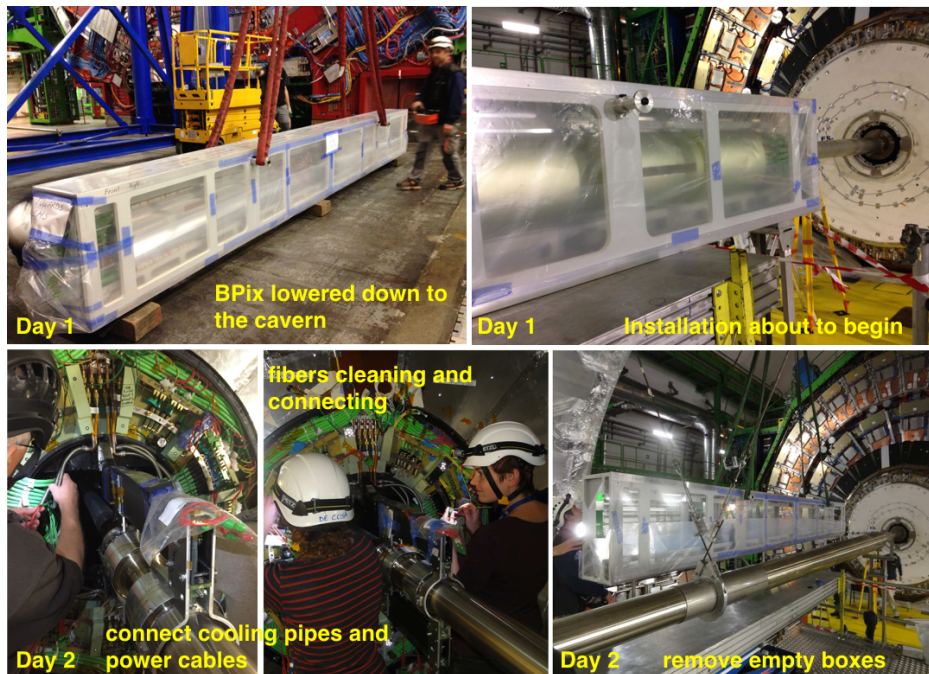


Figure 15.21: Pictures illustrating the steps of the BPix re-installation in December 2014. The operation has been completed in 2 days.

5110 After the installation, the detector was then checked out at room temperature of about
 5111 16 °C. The basic set of calibrations was run from the CMS control room aimed at assessing
 5112 the detector status and setting the basic operating parameters. These include calibrations
 5113 of the Delay25 chip, FED baseline, AOH bias and gain, TBM and ROC UB, and address
 5114 levels. The absence of a good quality TBM signal in the FED (Fig. 15.9) or bad address levels
 5115 indicate poor optical connections. This kind of problems were immediately established and
 5116 solved underground on the platform by re-cleaning the optical connectors with special tools.
 5117 Few iterations were needed. These operations were completed in about 3 days establishing
 5118 the functionality of the whole BPix detector. Only 1% dead or disabled channels were found
 5119 and most of them were acknowledged during LS1. The check out procedure was repeated
 5120 after the insertion of the FPix.

5121 15.4.2 Calibrations at -10 °C

5122 As discussed at the beginning of this chapter, it was planned to operate the detector at -10 °C
 5123 since low temperatures are favorable to mitigate the effects of radiation damage and guarantee
 5124 excellent performance. Since the detector settings largely depend on the temperature, a full

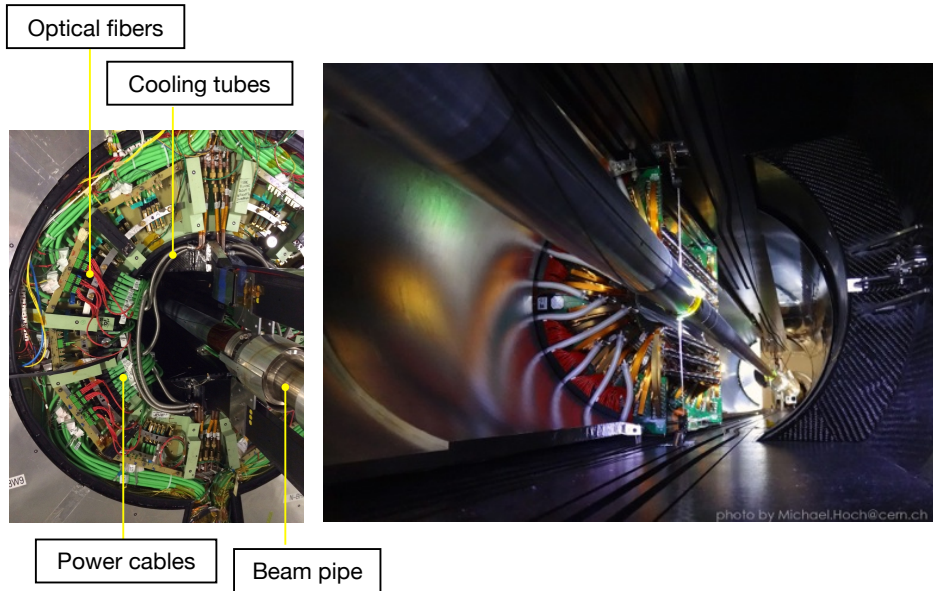


Figure 15.22: View of half of the barrel pixel detector in its final position inside CMS. The central beam pipe and the detector end-flanges with cooling lines and power and signal cables can be seen.

calibration of the detector under the new conditions has to be performed. Because of the limited amount of time, it was not possible to achieve this before the re-installation, and tests were conducted for only few sectors aimed at verifying some basic functionalities at such low temperatures. The full calibration procedure was instead run in January 2015 and completed in only 8 days, including the final optimization of the signal performance (Section 15.3.2). The improvements added to the procedure during LS1 as well as the time spent in practicing it were crucial to make these time consuming operations much faster and smoother with respect to 2011 and 2012.

The results of the optimization of the signal rise speed are presented in Fig. 15.23, which shows the distributions in DT for all the ROCs at the beginning and at the end of the procedure. A value for the DT of 12 V_{cal} was chosen as a target. The corresponding average current per ROC measured from the power supplies for each power group are also shown separately for layers 1 and 2 (Fig. 15.23(b)), and layer 3 ((Fig. 15.23(c))).

Figure 15.24 shows the final threshold and noise distributions for all pixels obtained after the procedure of minimization described in Section 15.3.2. The spread of the thresholds in each ROC is also shown, quantified by the RMS of the individual ROC distributions. A final average threshold of ≈ 40 V_{cal} (2,200 electrons) was obtained showing agreement with the results of the tests performed in the clean room (Fig. 15.17) and with the Run 1 values (Fig. 15.3). Finally, the measured distributions of the gain and pedestal for each pixel used for the offline reconstruction of clusters are presented in Fig. 15.25. The distribution of the linearity parameter of the response curve as extracted from the fits is also shown.

15.5 Performance at the start of Run 2

The detector re-calibration discussed in the previous section has been crucial to ensure excellent performance during the start-up of data-taking in 2015. Figure 15.26 shows the average threshold, RMS and noise in units of 1 ke for each barrel pixel layer as a function

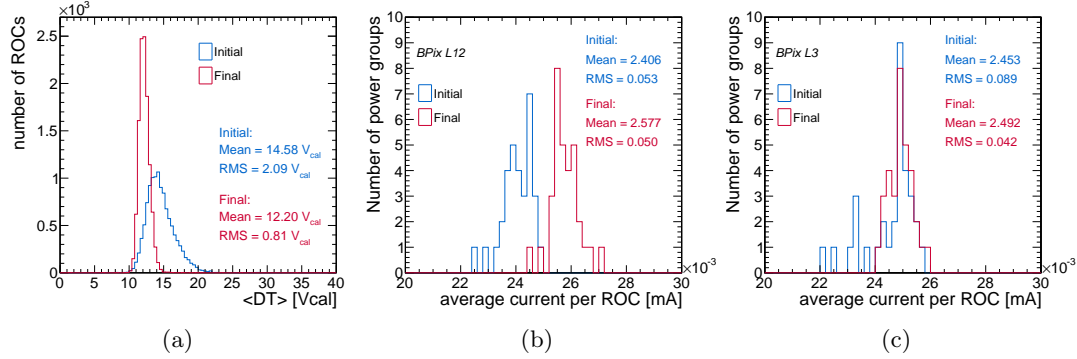


Figure 15.23: (a) Distributions in DT at the beginning and end of the optimization of the signal rise speed performed in 2015 for BPix Run 2 commissioning. (b-c) Corresponding average analog current per ROC after reaching the target DT value of 12 V_{cal} .

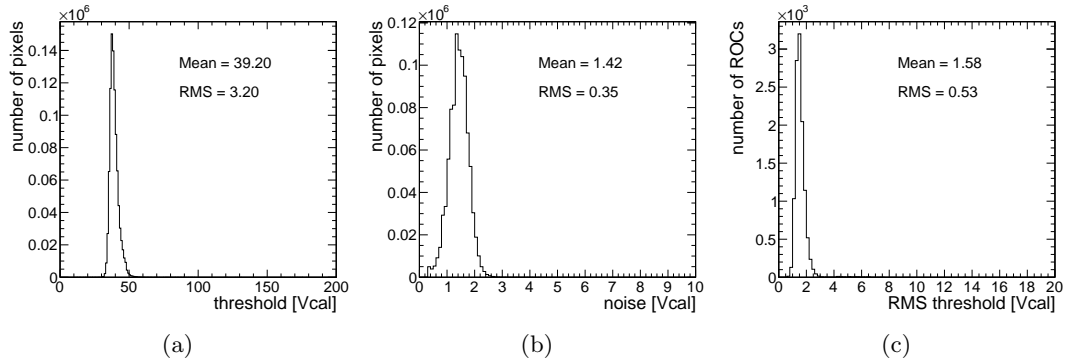


Figure 15.24: (a) Threshold and (b) noise distribution for pixels after the calibrations performed in 2015 for Run 2 commissioning. (c) The RMS of the threshold distributions within single ROCs quantifying its spread among cells. All distributions are in units of V_{cal} (1 V_{cal} = 65.5 electrons).

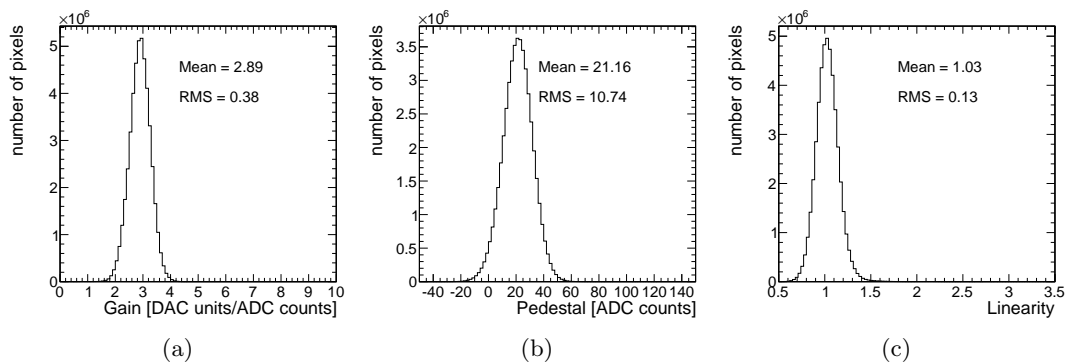


Figure 15.25: Gain (a) and pedestal (b) distributions extracted from the linear fits to the gain response curves of all pixels. These parameters are used for the offline reconstruction of clusters. (c) Distribution of the linearity parameter of the response curve as extracted from the fit.

of the integrated luminosity delivered in 2015. Due to the different levels of irradiation, the old and new modules have been monitored separately. The threshold of the new modules rapidly increased with irradiation as was observed also in Run 1 (Fig. 15.3). The noise quickly reached similar values as that of the old modules, which no longer experience such large changes due to irradiation.

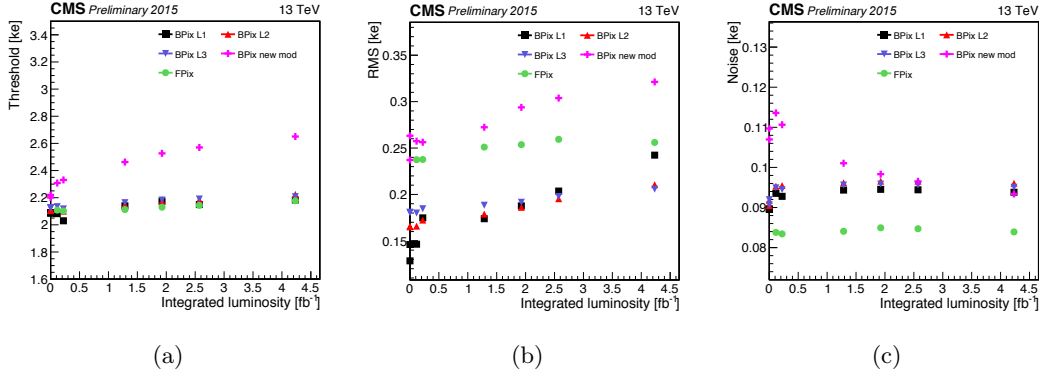


Figure 15.26: Average pixel thresholds (a), RMS (b), and noise (c) measured with charge injection, using the S-curve method. The BPix modules substituted during LS1 are considered separately [57].

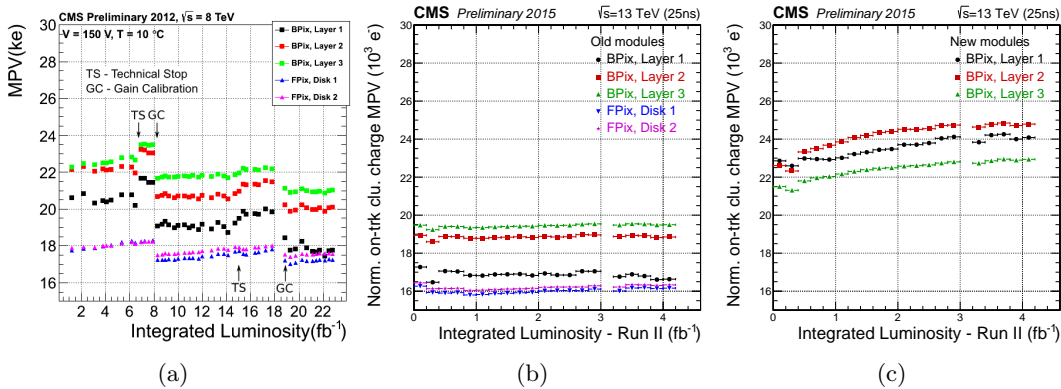


Figure 15.27: The MPV of the on-track cluster charge as a function of integrated luminosity (a) in 2012, and in 2015 separately for (b) old and (c) new modules [57].

Cluster properties like charge and size are important indicators of detector conditions and they have been monitored throughout the year by the pixel group. The cluster charge is determined by fitting the Landau distribution (Fig. 14.3) arising from the hits of tracks with $p_T > 1 \text{ GeV}$ and extracting the MPV parameter. In the Run 1 measurements, the MPV changed significantly throughout the year and also after calibrations during technical stop periods (Fig. 15.27(a)). While the MPV of old modules did not change much in 2015 (Fig. 15.27(b)), the new modules showed a rapid increase (Fig. 15.27(c)). This behavior was also observed for old modules in Run 1 in the beginning of their lifetime. No significant change in the cluster size (Fig. 15.28) was observed.

Finally, the hit resolution has also been measured by the pixel group for layer 2 with tracks that have hits on layer 1 and layer 3. The tracks are re-fitted without the hit in the middle, and the residual between the original and the interpolated hit positions are measured.

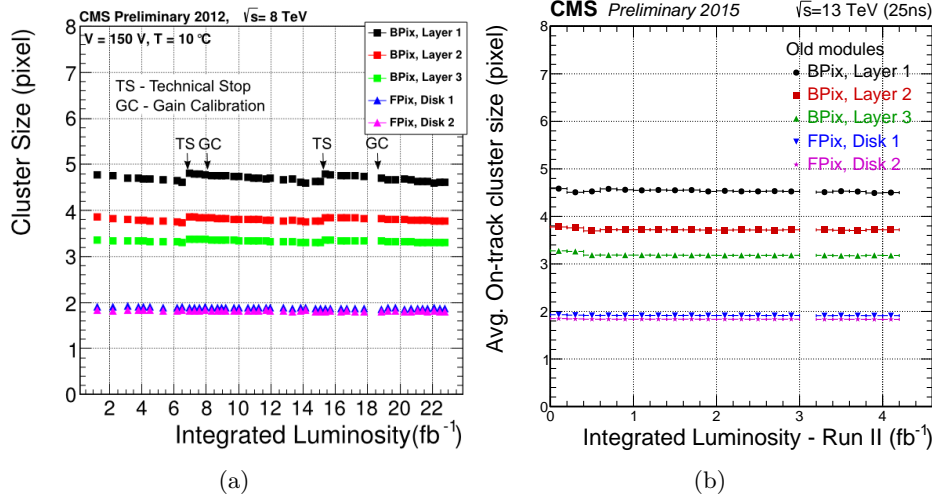


Figure 15.28: Average on-track cluster size as a function of integrated luminosity in (a) Run 1 and (b) Run 2. Both old and new modules showed very similar behavior [57].

5168 The residual distribution is then fitted with a student-t function. Figure 15.29 shows the
 5169 hit resolution as a function of the delivered luminosity in 2015. A large improvement was
 5170 observed with respect to the measurements performed at the end of Run 1 (Fig. 15.4).

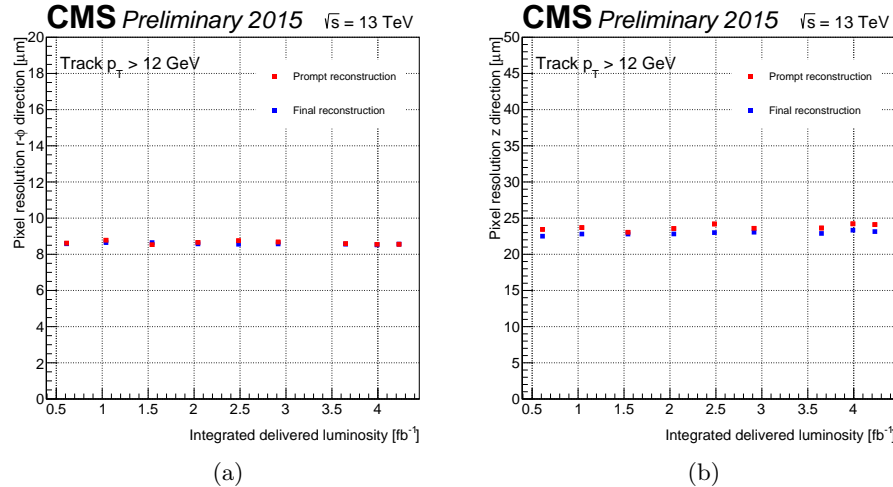


Figure 15.29: Hit resolution of barrel pixel modules in (a) the $r\phi$ and (b) the beam direction as a function of integrated luminosity in 2015 [57].

5171

5172

5173

Phase I upgrade of the CMS pixel barrel detector

5174

The present pixel detector will be replaced with a new pixel system in order to maintain the excellent tracking performance of CMS with the upcoming higher luminosity conditions at the LHC. This project is referred to as *Phase I pixel upgrade* [189]. The new upgrade detector comprises four barrel layers and three forward disks at each endcap to provide on average one more spatial point measurement per track compared to the present system, in the whole detector acceptance. It also provides improved track impact parameter resolution reducing the radius of the innermost layer and increasing radial acceptance. Further improvement is obtained thanks to optimized engineering of the mechanical design and services of the detector, that provide a substantial reduction of the passive material in the tracking volume despite the addition of one barrel layer. Since the innermost sensitive layer is closer to the interaction point compared to the present detector, faster front-end electronics have been developed to operate with high hit efficiency and low dead-time. In this chapter, the main features of the new barrel pixel system are introduced.

5188

At the end of LS1 eight prototype Phase-1 pixel modules were installed in the CMS detector, on the third unpopulated forward disk. This so-called pilot system was commissioned and integrated into the central DAQ and control system with the aim of gaining operation experience under realistic conditions [190].

5193

As for the present barrel pixel detector, the supply tubes have been assembled and tested at the University of Zurich, while the modules have been mounted on the detector mechanical structure at PSI. The integration of the supply tubes with the detector is currently ongoing and the installation into CMS and commissioning of the complete system is planned for March 2017.

5198

Several procedures for testing the new system have been developed over the last three years, thanks to a test stand assembled at the University of Zurich. The test stand, described in this chapter, includes a slice of the CMS pixel data-acquisition system and all components of the upgrade readout chain, together with a number of detector modules. It allowed for detailed evaluation and verification of the components placed on the supply tubes before their integration. I have contributed to the assembly of the test system and I implemented some of its functionalities. Furthermore, I employed the system to test new calibration procedures that I developed to be included in the main pixel online software. The aim of the procedure is to guarantee a quick verification of the detector functionality during assembly and commissioning. This work, detailed in the following, has been crucial to gain experience with the new barrel pixel system and to acknowledge and implement several modifications to the pixel software to be able to operate with the detector.

5210 16.1 Motivations

5211 The proposed upgrade of the CMS pixel detector aims at maintaining the excellent performance
 5212 of the present detector up to and beyond an instantaneous luminosity of $2 \times 10^{34} \text{ cm}^{-2} \text{ s}^{-1}$
 5213 and a pileup of 50. The limitations of the present detector for increased luminosity and
 5214 pileup can be seen in Fig. 16.1, which shows the hit efficiency for the various layers of the
 5215 present pixel detector in collisions during 2016. The leading effect is a dynamic data loss
 5216 in the readout chip which increases with instantaneous luminosity and trigger rate. This
 5217 loss of data depends on both the occupancy and trigger rates and comes primarily from
 5218 two sources, buffer size and readout speed. Between L1 triggers, pixel hits are stored in a
 5219 finite sized buffer before being readout at the next L1 trigger. Therefore, if this buffer is full
 5220 the ROC cannot record any more hits and subsequent hits are lost. Furthermore, when a
 5221 L1 trigger initiates the readout, the involved double columns are blocked from having hits
 5222 recorded and the buffer is cleared only after data have been sent. Thus, data can be lost if
 5223 the readout is slow or the L1 trigger rate is very high. Simulation studies showed that for
 5224 an instantaneous luminosity of $2 \times 10^{34} \text{ cm}^{-2} \text{ s}^{-1}$ and a bunch crossing time of 25 ns (50 ns),
 5225 the expected dynamic inefficiency for the present pixel detector increases up to 15% (50%)
 5226 for ROCs in the first barrel layer. As a consequence, the track reconstruction efficiency is
 5227 affected. This can be seen in Fig. 16.2, which shows the track reconstruction efficiency for
 5228 muons coming from the Z boson decay as a function of the number of primary vertices, as
 5229 measured in 2016 data with a T&P method. The efficiency is high and well described in the
 5230 simulation, but slowly degrades as the number of pileup events increases. A new ROC for
 5231 the upgrade pixel detector will largely reduce these effects.

5232

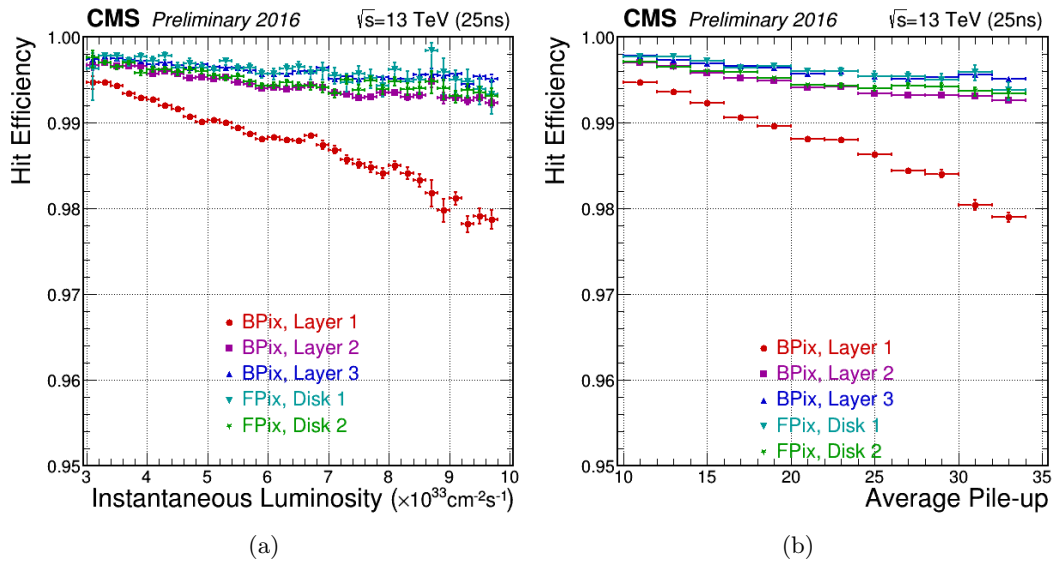


Figure 16.1: Hit efficiency for the various layers of the present pixel detector for 2016 collisions as a function of (a) the instantaneous luminosity and (b) the average number of inelastic pp collisions [57].

5233 Further effects contributing to inefficiencies in the track reconstruction arise from failures in
 5234 the tracking algorithms for events with a large number of hits. In fact, with more interactions
 5235 per crossing giving rise to additional hits in the tracking detectors, the pattern recognition
 5236 becomes more challenging. Under these conditions, the CPU time required for tracking largely

increases in both the HLT and offline processing. In addition, keeping the same level of tracking efficiency results in a higher level of fake tracks; alternatively, the tracking can be tuned for lower fake rate at the expense of reduced efficiency. In order to keep both the CPU time and fake rate under control for luminosities of $2 \times 10^{34} \text{ cm}^{-2} \text{ s}^{-1}$, the tracking has to be tuned to have generally lower efficiency than at lower luminosities. This is obtained requiring hits in 3 pixel barrel layers. With an extra pixel layer negative effects of pileup can be partly mitigated.

5243

Degradation in the performance of the present detector are further due to radiation damage resulting in reduced charge collection and hence, in degradation of hit detection efficiency and resolution. Although the degradation can initially be mitigated mostly by increasing the voltage, and modification of the pixel cluster hit templates, eventually the reduced collected charge cannot be compensated. The hit efficiency is expected to be less affected but the reduced charge sharing and eventual breaking up of clusters will degrade the hit resolution. The upgrade pixel sensor would suffer similar radiation damage, however, such effects can be compensated by a much lower comparator threshold for the new readout chip. This improvement largely mitigates the effects of reduced collected charge, so degradation in hit resolution should be much reduced comparing to the same radiation fluence.

5254

The passive material in the tracking volume is known to lead to tracking inefficiencies. In particular, a significant portion of material is present in the region near $|\eta| = 1.5$ where the end flange with services from BPix meets the FPix. This material also contributes to additional challenges for track pattern recognition in a high-pileup environment. The upgrade pixel detector, even with an extra layer features less passive material in the tracking volume, due to a new lightweight construction, cooling, and relocation of passive material out of the tracking region.

5262

Details on the new detector layout and front-end electronics are given in the next chapter.

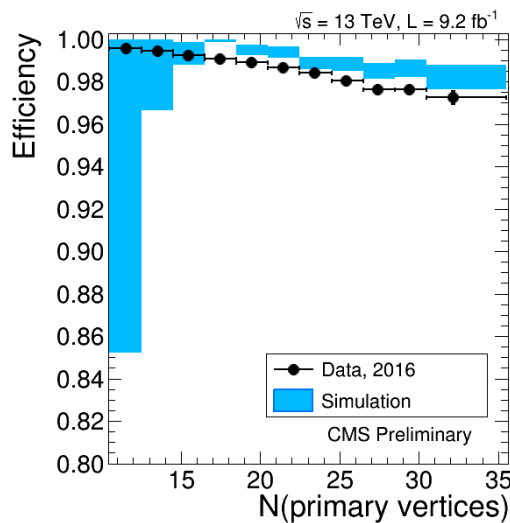


Figure 16.2: Track reconstruction efficiency for 2016 data and simulation for muons coming from the Z decay as a function of the number of primary vertices [94].

5263 16.2 Detector layout

5264 The proposed upgrade pixel detector consists of four barrel layers and three disks on either
 5265 side of the interaction point. The layouts of the present and upgrade pixel systems are
 5266 compared in Fig. 16.3. The barrel layers have a length of 548.8 mm and are placed at radii
 5267 of 30, 68, 109, and 160 mm. Compared to the present BPix, there is one new layer at high
 5268 radius. The radius of the innermost layer is reduced by 10 mm while layers 2 and 3 are almost
 5269 unchanged.

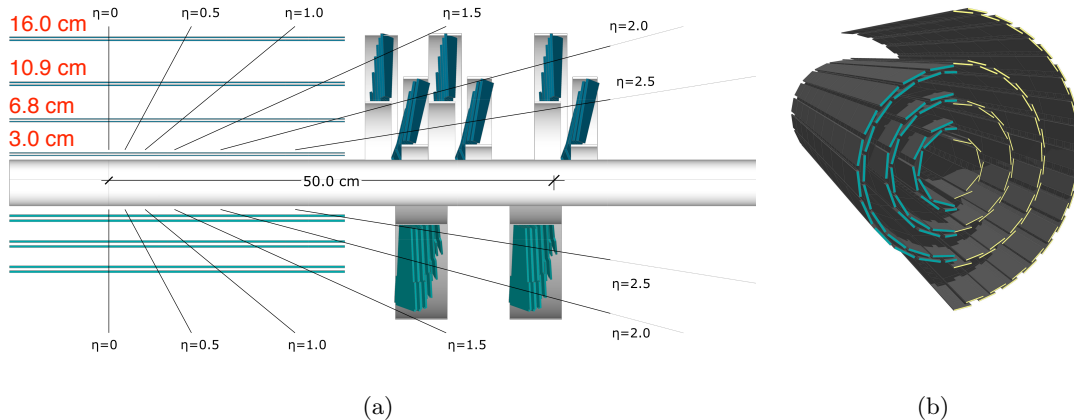


Figure 16.3: (a) Layout of the proposed upgrade pixel detector compared to the present detector in longitudinal view. (b) Three-dimensional view of the upgrade and present BPix detectors.

5270 The total number of BPix modules will increase to 1,184 compared to 768 modules in
 5271 the present detector, with an increase in the number of pixel channels from 48 million to 79
 5272 million. The modules are mounted on lightweight mechanical structures built from carbon
 5273 fiber. The design and composition of the modules are similar in the whole pixel detector,
 5274 except for the innermost layer where a considerable higher data rate is expected. Furthermore,
 5275 half modules are no longer used to join the two halves, whereas a slightly more complex
 5276 design of the mechanical support structure enables the use of full modules throughout. The
 5277 pixel detector modules will be described in more details in the next section.

5278 The cooling pipe diameter is significantly reduced with respect to the present detector
 5279 thanks to the usage of a two-phase CO₂ cooling system, which requires a much smaller mass
 5280 flow than C₆F₁₄. This reduces substantially the amount of material in the tracking region.
 5281 A further, significant reduction is achieved by moving the module connector area from the
 5282 detector end flange to higher z , outside of the tracker acceptance, by using longer and more
 5283 flexible module cables. As a replacement, micro twisted pair cables made of copper and with
 5284 a diameter of only 127 μm are used. Multiple twisted pairs are used to transmit the different
 5285 signals, including clock and trigger, I²C and data signals. Power is transmitted in parallel
 5286 through multiple copper cladded aluminium wires with a diameter of 90 μm . Signal and
 5287 power cables are braided into a single strand. Module cables have lengths between 95 and
 5288 110 cm depending on the position. Each wire of the strand is soldered onto a custom made
 5289 board that fits into a commercial connector. The connector on the module side is soldered
 5290 to the HDI. The obtained reduction in the material budget can bee seen in Fig. 16.4, which
 5291 shows a comparison of the radiation length and nuclear interaction length of the present and
 5292 upgrade pixel detectors as a function of η .

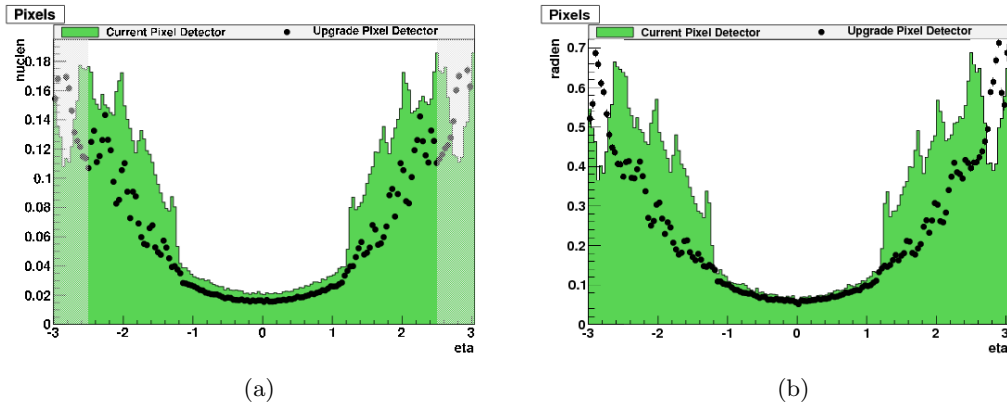


Figure 16.4: Material budget in the pixel detector shown in units of radiation length (a), and in units of nuclear interaction length (b) as a function of η ; this is given for the present (green histogram) and upgrade (black points) pixel detector. The shaded region at high η is outside the region for track reconstruction [189].

The overall layout of the system is unchanged. The detector barrel is complemented with four supply tubes on the $+z$ and $-z$ sides. The supply tubes carry electrical connections and cooling lines from the patch panels to the barrel detector, and house auxiliary front-end electronics. The upgrade system has to fit in the same mechanical envelope as the present system and reuse existing services, power cables and optical fibers. This puts strong constraints on the design of the new system. In particular, higher bandwidth electronics is need. Since the upgrade detector has 1.9 times more channels than the present detector, the power consumption increases accordingly. The upgrade system uses DC-DC power converters [191] to supply the necessary current to the modules while reusing the existing infrastructure.

16.3 Pixel modules

The pixel modules for the upgrade are of similar design compared to the ones employed in the present detector. The main changes concern the design of the ROCs and the TBMs, as described in the following. Figure 16.5 shows a drawing of the pixel module employed for the outer barrel layers. The innermost barrel layer features a different ROC that allows to cope with even more extreme conditions at such small radii, while its modules differ mostly by the way they are mounted and by the cables used. Furthermore, they feature two TBMs mounted on the HDI. From top to bottom, the figure shows the cables with a connector print, the HDI with the TBM mounted in the center, the silicon pixel sensor, 2×8 ROCs and base strips for mounting.

The sensor used in the upgrade is built with the same technology as the one used in the present detector. For the innermost layer, where the close proximity to the interaction point leads to the highest radiation damage, the sensor is expected to operate up to an integrated luminosity of 250 fb^{-1} . For this reason it is planned to exchange this layer once during the detector's expected lifetime of 500 fb^{-1} . The sensors in the rest of the detector can sustain the entire duration because of the greater distance from the interaction point.

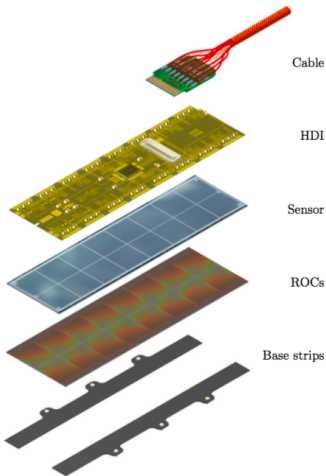


Figure 16.5: Exploded view of the new pixel module employed for the outer barrel layers of the upgrade BPix detector.

5319 16.3.1 The digital ROC

5320 The ROC for the upgrade detector [192] is not a completely new development but rather an
 5321 evolution of the well-proven ROC operating in CMS since its commissioning. It is designed
 5322 in the same 250 nm CMOS technology and the well-understood core of its double-column
 5323 architecture is mostly unaltered. However, to cope with the higher data bandwidth the
 5324 readout protocol has been changed from a 40 MHz analog to a 160 MBit/s digital readout.
 5325 An ADC digitizes the analog pulse height information in the ROC periphery. The key
 5326 additional elements are an 8-bit successive approximation current ADC running at 80 MHz
 5327 with a programmable range, and a PLL which generates the 160 and 80 MHz clocks for the
 5328 serial readout links and the ADC, respectively, from the 40 MHz LHC master clock. To
 5329 reduce data losses, the number of hit buffer cells in each double column has been increased
 5330 from 32 to 80 and the time stamp buffers have been increased from 12 to 24. To limit the
 5331 increase of the area used by the buffers the layout has been entirely redesigned. An additional
 5332 readout buffer stage has been introduced in the ROC periphery to reduce dead time during
 5333 the column readout: the data is transferred (after being digitized) into the new readout
 5334 buffer immediately after the trigger arrives so that the double columns are again operative.
 5335 Improved performance of the analog amplifier and the discriminator in the pixel unit cell
 5336 allow for operations at lower threshold, which is reduced from about 3,500 electrons in the
 5337 present detector to under 2,000 electrons after the upgrade. This guarantees higher radiation
 5338 tolerance and therefore, a longer lifetime of the detector.

5339 The chip just described is suitable for the whole upgrade pixel detector except for the
 5340 innermost barrel layer, where the data rates up to 600 MHz/cm^2 are expected, four times
 5341 higher compared to the second layer. In order to cope with such extreme conditions the
 5342 newly developed PROC600 [193] readout chip is used in the innermost layer. The new chip
 5343 features a new 40 MHz dynamic cluster column drain mechanism based on dynamic cluster
 5344 (2×2 pixels) finding in the double column.

5345 16.3.2 The TBM and readout

5346 In contrast to the present detector, for the upgrade all barrel modules use at least two data
 5347 channels in order to improve the bandwidth of the readout. Because of the limited number of

fibers available for this purpose, two channels are always multiplexed into one data stream through a Data-Keeper multiplexer and encoder. For this purpose few modifications have been applied to the TBM. In particular, it now combines the digital 160 Mbit/s readout from the ROCs from two buses into a 320 Mbit/s signal to which it then applies 4-to-5 bit encoding. This results in a 400 Mbit/s data stream. The readout scheme is adapted to the different barrel layers (Fig. 16.6). Layers 3 and 4 employ a dual core TBM, referred to as TBM08, that passes two tokens simultaneously to achieve the parallel readout of two groups of 8 ROCs, called Port 0 (or Channel α) and Port 1 (or Channel β). The data are then combined into one data stream as described above, readout over a single optical fiber. Except for the multiplexing step, this is very similar to the method used for the first two layers of the present detector (Section 14.2.3). Layer 2 employs a different TBM, called TBM09. For the readout this TBM behaves as two TBM08s (TBM A and TBM B in Fig. 16.6), each equipped with its own Data-Keeper. This TBM is capable of issuing four tokens simultaneously, so that the 16 ROCs are therefore divided into four groups that are readout in parallel. The two Data-Keepers then produce one 400 Mbit/s data stream each and two fibers are required for the readout. For the modules of the innermost layer, the TBM10 is used, which consists of two identical TBM09 chips identified by two different HUB addresses. In this case eight tokens are passed in parallel on these modules, resulting in four 400 Mbit/s data streams and hence, four fibers for transmission.

An extensive set of control registers have been built into the TBM, which allow various functions and operating modes of the TBM to be controlled by issuing commands to the TBM through the communication control HUB. For the TBM09 the commands have to be issued to both TBM08s controlled by one unique HUB.

As for the present detector, the module output signal is characterized by TBM header and trailer, ROC headers and pixel hit information, which are now encoded in binary data as shown in Fig. 16.7. A TBM readout begins by transmitting a twelve clock cycle (160 MHz) header sequence. The next sixteen clock cycles of the header are used to transmit the 8-bit event counter, 2 bits of error information, and 8 bits encoding the data contained in the last 8-bit TBM register accessed. Coincident with the next to last clock cycle, the token is transmitted to the ROCs. The TBM now goes into standby mode, waiting for the last ROC in the chain to return the token to the TBM. At this stage, the TBM transmits a twelve clock cycle trailer sequence. The next sixteen clock cycles of the trailer include 10 bits with the values programmed in the TBM registers that control its mode of operations, and a 6-bit stack count value. The counting is used to monitor the timeout on the token returning. If the token fails to return, before the timer expires, the TBM will automatically issue a ROC reset, ending the token pass. The data contained in the ROCs are deleted, and error bits are returned in the TBM trailer 8 clock cycles later. The ROC data consist of 12 bits for the header, 16 bits used for the pixel hit address and the final 8 bits for the pulse height.

In order to readout the new fully digital pixel system a VME-digital FED has been firstly designed. It is a hybrid solution featuring new daughter boards on the existing FED, and it has been used at the beginning of the operations with the pilot system and with test stands. This solution will be replaced by a μ TCA system with high-speed signal links providing data rates up to 10 Gbits/sec. Since the results presented in this work are based on the VME system, only this is described in the following.

The ADC daughter boards of the analog FED are not needed anymore for digital transmission. For the purpose of system developments, a special add-on board was produced, which is mounted on the current VME module for data readout, receives the 400 Mbit/s digitized data, and passes the data to the FPGAs in the same format as the present system.

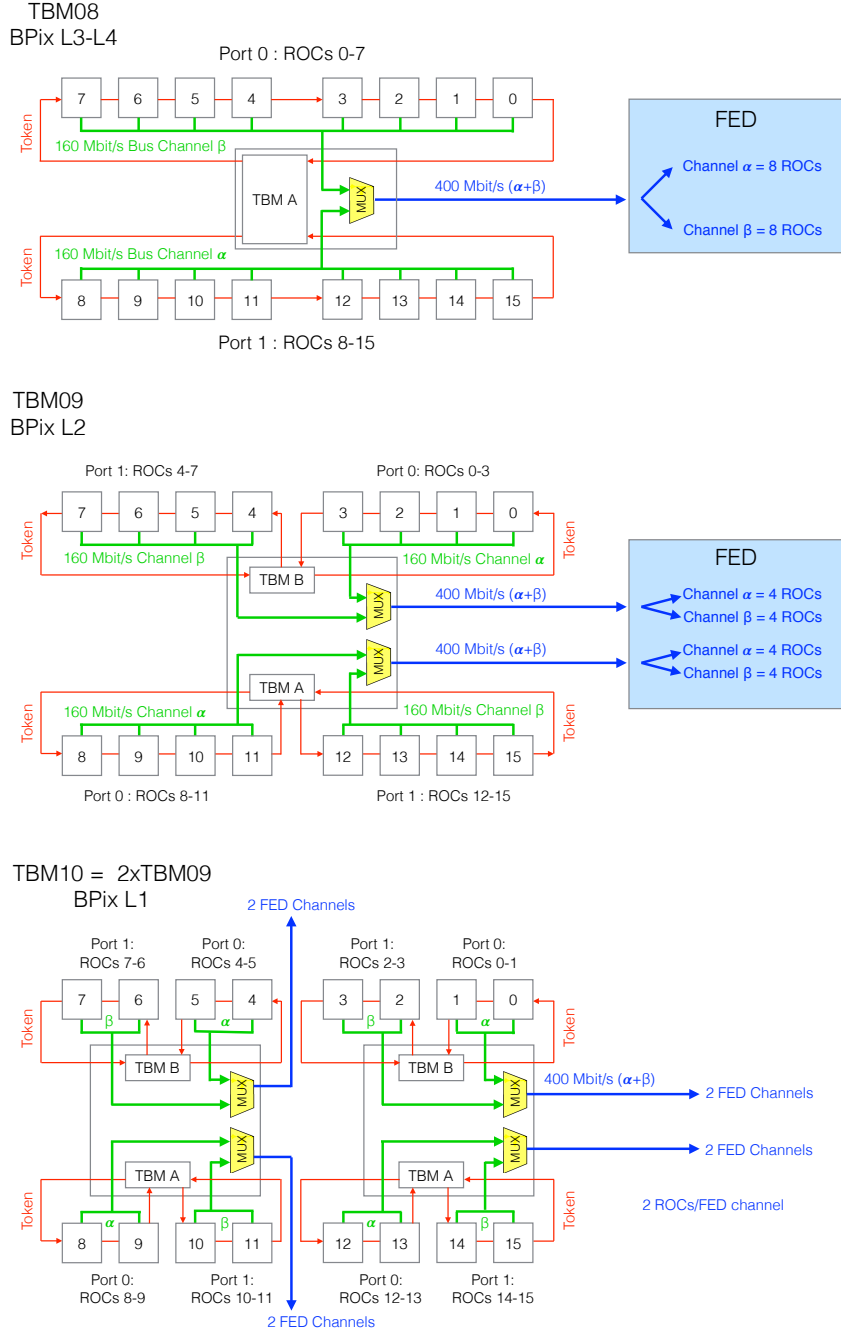


Figure 16.6: Readout scheme of the different TBMs used in the BPix layers.

5397 Thanks to this modular approach, the other parts of the FED did not require any hardware
 5398 modification, allowing for a quick start of the tests with the new upgrade pixel system.

5399 As shown in Fig. 16.6, the signal from each fiber is split at the FED into two channels,
 5400 whose content is buffered and processed in the FIFOs. Each channel will then correspond to
 5401 the data from half of the initial number of ROCs originally present in one fiber.

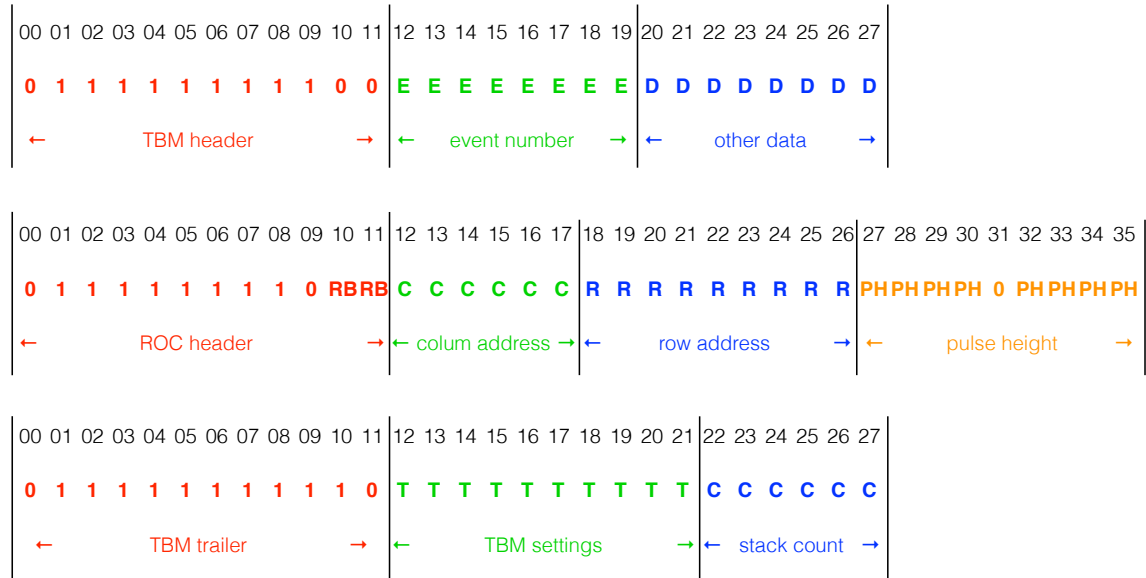


Figure 16.7: Decoding of the module digital output data.

5402 16.4 Supply tubes

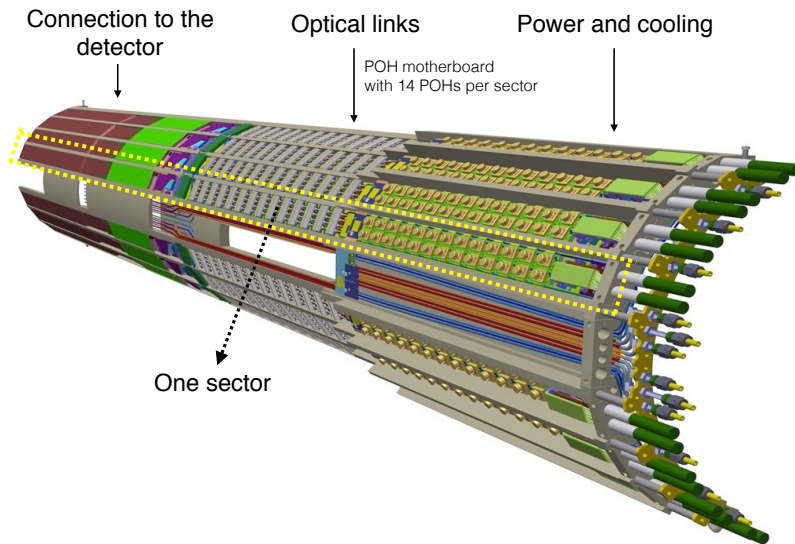


Figure 16.8: Layout of one of the four supply tubes for BPix equipped with the new electronic components. Each supply tube is divided into 8 sectors.

5403 As for the present detector, the power, readout and control circuits, as well as the cooling
 5404 lines are housed by four half-cylinder supply tubes. Figure 16.8 shows the layout of one
 5405 supply tube together with some of the new electronic components. The mechanical structure
 5406 of the supply tubes is made from layers of carbon fiber foam. Each supply tube is divided

5407 into 8 sectors, which hold the electronics for one readout group of detector modules.
 5408 Each sector includes DOHs as well as the auxiliary
 5409 chips (PLL, Delay25, Gate-Keeper) for the transmission
 5410 of control, clock and trigger signals. The change
 5411 from analog to digital module readout in the upgrade
 5412 system also requires the adoption of new optical links.
 5413 So-called pixel opto-hybrids (POHs) [194] are used
 5414 for the transmission of the module readout data as
 5415 a replacement of the AOHs used for the present de-
 5416 tector. The POHs are built from four transmitter
 5417 optical subassemblies (TOSA), linear laser-driver and
 5418 level-translator chips and have been designed specific-
 5419 ally for their use in the pixel upgrade system. All other
 5420 components used in the control and readout chain are
 5421 identical to the ones used in the present system. CCU
 5422 chips are used for slow control, monitoring and timing
 5423 distribution. Furthermore, pairs of DC-DC converters
 5424 are mounted on the service cylinders. Each sector
 5425 consists of a stack of boards, DC-DC converters, op-
 5426 tical links and cooling loops, resulting in tight space
 5427 constraints and a non-trivial assembly procedure.

5428 The complete supply tube system has been integ-
 5429 rated and tested sector by sector at the University
 5430 of Zurich. A picture of one supply tube after integrating all its components are shown in
 5431 Fig. 16.9.

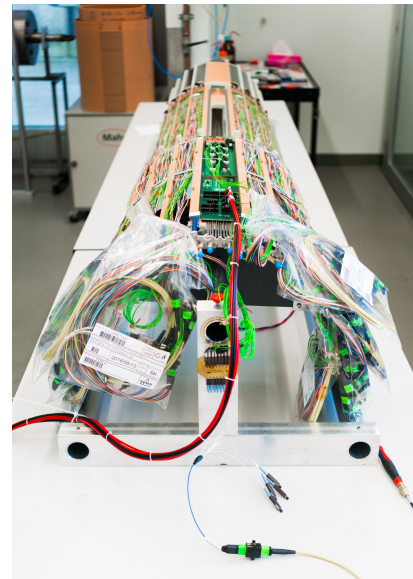


Figure 16.9: Picture of one of the four supply tubes with all its components assembled at the University of Zurich.

5432 16.5 The test stand

5433 In order to test the performance of the complete upgrade pixel system and gain experience
 5434 in its operations, a test stand for BPix has been set up at the University of Zurich in 2014.
 5435 The setup includes a slice of the full CMS pixel DAQ system together with prototypes of
 5436 all components of the upgrade power system, control and readout chain as well as a number
 5437 of detector modules. The system test was operated at UZH until November 2016 when the
 5438 integration of the supply tubes started. Its main goals include:

- 5439 • evaluate all components of the detector system prior to full production;
- 5440 • establish test and calibration procedures for the assembly and commissioning (Sec-
 5441 tion 16.6);
- 5442 • exercise the transition from the VME- to the μ TCA-based DAQ system.

5443 Figure 16.10 shows a picture of the test stand, which consists of several sensor modules,
 5444 electronics for their operation, a CAEN power supply and a VME back-end system to control
 5445 and readout the modules. The test stand is also equipped with a linux PC connected to the
 5446 VME and used to run and control the system through the installed XDAQ applications.

5447 Most of the tests that have been conducted with this system make use of a standalone
 5448 software based on the socket technology provided by the PYTHON framework, which allows
 5449 for a direct communication with the hardware. These tools have been firstly developed
 5450 for the testing of the present pixel detector prior to assembly [195], and necessitated many
 5451 fundamental changes to be able to operate with the upgrade system. I implemented part

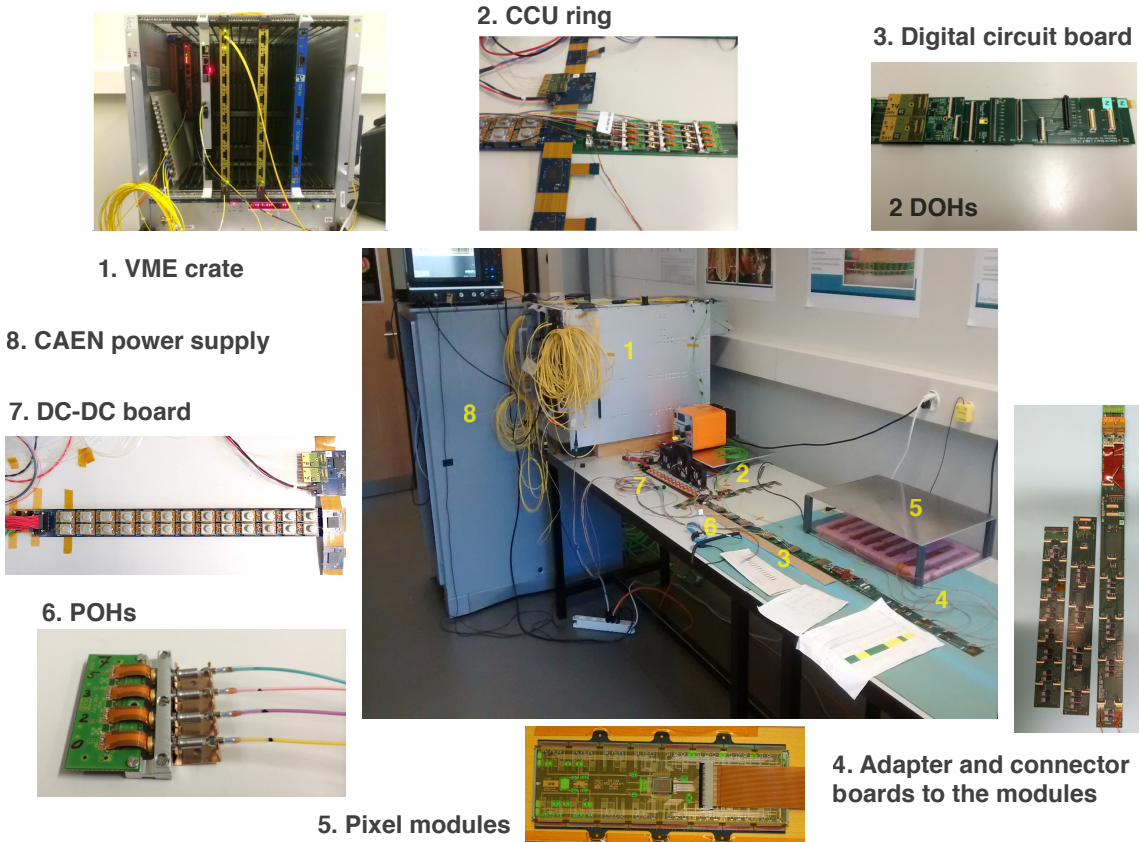


Figure 16.10: Test stand setup at UZH including all components of one BPix sector together with a few pixel modules. The CAEN power supply and the VME back-end system are also indicated.

of this transition and I was able to perform the first tests with the POHs. In the example shown in Fig. 16.11, the POH laser bias setting is varied from 0 to 40 and for each value the ADC counts (or optical power) at the VME-analog FED are checked. This scan is performed for different values of POH laser gain setting. The optical power sharply increases until the saturation of the receiver at the FED is reached. This test ensures the slow I²C communication with the auxiliary electronic components of the system. Other tests have been performed after pixel modules have been added to the system and aimed at establishing the functionality of the fast I²C communication to/from the TBM. This was checked by verifying for instance the presence of the TBM signal at the corresponding POH output through an optical probe plugged into the oscilloscope. If the fast I²C communication through the digital circuit is functional, the TBM sends the 400 Mbit/s data stream upon the arrival of a trigger as shown in Fig. 16.12.

This kind of tests is not suitable when dealing with a large number of channels. For detector assembly and commissioning the full functionality of each module has to be checked and calibrations have to be performed over the whole detector. In order to achieve this in a reasonable amount of time, the full pixel online software (Section 14.4) has to be used and upgraded to be able to operate with the new system. Many fundamental changes to the software have been firstly applied for the pilot system, as well as for operations with the FPix test stand at CERN. These changes mainly concerned the `FEDIInterface` class, where the new features of the digital VME-FED had to be implemented. In order to test and

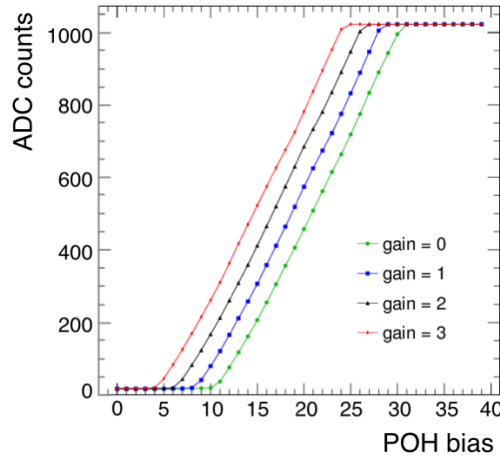


Figure 16.11: Typical result of the scan of a POH laser bias and gain. For each value of the laser settings, the optical power is readout at the VME-analog FED.

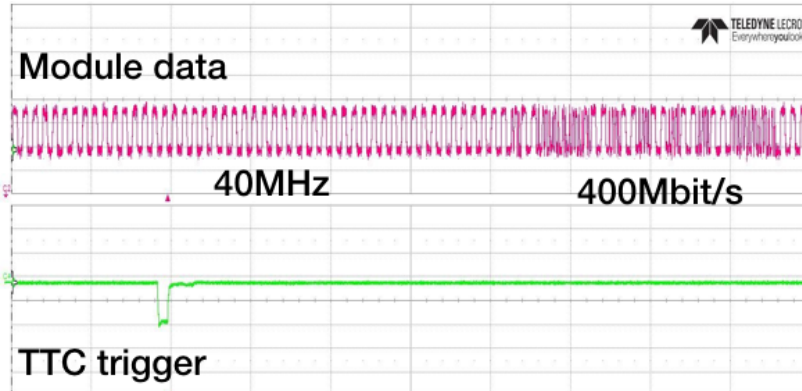


Figure 16.12: Module output signal initialized by a trigger sent by the TTC. The signal is acquired at the oscilloscope with an optical probe connected to the POH laser output. The 400 Mbit/s signal contains TBM trailer and header, and the headers from 8 ROCs.

5472 debug the new developments I installed POS and applied the modifications required to run it
 5473 with the system test at UZH. After establishing the basic functionalities, I developed new
 5474 calibrations for the upgrade detector as described in the next section. This work represents
 5475 the first attempt to operate the upgrade BPix system with POS and hence, has been crucial
 5476 to understand, implement and test new BPix specific developments.

5477 In mid-2016 a separate table has been setup in the same laboratory to operate the upgrade
 5478 electronics with the μ TCA DAQ system as this became available only at a later time. A new
 5479 μ TCA version of POS was developed in the meantime by the FPix group, and the second test
 5480 stand has been very useful to gain expertise with the new developments. Several of the new
 5481 features for the upgrade system that I included in the VME-POS have been easily exported
 5482 to the μ TCA-POS. The transition has been straightforward since I developed the new code
 5483 such that it is transparent with respect to the parts of the software handling the μ TCA or
 5484 VME communication.

16.6 Testing and calibration

5485 Since the upgrade system features a new digital readout, some of the steps int the calibration
5487 procedures developed for the present detector become obsolete, whereas new kind of tests
5488 are needed. In particular, the adjustment of the FED receiver offset, of the UB and address
5489 levels are dropped for obvious reasons. In this section, a calibration procedure for the Phase-1
5490 detector is described with main focus on the new developments. This procedure is suitable
5491 for testing each sector of the detector after assembly at PSI as well as for the commissioning
5492 of the whole detector at CERN. It is implemented in several steps, each aimed at testing one
5493 particular functionality. Each step produces new detector settings, such as POH bias and
5494 gain or TBM and ROC DACs, after a dedicated scan of a set of parameters. The procedure
5495 has been fully tested with the table top system at UZH and few pixel modules, and results
5496 will be presented and discussed in the following. Only modules equipped with TBM08 and
5497 TBM09 have been used for these tests, since the TBM10 was not available at the time of
5498 this work. The TBM10 features slightly different readout and programming mechanisms,
5499 and additional modifications to the software are required. Further improvements to this
5500 preliminary version of the procedure have been implemented later on by the BPix group
5501 in order to have a finalized version for detector commissioning that also includes specific
5502 developments to operate with the TBM10.

16.6.1 Delay adjustments

5503 The synchronization between the 160 Mbit/s ROC data and the 400 Mbit/s final output data
5504 stream has to be adjusted in order to be able to correctly readout the module output signal.
5505 The data alignment can be adjusted by programming two 8-bit registers internal to the TBM.
5506 The first register controls the phases of the 160 MHz and 400 MHz PLLs integrated in the
5507 TBM. For the TBM09 only one of the two cores (TBM A and TBM B in Fig. 16.6) has to be
5508 programmed since the PLLs are common to both. The second register controls the delay in
5509 the data stream of the two readout groups of ROCs (Port 0 and Port 1 in Fig. 16.6), and for
5510 TBM09 it has to be programmed for each core. All the above timing settings can be varied
5511 in the range 0–7 ns in steps of 1 ns so that 3 bits are sufficient for each of them.

5512 After configuring the settings of the Delay25 chip to ensure communication between the
5513 pxFEC and the modules, the first step is to perform a scan of the TBM PLL phases. For
5514 each set of values the digital data are readout at the FED, and it is checked that the TBM
5515 had sent header and trailer. This is done for a number of triggers defined by the user and
5516 for each FED channel corresponding to the same module (Fig. 16.6). The TBM header and
5517 trailer are only available in the FIFO1, which can be accessed only if the normal data flow
5518 to the other FIFOs is interrupted. This is achieved by programming a FED register. An
5519 example of such scan for one module is shown in Fig. 16.13(a). where the efficiency for
5520 TBM header and trailer to be recorded is measured as a function of the two phases. The
5521 efficiency is averaged over all the FED channels. At the end of the test new settings for the
5522 TBM are produced, corresponding to a pair of phase values corresponding to 100% efficiency.
5523 Since there might be more than one bin corresponding to 100% efficiency only the first one
5524 is chosen. However, this algorithm can be improved by picking a bin from a region that
5525 presents small variations. If no 100% efficiency bins are found, the bin corresponding to
5526 the maximum is picked and a error flag is saved in the output file. The histogram with the
5527 resulting scan is also saved for each module. This test ensures that the TBM settings are
5528 correct to be able to read out the signal. It is also very useful to have a feedback on the
5529 status of the detector, for instance after installation, similarly to the FED baseline calibration
5530 for the present detector (Fig. 15.9). In fact, with this test it is verified that clock, trigger

and programming signals are correctly arriving at the pixel modules and that the TBM can be programmed. In addition, low efficiency might indicate poor optical connections and the problem can be immediately solved by cleaning the fibers. Issues in the mapping between modules and FED channels, as well as possible broken channels, can also be identified at this stage.

5536

The second step consists of scanning the ROC delays, and for each set of values it is checked that each ROC had sent the header. As for the scan of the TBM PLL phases, this is done for a number of triggers defined by the user, and the efficiency is measured for each ROC. For the TBM09 the same value is programmed for the two cores. A histogram is produced with the efficiency averaged over all ROCs and FED channels for each pair of delay values, as shown in Fig. 16.13(b). New settings for the TBM are also produced, corresponding to the delay values giving 16 ROC headers recorded at the FED. The choice of the best settings follows the same strategy described above for the TBM PLL phases. This test ensures that the TBM settings are correct to be able to read out the signal and it also verifies the functionality of the token passage.

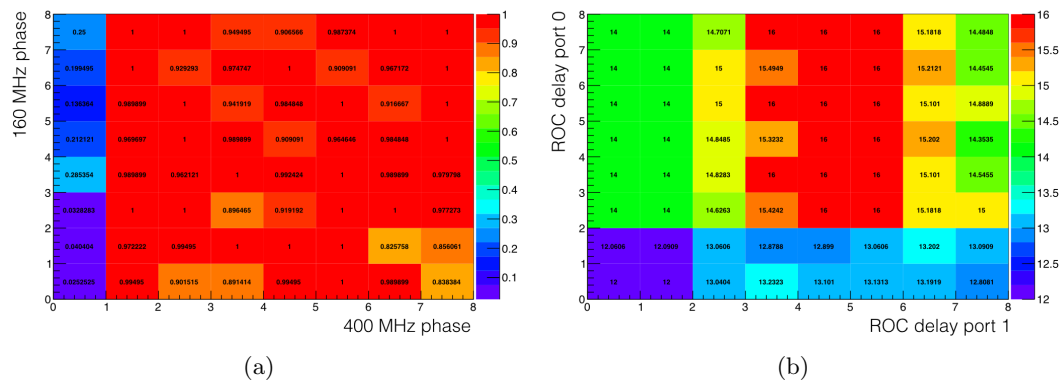


Figure 16.13: (a) Example of scan of the TBM PLL phases for one module. For each pair of values the module signal is read out several times at the digital FED, and the presence of TBM header and trailer is verified. An efficiency is obtained by dividing by the number of times the signal has been read out. (b) Example of scan of the delays in the data from the two ROC readout groups. For each pair of values the presence of each ROC header in the readout data at the digital FED is verified. The average number of ROCs that sent the header is obtained by dividing by the number of times the signal has been read out.

5547 16.6.2 POH bias and gain

The tests described in the previous section assume that the POH laser settings are good enough to allow for a correct readout of the signal. In fact, a too low laser bias and gain result in a small difference between the 0 and 1 levels of the digital signal and consequently to a large error bit rate. It has been found with the test stand that a bias of 40 and a gain of 3 are sufficient to be able to correctly read out the signal so that the tests of the previous section can be safely run with such values. However, once the functionality of the TBM has been verified a scan of the POH setting should be run to obtain a finer adjustment aimed at minimizing the power consumption. An approximate indication of the error bit rate can be obtained by measuring the known TBM signal. In this calibration, a scan of the POH bias and gain is performed, and for each value it is checked that the TBM had sent header and

trailer. An example of such scan is shown in Fig. 16.14. At the end of the calibration new settings are produced corresponding to a safe area, i.e. 5 units above the beginning of the saturation.

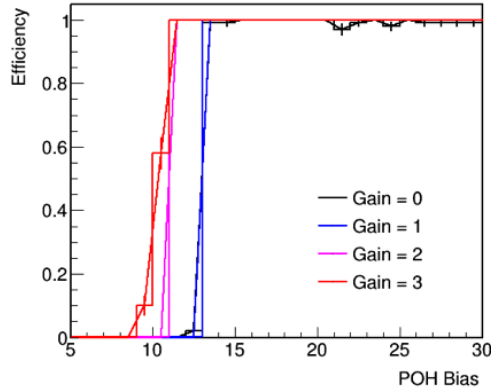


Figure 16.14: Example of scan of a POH laser bias and gain. For each value of the laser settings the module signal is read out several times at the digital FED and the presence of TBM header and trailer is verified.

16.6.3 Read back test

As discussed in Section 16.3.2, the ROC header is followed by 3 bits where the first one is always a 0, and the other two contain one bit for a start signal and one bit for the so called read back data as explained in the following. The read back data contain different information depending on the value programmed in the ROC read back register. For instance, for a value of 12 the ROC analog current is returned. It has been found after several tests that not all delay settings allow for a correct read out of the information contained in the ROC read back data. Hence, another scan of the TBM PLL phases and ROC delays is performed and for each value the information in the read back data is verified as explained in the following.

The read back word is encoded in sixteen bits (Table 16.1), which cannot be sent at once given the limited size of the ROC data stream. As mentioned above, every time the readout is initialized by a trigger, one bit is sent for the message data and another one is sent to indicate the start of the word. Thus, sixteen triggers have to be sent before the entire word can be decoded. Of the sixteen bits collected, the first eight bits are used for the required information (for instance the analog current), four bits contain the value written to the read back register (for instance 12 for the analog current), and the last four bits encode the ROC I²C address (from 0 to 15).

In order to ensure that the TBM settings chosen by the previous algorithms allow for a correct read back, a scan is performed over the TBM PLL phases and ROC delays, and for each value it is checked that the ROC address in the read back word is the expected one. This is indeed known from the mapping of FED channels and ROCs specified in the detector configuration database. At the end of the scan, it is verified that the current settings from previous calibrations give a correct read back of the ROC address for each ROC, otherwise new settings are produced. Examples of such scans are shown in Fig. 16.15. In order to acquire statistics the 16-bit word is read several times. The algorithm to chose the optimal phases or delays is the same as for the tests described in Section 16.6.1.

Table 16.1: Mechanism used by the ROC to send read back data. Sixteen triggers are needed to read out the full 16-bit word. One bit is used to indicate the start of the message. In this example, the ROC 2 is read out, and the value written in the read back register is 12, which allows for the readout of the analog current. The latter is equal to 88 ADC counts.

Trigger #	1	2	3	4	5	6	7	8	9	10	11	12	13	14	15	16
Message start	0	0	0	0	0	0	0	0	0	0	0	0	0	0	0	1
Message data	0	0	1	0	1	1	0	0	0	1	0	1	1	0	0	0
Comment	ROC I ² C address				last value written to the read back register											

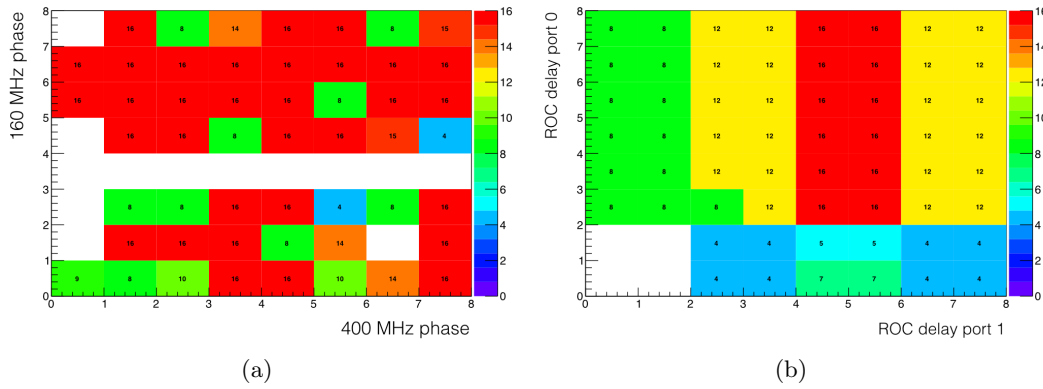


Figure 16.15: (a) Example of scan of the TBM PLL phases (a) and ROC delays (b) for one module. For each pair of values it is verified that the message data obtained with the read back mechanism contain the expected ROC I²C address. If the timing is correct, 16 ROCs per module have to be correctly identified.

16.6.4 ROC analog current and digital voltage

The read back mechanism described in the previous section allows to access the ROC analog current information (*Iana*). For the present detector it is possible to access only the total current of a large number of ROCs provided by a reading of the power supply, so that only an average value per ROC can be obtained. As discussed in Chapter 15, the analog current increases with irradiation and a re-calibration of the ROC analog voltage setting *Vana* is necessary to bring back the current in the safe range and recover the optimal ROC performance (Fig. 15.3(b)). The *Vana* calibration for each ROC is a time consuming procedure that converges after a large number of iterations of the S-curve test, which provides measurements of the threshold every time the settings are changed (Section 15.3.2). A much more simple procedure has been developed for the upgrade ROCs, since the measurement of the analog current is directly provided in the read back data. The value is returned in ADC units and a conversion curve measured for each ROC during module testing is applied to obtain the corresponding value in mA. The curve is of the form

$$Iana(\text{ADC}) = a + b \times Iana(\text{mA}) + c \times Iana^2(\text{mA}), \quad (16.1)$$

and its parameters are saved for each ROC in the detector configuration database. As shown in Fig. 16.16, for each value of the *Vana* setting the analog current is read out from the ROC read back bits, and the conversion curve above applied to the original value in ADC.

5604 At the end of the scan, a V_{ana} setting corresponding to the target I_{ana} value of 25 mA is
5605 chosen.

5606 The same calibration code can be also configured to perform a measurement of the digital
5607 voltage V_d for each ROC. This parameter is controlled by a corresponding DAC and it is
5608 useful to monitor it as well during operations. Its value can be returned by using the same
5609 read back mechanism but by changing the value written in the read back register. As for
5610 the analog current, a ADC/mV conversion curve has been measured for each ROC during
5611 module testing and it is applied in the final result of this measurement.

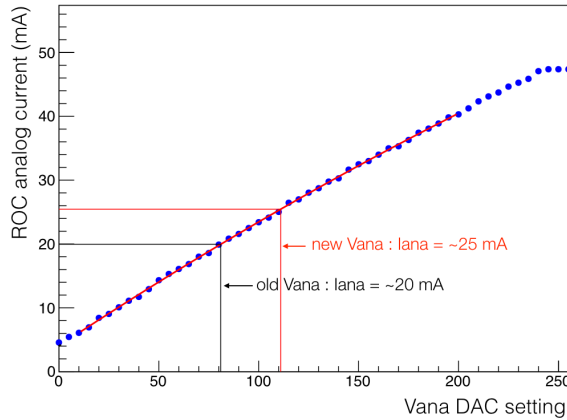


Figure 16.16: ROC analog current as readout with the ROC read back mechanism as a function of the analog voltage regulator setting.

Conclusions

5615 The contributions to the calibration and upgrade of the CMS pixel barrel detector have been
5616 presented in this part of thesis. First, a major effort was made during the first long shut-down
5617 to recover the full detector performance after the first LHC physics run. This effort included
5618 the replacement of broken components and the re-calibration of detector parameters at low
5619 temperature needed to compensate for the effects of radiation damage. The detector was
5620 re-installed into CMS in December 2014 and commissioned in January 2015 for the second
5621 LHC physics run at the highest center-of-mass energy of 13 TeV. The entire operation was
5622 completed in only a few days thanks to the expertise gained during the long shut-down. The
5623 first pp collision at 13 TeV occurred on March, 21st 2015 and since then the detector was
5624 running stable with a high data-taking efficiency.

5625 Furthermore, I contributed to the Phase 1 upgrade pixel project. The upgrade detector
5626 will allow to maintain the excellent tracking performance of CMS at the upcoming higher
5627 luminosity conditions at the LHC. A test stand at the University of Zurich has been set
5628 up and run with the aim of testing the performance of the complete upgrade pixel system
5629 and gain experience in its operations. The setup includes a slice of the full CMS pixel DAQ
5630 together with all the upgrade electronics for the power, readout and control systems as well
5631 as newly developed pixel modules. The test system has been employed to implement and test
5632 new developments in the pixel online software used to operate with the detector. Although
5633 the software architecture remains unchanged, several calibration procedures for the present
5634 detector become obsolete with the new digital readout of the upgrade system, whereas novel
5635 tests have been developed. Additional fundamental modifications had to be understood and
5636 implemented to be able to operate the software with the upgrade detector. The Phase 1 pixel
5637 upgrade project is now at its last stage of assembly and testing of the entire system. The
5638 novel calibration procedures are aimed at guaranteeing the success of these operations, as
5639 well as of the installation and commissioning of the new system planned for March 2017.

5640

Part III

5641

Summary

5642 This thesis presented the results of a search with the CMS detector for new heavy
 5643 resonances decaying into a pair of vector bosons (WW/WZ) or into a W and a Higgs boson
 5644 (WH). Such a search represents a key aspect of the research program of the ATLAS and
 5645 CMS experiments at the LHC aimed at finding confirmation of the existence of new physics
 5646 beyond the standard model. In fact, despite its predictions experimentally verified with
 5647 great precision, it is broadly believed that the standard model is an incomplete theory and
 5648 attempts have been made to propose theoretical solutions able to explain its deficiencies. New
 5649 theoretical extensions could for instance explain the “unnaturally” large difference between
 5650 the electroweak and the gravitational scales, commonly referred to as hierarchy problem. A
 5651 prominent feature of these new developments is the prediction of new resonances with masses
 5652 in the TeV range, which can be produced in pp collisions at the LHC thanks to the highest
 5653 energies of the proton beam. Moreover, these new particles can be directly measured by the
 5654 LHC experiments by reconstructing their highly preferred decay into a pair of well-known
 5655 SM particles, such as vector and Higgs bosons.

5656 The lepton+jet decay modes of the two SM bosons are exploited in this work, taking
 5657 advantage of the large rejection of the prominent multijet background achievable thanks to the
 5658 striking signature of the lepton, together with the high branching fractions provided by the
 5659 $W/Z \rightarrow q\bar{q}^{(\prime)}$ and $H \rightarrow b\bar{b}$ decays. In addition, these final states allow the invariant mass of
 5660 the diboson system to be fully reconstructed, such that the spectrum is measured to search for
 5661 the signal appearing as a local enhancement over a smoothly falling background distribution.
 5662 On the other hand, these final states are also notably challenging as for a resonance with
 5663 mass of order of a TeV the bosons have such large momenta that the particles emerging from
 5664 the boson decays are very collimated. In particular, the hadronization products from the
 5665 decay of the highly boosted bosons are contained within a single reconstructed jet such that
 5666 the bosons are identified by studying the substructure of this merged jet. Newly developed
 5667 and dedicated V-tagging and H-tagging techniques that exploit the substructure of such
 5668 objects are applied to resolve the decays of the bosons and suppress SM backgrounds, making
 5669 diboson signatures standard candles for the quest for new physics at the LHC.

5670 The data collected in pp collisions at $\sqrt{s} = 8$ TeV and corresponding to 19.7 fb^{-1} of
 5671 integrated luminosity are analyzed within this work to search for a WH resonance in the
 5672 $\ell\nu b\bar{b}$ decay channel. The analysis, published in Ref. [165], reported an interesting excess
 5673 of events corresponding to 2.2 standard deviations with respect to the SM expectations.
 5674 At about the same time the ATLAS collaboration reported an excess in the all-jets search,
 5675 corresponding to a local significance of 3.4 standard deviations for a resonance with a mass
 5676 of 2 TeV. These exciting results made the searches in diboson final states smoking guns of
 5677 the research programs of the two collaborations. In fact, because of the large interest in
 5678 the possibility of confirming the presence of a signal, these searches have been prioritized
 5679 immediately at the restart of pp collisions at $\sqrt{s} = 13$ TeV in 2015. The analysis of the first
 5680 13 TeV data, corresponding to 2.3 fb^{-1} of integrated luminosity, aimed at searching for a WZ
 5681 or WW resonance in the $\ell\nu q\bar{q}$ decay channel, has been presented in this thesis. In particular,
 5682 keeping in mind the interest in confirming a potential signal, the analysis has been optimized
 5683 to guarantee a significant discrimination between signals due to a spin-1 or a spin-2 resonance,
 5684 as well as a charged or neutral one. The results, published in Ref. [86], did not show evidence
 5685 for a signal and in particular, the excesses at a resonance mass of ≈ 2 TeV observed previously
 5686 are not confirmed. A statistical combination of all the 8 and 13 TeV CMS searches for heavy
 5687 resonances decaying to a pair of SM bosons has afterwards been performed as presented in
 5688 this thesis. For the first time, the overall experimental status of the searches with boosted W,
 5689 Z, and Higgs bosons is provided in such extent, showing that a large gain in sensitivity can
 5690 be achieved by combining the results, compared to the similar sensitivities of the individual

5691 analysis.

5692 As no evidence for a signal is found in any of these searches, upper limits are set on
 5693 the production cross section of the resonance under the assumption of a natural width
 5694 negligible compared to the experimental resolution. The limits are interpreted in the context
 5695 of theoretical extensions of the standard model that attempt to solve the aforementioned
 5696 hierarchy problem. It has been shown in this thesis that narrow-width, spin-1 resonances
 5697 with masses up to 2.4 TeV, as predicted by a simplified theoretical approach representing
 5698 scenarios such as composite Higgs models, have been excluded by these searches. For a
 5699 narrow-width graviton as predicted by warped extra dimension models, the analyses have
 5700 not reached yet enough sensitivity to exclude such signal because of the small values of the
 5701 predicted production cross sections.

5702 Despite the absence of a signal so far, it is possible that a new resonance will emerge with
 5703 the large amount of data that will be collected by the experiments in the upcoming two years
 5704 of LHC collisions. In fact, about 40 fb^{-1} of integrated luminosity have been delivered in 2016,
 5705 and additional data equivalent of approximately 100 fb^{-1} are expected to be collected by the
 5706 end of 2018. The large amount of data will allow a more precise measurement of the mass
 5707 spectrum, especially in the high-mass tail where a possible signal is expected, hence improving
 5708 the sensitivity of this type of searches. In addition to this, it is of utmost importance in the
 5709 search for new and rare physical phenomena, that the CMS detector maintains its excellent
 5710 performance. This is achieved by constantly monitoring and optimizing its subdetectors. In
 5711 particular, important contributions to the pixel barrel subdetector have been made in the
 5712 context of this thesis. The extensive work carried out to install into CMS, commission and
 5713 calibrate the detector before the beginning of 13 TeV collisions, guaranteed its successful
 5714 and stable operation during data-taking in 2015 and 2016. The original pixel detector that
 5715 took the data analyzed in this thesis has been recently replaced by a new, upgraded system
 5716 designed to maintain and improve the performance with the upcoming high luminosities of
 5717 the LHC in the next years.

5718 The installation of the new detector into CMS and its commissioning are the last steps
 5719 of several years of work carried out by many institutes around the world. In particular, the
 5720 University of Zurich has been responsible for the design, construction, integration and testing
 5721 of the service cylinders, a complex system that carries the services along the beam pipe,
 5722 accommodate the cooling lines and house the electronics for detector readout and control.
 5723 Prior to the assembly of the service cylinders a major effort was put forth setup a test stand
 5724 at the University of Zurich with multiple goals. The first goal was to test the prototypes
 5725 of the detector components prior to full production. Secondly, it has been fundamental to
 5726 establish test and calibration procedures that had been used to verify the functionality of
 5727 millions of pixel channels during the operations of integration, installation and commissioning
 5728 of the full system.

5729 The LHC collisions will restart in summer 2017 and the new pixel detector will start
 5730 its operation guaranteeing the success of data-taking with the CMS experiment up to 2023,
 5731 when an upgrade of the collider will further increase the instantaneous luminosity extending
 5732 so its discovery potential.

Studies on track reconstruction problems

5733

5734

5735

5736

5737 A scan of the displays of all the events in 8 TeV data with $m_{\text{WH}} > 1.6 \text{ TeV}$ passing all the
 5738 selection criteria for the $\ell\nu b\bar{b}$ final state (Table 8.1), reported that presence of two events
 5739 characterized by a rare specific kind of noise. This noise arises from an anomalous behaviour
 5740 of the tracking algorithm in the transition region between the barrel (TOB) and endcap (TEC)
 5741 regions of the silicon tracker, namely, in the pseudorapidity range $1 < |\eta| < 1.5$ (Fig. 3.5).
 5742 As a consequence, many fake (displaced) tracks are associated to the selected H jet candidate.
 5743 Figure A.1 shows the event display of one of the two events affected by this problem, while
 5744 Figure A.2 shows the same feature in simulation.

5745 In order to reject this type of noise, it is common in CMS analyses to apply a standard
 5746 filtering algorithm that discards the event if there is an anomalous amount of tracks that
 5747 have been seeded in the TOB-TEC transition region. The efficiency of this filter on signal
 5748 events is about 97% independently on the H jet p_T .

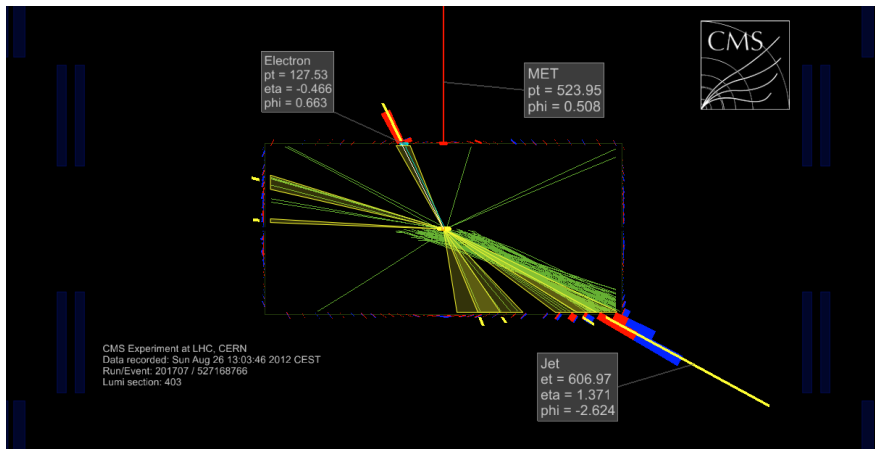


Figure A.1: Display of one typical anomalous event found in data recorded by the CMS experiment. Many fake and displaced tracks are reconstructed creating a bias in the jet reconstruction. Only tracks with p_T larger than 2 GeV are shown.

5749 However, further checks performed on the anomalous events showed that after applying
 5750 the standard filter residual noise can still be identified in the problematic η region. Therefore,
 5751 it has been decided for the analysis described in this work to apply an additional requirement
 5752 on the η of the selected H jet candidate (Section 6.4.2). In particular, CA8 jets are rejected
 5753 if their pseudorapidity falls in the problematic region $1 < |\eta| < 1.8$. As described in the
 5754 following, the choice for this fiducial cut is motivated by the disagreement between data and
 5755 simulation in the rate at which the noise occur.

5756 The efficiency of the standard filter is studied as a function of the H jet p_T and η in a dijet
 5757 sample with high statistics in both data and simulation. The sample is selected requiring at
 5758 least two jets, with $p_T > 400 \text{ GeV}$ for the leading jet and $p_T > 80 \text{ GeV}$ for the sub-leading

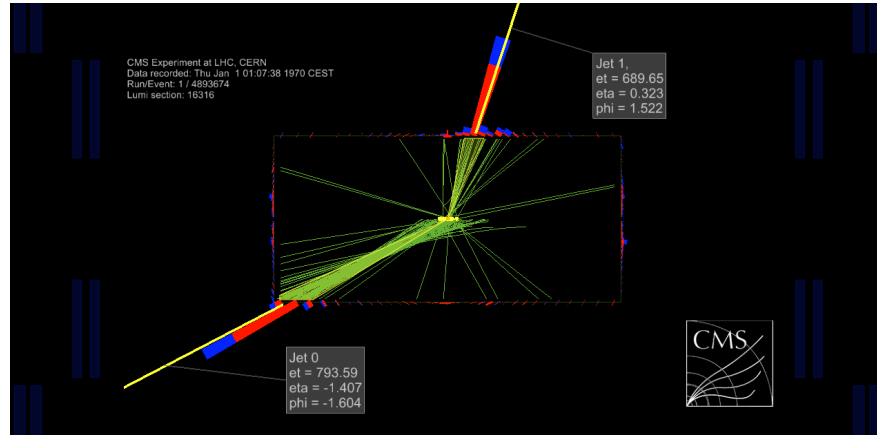


Figure A.2: Display of one typical anomalous event in simulation. Only tracks with p_T larger than 2 GeV are shown.

one. At least one of the jet has to be b-tagged using the same combined b tagging algorithm as for the main analysis selection, representing thus the H jet candidate. The jet that fails the b tagging is required to have low pruned mass ($m_{jet} < 40$ GeV).

Figure A.3 shows the effect of the filter on the jet η distribution comparing data, simulated signal and QCD background: the signal distribution is rather unaffected while data and QCD background distributions show a reduction of events in the problematic η region after applying the filter, as expected.

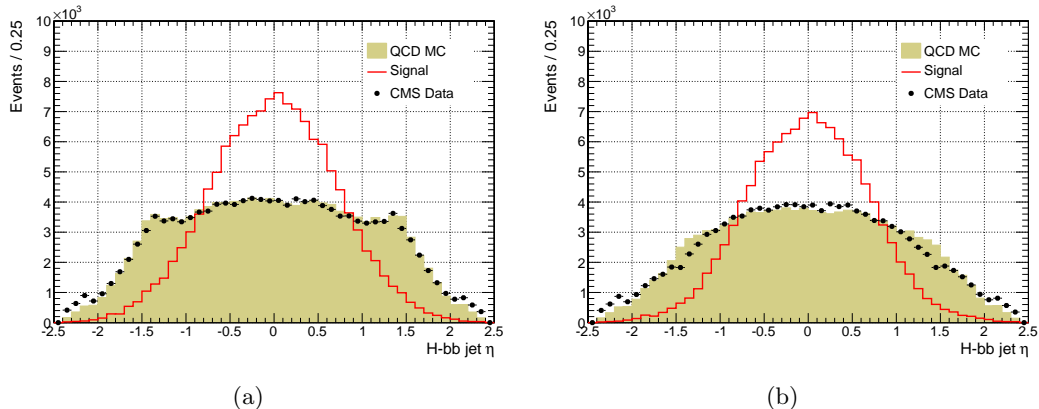


Figure A.3: Comparison of the H jet η distributions for data, and simulated signal and QCD background before (a) and after (b) applying the tracking noise filter. Signal jets are mostly central in the detector.

Figure A.4 shows the filter efficiency on data and simulated signal and QCD background as a function of the H jet candidate p_T for different jet η regions. A little dependence of the filter efficiency with the jet p_T is observed in the regions $0 < |\eta| < 1$ and $1.0 < |\eta| < 1.5$, while in the forward region $1.5 < |\eta| < 2.4$ the efficiency decreases with the jet p_T . The performance of the filter in the different η regions is summarized in Figure A.5(a). A large discrepancy between data and simulation is found in the pseudorapidity region $1.0 < |\eta| < 1.8$, where the simulation does not sufficiently well describe the full material budget of the tracking detector. The same studies are also performed removing the b-tagging requirement. The filter efficiency as a function of the leading jet η for this case is shown in Fig. A.5(b), for both data and

simulation. The increase in efficiency compared to what obtained in b-tagging shows that the b-tagging requirement enriches the samples with events characterized by this noise up to 30%, making this analysis systematically prone to it.

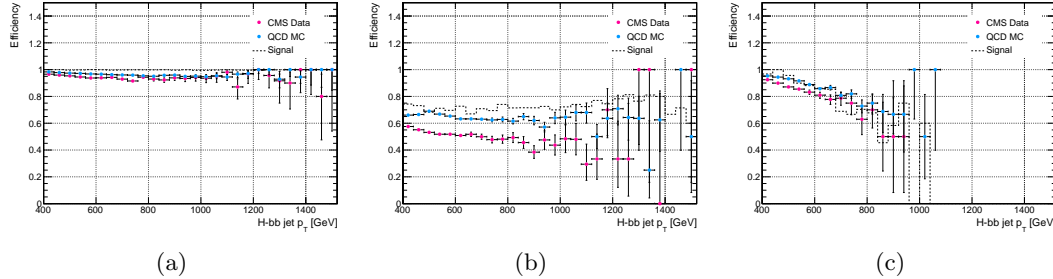


Figure A.4: Efficiency of the tracking noise filter as a function of the H jet p_T for data, and simulated signal and QCD background for jets reconstructed in the pseudorapidity regions $0 < |\eta| < 1$ (a), $1.0 < |\eta| < 1.5$ (b), and $1.5 < |\eta| < 2.4$ (c).

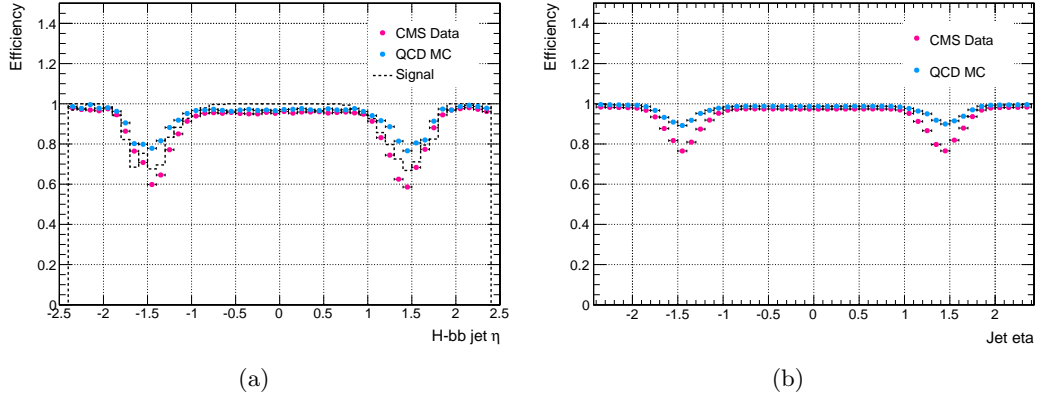


Figure A.5: Efficiency of the tracking noise filter as a function of the leading jet p_T for data, and simulated signal and QCD background. (a) The leading jet is required to be b-tagged with the combined b tagging algorithm used in the main analysis. (b) The b tagging requirements for the leading jet are removed.

Bibliography

- [1] F. Mandl and G. Shaw, “Quantum Field Theory”. Wiley, 1984.
- [2] ATLAS Collaboration, “Observation of a new particle in the search for the Standard Model Higgs boson with the ATLAS detector at the LHC”, *Phys. Lett. B* **716** (2012) 1, doi:10.1016/j.physletb.2012.08.020, arXiv:1207.7214.
- [3] CMS Collaboration, “Observation of a new boson with mass near 125 GeV in pp collisions at $\sqrt{s} = 7$ and 8 TeV”, *JHEP* **06** (2013) 081, doi:10.1007/JHEP06(2013)081, arXiv:1303.4571.
- [4] L. Randall and R. Sundrum, “A Large mass hierarchy from a small extra dimension”, *Phys. Rev. Lett.* **83** (1999) 3370, doi:10.1103/PhysRevLett.83.3370, arXiv:hep-ph/9905221.
- [5] K. Agashe, H. Davoudiasl, G. Perez, and A. Soni, “Warped gravitons at the LHC and beyond”, *Phys. Rev. D* **76** (2007) 036006, doi:10.1103/PhysRevD.76.036006, arXiv:hep-ph/0701186.
- [6] B. Bellazzini, C. Csaki, and J. Serra, “Composite Higgses”, *Eur. Phys. J. C* **74** (2014) 2766, doi:10.1140/epjc/s10052-014-2766-x, arXiv:1401.2457.
- [7] R. Contino, D. Marzocca, D. Pappadopulo, and R. Rattazzi, “On the effect of resonances in composite Higgs phenomenology”, *JHEP* **10** (2011) 081, doi:10.1007/JHEP10(2011)081, arXiv:1109.1570.
- [8] Tevatron Electroweak Working Group, CDF, DELPHI, SLD Electroweak and Heavy Flavour Groups, ALEPH, LEP Electroweak Working Group, SLD, OPAL, D0, L3 Collaboration, “Precision Electroweak Measurements and Constraints on the Standard Model”, arXiv:1012.2367.
- [9] ZEUS, H1 Collaboration, “Combination of measurements of inclusive deep inelastic $e^\pm p$ scattering cross sections and QCD analysis of HERA data”, *Eur. Phys. J. C* **75** (2015) 580, doi:10.1140/epjc/s10052-015-3710-4, arXiv:1506.06042.
- [10] Particle Data Group Collaboration, “Review of Particle Physics”, *Chin. Phys. C* **40** (2016) 100001, doi:10.1088/1674-1137/40/10/100001.
- [11] S. L. Glashow, “Partial-symmetries of weak interactions”, *Nucl. Phys.* **22** (1961) 579, doi:10.1016/0029-5582(61)90469-2.
- [12] S. Weinberg, “A Model of Leptons”, *Phys. Rev. Lett.* **19** (1967) 1264, doi:10.1103/PhysRevLett.19.1264.
- [13] A. Salam, “Gauge unification of fundamental forces”, *Rev. Mod. Phys.* **52** (1980) 525, doi:10.1103/RevModPhys.52.525.
- [14] F. Englert and R. Brout, “Broken Symmetry and the Mass of Gauge Vector Mesons”, *Phys. Rev. Lett.* **13** (1964) 321, doi:10.1103/PhysRevLett.13.321.
- [15] P. Higgs, “Broken symmetries, massless particles and gauge fields”, *Physics Letters* **12** (1964) 132, doi:10.1016/0031-9163(64)91136-9.

- 5817 [16] P. W. Higgs, “Broken Symmetries and the Masses of Gauge Bosons”, *Phys. Rev. Lett.*
5818 **13** (1964) 508, doi:10.1103/PhysRevLett.13.508.
- 5819 [17] P. W. Higgs, “Spontaneous Symmetry Breakdown without Massless Bosons”, *Phys.*
5820 *Rev.* **145** (1966) 1156, doi:10.1103/PhysRev.145.1156.
- 5821 [18] G. S. Guralnik, C. R. Hagen, and T. W. B. Kibble, “Global Conservation Laws and
5822 Massless Particles”, *Phys. Rev. Lett.* **13** (1964) 585,
5823 doi:10.1103/PhysRevLett.13.585.
- 5824 [19] UA1 Collaboration, “Recent Results on Intermediate Vector Boson Properties at the
5825 CERN Super Proton Synchrotron Collider”, *Phys. Lett. B* **166** (1986) 484,
5826 doi:10.1016/0370-2693(86)91603-5.
- 5827 [20] UA2 Collaboration, “Measurement of the Standard Model Parameters from a Study of
5828 W and Z Bosons”, *Phys. Lett. B* **186** (1987) 440,
5829 doi:10.1016/0370-2693(87)90324-8.
- 5830 [21] DELPHI, OPAL, LEP Electroweak, ALEPH, L3 Collaboration, “Electroweak
5831 Measurements in Electron-Positron Collisions at W-Boson-Pair Energies at LEP”,
5832 *Phys. Rept.* **532** (2013) 119, doi:10.1016/j.physrep.2013.07.004,
5833 arXiv:1302.3415.
- 5834 [22] CDF, D0 Collaboration, “Combination of CDF and D0 W-Boson Mass Measurements”,
5835 *Phys. Rev. D* **88** (2013) 052018, doi:10.1103/PhysRevD.88.052018,
5836 arXiv:1307.7627.
- 5837 [23] LHC Higgs Cross Section Working Group Collaboration, “Handbook of LHC Higgs
5838 Cross Sections: 1. Inclusive Observables”, doi:10.5170/CERN-2011-002,
5839 arXiv:1101.0593.
- 5840 [24] ATLAS, CMS Collaboration, “Combined Measurement of the Higgs Boson Mass in pp
5841 Collisions at $\sqrt{s} = 7$ and 8 TeV with the ATLAS and CMS Experiments”, *Phys. Rev.*
5842 *Lett.* **114** (2015) 191803, doi:10.1103/PhysRevLett.114.191803,
5843 arXiv:1503.07589.
- 5844 [25] ATLAS, CMS Collaboration, “Measurements of the Higgs boson production and decay
5845 rates and constraints on its couplings from a combined ATLAS and CMS analysis of
5846 the LHC pp collision data at $\sqrt{s} = 7$ and 8 TeV”, *JHEP* **08** (2016) 045,
5847 doi:10.1007/JHEP08(2016)045, arXiv:1606.02266.
- 5848 [26] ATLAS Collaboration, “Study of the spin and parity of the Higgs boson in diboson
5849 decays with the ATLAS detector”, *Eur. Phys. J.* **C75** (2015), no. 10, 476,
5850 doi:10.1140/epjc/s10052-015-3685-1, 10.1140/epjc/s10052-016-3934-y,
5851 arXiv:1506.05669. [Erratum: Eur. Phys. J.C76,no.3,152(2016)].
- 5852 [27] CMS Collaboration, “Study of the Mass and Spin-Parity of the Higgs Boson Candidate
5853 Via Its Decays to Z Boson Pairs”, *Phys. Rev. Lett.* **110** (2013), no. 8, 081803,
5854 doi:10.1103/PhysRevLett.110.081803, arXiv:1212.6639.
- 5855 [28] CMS Collaboration, “Constraints on the spin-parity and anomalous HVV couplings of
5856 the Higgs boson in proton collisions at 7 and 8 TeV”, *Phys. Rev. D* **92** (2015) 012004,
5857 doi:10.1103/PhysRevD.92.012004, arXiv:1411.3441.

- [29] S. Dimopoulos, S. Raby, and F. Wilczek, “Supersymmetry and the scale of unification”, *Phys. Rev. D* **24** (1981) 1681, doi:10.1103/PhysRevD.24.1681.
- [30] J. A. Casas, J. R. Espinosa, and M. Quiros, “Improved Higgs mass stability bound in the standard model and implications for supersymmetry”, *Phys. Lett. B* **342** (1995) 171, doi:10.1016/0370-2693(94)01404-Z, arXiv:hep-ph/9409458.
- [31] V. C. Rubin, N. Thonnard, and J. Ford, W. K., “Extended rotation curves of high-luminosity spiral galaxies”, *Astrophys. J. L.* **225** (1978) 107, doi:10.1086/182804.
- [32] F. Iocco, M. Pato, and G. Bertone, “Evidence for dark matter in the inner Milky Way”, *Nature Phys.* **11** (2015) 245, doi:10.1038/nphys3237, arXiv:1502.03821.
- [33] Planck Collaboration, “Planck 2015 results. XIII. Cosmological parameters”, *Astron. Astrophys.* **594** (2016) A13, doi:10.1051/0004-6361/201525830, arXiv:1502.01589.
- [34] K. Becker, M. Becker, and J. H. Schwarz, “String Theory and M-Theory: A Modern Introduction”. Wiley, 2006.
- [35] N. Arkani-Hamed, S. Dimopoulos, and G. R. Dvali, “The Hierarchy problem and new dimensions at a millimeter”, *Phys. Lett. B* **429** (1998) 263, doi:10.1016/S0370-2693(98)00466-3, arXiv:hep-ph/9803315.
- [36] C. D. Hoyle et al., “Sub-millimeter tests of the gravitational inverse-square law”, *Phys. Rev. D* **70** (2004) 042004, doi:10.1103/PhysRevD.70.042004, arXiv:hep-ph/0405262.
- [37] A. L. Fitzpatrick, J. Kaplan, L. Randall, and L.-T. Wang, “Searching for the Kaluza-Klein graviton in bulk RS models”, *JHEP* **09** (2007) 013, doi:10.1088/1126-6708/2007/09/013, arXiv:hep-ph/0701150.
- [38] D. Marzocca, M. Serone, and J. Shu, “General composite Higgs models”, *JHEP* **08** (2012) 013, doi:10.1007/JHEP08(2012)013, arXiv:1205.0770.
- [39] T. Han, H. E. Logan, B. McElrath, and L.-T. Wang, “Phenomenology of the little Higgs model”, *Phys. Rev. D* **67** (2003) 095004, doi:10.1103/PhysRevD.67.095004, arXiv:hep-ph/0301040.
- [40] M. Perelstein, “Little Higgs models and their phenomenology”, *Prog. Part. Nucl. Phys.* **58** (2005) 247, doi:10.1016/j.ppnp.2006.04.001, arXiv:hep-ph/0512128.
- [41] M. Schmaltz and D. Tucker-Smith, “Little Higgs review”, *Ann. Rev. Nucl. Part. Sci.* **55** (2005) 229, doi:10.1146/annurev.nucl.55.090704.151502, arXiv:hep-ph/0502182.
- [42] N. Arkani-Hamed, A. G. Cohen, E. Katz, and A. E. Nelson, “The Littlest Higgs”, *JHEP* **07** (2002) 034, doi:10.1088/1126-6708/2002/07/034, arXiv:hep-ph/0206021.
- [43] G. Burdman, M. Perelstein, and A. Pierce, “Large Hadron Collider tests of a little Higgs model”, *Phys. Rev. Lett.* **90** (2003) 241802, doi:10.1103/PhysRevLett.90.241802, arXiv:hep-ph/0212228. [Erratum: *Phys. Rev. Lett.* 92, 049903(2004)].

- 5899 [44] D. Pappadopulo, A. Thamm, R. Torre, and A. Wulzer, “Heavy Vector Triplets:
5900 Bridging Theory and Data”, *JHEP* **09** (2014) 060, doi:10.1007/JHEP09(2014)060,
5901 arXiv:1402.4431.
- 5902 [45] V. Barger, W. Y. Keung, and E. Ma, “Gauge model with light W and Z bosons”,
5903 *Phys. Rev. D* **22** (1980) 727, doi:10.1103/PhysRevD.22.727.
- 5904 [46] G. Altarelli, B. Mele, and M. Ruiz-Altaba, “Searching for new heavy vector bosons in
5905 $p\bar{p}$ colliders”, *Z. Phys. C* **45** (1989) 109, doi:10.1007/BF01556677.
- 5906 [47] L. Evans and P. Bryant, “LHC Machine”, *JINST* **3** (2008) S08001.
- 5907 [48] W.J. Stirling, “Parton luminosity and cross section plots”.
5908 <http://www.hep.ph.ic.ac.uk/~wstirlin/plots/plots.html>. *Private*
5909 *communication*.
- 5910 [49] ATLAS Collaboration, “The ATLAS Experiment at the CERN Large Hadron
5911 Collider”, *JINST* **3** (2008) S08003, doi:10.1088/1748-0221/3/08/S08003.
- 5912 [50] CMS Collaboration, “The CMS experiment at the CERN LHC”, *JINST* **3** (2008)
5913 S08004, doi:10.1088/1748-0221/3/08/S08004.
- 5914 [51] LHCb Collaboration, “The LHCb Detector at the LHC”, *JINST* **3** (2008) S08005,
5915 doi:10.1088/1748-0221/3/08/S08005.
- 5916 [52] ALICE Collaboration, “The ALICE experiment at the CERN LHC”, *JINST* **3** (2008)
5917 S08002, doi:10.1088/1748-0221/3/08/S08002.
- 5918 [53] F. Marcastel, “CERN’s Accelerator Complex”.
5919 <https://cds.cern.ch/record/1621583>. General Photo, 2013.
- 5920 [54] CMS Collaboration, “CMS Public Luminosity Results”.
5921 <https://twiki.cern.ch/twiki/bin/view/CMSPublic/LumiPublicResults>.
- 5922 [55] N. Cartiglia, “Measurement of the proton-proton total, elastic, inelastic and diffractive
5923 cross sections at 2, 7, 8 and 57 TeV”, arXiv:1305.6131.
- 5924 [56] CMS Collaboration, “The CMS tracker system project”, CMS Technical Design Report
5925 CERN-LHCC-98-006, CERN, 1997.
- 5926 [57] CMS Collaboration, “Pixel Performance Results”.
5927 <https://twiki.cern.ch/twiki/bin/view/CMS/PixelOfflinePlots>.
- 5928 [58] CMS Collaboration, “The CMS electromagnetic calorimeter project”, CMS Technical
5929 Design Report CERN-LHCC-97-033, CERN, 1997.
- 5930 [59] CMS Collaboration, “The CMS hadron calorimeter project”, CMS Technical Design
5931 Report CERN-LHCC-97-031, CERN, 1997.
- 5932 [60] P. Adzic et al., “Energy resolution of the barrel of the CMS electromagnetic
5933 calorimeter”, *JINST* **2** (2007) P04004, doi:10.1088/1748-0221/2/04/P04004.
- 5934 [61] M. A. Dobbs et al., “Les Houches guidebook to Monte Carlo generators for hadron
5935 collider physics”, in *Proceedings of the Workshop on Physics at TeV Colliders, Les
5936 Houches, France, May 26-June 3, 2003*, p. 411. 2004. arXiv:hep-ph/0403045.

- 5937 [62] J. C. Collins and D. E. Soper, “The Theorems of Perturbative QCD”, *Ann. Rev. Nucl.
5938 Part. Sci.* **37** (1987) 383, doi:10.1146/annurev.ns.37.120187.002123.
- 5939 [63] ZEUS Collaboration, “The ZEUS detector: Status report 1993”, .
- 5940 [64] H1 Collaboration, “The H1 detector at HERA”, *Nucl. Instrum. Meth. A* **386** (1997),
5941 no. 2, 310, doi:10.1016/S0168-9002(96)00893-5.
- 5942 [65] G. Altarelli and G. Parisi, “Asymptotic freedom in parton language”, *Nucl. Phys. B*
5943 **126** (1977), no. 2, 298, doi:10.1016/0550-3213(77)90384-4.
- 5944 [66] J. Pumplin et al., “New generation of parton distributions with uncertainties from
5945 global QCD analysis”, *JHEP* **07** (2002) 012,
5946 doi:10.1088/1126-6708/2002/07/012, arXiv:hep-ph/0201195.
- 5947 [67] H.-L. Lai et al., “New parton distributions for collider physics”, *Phys. Rev. D* **82**
5948 (2010) 074024, doi:10.1103/PhysRevD.82.074024, arXiv:1007.2241.
- 5949 [68] R. D. Ball et al., “Impact of Heavy Quark Masses on Parton Distributions and LHC
5950 Phenomenology”, *Nucl. Phys. B* **849** (2011) 296,
5951 doi:10.1016/j.nuclphysb.2011.03.021, arXiv:1101.1300.
- 5952 [69] T. Sjöstrand, S. Mrenna, and P. Z. Skands, “A Brief Introduction to PYTHIA 8.1”,
5953 *Comput. Phys. Commun.* **178** (2008) 852, doi:10.1016/j.cpc.2008.01.036,
5954 arXiv:0710.3820.
- 5955 [70] T. Sjöstrand, S. Mrenna, and P. Z. Skands, “PYTHIA 6.4 Physics and Manual”, *JHEP*
5956 **05** (2006) 026, doi:10.1088/1126-6708/2006/05/026, arXiv:hep-ph/0603175.
- 5957 [71] J. Alwall et al., “MadGraph 5 : Going Beyond”, *JHEP* **06** (2011) 128,
5958 doi:10.1007/JHEP06(2011)128, arXiv:1106.0522.
- 5959 [72] S. Hoeche et al., “Matching parton showers and matrix elements”, in *Proceedings of
5960 the Workshop on the implications of HERA for LHC physics: Proceedings Part A*,
5961 pp. 288–289. 2005. arXiv:hep-ph/0602031. doi:10.5170/CERN-2005-014.288.
- 5962 [73] S. Frixione, P. Nason, and C. Oleari, “Matching NLO QCD computations with Parton
5963 Shower simulations: the POWHEG method”, *JHEP* **11** (2007) 070,
5964 doi:10.1088/1126-6708/2007/11/070, arXiv:0709.2092.
- 5965 [74] S. Frixione, P. Nason, and B. R. Webber, “Matching NLO QCD and parton showers in
5966 heavy flavor production”, *JHEP* **08** (2003) 007,
5967 doi:10.1088/1126-6708/2003/08/007, arXiv:hep-ph/0305252.
- 5968 [75] GEANT4 Collaboration, “GEANT4 — a simulation toolkit”, *Nucl. Instrum. Meth. A*
5969 **506** (2003) 250, doi:10.1016/S0168-9002(03)01368-8.
- 5970 [76] CMS Collaboration, “Measurement of the Underlying Event Activity at the LHC with
5971 $\sqrt{s} = 7$ TeV and Comparison with $\sqrt{s} = 0.9$ TeV”, *JHEP* **09** (2011) 109,
5972 doi:10.1007/JHEP09(2011)109, arXiv:1107.0330.
- 5973 [77] CMS Collaboration, “Study of the underlying event at forward rapidity in pp collisions
5974 at $\sqrt{s} = 0.9, 2.76$, and 7 TeV”, *JHEP* **04** (2013) 072,
5975 doi:10.1007/JHEP04(2013)072, arXiv:1302.2394.

- 5976 [78] J. M. Campbell, R. K. Ellis, and D. L. Rainwater, “Next-to-leading order QCD
5977 predictions for $W + 2$ jet and $Z + 2$ jet production at the CERN LHC”, *Phys. Rev. D*
5978 **68** (2003) 094021, doi:10.1103/PhysRevD.68.094021, arXiv:hep-ph/0308195.
- 5979 [79] J. M. Campbell, R. K. Ellis, and C. Williams, “Vector boson pair production at the
5980 LHC”, *JHEP* **07** (2011) 018, doi:10.1007/JHEP07(2011)018, arXiv:1105.0020.
- 5981 [80] J. M. Campbell and R. K. Ellis, “Top-quark processes at NLO in production and
5982 decay”, *J. Phys. G* **42** (2015) 015005, doi:10.1088/0954-3899/42/1/015005,
5983 arXiv:1204.1513.
- 5984 [81] J. M. Campbell, R. K. Ellis, and F. Tramontano, “Single top production and decay at
5985 next-to-leading order”, *Phys. Rev. D* **70** (2004) 094012,
5986 doi:10.1103/PhysRevD.70.094012, arXiv:hep-ph/0408158.
- 5987 [82] Y. Li and F. Petriello, “Combining QCD and electroweak corrections to dilepton
5988 production in FEWZ”, *Phys. Rev. D* **86** (2012) 094034,
5989 doi:10.1103/PhysRevD.86.094034, arXiv:1208.5967.
- 5990 [83] M. Czakon and A. Mitov, “Top++: A Program for the Calculation of the Top-Pair
5991 Cross-Section at Hadron Colliders”, *Comput. Phys. Commun.* **185** (2014) 2930,
5992 doi:10.1016/j.cpc.2014.06.021, arXiv:1112.5675.
- 5993 [84] P. Skands, S. Carrazza, and J. Rojo, “Tuning PYTHIA 8.1: the Monash 2013 Tune”,
5994 *Eur. Phys. J. C* **74** (2014) 3024, doi:10.1140/epjc/s10052-014-3024-y,
5995 arXiv:1404.5630.
- 5996 [85] CMS Collaboration, “Event generator tunes obtained from underlying event and
5997 multiparton scattering measurements”, *Eur. Phys. J. C* **76** (2016) 155,
5998 doi:10.1140/epjc/s10052-016-3988-x, arXiv:1512.00815.
- 5999 [86] CMS Collaboration, “Search for massive resonances decaying into WW, WZ or ZZ
6000 bosons in proton-proton collisions at $\sqrt{s} = 13$ TeV”, arXiv:1612.09159. Submitted to
6001 *JHEP*.
- 6002 [87] CMS Collaboration, “Description and performance of track and primary-vertex
6003 reconstruction with the CMS tracker”, *JINST* **9** (2014) P10009,
6004 doi:10.1088/1748-0221/9/10/P10009, arXiv:1405.6569.
- 6005 [88] W. Adam, B. Mangano, T. Speer, and T. Todorov, “Track Reconstruction in the CMS
6006 tracker”, Technical Report CMS-NOTE-2006-041, CERN, 2006.
- 6007 [89] P. Billoir, “Progressive track recognition with a Kalman like fitting procedure”,
6008 *Comput. Phys. Commun.* **57** (1989) 390, doi:10.1016/0010-4655(89)90249-X.
- 6009 [90] R. Fruhwirth, “Application of Kalman filtering to track and vertex fitting”, *Nucl.*
6010 *Instrum. Meth. A* **262** (1987) 444, doi:10.1016/0168-9002(87)90887-4.
- 6011 [91] T. Speer et al., “Vertex Fitting in the CMS Tracker”, Technical Report
6012 CMS-NOTE-2006-032, CERN, 2006.
- 6013 [92] K. Rose, “Deterministic annealing for clustering, compression, classification, regression,
6014 and related optimization problems”, *Proceedings of the IEEE* **86** (Nov, 1998) 2210,
6015 doi:10.1109/5.726788.

- 6016 [93] W. Waltenberger, R. Frhwirth, and P. Vanlaer, “Adaptive vertex fitting”, *J. Phys. G*
 6017 **34** (2007), no. 12, N343.
- 6018 [94] CMS Collaboration, “Tracking Performance Results”.
 6019 <https://twiki.cern.ch/twiki/bin/view/CMSPublic/PhysicsResultsTRK>.
- 6020 [95] S. Baffioni et al., “Electron reconstruction in CMS”, *Eur. Phys. J. C* **49** (2007) 1099,
 6021 [doi:10.1140/epjc/s10052-006-0175-5](https://doi.org/10.1140/epjc/s10052-006-0175-5).
- 6022 [96] CMS Collaboration, “Commissioning of the Particle-flow Event Reconstruction with
 6023 the first LHC collisions recorded in the CMS detector”, CMS Physics Analysis
 6024 Summary CMS-PAS-PFT-10-001, CERN, 2010.
- 6025 [97] CMS Collaboration, “Particle-Flow Event Reconstruction in CMS and Performance for
 6026 Jets, Taus, and MET”, CMS Physics Analysis Summary CMS-PAS-PFT-09-001,
 6027 CERN, 2009.
- 6028 [98] W. Adam, R. Fröhwirth, A. Strandlie, and T. Todorov, “Reconstruction of electrons
 6029 with the Gaussian-sum filter in the CMS tracker at the LHC”, *J. Phys. G* **31** (2005)
 6030 N9.
- 6031 [99] CMS Collaboration, “Measurements of Inclusive W and Z Cross Sections in pp
 6032 Collisions at $\sqrt{s} = 7$ TeV”, *JHEP* **01** (2011) 080, [doi:10.1007/JHEP01\(2011\)080](https://doi.org/10.1007/JHEP01(2011)080),
 6033 [arXiv:1012.2466](https://arxiv.org/abs/1012.2466).
- 6034 [100] CMS Collaboration, “Performance of Electron Reconstruction and Selection with the
 6035 CMS Detector in Proton-Proton Collisions at $\sqrt{s} = 8$ TeV”, *JINST* **10** (2015)
 6036 P06005, [doi:10.1088/1748-0221/10/06/P06005](https://doi.org/10.1088/1748-0221/10/06/P06005), [arXiv:1502.02701](https://arxiv.org/abs/1502.02701).
- 6037 [101] CMS Collaboration, “ECAL Performance Results”.
 6038 <https://twiki.cern.ch/twiki/bin/view/CMSPublic/EcalDPGResults>.
- 6039 [102] CMS Collaboration, “Search for physics beyond the standard model in dilepton mass
 6040 spectra in proton-proton collisions at $\sqrt{s} = 8$ TeV”, *JHEP* **04** (2015) 025,
 6041 [doi:10.1007/JHEP04\(2015\)025](https://doi.org/10.1007/JHEP04(2015)025), [arXiv:1412.6302](https://arxiv.org/abs/1412.6302).
- 6042 [103] CMS Collaboration, “Performance of CMS muon reconstruction in pp collision events
 6043 at $\sqrt{s} = 7$ TeV”, *JINST* **7** (2012) P10002, [doi:10.1088/1748-0221/7/10/P10002](https://doi.org/10.1088/1748-0221/7/10/P10002),
 6044 [arXiv:1206.4071](https://arxiv.org/abs/1206.4071).
- 6045 [104] CMS Collaboration, “CMS Physics: Technical Design Report Volume 1: Detector
 6046 Performance and Software”, CMS Technical Design Report CERN-LHCC-2006-001,
 6047 CERN, 2006.
- 6048 [105] CMS Collaboration, “CMS Performance Results for EPS 2015”, CMS Detector
 6049 Performance Note CMS-DP-2015-016, CERN, 2015.
- 6050 [106] R. Radogna, “Search for high-mass resonances decaying into muon pairs with the CMS
 6051 experiment at LHC”. PhD thesis, Università degli Studi di Bari Aldo Moro, 2016.
- 6052 [107] CMS Collaboration, J. Brooke, “Performance of the CMS Level-1 Trigger”, in
 6053 *Proceedings of the 36th International Conference on High Energy Physics, Melbourne,*
 6054 *Australia, July 4-11, 2012*, p. 508. 2013. [arXiv:1302.2469](https://arxiv.org/abs/1302.2469).

- 6055 [108] G. P. Salam and G. Soyez, “A Practical Seedless Infrared-Safe Cone jet algorithm”,
 6056 *JHEP* **05** (2007) 086, doi:10.1088/1126-6708/2007/05/086, arXiv:0704.0292.
- 6057 [109] S. Catani, Y. L. Dokshitzer, M. H. Seymour, and B. R. Webber, “Longitudinally
 6058 invariant k_t clustering algorithms for hadron hadron collisions”, *Nucl. Phys. B* **406**
 6059 (1993) 187, doi:10.1016/0550-3213(93)90166-M.
- 6060 [110] S. D. Ellis and D. E. Soper, “Successive combination jet algorithm for hadron
 6061 collisions”, *Phys. Rev. D* **48** (1993) 3160, doi:10.1103/PhysRevD.48.3160,
 6062 arXiv:hep-ph/9305266.
- 6063 [111] Y. L. Dokshitzer, G. D. Leder, S. Moretti, and B. R. Webber, “Better jet clustering
 6064 algorithms”, *JHEP* **08** (1997) 001, doi:10.1088/1126-6708/1997/08/001,
 6065 arXiv:hep-ph/9707323.
- 6066 [112] M. Wobisch and T. Wengler, “Hadronization corrections to jet cross-sections in deep
 6067 inelastic scattering”, in *Proceedings of the Workshop on Monte Carlo generators for*
 6068 *HERA physics, Hamburg, Germany, April 27-30, 1998*, p. 270. 1998.
 6069 arXiv:hep-ph/9907280.
- 6070 [113] M. Cacciari, G. P. Salam, and G. Soyez, “The anti- k_t jet clustering algorithm”, *JHEP*
 6071 **04** (2008) 063, doi:10.1088/1126-6708/2008/04/063, arXiv:0802.1189.
- 6072 [114] CMS Collaboration, “Identification techniques for highly boosted W bosons that decay
 6073 into hadrons”, *JHEP* **12** (2014) 017, doi:10.1007/JHEP12(2014)017,
 6074 arXiv:1410.4227.
- 6075 [115] CMS Collaboration, “Jet energy scale and resolution in the CMS experiment in pp
 6076 collisions at 8 TeV”, arXiv:1607.03663. Submitted to *JINST*.
- 6077 [116] CMS Collaboration, “Determination of Jet Energy Calibration and Transverse
 6078 Momentum Resolution in CMS”, *JINST* **6** (2011) P11002,
 6079 doi:10.1088/1748-0221/6/11/P11002, arXiv:1107.4277.
- 6080 [117] M. Cacciari, G. P. Salam, and G. Soyez, “FastJet User Manual”, *Eur. Phys. J. C* **72**
 6081 (2012) 1896, doi:10.1140/epjc/s10052-012-1896-2, arXiv:1111.6097.
- 6082 [118] M. Cacciari and G. P. Salam, “Dispelling the N^3 myth for the k_t jet-finder”, *Phys.*
 6083 *Lett. B* **641** (2006) 57, doi:10.1016/j.physletb.2006.08.037,
 6084 arXiv:hep-ph/0512210.
- 6085 [119] M. Cacciari and G. P. Salam, “Pileup subtraction using jet areas”, *Phys. Lett. B* **659**
 6086 (2008) 119, doi:10.1016/j.physletb.2007.09.077, arXiv:0707.1378.
- 6087 [120] CMS Collaboration, “Jet energy scale and resolution performances with 13 TeV data”,
 6088 CMS Detector Performance Note CMS-DP-2016-020, CERN, 2016.
- 6089 [121] CMS Collaboration, “Jet Performance in pp Collisions at 7 TeV”, CMS Physics
 6090 Analysis Summary CMS-PAS-JME-10-003, CERN, 2010.
- 6091 [122] CMS Collaboration, “Search for resonant pair production of Higgs bosons decaying to
 6092 $b\bar{b}$ and $\tau^+\tau^-$ in proton-proton collisions at $\sqrt{s} = 8$ TeV”, CMS Physics Analysis
 6093 Summary CMS-PAS-EXO-15-008, CERN, 2015.

- 6094 [123] CMS Collaboration, “Identification of b-quark jets with the CMS experiment”, *JINST*
 6095 **8** (2013) P04013, doi:10.1088/1748-0221/8/04/P04013, arXiv:1211.4462.
- 6096 [124] W. Waltenberger, “Adaptive Vertex Reconstruction”, Technical Report
 6097 CMS-NOTE-2008-033, CERN, 2008.
- 6098 [125] CMS Collaboration, “Measurement of $B\bar{B}$ Angular Correlations based on Secondary
 6099 Vertex Reconstruction at $\sqrt{s} = 7$ TeV”, *JHEP* **03** (2011) 136,
 6100 doi:10.1007/JHEP03(2011)136, arXiv:1102.3194.
- 6101 [126] CMS Collaboration, “Performance of b tagging at $\sqrt{s} = 8$ TeV in multijet, $t\bar{t}$ and
 6102 boosted topology events”, CMS Physics Analysis Summary CMS-PAS-BTV-13-001,
 6103 CERN, 2013.
- 6104 [127] CMS Collaboration, “Identification of b quark jets at the CMS Experiment in the LHC
 6105 Run 2”, CMS Physics Analysis Summary CMS-PAS-BTV-15-001, CERN, 2016.
- 6106 [128] CMS Collaboration, “Missing transverse energy performance of the CMS detector”,
 6107 *JINST* **6** (2011) P09001, doi:10.1088/1748-0221/6/09/P09001, arXiv:1106.5048.
- 6108 [129] CMS Collaboration, “Performance of the CMS missing transverse momentum
 6109 reconstruction in pp data at $\sqrt{s} = 8$ TeV”, *JINST* **10** (2015) P02006,
 6110 doi:10.1088/1748-0221/10/02/P02006, arXiv:1411.0511.
- 6111 [130] J. Bauer, “Prospects for the Observation of Electroweak Top-Quark Production with
 6112 the CMS Experiment”. PhD thesis, Karlsruher Institut für Technologie, 2010.
- 6113 [131] CMS Collaboration, “Studies of jet mass in dijet and W/Z + jet events”, *JHEP* **05**
 6114 (2013) 090, doi:10.1007/JHEP05(2013)090, arXiv:1303.4811.
- 6115 [132] S. D. Ellis, C. K. Vermilion, and J. R. Walsh, “Techniques for improved heavy particle
 6116 searches with jet substructure”, *Phys. Rev. D* **80** (2009) 051501,
 6117 doi:10.1103/PhysRevD.80.051501, arXiv:0903.5081.
- 6118 [133] S. D. Ellis, C. K. Vermilion, and J. R. Walsh, “Recombination Algorithms and Jet
 6119 Substructure: Pruning as a Tool for Heavy Particle Searches”, *Phys. Rev. D* **81**
 6120 (2010) 094023, doi:10.1103/PhysRevD.81.094023, arXiv:0912.0033.
- 6121 [134] J. Thaler and K. Van Tilburg, “Identifying Boosted Objects with N-subjettiness”,
 6122 *JHEP* **03** (2011) 015, doi:10.1007/JHEP03(2011)015, arXiv:1011.2268.
- 6123 [135] CMS Collaboration, “Search for massive resonances decaying into pairs of boosted
 6124 bosons in semi-leptonic final states at $\sqrt{s} = 8$ TeV”, *JHEP* **08** (2014) 174,
 6125 doi:10.1007/JHEP08(2014)174, arXiv:1405.3447.
- 6126 [136] CMS Collaboration, “Search for massive resonances in dijet systems containing jets
 6127 tagged as W or Z boson decays in pp collisions at $\sqrt{s} = 8$ TeV”, *JHEP* **08** (2014)
 6128 173, doi:10.1007/JHEP08(2014)173, arXiv:1405.1994.
- 6129 [137] CMS Collaboration, “V Tagging Observables and Correlations”, CMS Physics Analysis
 6130 Summary CMS-PAS-JME-14-002, CERN, 2014.
- 6131 [138] CMS Collaboration, “Jet algorithms performance in 13 TeV data”, CMS Physics
 6132 Analysis Summary CMS-PAS-JME-16-003, CERN, 2014.

- 6133 [139] M. Bahr et al., “Herwig++ Physics and Manual”, *Eur. Phys. J. C* **58** (2008) 639,
6134 [doi:10.1140/epjc/s10052-008-0798-9](https://doi.org/10.1140/epjc/s10052-008-0798-9), [arXiv:0803.0883](https://arxiv.org/abs/0803.0883).
- 6135 [140] CMS Collaboration, “Search for heavy resonances decaying into a vector boson and a
6136 Higgs boson in final states with charged leptons, neutrinos, and b quarks”,
6137 [arXiv:1610.08066](https://arxiv.org/abs/1610.08066). Submitted to *Phys. Lett. B*.
- 6138 [141] M. Czakon, D. Heymes, and A. Mitov, “High-precision differential predictions for
6139 top-quark pairs at the LHC”, *Phys. Rev. Lett.* **116** (2016) 082003,
6140 [doi:10.1103/PhysRevLett.116.082003](https://doi.org/10.1103/PhysRevLett.116.082003), [arXiv:1511.00549](https://arxiv.org/abs/1511.00549).
- 6141 [142] M. J. Oreglia, “A study of the reactions $\psi' \rightarrow \gamma\gamma\psi'$ ”. PhD thesis, Stanford University,
6142 1980. SLAC Report SLAC-R-236.
- 6143 [143] CMS Collaboration, “Measurement of the single-top-quark *t*-channel cross section in
6144 pp collisions at $\sqrt{s} = 7$ TeV”, *JHEP* **12** (2012) 035,
6145 [doi:10.1007/JHEP12\(2012\)035](https://doi.org/10.1007/JHEP12(2012)035), [arXiv:1209.4533](https://arxiv.org/abs/1209.4533).
- 6146 [144] P. Kant et al., “HatHor for single top-quark production: Updated predictions and
6147 uncertainty estimates for single top-quark production in hadronic collisions”, *Comput.
6148 Phys. Commun.* **191** (2015) 74, [doi:10.1016/j.cpc.2015.02.001](https://doi.org/10.1016/j.cpc.2015.02.001),
6149 [arXiv:1406.4403](https://arxiv.org/abs/1406.4403).
- 6150 [145] CMS Collaboration, “Measurement of W^+W^- and ZZ production cross sections in pp
6151 collisions at $\sqrt{s} = 8$ TeV”, *Phys. Lett. B* **721** (2013) 190,
6152 [doi:10.1016/j.physletb.2013.03.027](https://doi.org/10.1016/j.physletb.2013.03.027), [arXiv:1301.4698](https://arxiv.org/abs/1301.4698).
- 6153 [146] T. Gehrmann et al., “ W^+W^- Production at Hadron Colliders in Next to Next to
6154 Leading Order QCD”, *Phys. Rev. Lett.* **113** (2014) 212001,
6155 [doi:10.1103/PhysRevLett.113.212001](https://doi.org/10.1103/PhysRevLett.113.212001), [arXiv:1408.5243](https://arxiv.org/abs/1408.5243).
- 6156 [147] CMS Collaboration, “Energy Calibration and Resolution of the CMS Electromagnetic
6157 Calorimeter in pp Collisions at $\sqrt{s} = 7$ TeV”, *JINST* **8** (2013) P09009,
6158 [doi:10.1088/1748-0221/8/09/P09009](https://doi.org/10.1088/1748-0221/8/09/P09009), [arXiv:1306.2016](https://arxiv.org/abs/1306.2016).
- 6159 [148] CMS Collaboration, “CMS Luminosity Measurement for the 2015 Data Taking
6160 Period”, CMS Physics Analysis Summary CMS-PAS-LUM-15-001, CERN, 2015.
- 6161 [149] CMS Collaboration, “CMS Luminosity Based on Pixel Cluster Counting - Summer
6162 2013 Update”, CMS Physics Analysis Summary CMS-PAS-LUM-13-001, CERN, 2013.
- 6163 [150] M. Cacciari et al., “The $t\bar{t}$ cross-section at 1.8 and 1.96 TeV: A Study of the
6164 systematics due to parton densities and scale dependence”, *JHEP* **04** (2004) 068,
6165 [doi:10.1088/1126-6708/2004/04/068](https://doi.org/10.1088/1126-6708/2004/04/068), [arXiv:hep-ph/0303085](https://arxiv.org/abs/hep-ph/0303085).
- 6166 [151] S. Catani, D. de Florian, M. Grazzini, and P. Nason, “Soft gluon resummation for
6167 Higgs boson production at hadron colliders”, *JHEP* **07** (2003) 028,
6168 [doi:10.1088/1126-6708/2003/07/028](https://doi.org/10.1088/1126-6708/2003/07/028), [arXiv:hep-ph/0306211](https://arxiv.org/abs/hep-ph/0306211).
- 6169 [152] M. Botje et al., “The PDF4LHC Working Group Interim Recommendations”,
6170 [arXiv:1101.0538](https://arxiv.org/abs/1101.0538).
- 6171 [153] S. Alekhin et al., “The PDF4LHC Working Group Interim Report”, [arXiv:1101.0536](https://arxiv.org/abs/1101.0536).

- 6172 [154] A. D. Martin, W. J. Stirling, R. S. Thorne, and G. Watt, “Parton distributions for the
 6173 LHC”, *Eur. Phys. J. C* **63** (2009) 189, doi:10.1140/epjc/s10052-009-1072-5,
 6174 arXiv:0901.0002.
- 6175 [155] R. D. Ball et al., “Impact of heavy quark masses on parton distributions and LHC
 6176 phenomenology”, *Nucl. Phys. B* **849** (2011) 296,
 6177 doi:10.1016/j.nuclphysb.2011.03.021, arXiv:1101.1300.
- 6178 [156] A. L. Read, “Presentation of search results: The CL_S technique”, *J. Phys. G* **28**
 6179 (2002) 2693, doi:10.1088/0954-3899/28/10/313.
- 6180 [157] T. Junk, “Confidence level computation for combining searches with small statistics”,
 6181 *Nucl. Instrum. Meth. A* **434** (1999) 435, doi:10.1016/S0168-9002(99)00498-2,
 6182 arXiv:hep-ex/9902006.
- 6183 [158] G. Cowan, K. Cranmer, E. Gross, and O. Vitells, “Asymptotic formulae for
 6184 likelihood-based tests of new physics”, *Eur. Phys. J. C* **71** (2011) 1554,
 6185 doi:10.1140/epjc/s10052-011-1554-0, 10.1140/epjc/s10052-013-2501-z,
 6186 arXiv:1007.1727. [Erratum: *Eur. Phys. J. C* **73** (2013) 2501].
- 6187 [159] A. Wald, “Tests of Statistical Hypotheses Concerning Several Parameters When the
 6188 Number of Observations is Large”, *Transactions of the American Mathematical
 6189 Society* **54** (1943) 426.
- 6190 [160] S. S. Wilks, “The Large-Sample Distribution of the Likelihood Ratio for Testing
 6191 Composite Hypotheses”, *Ann. Math. Statist.* **9** (03, 1938) 60,
 6192 doi:10.1214/aoms/1177732360.
- 6193 [161] E. Gross and O. Vitells, “Trial factors or the look elsewhere effect in high energy
 6194 physics”, *Eur. Phys. J. C* **70** (2010) 525, doi:10.1140/epjc/s10052-010-1470-8,
 6195 arXiv:1005.1891.
- 6196 [162] F. Garwood, “Fiducial Limits for the Poisson Distribution”, *Biometrika* **28** (1936)
 6197 437, doi:10.1093/biomet/28.3-4.437.
- 6198 [163] CMS Collaboration, “Search for a massive resonance decaying into a Higgs boson and
 6199 a W or Z boson in hadronic final states in proton-proton collisions at $\sqrt{s} = 8$ TeV”,
 6200 *JHEP* **02** (2016) 145, doi:10.1007/JHEP02(2016)145, arXiv:1506.01443.
- 6201 [164] CMS Collaboration, “Search for new resonances decaying via WZ to leptons in
 6202 proton-proton collisions at $\sqrt{s} = 8$ TeV”, *Phys. Lett. B* **740** (2015) 83,
 6203 doi:10.1016/j.physletb.2014.11.026, arXiv:1407.3476.
- 6204 [165] CMS Collaboration, “Search for massive WH resonances decaying into the $\ell\nu b\bar{b}$ final
 6205 state at $\sqrt{s} = 8$ TeV”, *Eur. Phys. J. C* **76** (2016) 237,
 6206 doi:10.1140/epjc/s10052-016-4067-z, arXiv:1601.06431.
- 6207 [166] CMS Collaboration, “Search for Narrow High-Mass Resonances in Proton-Proton
 6208 Collisions at $\sqrt{s} = 8$ TeV Decaying to a Z and a Higgs Boson”, *Phys. Lett. B* **748**
 6209 (2015) 255, doi:10.1016/j.physletb.2015.07.011, arXiv:1502.04994.
- 6210 [167] ATLAS Collaboration, “Search for high-mass diboson resonances with boson-tagged
 6211 jets in proton-proton collisions at $\sqrt{s} = 8$ TeV with the ATLAS detector”, *JHEP* **12**
 6212 (2015) 055, doi:10.1007/JHEP12(2015)055, arXiv:1506.00962.

- 6213 [168] CERN, “LHC commissioning schedule”. <https://lhcb-commissioning.web.cern.ch/lhc-commissioning/schedule/LHC-long-term.htm>.
- 6214
- 6215 [169] H. C. Kästli et al., “CMS barrel pixel detector overview”, *Nucl. Instrum. Meth. A* **582** (2007) 724, doi:10.1016/j.nima.2007.07.058, arXiv:physics/0702182.
- 6216
- 6217 [170] Y. Allkofer et al., “Design and performance of the silicon sensors for the CMS barrel pixel detector”, *Nucl. Instrum. Meth. A* **584** (2008) 25, doi:10.1016/j.nima.2007.08.151, arXiv:physics/0702092.
- 6218
- 6219
- 6220 [171] H. C. Kästli et al., “Design and performance of the CMS pixel detector readout chip”, *Nucl. Instrum. Meth. A* **565** (2006) 188, doi:10.1016/j.nima.2006.05.038, arXiv:physics/0511166.
- 6221
- 6222
- 6223 [172] E. Bartz, “The 0.25um Token Bit Manager Chip for the CMS Pixel Readout”, in *Proceedings of the 11th Workshop on Electronics for LHC and Future Experiments, Heidelberg, Germany, 12–16 September, 2005*, p. 153. 2005. doi:10.5170/CERN-2005-011.153.
- 6224
- 6225
- 6226
- 6227 [173] S. König et al., “Assembly of the CMS pixel barrel modules”, *Nucl. Instrum. Meth. A* **565** (2006) 62, doi:10.1016/j.nima.2006.04.081.
- 6228
- 6229 [174] M. Pernicka et al., “The CMS Pixel FED”, in *Proceedings of the Topical Workshop on Electronics for Particle Physics, Prague, Czech Republic, 3–7 September, 2007*, p. 487. 2007. doi:10.5170/CERN-2007-007.487.
- 6230
- 6231
- 6232 [175] K. A. Gill et al., “Progress on the CMS Tracker control system”, in *Proceedings of the 11th Workshop on Electronics for LHC and Future Experiments, Heidelberg, Germany, 12–16 September, 2005*, p. 353. 2005. doi:10.5170/CERN-2005-011.353.
- 6233
- 6234
- 6235 [176] B. G. Taylor, “Timing distribution at the LHC”, in *Proceedings of the 8th Workshop on Electronics for LHC Experiments, Colmar, France, 9–13 September, 2002*, p. 63. 2002. doi:10.5170/CERN-2002-003.63.
- 6236
- 6237
- 6238 [177] D. Kotliński et al., “The control and readout systems of the CMS pixel barrel detector”, *Nucl. Instrum. Meth. A* **565** (2006) 73, doi:<http://dx.doi.org/10.1016/j.nima.2006.04.065>.
- 6239
- 6240
- 6241 [178] J. Troska et al., “Optical readout and control systems for the CMS tracker”, *IEEE Trans. Nucl. Sci.* **50** (2003) 1067, doi:10.1109/TNS.2003.815124.
- 6242
- 6243 [179] P. Placidi, A. Marchioro, and P. Moreira, “CMS Tracker PLL Reference Manual”, Manual, CERN EP Microelectronics Group, 2000.
- 6244
- 6245 [180] P. M. H. Correia, A. Marchioro and J. Schrader, “Delay25 - A 4 channel 1/2 ns programmable delay line”, Manual, CERN EP Microelectronics Group, 2005.
- 6246
- 6247 [181] C. Paillard, C. Ljuslin, and A. Marchioro, “The CCU25: a network oriented communication and control unit integrated circuit in a 0.25 μ m CMOS technology”, in *Proceedings of the 8th Workshop on Electronics for LHC Experiments, Colmar, France, 9–13 September, 2002*, p. 174. 2002. doi:10.5170/CERN-2002-003.174.
- 6248
- 6249
- 6250
- 6251 [182] Ryd, Anders and Stroiney, Steve and Das, Souvik and Ecklund, Karl, “CMS Pixel Online Software and Calibrations”, Manual, Cornell University, CERN, 2012.
- 6252

- 6253 [183] V. Brigljevic et al., “Using XDAQ in application scenarios of the CMS experiment”,
6254 *eConf C* **0303241** (2003) MOGT008, [arXiv:hep-ex/0305076](https://arxiv.org/abs/hep-ex/0305076).
- 6255 [184] CMS Collaboration, “A library developed for the CMS data acquisition system at
6256 CERN”, Manual, CERN, 2012.
- 6257 [185] CMS Collaboration, “Operational Issues of the Present CMS Pixel Detector”, *PoS*
6258 **Vertex2012** (2013) 051.
- 6259 [186] N. Wermes, L. Rossi, P. Fischer, and T. Rohe, “Pixel Detectors, From Fundamentals
6260 to Applications”. Springer-Verlag, 2006.
- 6261 [187] CMS Pixel Collaboration, “Status of the CMS Pixel detector”, *JINST* **4** (2009)
6262 P03019, [doi:10.1088/1748-0221/4/03/P03019](https://doi.org/10.1088/1748-0221/4/03/P03019).
- 6263 [188] CMS Collaboration, “CMS Pixel status”, *Nucl. Instrum. Meth. A* **731** (2013) 13,
6264 [doi:10.1016/j.nima.2013.04.001](https://doi.org/10.1016/j.nima.2013.04.001).
- 6265 [189] A. Dominguez et al., “The Pixel Detector Upgrade”, CMS Technical Design Report
6266 CERN-LHCC-2012-016. CMS-TDR-11, CERN, 2012.
- 6267 [190] CMS Collaboration, “Pilot system for the Phase 1 pixel upgrade of CMS”, *PoS*
6268 **VERTEX2015** (2015) 018.
- 6269 [191] L. Feld et al., “The DC-DC conversion power system of the CMS Phase-1 pixel
6270 upgrade”, *JINST* **10** (2015) C01052, [doi:10.1088/1748-0221/10/01/C01052](https://doi.org/10.1088/1748-0221/10/01/C01052).
- 6271 [192] H. Kästli, “Frontend electronics development for the CMS pixel detector upgrade”,
6272 *Nucl. Instrum. Meth. A* **731** (2013) 88, [doi:10.1016/j.nima.2013.05.056](https://doi.org/10.1016/j.nima.2013.05.056).
- 6273 [193] A. Starodumov, P. Berger, and M. Meinhard, “High rate capability and radiation
6274 tolerance of the PROC600 readout chip for the CMS pixel detector”, *JINST* **12**
6275 (2017) C01078.
- 6276 [194] J. Troska et al., “Prototype pixel optohybrid for the CMS phase 1 upgraded pixel
6277 detector”, *JINST* **7** (2012) C01113, [doi:10.1088/1748-0221/7/01/C01113](https://doi.org/10.1088/1748-0221/7/01/C01113).
- 6278 [195] L. M. Caminada, “Study of the Inclusive Beauty Production at CMS and Construction
6279 and Commissioning of the CMS Pixel Barrel Detector”. PhD thesis, Zurich, ETH,
6280 2010.